Experimental Investigations of the Interaction of Multi-GeV Particles with Strong Crystalline Fields

- and Applications in High Energy Beamlines

Ulrik Mikkelsen

Institute for Storage Ring Facilities, ISA, University of Aarhus,
DK–8000 Aarhus C, Denmark
and
SL-EA, CERN,
CH-1211 Geneva 23, Switzerland
E-mail: ulrik@dfi.aau.dk, ulrik.mikkelsen@cern.ch

October 29, 1997

The front-page shows the CERN accelerator complex:

LEP The Large Electron Positron collider

SPS The Super Proton Synchrotron

PS and PSB The Proton Synchrotron and its Booster

LEAR The Low Energy Antiproton Ring

AAC The Antiproton Accumulator Complex

ISOLDE The Isotope Separator OnLine DEvice

LINAC The LINear ACcelerators for protons and lead ions

The experiments described in this thesis were performed in the North Area of the SPS.

Contents

Part I
Preface

This thesis presents some of the results obtained over three years in experiments done at the CERN SPS. The main topic is an investigation of the interactions of light and heavy particles as well as photons with strong crystalline fields. As will become apparent, a number of the phenomena related to these interactions are characteristic of the interaction with strong electromagnetic fields, be it in a crystal or elsewhere. On the one hand, these phenomena therefore present useful tools in the investigations of effects in Quantum Electrodynamics related to the presence of extremely strong fields. On the other hand, interactions of charged particles with the strong crystalline fields in a curved crystal open the possibility of deflecting particles with smaller radii of curvature than by any other method. This means that interactions with strong crystalline fields are not only interesting in terms of fundamental processes, they can also in many cases be applied as solutions in beam-transport systems and in particle production.

A number of investigations connected to the basic effects as well as applications are presented. The presence of radiative cooling in radiation emission processes in crystals is shown experimentally in remarkable agreement with theoretical estimates. It turns out that electrons can obtain a smaller divergence after the radiation event, whereas positrons can not. A proof-of-principle experiment to produce and detect a linearly polarized beam of high energy photons is treated and the existence of coherent resonances for pair production in strong crystalline fields is discussed. These phenomena in the pair production and radiation emission processes in crystals are examined for values of the 'recoil-parameter', χ, close to 1 and thus represent investigations of emission processes in extremely strong fields. In such fields the scaling properties of e.g. the emission probability with the energy of the incident particle changes completely compared to the behaviour in weaker fields. Moreover, the emission probability is rapidly increased compared to in an amorphous substance when χ is brought above $\simeq 1$. This is due to the coherent effect of the fields from the crystal nuclei. This increase has for instance found an application in the construction of a trigger where it is important that the ratio of nuclear interaction length to radiation length is as large as possible.

Based on discrepancies between theoretical and experimental values for pair production, especially for the heavier crystals, it is suggested that at least part of this disagreement can be understood in terms of inhibiting effects which so far have not been included in calculations. These effects include those of the Landau-Pomeranchuk type; effects which have recently been shown to be of importance for radiation emission from energetic particles in crystals.

Furthermore, important questions in recent years investigations connected to deflection of charged particles in crystals are answered experimentally: The influence of radiation damage on the deflection properties of a crystal and the advantage of using crystals made from materials of high nuclear charge. With respect to the radiation tolerance it is found that only at very high fluences will a crystalline deflector of silicon suffer from radiation damage. Secondly, it is shown that the hitherto succesful model to describe the efficiency as a function of the bending angle of a silicon crystal predicts the observed variation of efficiency with angle for germanium as well. These results give confidence in the utilization of crystals as beam elements and extraction devices in present as well as planned accelerators.

Part II
Introduction

1 Outline

Apart from this outline, part II is a general introduction to fundamental terms in channeling which are being used throughout the thesis. These include the continuum approximation, doughnuts, surface transmission and dechanneling as well as a short section on the electromagnetic fields present in crystals. A discussion of the applicability of classical concepts in channeling is included to show that classical concepts are adequate to describe the motion of particles of sufficiently high energy.

Part III treats some aspects of the theory of strong field effects. These are fundamental to the understanding of the pair production experiments presented in part IV. First, basic terms are presented and a short historical review of the topic is given. Further, a brief introduction to channeling radiation is given with comments on the various physical effects as a motivation for the work presented later and to put it in context. Through a calculation of the typical photon energies emitted by an electron in a magnetic field it is shown that classical electrodynamics becomes insufficient at high energies and the term critical field is introduced and related to the fields present in crystals. A fundamental concept, the enhancement, is introduced and its connection to the so-called formation length and coherence length is explained. Then a short resume of the emission observed from the passage of e.g. electrons in thin amorphous foils (the Bethe-Heitler mechanism) is given and subsequently the Constant Field Approximation (CFA) is found by means of a substitution in the classical spectrum and in a non-rigourous approach to the so-called semi-classical approximation, illuminating the importance of the formation length. It is stressed that the onset of quantum corrections to the classical synchrotron emission can be parametrized by an invariant, χ, and that this parameter separates domains of completely different behaviour with respect to photon emission probabilities as well as pair production probabilities. The extension of the CFA introduced recently which shows coherent resonances in radiation emission as well as in pair production as a function of angle to the axis is explained and the chapter is closed with a discussion of effects that may disturb the emission process and thus suppress the enhancement.

Part IV, which describes the experiments, starts with a description of the experimental equipment: the beam, counters, drift chambers, data acquisition system and electronics. A section on the analysis procedure includes first a discussion of special problems related to the use of drift chambers as position sensitive detectors and second

a discussion on the reconstruction of photon energies by means of the pair spectrometer which consists of four drift chambers and a magnet. Backgrounds which contribute the largest factor to the systematic uncertainties is treated thoroughly. Radiative loss of the produced particles in the crystal after the conversion is analyzed to determine its influence on the measured spectra for pair production. A number of cross-checks performed in order to ensure a correct understanding of the results obtained from e.g. the pair spectrometer are discussed - among others a Monte Carlo simulation. Emphasis in this part is on the analysis of results for pair production, since for this type of analysis nearly all aspects of the analysis for radiation emission are treated as well.

The presentation of the results is divided into five sections: Enhanced radiation emission, radiative cooling, polarization and pair production on and off axis. Recent results for radiation emission by electrons and positrons on and near an axis in diamond is treated with emphasis on the measurement of the average number of photons emitted, the so-called photon multiplicity. This leads to the section of radiative cooling where the high multiplicity measured under axial alignment can be explained by a self-amplifying effect of radiative cooling. Furthermore, the first direct evidence of radiative cooling is given by a comparison of incident and exit angles for different energies lost to the emitted photon. It is shown - in remarkable agreement with theoretical estimates - that a reduction or increase in angular spread of the beam will result, depending on the charge of the incident particle. Next, a proof-of-principle experiment to investigate the production and detection of polarized photons in the 100 GeV region is described. The first of the sections on pair production treats the results obtained for photons aligned with the axis for which there exists earlier measurements with which the results are compared. The second section on pair production treats the behaviour when the photon is aligned with the (110) plane at an angle to the axis. This section also presents completely new results, testing the theory of coherent resonances in the strings-of-strings region and thus the behaviour of QED in periodic strong fields.

Thus, in the first half of the thesis, radiation and pair production at high energies will be investigated with the main topic being the examination of a special kind of quantum effect - emission under recoil and the connected rapid increase in pair production probability. In the beginning it is shown that this is the only remaining quantum effect at sufficiently high energies, since the motion of the particle becomes more classical the higher the energy such that only the emission process can be affected by quantum corrections.

In the second half of the thesis, the investigation of the strong fields in crystals is directed towards deflection of charged particles by means of these fields in curved crystals. Part V presents the additional theoretical concepts needed for this discussion. Among these the centrifugal term, critical radius and dechanneling fraction related to

the motion in a curved crystal are introduced and the modification of the dechanneling length is treated. This leads to a model for the deflection efficiency where parameters relevant for the construction of a bent crystal as a beam element are emphasized. A main point in recent years discussion on crystal-bending, the effect of radiation damage on the deflection properties of a bent crystal is then treated.

Part VI presents the experimental conditions for the investigation of the deflection properties with a treatment of the beam, the alignment method, the bending jig and the data acquisition system. Subsequently the two experiments with a strongly irradiated silicon crystal and with a germanium crystal are presented where each part is dealt with through a discussion of the experimental procedure, the analysis and the results. Emphasis here will be on the understanding of the mechanisms responsible for the deflection of charged particles in crystals and on the mechanisms that may disturb this effect. This is done to be able to make as reliable predictions as possible about for example the deflection efficiencies at hitherto unexplored energies. It is shown that a relatively simple model gives results in remarkably good agreement with experiment and a compact analytical expression is given as an estimate of the deflection efficiency.

Both of the parts IV and VI on experimental results are ended with a discussion of the possible areas of application for the efficient production of pairs and radiation emission in a crystal and for the deflection phenomenon, respectively. It is stressed that some of the subjects mentioned are already introduced in running experiments and a few outlooks at new proposed applications of the strong crystalline fields are given.

Part VII summarizes and concludes from the experiments. It is shown that the results presented offer new insight in the field of interactions with strong crystalline fields, both from the aspect of fundamental physics and related to the field of applications. Furthermore, an outlook is given where recent experiments are taken as an indication of the future development of the field.

2 Channeling

Channeling was discovered in the early 1960's as an unusually large range of positively charged particles in crystal lattices[1]. Shortly after, Lindhard [2] explained the observations and gave a theoretical basis for essentially all subsequent work in the field of channeling. The field has since evolved enormously into such diverse branches as e.g. channeling radiation, defect studies and nuclear physics and presents a number of interesting applications in high energy physics as well.

2.1 Continuum approximation and transverse energy

Consider a charged particle incident on a single crystal. For small angles of incidence to the crystal axis or plane, the correlated scattering off the atoms in the lattice can be approximated by 'smearing' the potential arising from the screened nuclei along the direction and then calculating the motion of the particle as arising from the averaged transverse potential, $V(x)$, where x is the transverse coordinate. As pictured in figure 1 the result of adding all the binary collisions along the string can be well approximated by using a continuum along the string.

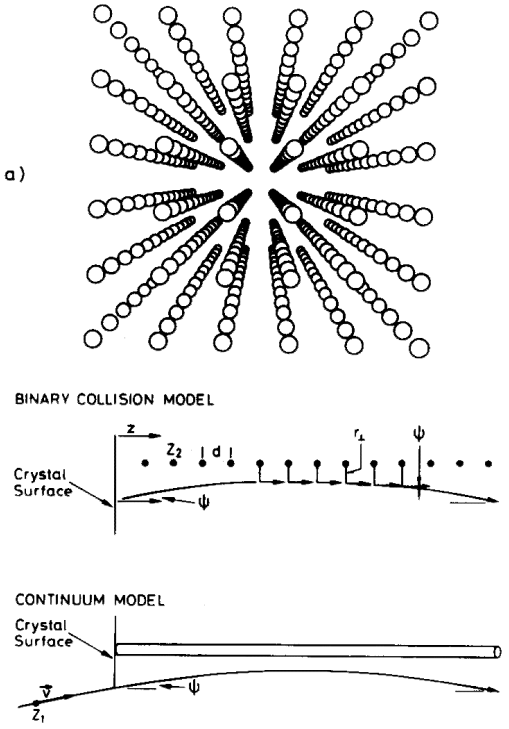

Figure 1: *a) Perspective view of the positions of individual atoms in a simple cubic lattice. Below, the deflection of an incident particle by a string of atoms in b) the binary collision picture and c) the continuum picture [3].*

[1]It was, however, predicted much earlier by Stark [1].

This is the basis of the continuum approximation introduced by Lindhard [2]. Thus, in a transverse potential the motion is determined by [4], [5]:

$$\frac{d}{dt}\gamma m\dot{x} = -\frac{d}{dx}V(x(t)) \tag{1}$$

where m is the mass of the penetrating particle, $\gamma = 1/\sqrt{1 - v^2/c^2}$ is the relativistic Lorentz factor, v being the particle speed, c the speed of light and the dot denotes differentiation with respect to time, t. The energy conservation:

$$\frac{d}{dt}\gamma mc^2 = -\frac{d}{dt}V(x(t)) \tag{2}$$

leads to:

$$\gamma(t)m\ddot{x} = -(1 - (\frac{\dot{x}}{c})^2)\frac{d}{dx}V \tag{3}$$

which reduces to

$$\gamma m\dot{x}^2/2 + V(x(t)) = E_\perp \tag{4}$$

if γ is taken as constant ($V/\gamma mc^2 \approx 10^{-9}$) and the quantity $(\dot{x}/c)^2 \simeq E_\perp/\gamma mc^2$ is neglected. Thus, in the absence of uncorrelated scattering in the crystal, the transverse energy, $E_\perp$, is almost exactly conserved.

The transverse potential or field obtained by averaging in the longitudinal direction can be obtained from different approximations, e.g. the Lindhard 'standard' potential [2], the Molière [6] or the Doyle-Turner potential [7]. The Doyle-Turner potential has been found to be the most precise in predictions of channeling radiation (see section 3.2, p. 16) which is very sensitive to the shape of the potential [8] - this potential has therefore been used in the calculations of precise quantities used for this work. However, Doyle and Turner have not given data for heavy crystals - data of this type have become available only recently [9]. The potentials are valid for a static lattice, but thermal effects can be introduced by a Gaussian distribution of the atoms on the lattice, with a one-dimensional thermal vibration amplitude, u_1.

2.2 Quantum effects of motion at relativistic velocities?

Bohr [10] introduced the parameter $\kappa_B = 2Z_1Z_2\alpha/\beta$ to characterize an atomic collision, where α is the fine-structure constant, Z_1e is the charge of the penetrating particle, Z_2e is the charge of the nuclei in the lattice and $\beta = v/c$ is the speed in units of the speed of light, c. For $\kappa_B > 1$, i.e. low velocities, a classical description of the collision suffices whereas for $\kappa_B < 1$ quantum effects must be taken into consideration. This condition becomes even more strict when considering a screened potential [2]. In this picture, quantum tunneling to classically forbidden regions would thus become more and more probable the higher the velocity. However, a 'transverse kappa', $\kappa_\perp =$

$[(M/m)Z_1Z_2^{1/3}a_0/d]^{1/2}$ was found to separate the classical ($\kappa_\perp > 1$) and quantum ($\kappa_\perp < 1$) regions [2] for channeled particles, where a_0 is the Bohr radius, d the atomic spacing along the string, M denotes the mass of the penetrating particle and m the rest-mass of the electron. Thus for protons and heavier particles the motion is classical, but more surprisingly the formula for $\kappa_\perp$ was shown [11] to be valid for relativistic particles if for M the relativistic mass of the particle was used. Thus even electrons and positrons behave classically if the energy is sufficiently high.

2.3 Critical angles and doughnuts

The condition for the particle to be channeled is expressed by Lindhard's critical angle, ψ_c:

$$\frac{1}{2}pv\psi^2 \leq \frac{1}{2}pv\psi_c^2 = U_0 \;\Leftrightarrow\; \psi \leq \psi_c = \sqrt{\frac{2U_0}{pv}} \tag{5}$$

where ψ and p are the angle to the crystallographic direction and the momentum of the penetrating particle, respectively. Eq. (5) states that the transverse energy must be smaller than the height of the transverse potential, U_0. In table 1 critical angles calculated from the 'standard' potential are given. The axial and planar critical angles are given as $\psi_1 = \sqrt{4Z_1Z_2e^2/pvd}$ and $\psi_p = \sqrt{4Z_1Z_2e^2Nd_pCa_{\mathrm{TF}}/pv}$ respectively, where Nd_p is the planar density of atoms, N being the atomic density and d_p the planar spacing, $C \simeq \sqrt{3}$ is Lindhard's constant and a_{TF} is the Thomas-Fermi screening distance.

	Si	Ge	W
$\psi_p^{\langle 110\rangle}$	5	6	11
$\psi_1^{\langle 110\rangle}$	14	21	31

Table 1: *Critical angles in μrad for Si, Ge and W at 1 TeV*

If the incident particle furthermore is in a transverse potential well all along the direction of motion, e.g. trapped between planes, the particle will follow the lattice. However, a channeled particle will not necessarily follow the lattice strictly - an axially channeled positively charged particle, for example, is not confined to move along a single string, but may scatter off many strings on its way through the crystal. On the other hand, an axially channeled negatively charged particle will in nearly all cases be in a bound motion around one string. Thus, in some cases the guidance becomes less strict even though the particle is still channeled, see figure 2, curve (2).

In case the particle is channeled, close-encounter processes such as wide-angle scattering or nuclear interactions are strongly reduced for positively charged particles and

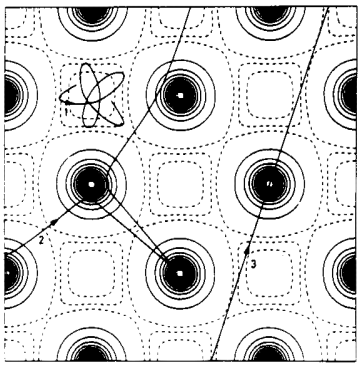

Figure 2: *Contours of the crystal potential of Ge* $\langle 100 \rangle$ *with channeled (1), (2), and non-channeled (3) particles [3].*

enhanced for negatively charged particles. This is due to the redistribution of the initially uniform beam resulting from the interaction with the crystalline field. In other words, the negatively charged particles are attracted to the strings or planes of atoms where the nuclear and electronic density is high, and the positively charged particles are repelled from these regions due to the different shapes of the potential, see figure 3.

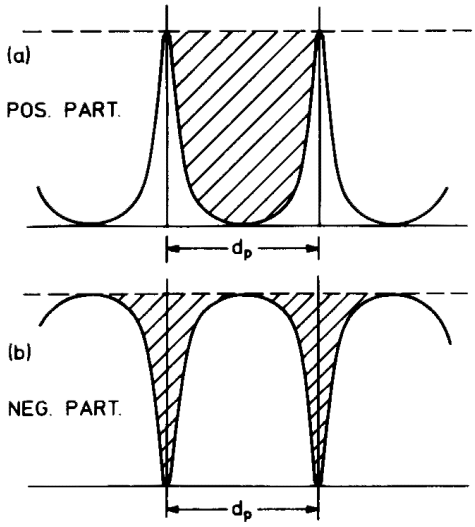

Figure 3: *Transverse planar continuum potentials for positively and negatively charged particles showing the basic difference in shape [3].*

It is worth noting in this context that the continuum approximation is valid not only for channeled particles, but up to angles of the order of several tens of ψ_1 for the extinction of close-encounter processes. This for instance manifests itself in the doughnut scattering region which extends far beyond the axial critical angle, ψ_1: Along

an axial direction, an incident, positively charged particle in a beam scatters off many atomic strings and while the polar angle to the string is conserved in the continuum approximation, the azimuthal angle will change and the beam will reach an equilibrium state giving a uniform doughnut in angle space after the ensemble of particles has traversed a length given for $\psi \leq \psi_1$ by [2]:

$$\lambda_{\perp}^{\text{in}} \simeq \frac{4\psi}{\pi^2 N d a_{\text{TF}} \psi_1^2} \tag{6}$$

and for $\psi \geq \psi_1$ roughly as [12], [13]:

$$\lambda_{\perp}^{\text{out}} \approx 4\lambda_{\perp}^{\text{in}} \frac{\psi^2 u_1}{\psi_1^2 a_{\text{TF}}} \tag{7}$$

The fact that doughnuts exist for angles larger than ψ_1, implying that the continuum approximation is valid also for non-channeled particles, was not realized until the late 70's, when experiments with pions and protons at roughly 10 GeV were performed [13], [14], [15].

2.4 Surface transmission and dechanneling

When entering and passing a crystal, a particle with a sufficiently small angle to fulfil the channeling criterion, eq. (5), may not channel through the entire crystal after all. The two mechanisms responsible for losses of these (potentially) channeled particles to non-channeled - also known as above-barrier or random particles - are the surface transmission and dechanneling.

2.4.1 Surface transmission

One type of selection of channeled particles originates from the distribution of particles in the transverse direction, which can be taken as initially uniform on the scale of planar distances. When the particle enters the crystal, it acquires a potential energy depending on the entry position with respect to the plane. This potential energy is gained at the expense of longitudinal kinetic energy, such that the transverse kinetic energy it had outside the crystal, $pv\psi^2/2$, is conserved and adds to the potential energy to give

$$E_{\perp} = \frac{1}{2} pv\psi_{\text{in}}^2 + U(r_{\perp}^{\text{in}}) \tag{8}$$

The result is that most of the particles incident close to the plane can not channel and have an increased probability of scattering off a nucleus. The distance, x_c, from the plane at which this happens has been determined for protons as being roughly equal to $x_c = 2.5u_1$ [16]. Likewise, a particle incident on the crystal with a relatively large angle ψ to the particular crystallographic direction, enters the transverse potential in a high-lying state which means that it may not channel.

Therefore the available phase-space, (x, ψ), for channeling is restricted by the effective critical angle as a function of impact position in the transverse plane and the minimum distance to the plane - this is the basis of the so-called surface transmission, i.e. the fraction of the incident beam which can channel. Note that even for a completely parallel beam, the surface transmission is $\varepsilon_{\mathrm{S}} = 1 - 2 \cdot 2.5u_1/d_p \simeq 0.6 - 0.9$ and that the surface transmission can be increased by cooling the crystal.

To estimate the angular part[2] of the surface transmission for a non-parallel beam one may calculate e.g. the planar critical angle by use of the 'standard' potential, ψ_p, and assume a 'top-hat' model where particles within ψ_p are accepted and particles outside are rejected. For a beam with a gaussian angular distribution of RMS σ_ψ the surface transmission is then approximately $\mathrm{erf}(\psi_p/\sqrt{2}\sigma_\psi)$, where $\mathrm{erf}(x)$ is the error function, see ref. [17, p. 163], tabulated e.g. in [18]. This procedure has an estimated relative error in the surface transmission of a few percent, e.g. for a beam with $\sigma_\psi = \psi_p$ in Ge (110) one gets 68%, whereas a proper calculation using the Doyle-Turner potential yields 64%.

Summarizing, the approximate surface transmission for a planar channeled high energy proton or positron is

$$\varepsilon_{\mathrm{S}} \simeq (1 - \frac{2 \cdot 2.5u_1}{d_p})\mathrm{erf}(\frac{\psi_p}{\sqrt{2}\sigma_\psi}) \tag{9}$$

This equation has not been used in the following - instead more accurate values have been found by use of the Doyle-Turner potential.

2.4.2 Dechanneling

According to eq. (5) an increase in the transverse energy will eventually result in the transfer of a channeled particle to the non-channeled beam. This increase is mainly mediated by multiple Coulomb scattering (MCS) on electrons, for which the typical angle scales as $\theta_{\mathrm{MCS}} \propto Z_1/\beta cp$. Therefore it is expected that the characteristic length, L_{D}, over which this transfer takes place scales as pv/Z_1 since $\theta^2_{\mathrm{MCS}}/\psi_c^2 \propto LZ_1/pv$. Since channeled, positively charged particles are kept away from the atoms along the crystallographic direction, the multiple Coulomb scattering is reduced with respect to the scattering in an amorphous material. Therefore, at sufficiently high energy, a typical channeled proton can traverse crystals with lengths of several tens of centimeters without being transferred to the random beam.

The length, L_{D}, over which a planar channeled beam of protons has been reduced to the fraction 1/e of the initial intensity by transfer to the random beam is given for

[2] The angular and spatial parts are not independent, but as an estimate one can approximate the available ellipse in phase-space by a suitably chosen square.

$\gamma \gg 1$ by [19], [20]:

$$L_{\mathrm{D}} = \frac{256}{9\pi^2} \frac{pv}{\ln(2\gamma mc^2/I) - 1} \frac{a_{\mathrm{TF}} d_p}{Z_1 e^2} \tag{10}$$

where I is the ionisation potential. This approach ignores the dependence on the temperature. Nevertheless eq. (10) has been shown to be in good agreement with measured values of L_{D} at room temperature [20].

As expected from the MCS, the dechanneling length increases proportionally to pv/Z_1 and with the width of the channel, d_p. For Si (110), Ge (110) and W (110) the dechanneling lengths[3] at 450 GeV and 7 TeV are given in table 2.

	Si (110)	Ge (110)	W (110)
450 GeV (SPS)	0.22	0.19	0.18
7.0 TeV (LHC)	2.9	2.5	2.2

Table 2: *Dechanneling lengths in m for (110) planes in Si, Ge and W according to eq. (10).*

2.5 Crystalline fields

Macroscopic electric fields, as e.g. those in a standing wave RF-cavity in a synchrotron, can reach values in the region of $\mathcal{E}_{\mathrm{RF}}$=5-10 MV/m. Similarly, the magnetic fields in a large superconducting magnet is of the order of 10-20 Tesla and even pulsed (non-destructive) magnets are limited to less than 100 Tesla [22]. In comparison, one can evaluate the field at the surface of a bare nucleus by use of $\mathcal{E} = Z_2 e/r^2$, $r \simeq 1.2 \cdot A^{1/3}$ fm and $A \simeq 5Z_2/2$ which leads to

$$\mathcal{E} = Z_2 \alpha \frac{\lambda\!\!\!^{-2}}{r^2} \cdot \mathcal{E}_0 \simeq 550 \cdot Z_2^{1/3} \cdot \mathcal{E}_0 \quad \text{with} \quad \mathcal{E}_0 = \frac{mc^2}{e\lambda\!\!\!^{-}} = 1.32 \cdot 10^{18} \text{ V/m} \tag{11}$$

where $\lambda\!\!\!^{-} = \hbar/mc$ is the Compton wavelength, A is the number of nucleons, r the nuclear radius and $\alpha = e^2/\hbar c \simeq 1/137$ is the fine-structure constant. $\mathcal{E}_0$ is the so-called critical field. So the bare nuclear field is a very strong, but microscopic, field. Moreover, in an atom or a solid the nuclear field is screened by the electrons such that the extension of the strong field is limited.

In the case of crystalline fields, however, the field in the continuum approximation extends over the entire length of the crystal which can be a macroscopic distance. As a very simple estimate, the peak electric field can be given in terms of the potential height[4], U_0, evaluated from e.g. the Doyle-Turner potential or the Molière potential,

[3] For the calculations of numerical values, numbers like d_p have been taken from [21]

[4] It is customary for singly charged particles to let the distinction between potential and potential energy appear from the context.

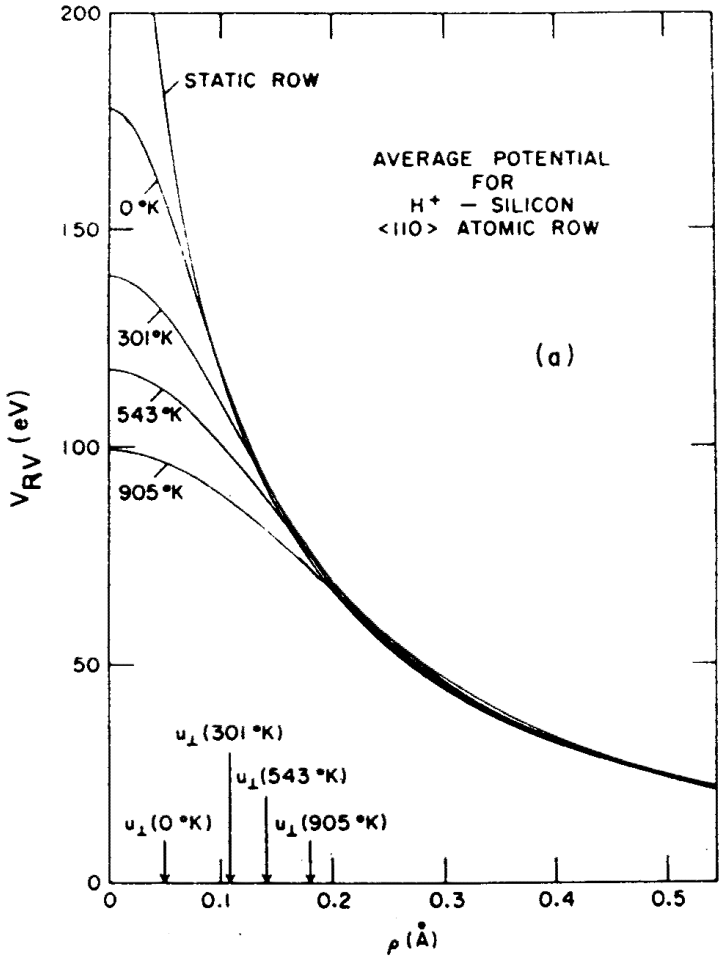

Figure 4: *Transverse potential for Si* $\langle 110 \rangle$ *at different temperatures in the Molière approximation. Note the variation of the potential height and* $u_\perp = \sqrt{2}u_1$ *with temperature [21].*

see figure 4, as

$$\mathcal{E} \simeq \frac{U_0}{e \cdot u_1} \tag{12}$$

which is of the order of $3 \cdot 10^{10}$ V/cm corresponding to 10^4 T for planes in a silicon crystal and 10^{12} V/cm corresponding to $3 \cdot 10^5$ T for an axis in W. These fields are not only large - they are macroscopic! According to figure 4, the dependence of the peak electric field on temperature is to a first approximation fairly well described by eq. (12) - a result that will be benefitted from in the evaluation of the threshold for strong field effects later. However, already at this point it worth noting that eq. (12) in some sense is the simplest possible estimate, one could equally well have used $u_\perp = \sqrt{2}u_1$ or other values instead of u_1. It should therefore not be surprising that estimates based on eq. (12) only yield qualitative results.

In the following, since only relativistic particles ($\gamma > 160$) are treated, the Lorentz force implies an equivalent force resulting from $\boldsymbol{\mathcal{E}}$ and $\boldsymbol{B} = 1/c \cdot \boldsymbol{v} \times \boldsymbol{\mathcal{E}}$ such that $\mathcal{E} \simeq B$ and therefore electric and magnetic fields will be used alternately. Furthermore, energy and momentum will be taken as the same since $p \gg mc$.

Part III
Strong field effects

The theory of strong field effects is very complicated and therefore the following is an attempt to explain key concepts and effects with emphasis on the physics content rather than mathematical detail. The important parameters for the determination of enhancement - the emission probability for an aligned crystal in units of the random value - are given and variation with angle, temperature and energy is sought described through simple approximations. In many cases this enables a quick estimate of many of these dependencies at the expense of accuracy. Closing the chapter is a discussion of effects that may reduce the enhancement.

3 Some fundamental concepts and history

In the beginning of this section it is argued on the basis of crossing symmetry that pair production and radiation emission can be treated on equal footing - a fact which is used frequently in the following. Subsequently, a short discussion of some key elements in channeling radiation is presented. This is done to put the following strong field effects in perspective and to illustrate that as the energy of the impinging particle is increased from the few MeV region to the multi-GeV region a sequence of appropriate descriptions is needed. These are quantum theory, classical electrodynamics, variation of longitudinal channeling motion due to relativistic effects and the main concept in what follows: The emission under recoil or, in other words, the reverse action of the photon on the emitting particle. Finally, a brief introduction to the development of the concept of strong fields in other branches of physics is given.

3.1 Pair production and radiation emission

When passing matter, a photon can convert into an electron-positron pair in the electromagnetic field of a nucleus or in rarer cases near a target electron. The presence of the external field is required to conserve energy and momentum in the creation process. Likewise, radiation emission can take place when a charged particle interacts with the external field.

By crossing symmetry pair production and radiation emission are two connected examples of the same physical process - consider for instance turning the Feynman diagram for bremsstrahlung a quarter of a turn to obtain the diagram for pair production, see figure 5.

Therefore the descriptions of the two processes are closely connected and e.g. their total cross sections differ only by a factor 7/9 due to different kinematic properties in the final state, see section 4.4, p. 27.

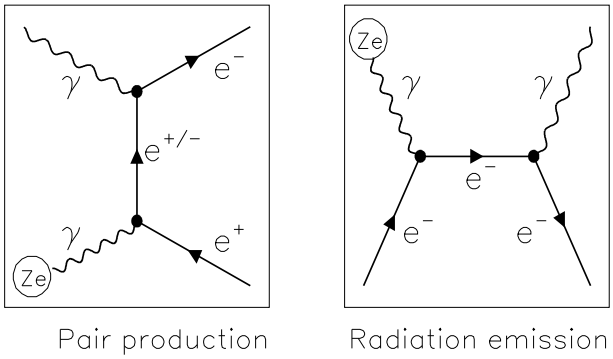

Figure 5: *Feynman graphs for pair production and radiation emission showing the interaction with the virtual photon of the nuclear field.*

The radiation from relativistic particles is mainly propagating within a narrow cone of width $1/\gamma$ along the forward direction of the emitting particle [23]. Based on the same mechanism, a pair created by a high energy photon is typically moving inside an angle $1/\gamma$ to the direction of the initial photon where γ is understood as $\hbar\omega/mc^2$. This typical value is of interest in connection with formation lengths to be discussed later.

In the following, since radiation emission, having a classical analogue, is often easier to explain in pictures, this case will be used occasionally even in cases where the prime goal is to explain the mechanisms governing pair production.

3.2 Channeling radiation

A consequence of the continuum approximation is a separation of the transverse and (average) longitudinal motion, such that a conserved transverse energy can be introduced. This means that transitions from one state in the transverse potential to another becomes possible under the emission or absorption of radiation, the so-called channeling radiation (ChR), also called Kumakhov radiation [24]. The reason why it is possible to detect this radiation even though the scale of the potential is in eV, is that ChR can be in the MeV range due to Lorentz-boosts. Qualitatively, the fields in the rest-frame of the emitting particle are boosted by γ and the Doppler-transformation back to the laboratory boosts the emitted photon by an additional 2γ. Yet, the level spacing or the characteristic photon frequency for a planar channeled positron decreases roughly as $\gamma^{-1/2}$ (see eq. (14) later) such that the emitted energy scales as $\gamma^{3/2}$ and can achieve very high values. This behaviour is true in the dipole approximation where the longitudinal velocity can be considered constant, i.e. as long as the transverse momentum is non-relativistic [5]. However, when the transverse momentum, $p_\perp$, gets relativistic

the longitudinal velocity, $\beta_z c$, is affected since:

$$\beta_z^2 = \beta^2 - \beta_x^2 = 1 - \frac{1}{\gamma^2}(1 + (\frac{p_\perp}{mc})^2) \tag{13}$$

such that the longitudinal motion becomes non-constant, even in the absence of direct forces in this direction. An explanation for this can be found in the interaction of the particle possessing a relativistic transverse velocity with the magnetic field in the average rest-frame of the longitudinal motion: This field imposes a force in the longitudinal direction which depends on the transverse velocity, i.e. the transverse position and direction in the channel, such that a 'figure-eight' motion results. In figure 6 is shown

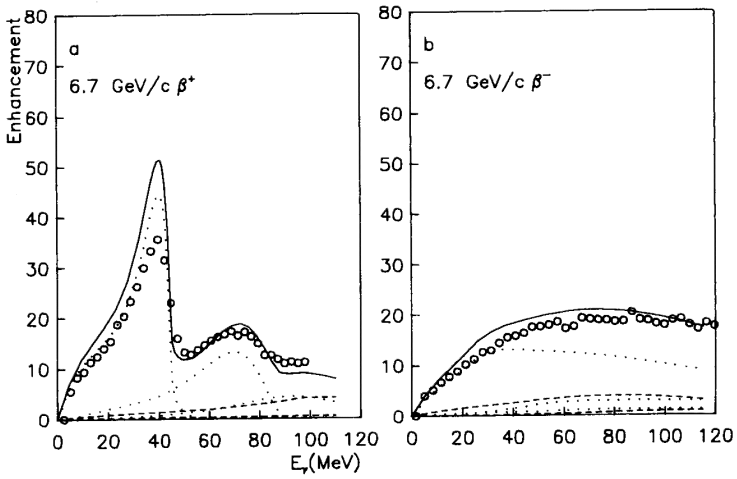

Figure 6: *Enhancement spectra for channeling radiation produced by 6.7 GeV/c e^+ (a) and e^- (b) incident along the (110) plane in a 0.1 mm Si crystal (open dots). The solid line represents the theoretically expected value [25].*

an experimental spectrum compared to a calculation where the relativistic transverse motion has been accounted for [25].

Traditionally, channeling radiation is separated into three groups depending on the energy of the penetrating particle (electron or positron, see e.g. [26]): At low energies, 10-100 MeV, the transverse potential contains a limited number of states when quantized such that a classical description is insufficient. At intermediate energies, 100 MeV-1 GeV, the number of states is so high that, according to the correspondence principle, a classical calculation of the spectrum is a good approximation. At high energies, above 1 GeV, the dipole approximation is no longer justified because the longitudinal velocity varies as a result of the relativistic effect mentioned above. This means that as the energy is increased, the appropriate description varies from a quantized transverse potential, through the dipole approximation in classical electrodynamics to a stage where transverse relativistic effects must be taken into account. It is the aim in the first part of the following to show that yet another stage is achieved when

the multi-GeV region is considered, namely where the quantum recoil of the emitting particle must be taken into account to describe the observed emission spectra. This effect is closely connected to the onset of a rapid rise in pair production probability with increasing energy [14].

In contrast to coherent bremsstrahlung, a significant difference between particles of opposite charges comes into play for ChR: The transverse potential for positively charged particles is very well approximated by a harmonic potential, whereas on the other hand, the reverse potential of a negatively charged particle is very anharmonic, see figure 3. This means that emission spectra for positrons exhibit peaks due to the almost harmonic motion[5], while emission spectra from electrons in general are more or less structureless at high energies. Furthermore, the redistribution of the channeled particles resulting from the attraction/repulsion by the atomic strings for negatively/positively charged particles will increase/decrease the multiple Coulomb scattering contributing to the difference between their emission spectra. These effects have been carefully investigated in the 80's at relatively high energies, a few GeV, and very good agreement with calculations based on classical electrodynamics was found [25].

3.3 Historical introduction to strong fields

3.3.1 The Klein paradox

Shortly after the introduction of the Dirac equation an apparent paradox appeared, due to the work of Klein [27]. In his paper, Klein showed that for 'very large values' of a potential-step, an incident electron appears with a negative energy after the passage of the step. Sauter, following Bohr's intuition, later showed that the value of the electric field required was $\mathcal{E}_0 = mc^2/e\lambda\!\!\!^{-}$, and concluded that 'Felder von dieser Stärke experimentell herzustellen, ist natürlich unmöglich.[6]' [28]. The paradox was resolved as being due to pair production which was realized after Dirac's postulate of the origin of the negative energy solutions to his equation and the following discovery of positrons by Anderson in 1932 [29]. Feynman [30] treated in 1948 a classical analogue of the Klein paradox where the principle of least action opens the opportunity of a classical particle moving backwards in time. The field required was found to be $\mathcal{E}_{\rm cl} = 2mc^2/er_e$, where $r_e = \alpha\lambda\!\!\!^{-}$ is the classical electron radius, i.e. $\mathcal{E}_{\rm cl}$ is $2 \cdot 137$ times higher than the so-called critical field, $\mathcal{E}_0$. In the same paper the usual pair production is ascribed to a tunneling process over the Compton wavelength into a potential of height $2mc^2/e$ during which the positron for the first time becomes the time-reversed electron.

[5]The peaks shown in figure 6 are actually the result of an interplay between the effect of anharmonicity and the non-constant longitudinal motion.

[6]'To produce fields of this strength experimentally, is obviously impossible.'

3.3.2 Coherent effects in Quantum Electrodynamics

Quantum Electrodynamics (QED) began in the late 1920's and soon after Klein and Nishina [31] calculated the scatter of photons off electrons using the new formalism. Later, in 1934, Bethe and Heitler [32] calculated the cross section for radiation emission and pair production in an amorphous substance using perturbation theory. In 1935, Williams [33, p. 38-39] considered the interference phenomena arising from scattering off two or more atoms in a solid. He concluded enhanced or suppressed radiation emission following the nature of the interference.

For the theory of the newly discovered synchrotron radiation [34], [35], Schwinger had in the late 40's in a brief discussion in his paper on classical synchrotron radiation considered the onset of quantum corrections, a work he elaborated upon for pair production in 1951 [23]. This work was extended by Robl and Toll in 1952 (see [36], [37] and references therein), Sokolov, Klepikov and Ternov in 1953 (see footnote in [38]), Klepikov and Schwinger in 1954 [38] [39] and Baier and Katkov in 1967 [40] who treated emission from 'particles of arbitrary spin moving in an arbitrary electromagnetic field'.

In 1955, Dyson and Überall [41] suggested the increase of bremsstrahlung emission for electrons penetrating e.g. a lead crystal close to a crystalline direction, compared to incidence along a random direction. Note that this actually is a precursor to the strong field theory, since contrary to the following coherence theories, the enhancement along crystallographic directions was predicted to be significantly larger than one. Shortly after this, the theory of coherent bremsstrahlung and coherent pair production, was developed, see e.g. [42].

3.3.3 Strong field effects

It was not until in the early 80's, that Kimball and Cue [43] and Baier, Katkov and Strakhovenko [44] predicted that the yield of pairs is increased when produced in a crystal where a high energy photon is incident with a direction close to an axis. Initially, the two groups did not agree on the magnitude of the yields, only on the behaviour with energy, and the requirement of Kimball and Cue of having a channeled electron after the pair creation was relaxed by Baier *et al.* who also considered electrons created in above-barrier states [45]. The effect was connected to the 'recoil-parameter', χ, being larger than 1 (see later).

The reason for this new behaviour at high energies can be seen as the possibility of achieving an enormously high field in the restframe of the emitting or produced particle. Emission and conversion probabilities can be calculated in this frame where the strong crystalline fields are Lorentz-boosted by γ and therefore become comparable to or even stronger than the critical field [46]. As Lindhard has phrased it: '[The electric forces on a channeled, relativistic electron in a single crystal has] an effect simulating that of an exceedingly large magnetic field of slowly varying magnitude.' [47] or the almost

equivalent by Baier: '...the crystal turns out to be a unique proving ground where quantum electrodynamics in an intense external field can be investigated.' [46].

The experiments described in the first part of this thesis thus provide a test of the radically different behaviour (of which there is a discussion later, see e.g. table 4, p. 33) of pair production and radiation emission, i.e. QED effects, in strong fields.

3.4 Do critical fields exist in nature?

Three areas apart from the interaction of high energy particles with crystals are influenced by strong electromagnetic fields:

1. Compact stellar remnants
2. Heavy ion collisions
3. Intense laser pulses

In compact stellar remnants such as e.g. neutron stars, the magnetic fields present in the original star are 'compressed' along with the gravitational contraction of the star when it collapses. Therefore these objects can have extremely intense fields and observations have concluded the existence of pulsars with $\kappa = B/B_0 = Be\lambda\!\!\!^{-}/mc^2$ up to $\simeq$0.3, possibly up to $\simeq$0.7 [48]. The observation of such fields relies on a measurement of the rate of change of the rotation period times the period, $P\dot{P}$, which through a model of the radiation process for a rotating magnetic dipole relates to the field as: $B = \sqrt{P\dot{P}} \cdot 3.2 \cdot 10^{19}$ Gauss. Therefore, in order to understand the radiation processes giving rise to pulsars, an understanding of radiation and pair production in large fields is necessary and investigations are pursuing critical effects such as photon-splitting, pair annihilation to a single photon and two-photon pair production [49].

Calculations show that for a combined charge $Z >$173 in a collision of two heavy ions, the most strongly bound electron will achieve a binding energy equal to twice the restmass of the electron whereby spontaneous pair creation becomes possible [50], [51]. Thus a critical field can be produced with the drawback that in order to overcome the Coulomb barrier between the nuclei the energy must be high and therefore the collision time is short, $\leq 10^{-21}$s, affecting the time in which the nuclear molecule can be considered as one nucleus.

The detection of characteristic lines (in a spectrum of counts as a function of energy) in the production of e^+, e^- pairs in collisions of heavy nuclei, hinted at the possible existence of a light, neutral particle (possibly the axion, see [52]). Since then, the interest in pair production processes in critical fields expanded. In the light of these experiments, an investigation was done using a crystalline target to achieve high fields in the search for this light, neutral particle. No evidence was found for the so-called

'Darmstadton' of mass $\approx$1.8 MeV/c^2, but in a comparison with a Monte-Carlo simulation, an excess of 9 counts over 1 was found in the range 2.1 to 3.5 MeV/c^2 [53]. Later heavy ion experiments have also cast some doubt on the interpretation of the characteristic lines as being the signature of a decay and not an experimental artifact [54].

Finally, very strong fields are available in intense laser pulses, as from e.g. the petawatt laser system under construction at the Lawrence Livermore National Laboratory. This laser will have an intensity of the order 10^{21} W/cm^2 corresponding to an electric field of the order of 10^{14} V/m [55].

4 Emission in an electromagnetic field

As shown by Schwinger [38] and later extended by Lindhard [47], the radiation spectrum including quantum effects can be obtained by a substitution in the classical spectrum. In Lindhards approach it originates from the replacement of the Thomson cross section for scattering of light on free electrons by the Klein-Nishina cross section. By use of this substitution rule the Constant Field Approximation is obtained in the following and for comparison the Bethe-Heitler yields for radiation emission and pair production in an amorphous substance is shown. It is noted that the same substitution rule applies for the coherence length in going from the correct quantal expression to the classical limit. Finally, a discussion on the relation between the formation length and the enhancement is included.

4.1 Classical or quantum description?

A critical field can be defined as a field in which a singly charged particle gains one electron-restmass in energy over a distance equal to the Compton wavelength. Not surprisingly, classical physics is not adequate for the description of interactions with such a field and one must use the full Dirac equation or the so-called semi-classical approximation where the motion of the emitting particle is treated classically whereas the emission process is treated by quantum theory. It turns out that the changeover from the region where quantum effects are unimportant to the region where they dominate can be described by one parameter, χ, and that relevant parameters such as pair production probabilities, critical energy of photon emission and radiative energy loss change drastically in their scaling with γ when going from one domain to the other.

There are three possible quantum effects in synchrotron radiation [47] [56]:

1. The electron motion can be quantized
2. The quantum recoil can be significant
3. The spin can affect the emission

Concerning the quantization of the electron motion in a crystal one may estimate the number of levels in a harmonic oscillator (as for a planar channeled positron) of potential height U_0 to be

$$n = \frac{1}{\hbar}\sqrt{\frac{\gamma m U_0}{2}}\frac{d_p}{2} \propto \sqrt{\gamma} \tag{14}$$

which is of the order of a thousand at 150 GeV. In the case of an unbound electron in a magnetic field one may evaluate the level distance with respect to the energy, $\hbar\omega/E$, by use of $L = n\hbar$ and the Lorentz force which leads to

$$\frac{1}{n} = \frac{\hbar\omega}{E} = \frac{B}{B_0}\frac{m^2}{p^2} = \kappa\frac{m^2}{p^2} \tag{15}$$

where B_0 is the critical (or Schwinger- [23], [38]) magnetic field:

$$B_0 = \frac{mc^2}{e\lambda\!\!\!^{-}} = 4.4 \cdot 10^9 \text{ T} \tag{16}$$

corresponding to the electric field $\mathcal{E}_0 = 1.32 \cdot 10^{16}$ V/cm and κ is the actual field in units of the critical field. Clearly, even for channeled particles and for large κ the motion is classical according to the correspondence principle as long as the electron is ultra-relativistic such that $\gamma \gg \sqrt{\kappa}$.

Concerning the recoil in the emission process, a classical calculation of the synchrotron radiation emission in a magnetic field leads to a spectrum which extends to $\omega_c \simeq 3\gamma^3 eB/p = 3\gamma^3\omega_0$, i.e.

$$\frac{\hbar\omega_c}{E} \simeq 3\gamma\frac{B}{B_0} = 3\gamma\kappa \equiv 3\chi \tag{17}$$

which for sufficiently large γ exceeds 1 such that the classically calculated radiation spectrum extends beyond the available energy [38], [57], [58][7]. In this case a quantum treatment is obviously necessary: '..the condition for quantum effects to be unimportant is that the momenta of the radiated quanta be small compared with the electron momentum.' [38]. Note that χ in eq. (17) is one of the 3 invariants that can be constructed from the electromagnetic field tensor, $F_{\mu\nu}$, and the current four-vector j_μ, see e.g. [56, p. 365]. Therefore γB is the same in any reference system and thus it is reasonable to transform to the electron frame. In this reference system by definition the Lorentz factor of the electron is 1 and the field present in the frame of the laboratory is boosted by $\gamma = E/mc^2$, where E is the kinetic energy of the electron in the laboratory. This means that the field in the rest-frame of the electron can become critical for achievable γ-values, $B = \gamma B_{\text{lab}}$.

[7]The exact coefficient, here taken as 3, is a matter of definition and is different from 3 in some cases [37].

What happens to eq. (17) if the recoil is taken into account? Let in this section the barred values denote the values where recoil (momentum $\hbar\omega/c$ lost to the photon) is taken into account and unbarred values denote variables where this is not the case. Then, following the notation of Jackson's estimate [57, section 14.4]:

$$\overline{\gamma} = \gamma(1 - \frac{\hbar\omega}{E}) \quad \Rightarrow \quad \overline{\rho} = \rho(1 - \frac{\hbar\omega}{E}) \tag{18}$$

where $E = \overline{E} = \gamma mc^2$ is the initial energy of the projectile and $\overline{\gamma}mc^2 = E - \hbar\omega$ such that

$$\overline{\omega} = E \cdot \frac{\omega}{E - \hbar\omega} \tag{19}$$

Thus the critical frequency will be

$$\overline{\omega}_c = 3\overline{\gamma}^2\gamma\overline{\omega} = \omega_c(1 - \frac{\hbar\omega}{E}) \tag{20}$$

since the radiation cone is limited by γ whereas the particle moves with velocity $\overline{\beta}c = c\sqrt{1 - 1/\overline{\gamma}^2}$. Suppose now the radiation emitted has the critical frequency, $\hbar\omega = \hbar\overline{\omega}_c$, then:

$$\frac{\hbar\overline{\omega}_c}{\overline{E}} = \frac{\hbar\omega_c}{E}(1 + \frac{\hbar\omega_c}{E})^{-1} \tag{21}$$

which is always less than 1 such that the conflict is removed, even if the estimate excluding recoil leads to $\hbar\omega_c/E > 1$. Note also that in the limit $\hbar\omega_c/E \ll 1$ the usual behaviour is obtained, $\hbar\omega_c/E \simeq \hbar\overline{\omega}_c/\overline{E}$ and that $\hbar\overline{\omega}_c/\overline{E}$ approaches 1 when $\chi \to \infty$.

From the above follows that the parameter which decides whether one should take quantum effects into account is χ. The quantum limit with emission under recoil is reached for $\chi \gg 1$, whereas for $\chi \ll 1$ the classical limit where $\hbar\omega \ll E$ is obtained. Already at $\chi \simeq 0.1$ the quantum effects appear and for $\chi \simeq 0.2$ the intensity calculated by use of the formulas for emission under recoil is half of the value found from classical electrodynamics [56, p. 186-187]. For an energy of 150 GeV in $\langle 110 \rangle$ Ge the parameter is $\chi \simeq 0.8$ [46].

Concerning the influence of spin on the radiation emission the contribution can be found by a substitution rule as shown in section 4.6, p. 29.

4.2 Coherence- and formation-lengths

The terms coherence- and formation-lengths are essential to the description of radiation and pair production in the nuclear field (for the Bethe-Heitler process e.g. when modified due to the Landau-Pomeranchuk effect, section 6.1, p. 37) and in the continuum field of a crystal axis or plane.

Photon emission or pair production for incidence close to a crystalline direction, becomes much more probable than emission in the corresponding amorphous substance. The measure of this increase is called the enhancement, see also the definition in section 8.5, p. 56. The formation length gives the approximate scaling behaviour of the enhancement, since only the scattering amplitudes within the formation length can add coherently. As shown below, the formation length increases with the energy of the penetrating particle, thus it can be expected that the enhancement rises for increasing energy. However, a 'self-suppression' due to the deflection in the strong field, eventually decreases the yield for increasing energy.

4.2.1 Coherence length

The coherence length is given for emission of radiation as [59]:

$$\lambda_{\text{coh.}}^{\text{rad}} = \frac{2\gamma^2 c}{\omega^*} = \frac{2E(E-\hbar\omega)}{\hbar\omega mc^2}\not{\lambda} \quad \text{with} \quad \omega^* = E \cdot \frac{\omega}{E-\hbar\omega} \simeq \omega \tag{22}$$

calculated by use of the minimum longitudinal momentum transfer to the nucleus, $q_{\parallel} = p_1 - p_2 - \hbar\omega/c$ and using $\lambda_{\text{coh.}} = \hbar/q_{\parallel}$. Note that ω^* coincides with $\overline{\omega}$ from eq. (19), i.e. the last approximation in eq. (22) is in the classical or recoil-less limit, $\hbar\omega \ll E$.

For pair production the coherence length becomes:

$$\lambda_{\text{coh.}}^{\text{pair}} = \frac{2\gamma^2 c}{\omega^{\#}} = \frac{2\xi_+\xi_-\hbar\omega}{mc^2}\not{\lambda} \quad \text{with} \quad \omega^{\#} = \frac{\omega}{\xi_+\xi_-} \tag{23}$$

where $\xi_{\pm}$ is defined as $E_{\text{e}\pm}/\hbar\omega$ with $E_{\text{e}\pm}$ being the energy of the electron or positron and $\gamma \equiv \hbar\omega/mc^2$. Note that $\lambda_{\text{coh.}}^{\text{pair}}$ increases with increasing energy of the pair, whereas $\lambda_{\text{coh.}}^{\text{rad}}$ decreases with increasing energy of the emitted photon for fixed energy of the radiating particle - this turns out to be important for the Landau-Pomeranchuk effect (section 6.1, p. 37). Note the similarity between the two coherence lengths when expressed as functions of γ, ω^* and $\omega^{\#}$.

An alternative derivation shows the dependence on energy more clearly: For the emission of photons one can derive (within a factor 2π since the argument is not given in reciprocal space) the coherence length, $\lambda_{\text{coh.}}^{\text{rad}}$, in the classical limit, $\hbar\omega \ll E$, as the distance it takes to separate the incoming electron and the photon by one photon-wavelength:

$$c\lambda_{\text{coh.}}^{\text{rad}}\left(\frac{1}{v} - \frac{1}{c}\right) = \lambda_{\text{photon}} = \frac{2\pi c}{\omega} \;\Leftrightarrow\; \lambda_{\text{coh.}}^{\text{rad}} = 2\pi\frac{2\gamma^2 c}{\omega} = 2\gamma^2\lambda_{\text{photon}} \tag{24}$$

In this case, since $\lambda_{\text{photon}} \propto 1/\hbar\omega$ it is indicated why the coherence length is long for emission of low energy photons.

In the case of pair production, consider the length it takes to separate a created pair transversely by twice the Compton wavelength when emitted with the angle $1/\gamma$:

$$\lambda_{\gamma}^{\text{pair}} = \gamma \cdot \not{\lambda} \tag{25}$$

Therefore, the coherence length increases with the energy of the pair (where, again, γ is understood as $\hbar\omega/mc^2$).

The equations (22), (23) show the coherence length in the lab-frame. In the frame with a Lorentz factor of $\hbar\omega/mc^2$, the coherence length would become Lorentz contracted by γ: $\lambda_{\rm coh.}^{\rm pair}/\gamma = 2\gamma' \not{\chi}/\gamma \simeq \not{\chi}/2$ where $\gamma' \equiv \hbar\omega\xi_+\xi_-/mc^2$. This is roughly what one would expect in a strong field, eq. (16), since for $\kappa = 1$ a pair can be created over $2\not{\chi}$[8]. For the coherence length in the rest-frame of the radiating electron, the emission of $\zeta = \hbar\omega/E$ leads to

$$\frac{\lambda_{\rm coh.}^{\rm rad}}{\gamma} = \frac{2\gamma^* \not{\chi}}{\gamma} = \frac{2\not{\chi}(1-\zeta)}{\zeta} \tag{26}$$

which is $2\not{\chi}$ for $\zeta = \frac{1}{2}$ and decreases with increasing ζ. Here, $\gamma^* = \gamma \cdot (1-\zeta)/\zeta$. Bearing in mind the definition of the critical field, eq. (16), where mc^2 is produced over $\not{\chi}$ it is natural to expect that the formation length is given by the so-called field deflection length, i.e. the length over which the particle is deflected by an angle $1/\gamma$ by the transverse force $F_\perp$:

$$\lambda_\gamma = \frac{\mathcal{E}_0}{\mathcal{E}} \not{\chi} = \frac{\not{\chi}}{\kappa} = \frac{mc^2}{F_\perp} \tag{27}$$

leading to $\lambda_\gamma/\gamma = \not{\chi}/\chi$ such that the effective length for radiation decreases with increasing χ. Thus by setting $\lambda_\gamma = \lambda_{\rm coh.}^{\rm rad}$, according to eq. (26) the diminishing field deflection length leads to a 'preference' for radiation closer to the edge of the spectrum:

$$\zeta = \frac{2\chi}{2\chi + 1} \tag{28}$$

as is indicated in the discussion of critical frequencies, eq. (17). This behaviour with a minor modification is also obtained in the Constant Field Approximation later.

4.2.2 Formation length and enhancement

The formation length is defined as the length which has the main contribution to the matrix element

$$M_{\rm if} = \int V(r) \exp(i\boldsymbol{q}\boldsymbol{r}) dr \tag{29}$$

in perturbation theory where $\boldsymbol{q}$ is the momentum transfer. For a crystal in Ter-Mikaelian's notation [59] this leads, by use of the Golden Rule $w_{\rm if} = 2\not{\chi}|M_{\rm if}|^2\rho_{\rm f}/\hbar$ with $w_{\rm if}$ being the transition probability per unit time and $\rho_{\rm f}$ the density of final states, to:

$$d\sigma = d\sigma_{\rm BH} |\sum_j \exp(\frac{i\boldsymbol{q}\boldsymbol{r}_j}{\hbar})|^2 \tag{30}$$

[8] Alternatively, the length it takes to deflect a created positron of $p = \frac{1}{2}\gamma mc$ by an angle $\theta = 1/\gamma$ with respect to the photon direction in a critical, $\kappa = 1$, B-field is $2\not{\chi}/2$.

where $d\sigma_{\rm BH}$ is the Bethe-Heitler cross section, eq. (33) and $\boldsymbol{r}_j$ are the coordinates of the atoms. Thus, in the case of coherent bremsstrahlung, the formation length is equal to the coherence length, since $q = \hbar/\lambda_{\rm coh.}^{\rm rad}$. According to eq. (30), the usual Bethe-Heitler cross section for an amorphous material (where the additional factor gives the number of atoms N since the $\boldsymbol{r}_j$'s are distributed at random) is modified due to the periodicity of the lattice leading to interference.

From the definition of the coherence length, eq. (23), and the field deflection length, eq. (27), it follows:

$$\chi = 2\frac{\lambda_{\rm sym.}^{\rm pair}}{\lambda_\gamma} \tag{31}$$

where $\lambda_{\rm sym.}^{\rm pair} = \lambda_{\rm coh.}^{\rm pair}(\xi_\pm = 1/2)$. This means that the strong field parameter, χ, is twice the ratio of the 'classical' coherence length and the field deflection length. Therefore, when χ is large, the formation length shortens and consequently (as will be elaborated upon later) the effect is self-suppressing. The equality of coherence- and formation lengths ceases in the CFA once the field is sufficiently strong such that $\chi > 1$, but for $\chi < 1$ the formation length for characteristic photons coincides with the coherence length.

At this point it is useful to show by a qualitative argument why the condition $\chi \geq 1$ is sufficient to create a pair: If the formation length is $\lambda_\gamma = \not{\mathcal{E}}_0/\mathcal{E}$ then the formation time is $\Delta t = mc/e\mathcal{E}$. During this time a pair can be created if the energy conservation is violated by $\Delta E = 2\sqrt{p^2c^2 + m^2c^4} - 2pc \simeq mc^2/\gamma$. Then the Heisenberg uncertainty principle $\Delta E \Delta t \leq \hbar$ implies $mc^2/\gamma\mathcal{E}e\not{\lambda} \leq 1$, i.e. $\chi \geq 1$.

Summarizing, the important point in the context of formation- or coherence-length is the connection to the enhancement of the radiation or pair production with respect to random incidence. The scattering amplitudes along the path covered by the formation zone in an amorphous material add incoherently, but along a crystallographic direction they add coherently such that e.g. the radiation probability increases over that calculated from the incoherent addition.

4.3 An estimate of the threshold for strong field effects

As an estimate of the peak electric field originating from an axis in a crystal, one may set as in eq. (12) $E \simeq U_0/eu_1$, where U_0 is the potential height. From the definition of the critical field and χ, eqs. (16) and (17), then follows that the 'threshold', $\chi = 1$, for the quantum effects is obtained for

$$\hbar\omega_t = \gamma_t mc^2 = mc^2\frac{u_1 mc^2}{U_0\not{\lambda}} \tag{32}$$

where the field becomes critical in the Lorentz-frame boosted with γ_t or $\hbar\omega_t/mc^2$. Table 3 compares the values obtained from eq. (32) with the more accurate ones obtained by

	Estimate, eq. (32)	Baier *et al.* [60]
Si ⟨110⟩, 293K	72 GeV	120 GeV
Ge ⟨110⟩, 280K	52 GeV	70 GeV
Ge ⟨110⟩, 100K	32 GeV	50 GeV
W ⟨110⟩, 293K	10 GeV	22 GeV
W ⟨110⟩, 77K	6 GeV	13 GeV

Table 3: *Comparison of threshold values for the strong field effect from eq. (32) and Baier et al. [60].*

Baier *et al.* [60] in the Constant Field Approximation (CFA, see section 4.6, p. 29). As eq. (32) is a rather crude estimate (one could for example also have used a_{TF} or $\sqrt{2}u_1$ instead of u_1), it is not surprising that there is some disagreement. Moreover, Baier *et al.* have evaluated the energy for which the CFA yields the same as the Bethe-Heitler contribution, whereas here the 'threshold' is defined differently, simply as $\chi = 1$. In any case, the numbers clearly exhibit the same trend.

4.4 The Bethe-Heitler yields

The cross section for radiation emission in an amorphous foil can be found from the Bethe-Heitler formula [32], [61] which is derived in perturbative QED and is approximately given by:

$$\frac{d\sigma}{d\hbar\omega} = \frac{16}{3} Z_2^2 \alpha r_e^2 \frac{1}{\hbar\omega}\left(1 - \frac{\hbar\omega}{E} + \frac{3}{4}\left(\frac{\hbar\omega}{E}\right)^2\right) \ln(183 Z_2^{-1/3}) \tag{33}$$

where $r_e = e^2/mc^2 = \alpha\lambda\!\!\!^{-} = \alpha^2 a_0$ is the classical electron radius, $\alpha = e^2/\hbar c$ the fine-structure constant, a_0 the Bohr radius and the logarithmic factor indicates complete screening, $\gamma \gg 1$. From this and the number density of atoms, n, the radiation length, X_0, can be found

$$\frac{1}{X_0} = n \int_0^E \hbar\omega d\sigma/E = 4 Z_2^2 \alpha n r_e^2 \ln(183 Z_2^{-1/3}) \tag{34}$$

An incident particle statistically loses all but 1/e of its energy by emission of bremsstrahlung in passing a foil of thickness X_0. The radiation probability for emission with an energy between E and E_0 is found as

$$W = 1 - \exp(-\Delta t \cdot W_0) \quad \text{with} \quad W_0 = \int_{E_0}^{E} n \cdot d\sigma \simeq \frac{4}{3}\frac{1}{X_0}\left(\ln\frac{E}{E_0} - \frac{5}{8}\right) \tag{35}$$

where Δt is the thickness of the foil where the radiation takes place and the approximation for W_0 is valid when the incident energy is much larger than the cut-off due to acceptance, $E \gg E_0$.

From W the probability of emitting two photons is calculated according to a Poisson-distribution

$$f(N_\gamma) = \frac{p^{N_\gamma} e^{-p}}{N_\gamma!} \quad \text{with} \quad p = \Delta t W_0(E, E_0) \tag{36}$$

where N_γ is the number of photons. This distribution is in good agreement with photon spectra simulated by GEANT [63] as long as $E \gg E_0$.

In the above approach, the radiation produced by scattering off the target electrons has been neglected since this term is proportional to Z_2 and is small compared to eq. (33). A more accurate expression is thus obtained by replacing Z_2^2 by $Z_2(Z_2+1)$, in good agreement with data [17].

For pair production, the Bethe-Heitler theory [61] gives the number of pairs created per unit length, $N_p = n\sigma$, per relative energy of the electron/positron, $\xi_\pm = E_{e\pm}/\hbar\omega$ as approximately:

$$\frac{dN_p}{d\xi_\pm} = \frac{16}{3} Z_2^2 \alpha r_e^2 n (\frac{3}{4} - \xi_\pm + \xi_\pm^2) \ln(183 Z_2^{-1/3}) \tag{37}$$

or by use of eq. (34) simply

$$\frac{dN_p}{d\xi_\pm} = \frac{1}{X_0}(\xi_+^2 + \xi_-^2 + \frac{2}{3}\xi_+\xi_-) \tag{38}$$

with the total yield

$$N_p = \int_0^1 \frac{dN_p}{d\xi_\pm} d\xi_\pm = \frac{7}{9}\frac{1}{X_0} \tag{39}$$

Note here the similarity between the cross sections for radiation emission and pair production, eqs. (33) and (37), originating from the crossing symmetry of the processes.

4.5 The classical limit of synchrotron radiation

According to classical electrodynamics, the energy radiated per unit frequency (the intensity, I) and unit solid angle by a charged particle in synchrotronic motion can be expressed as [57, p. 670]:

$$\frac{d^2 I}{d\omega d\Omega} = \frac{e^2}{4\pi^2 c} \left| \int_{-\infty}^{\infty} \frac{\boldsymbol{n} \times [(\boldsymbol{n} - \boldsymbol{\beta}) \times \dot{\boldsymbol{\beta}}]}{(1 - \boldsymbol{\beta} \cdot \boldsymbol{n})^2} \exp(i\omega(t - \boldsymbol{n} \cdot \boldsymbol{r}(t)/c)) dt \right|^2 \tag{40}$$

where $\boldsymbol{\beta}(t) = \boldsymbol{v}(t)/c$ and $\boldsymbol{n}$ denotes the direction of photon propagation. Eq. (40) is based on the retarded Lienard-Wiechert potentials and leads to a counting spectrum [58, p. 21] by use of $dN/d\zeta = 1/E\hbar\omega \cdot dP/d\hbar\omega$ where the emitted power is $P = \omega_0 I/2\pi$, $\omega_0 = eB/p$:

$$\frac{dN}{d\zeta} = \frac{\alpha c}{\sqrt{3}\pi \lambda\!\!\!^{-}} \frac{1}{\gamma} [2K_{2/3}(\delta_c) - \int_{\delta_c}^{\infty} K_{1/3}(t) dt] \quad \text{(classical)} \tag{41}$$

where $\delta_c = 2\zeta/3\chi$, $\zeta = \hbar\omega/E$, K_ν is the modified Bessel function of order ν and χ is the invariant strong field parameter defined above, $\chi = \gamma B e \lambda\!\!\!^{-}/mc^2$.

4.6 The Constant Field Approximation (CFA)

4.6.1 Radiation emission

The classical spectrum of synchrotron radiation becomes modified when quantum corrections have to be taken into account as for emission in a sufficiently strong field. According to Schwinger [38] and Lindhard [47] following the correspondence principle, the approximate quantum spectrum can be found by a replacement of variable in eq. (41). The substitution $\omega \to \omega^* = E\omega/(E - \hbar\omega)$ in the rhs. of eq. (41) will take into account the quantum (recoil-) effects (see also [56, §59], eqs. (59.9) and (59.20) where the same result is derived from the semi-classical approach):

$$\zeta^* \equiv \frac{\hbar\omega^*}{E} = \frac{\hbar\omega}{E - \hbar\omega} = \frac{\zeta}{1 - \zeta} \tag{42}$$

where, as above, $\zeta = \hbar\omega/E$. This substitution reappears in the definition of the formation length, eq. (22) in going from the classical limit to the accurate expression. The result is thus a modification of eq. (41) where $\delta_c = 2\zeta/3\chi \to \delta = 2\zeta/3(1 - \zeta)\chi$ leading to

$$\frac{dN}{d\zeta} = \frac{\alpha c}{\sqrt{3}\pi\lambda\!\!\!^{-}}\frac{1}{\gamma}[2K_{2/3}(\delta) - \int_\delta^\infty K_{1/3}(t)dt] \quad \text{(substituted)} \tag{43}$$

In the Constant Field Approximation developed by Baier *et al.* [64] and Kimball and Cue [43] (reviewed in [60] and [65]) the corresponding result for emission of radiation is:

$$\frac{dN}{d\zeta} = \frac{\alpha c}{\sqrt{3}\pi\lambda\!\!\!^{-}}\frac{1}{\gamma}[(1 - \zeta + \frac{1}{1 - \zeta})K_{2/3}(\delta) - \int_\delta^\infty K_{1/3}(t)dt] \quad \text{(CFA)} \tag{44}$$

where as found above $\delta = 2\zeta/3(1 - \zeta)\chi$. Figure 7 shows in (a) the term in square brackets from eq. (44) multiplied by ζ/χ to obtain a power-spectrum and normalized such that the spectra become comparable.

In (b) is shown the contribution from the spin (see [58, p. 24], [47] and [56, eq. (59.20)] where the first factor depends on the spin), i.e. the difference between (a) and the square bracket term from the classical spectrum eq. (41) with the substitution $\omega \to \omega^*$ again multiplied by ζ/χ, see [58]. Evidently, the end of the spectrum is seriously affected by the spin for high energies. This contribution originates in Lindhards approach from the replacement of the Thomson cross-section by the Klein-Nishina cross-section which takes recoil and spin into account.

As a result of the quantum correction, the total radiated intensity for the classical emission is according to Schwinger reduced by a factor $1 - 55\sqrt{3}\lambda\!\!\!^{-}\omega_0\gamma^2/16c$ due to first order quantum corrections when $\chi \ll 1$ [38]. Including the second order term the reductions for small and large values of χ are [56]

$$I/I_{\rm cl} = 1 - 55\sqrt{3}\chi/16 + 48\chi^2 \qquad \chi \ll 1 \tag{45}$$

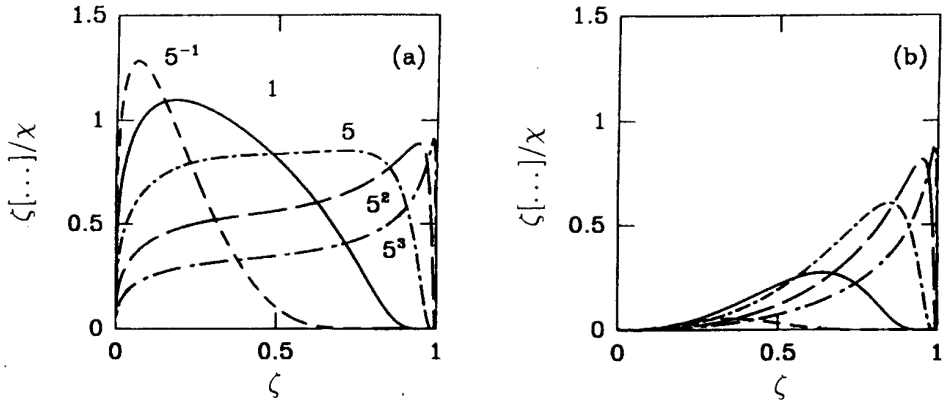

Figure 7: *Synchrotron radiation in a strong field, where (a) is the full spectrum according to eq. (44) and (b) shows the contribution from the spin, see text for details [58]. The labels on the curves denote the value of* χ.

$$I/I_{\rm cl} \simeq 1.2\chi^{-4/3} \qquad \chi \gg 1 \tag{46}$$

From this it is clear that the emission of synchrotron radiation is affected already at fairly small values of χ. At this point it is worth noting that even though the quantum corrections imply a *reduction* compared to the classical synchrotron law, the emission probabilities in the quantum regime are *enhanced* with respect to the Bethe-Heitler value, due to the coherence.

The endpoint of the radiation spectrum, $\hbar\omega_c$ - beyond which the frequencies are exponentially suppressed - is found in the CFA [46], [66] as being the approximate fraction of the incident energy:

$$\frac{\hbar\omega_c}{E} \simeq \frac{\chi}{1+\chi} \tag{47}$$

in good agreement with the estimate of the critical frequency, eqs. (28) and (21) combined with eq. (17)[9]. A more recent analysis by Kononets shows that in the limit $\gamma \to \infty$ the critical energy approaches $16E/63 \simeq E/4$ [67].

Summarizing, there is nothing extraordinary in the 'emission under recoil' in terms of the emission process in itself except that one has to take conservation of energy and momentum into account. It therefore seems natural that a full quantum mechanical calculation of these phenomena using the Dirac equation concludes that ultrarelativistic channeling does not involve quantum effects which are not included in the semi-classical treatment [68]. On the other hand, what is remarkable is the large enhancement with respect to random incidence which is a result of the large field in the rest-frame of the

[9]This agreement is not so surprising since in both the CFA and the above expressions, the replacement $\hbar\omega \to \hbar\overline{\omega} = E\cdot\hbar\omega/(E-\hbar\omega)$ in the classical expression has been performed to achieve the correct behaviour.

emitting particle. So, even though the emission process can be calculated reliably to first order in α it shows a surprisingly drastic change from the usual classical behaviour.

4.6.2 Pair production

For pair production the CFA leads to [44]:

$$\frac{dN}{d\xi_+} = \frac{\alpha}{\sqrt{3}\pi\chi}\frac{mc^2}{\hbar\omega}[(\frac{1-\xi_+}{\xi_+} + \frac{\xi_+}{1-\xi_+})K_{2/3}(\delta) - \int_\delta^\infty K_{1/3}(t)dt] \tag{48}$$

where $\delta = 2/3\xi_+\xi_-\chi$. Note here the similarity with the 'substitution rule' in the coherence length, eq. (23), going from ω to $\omega^\# = \omega/\xi_+\xi_-$ such that one can derive $\delta = 2/3\xi_+\xi_-\chi$ from δ_c merely on the basis of crossing symmetry. It should be noted, however, that due to the redistribution of channeled particles the calculation of radiation becomes more complicated than pair production for angles smaller than Lindhard's critical angle.

First-order corrections to eqs. (44) and (48) in the field of a crystal axis are proportional to θ^2 where θ is the angle to the axis. The correction term in $W = F_1 + (mc^2\theta/U_0)^2F_2$ has a positive coefficient, F_2 at small energies, a negative coefficient at high energies [60] and changes sign at an energy of roughly $7 - 7.5\hbar\omega_t$. Thus for energies larger than $7 - 7.5\hbar\omega_t$ the maximum conversion probability takes place for perfect alignment with the axis, $\theta = 0$.

Asymptotically, the pair production and radiation emission probability in the Constant Field Approximation decreases with increasing energy of the photon[10]:

$$N_{\hbar\omega\to\infty} \propto (\hbar\omega)^{-1/3} \tag{49}$$

and attains a maximum enhancement of [60]

$$\eta_\gamma^{\max} \simeq \eta_{\rm PP}^{\max} = \frac{W_{\rm CFA}^{\max}}{W_{\rm BH}} \simeq \frac{U_0 m a_s d}{3Z_2^2\alpha^2\hbar^2\ln(183Z_2^{-1/3})} \tag{50}$$

where a_s is an effective screening distance and d is the distance between atoms along the axial string. Note that according to eq. (49) the effect is self-suppressing at high energies as indicated in the discussion of the formation length. The maximum enhancement which can reach values of $\simeq$ 150 for both pair production and radiation emission is roughly inversely proportional to Z_2 and appears at an energy of approximately 100 times the threshold energy, $\hbar\omega_t$, i.e. in the (multi-)TeV region. For χ small, the Bessel function becomes exponentially small, $K_\nu(1/\chi) \to \sqrt{\chi}\exp(-1/\chi)$ such that the coherent contribution increases rapidly with γ in the region below and around the threshold, see eg. figure 8.

[10] This can be seen by noting that $2\chi = \lambda_{\rm coh}/\lambda_\gamma \propto \omega$, using the asymptotic behaviour of $K_\nu(1/\chi) \to 1/2\cdot\Gamma(\nu)(2\chi)^\nu$ for χ large and using the ω^{-1} which appears in the front factor of eq. (48).

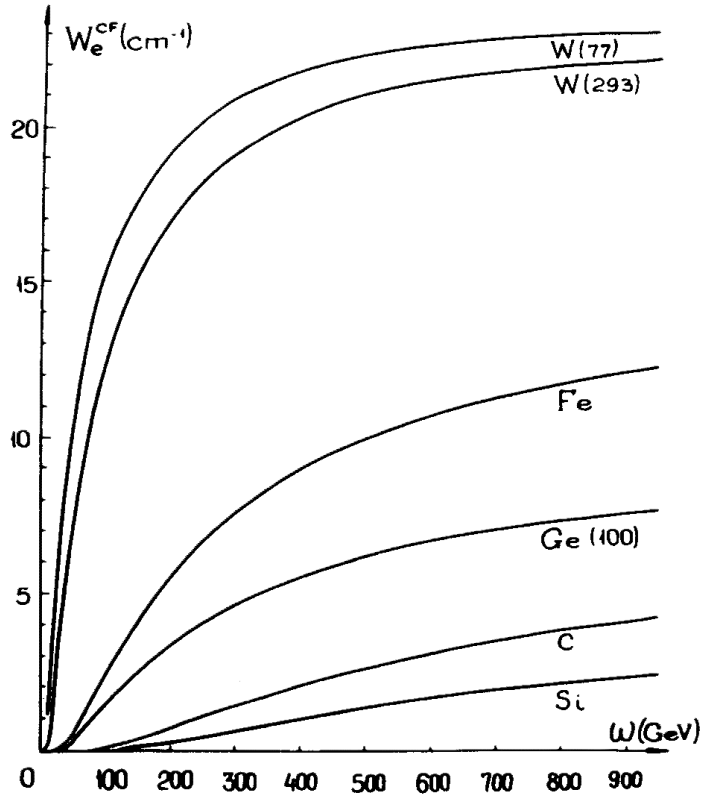

Figure 8: *Pair production probability as a function of energy by a photon incident along the* $\langle 111 \rangle$ *axis for C, Si, Fe and W and along* $\langle 110 \rangle$ *for Ge. The temperature, if different from 293 K, is given in the brackets. The values are according to the Constant Field Approximation by Baier et al. [60].*

For moderate χ, i.e. in the region just above threshold, the strong field yield behaves as roughly proportional to the formation length. This means that the distribution of pairs peaks at $\xi_+ = 1/2$ (as $\lambda_{\rm coh} \propto \xi_+\xi_-$ does)[11], whereas for very high energies it tends to a spectrum similar to the Bethe-Heitler for random incidence.

4.6.3 Variations with energy, material and temperature

The conclusion is that the strong field effects appear at lower energies the higher the Z of the crystal and the lower the temperature. The maximum enhancement, on the other hand, decreases with increasing Z and is only slightly dependent on temperature. Nevertheless, it can be useful to cool a crystal intended to serve as

[11] A better approximation to the shape of the differential spectrum considered in the experiments below would be $\xi_+\xi_-^n + \xi_+^n\xi_-$ with $n = 1 \to 3$ increasing for increasing energy, ie. a wider spectrum at high energies.

a target for conversion of photons, simply to reduce the threshold below the region of typical energies of the impinging photons and by these means obtain a significant increase in enhancement. This is due to the deeper transverse potential in a cooled crystal of high Z which implies a high field and thus $\chi = 1$ at a lower value of γ since $\chi = \gamma\mathcal{E}/\mathcal{E}_0$.

Clearly, the crystal material, orientation and temperature are crucial parameters for an application as a target for conversion of photons.

	$\chi \gg 1$	$\chi \ll 1$
$I \propto$	$\gamma^{2/3}$	γ^2
$W \propto$	$\gamma^{-1/3}$	γ^0
$\hbar\omega_c \propto$	γ	γ^2

Table 4: *Behaviour with γ for the intensity, the radiation and pair production probability and the critical energy of emission for the quantum and classical limits.*

Table 4 summarizes the behaviour of the intensity, I, the radiation probability, W, and the critical energy, $\hbar\omega_c$, with γ for the two limits $\chi \gg 1$ and $\chi \ll 1$ [69]. Note that the radiation probability and pair production probability have the same behaviour with γ in both the quantum and classical limits, in agreement with expectations from crossing symmetry[12]. These drastic changes in behaviour with γ from the classical to the quantum limit have so far only be investigated by means of the strong fields in crystals which thus provide unique tools for tests of QED and for predictions related to certain astrophysical emission processes.

4.6.4 Characteristic angle for CFA

Following Sørensen [70], conservation of transverse energy leads to

$$\frac{p^2}{2\gamma m}\psi_0^2 = \frac{p^2}{2\gamma m}(\psi_0 + \Delta\psi)^2 - U_0 \tag{51}$$

where ψ_0 and $\Delta\psi$ denote the incident and deflection angle, respectively. For $\Delta\psi \ll \psi_0$ this gives

$$\Delta\psi = \frac{1}{\gamma}\frac{U_0}{mc^2}\frac{1}{\psi_0} \tag{52}$$

such that the angle

$$\Theta_0 = \frac{U_0}{mc^2} \tag{53}$$

[12] Of course, pair production is always a quantum process so the separation between classical and quantum limits are understood as those belonging to the synchrotron radiation case, ie. $\chi \ll 1$ and $\chi \gg 1$. Likewise, the pair production probability for $\chi \ll 1$ is understood as the dominant process, ie. the Bethe-Heitler contribution, since the coherent part is exponentially small in this region of χ.

separates two regions where the deflection angle is larger than or smaller than the opening angle of the emission cone, $1/\gamma$. Thus it separates the regions where the radiation has dipole nature, $\psi \gg \Theta_0$, and where it has a synchrotron nature, $\psi \ll \Theta_0$. Θ_0 is the so-called Baier-angle. This characteristic angle does not depend on energy such that at relatively high energies, roughly when $\gamma \simeq 2mc^2/U_0$, i.e. a few GeV for axes in Si and Ge, we have $\psi_c < \Theta_0$ since $\psi_c \propto 1/\sqrt{\gamma}$. Furthermore, in accordance with the continuum approximation which also applies for angles $\psi > \psi_c$ (2.1, p. 6) the field registered by a particle incident at this angle can be considered constant along the string.

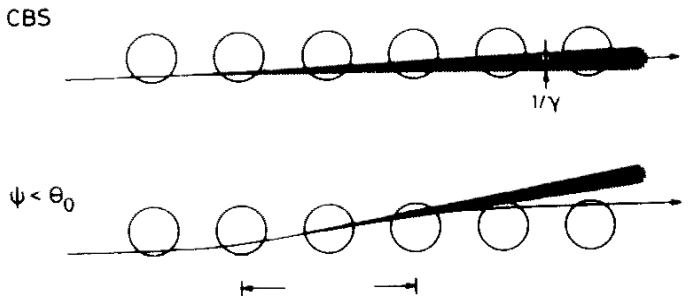

Figure 9: *Emission of bremsstrahlung by a charged particle crossing a string of atoms. In the upper part, the deflection due to the field from the string is sufficiently small such that coherent superposition can take place over many atoms - this is the limit with an angle $\psi > \Theta_0$ to the axis. The lower part reflects the increased deflection when incident with an angle $\psi < \Theta_0$ to the axis which results in a shorter distance for the coherent superposition [70].*

From eq. (52) and figure 9 it is again possible to conclude a 'self-suppression' effect of the strong field: Coherence takes place within the '$1/\gamma$-zone' which becomes shorter and shorter as ψ_0 decreases since $\Delta\psi$ increases, so the strong field enhancement is smaller than the enhancement calculated from coherent theory (Born approximation).

An alternative derivation shows the constant field more explicitly:

$$\Delta\mathcal{E} = \frac{U}{u_1 e} - \frac{U}{(u_1 + \Delta x)e} \ll \mathcal{E} = \frac{U}{u_1 e} \quad \Rightarrow \quad \Delta x \ll u_1 \tag{54}$$

where the approximation for $\mathcal{E}$ used previously is reused. Then

$$\Delta x = \frac{\psi_0 \not{\mathcal{E}}_0}{\mathcal{E}} = \frac{\psi mc^2 u_1}{U} \tag{55}$$

is the transverse displacement over the formation length, eq. (27). By use of eq. (54), this leads to $\psi \ll \Theta_0$ again with Θ_0 given by eq. (53), i.e. under the assumption that the field deflection length is the formation length, the field can be considered constant

during the creation process for incidence inside Θ_0. This assumption may not be valid for typical photon energies as has recently been shown [71].

For a comparison of theory and experiment, it is necessary to add the incoherent - slightly modified Bethe-Heitler, see [46, p. 984],[59, p. 60] - contribution to the CFA contribution. Good agreement with experiment has been obtained earlier by adding an incoherent contribution, W_M=0.28 cm^{-1} where $W_{\rm BH}$=0.32 cm^{-1} for Ge [72].

5 Coherent resonances in strong fields

Distinct coherent resonance peaks develop in the radiation and pair production spectra as the entry direction of the electron or photon is tilted out along a plane, maintaining a relatively small angle to the axis. In this case, the coherent resonances are obtained in passing the periodically spaced axes in the plane, in a way analogous to the passage of the planes for coherent bremsstrahlung and coherent pair production.

5.1 Radiation emission

In the early 90's it was found both experimentally by NA43 [73] and theoretically by Baier *et al.* [74] that electrons of energies in the hundred-GeV range incident on a single crystal with a small, non-zero angle to the axis along a plane would lead to a peak of high energy photons, see figure 10. Furthermore, the enhancement of such photons with respect to the emission from the equivalent amorphous material was found experimentally to be around 50 for diamond!

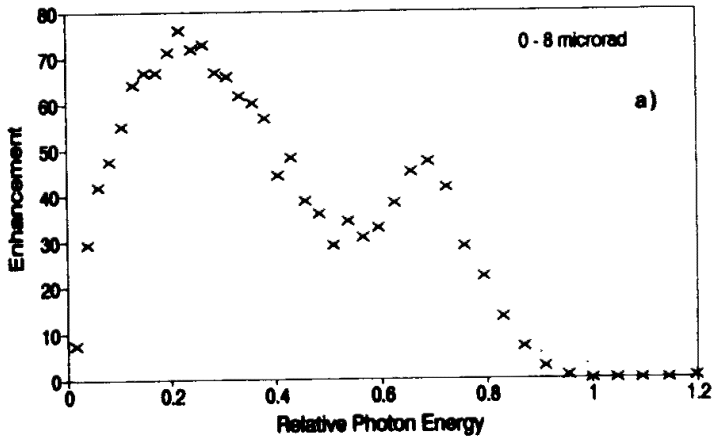

Figure 10: *Enhancement as a function of relative photon energy, $\zeta = \hbar/E_e$, for 150 GeV electrons incident on a 0.5 mm diamond at an angle 0.3 mrad to the $\langle 100 \rangle$ axis with angles $\pm 8 \mu$rad around the (110) plane [73]. The peak at $\zeta \simeq 0.7$ is due to coherent resonances obtained in passing the periodically spaced axes in the plane.*

The appearance of this peak was ascribed to a coherent resonance obtained when the

electron passes the strings forming the plane in the so-called strings-of-strings region. It is thus reminiscent of the usual coherent phenomenon obtained when the electron passes planes. Therefore the position of the peak in the spectrum is found as [78]

$$\hbar\omega_{\mathrm{CR}} = E_e \cdot (1 + \frac{A_{\mathrm{ax}} d_a}{n \cdot 2\pi \cdot 2\gamma\lambda\!\!\!^{-} \sin\theta})^{-1} \tag{56}$$

where $A_{\mathrm{ax}} = 1.282$, d_a is the transverse distance between the traversed atomic strings, θ is the angle to the axis and n is an integer - the peaks in coherent bremsstrahlung are obtained by replacing A_{ax} by $A_{\mathrm{pl}} = 1$ and d by d_p and setting θ as the angle to the plane, see also eq. (76). That $A_{\mathrm{ax}} \neq 1$ is due to the deflection in the strong field as shown in a comprehensive paper on the calculation of the coherent peaks by Kononets and Tupitsyn [78] who base the theory on the semi-classical approximation, the so-called Baier-Katkov formula, see appendix B, p. 133.

5.2 Pair production

Again in agreement with crossing symmetry, the coherent effects are present for the creation of pairs by energetic photons. Kononets and Tupitsyn [78] showed this in a calculation where the classical motion of the pair in the field of the axis family is introduced explicitly and then averaged over all different trajectories. In this way, non-uniform fields can be taken into account. Baier *et al.* have treated the case of incidence near planes, but sufficiently far from the axis for its effect to be negligible and in this case the threshold values for strong field effects from the plane are several hundred GeV, e.g. for Ge (110) the value $\hbar\omega_t$ =700 GeV is obtained [79]. The direct effect of the strong field of planes is thus extremely small at presently available energies.

Kononets and Tupitsyn find the angular position of the pair-creation rate maximum as

$$\theta_m(\omega) = \frac{4a_{\mathrm{TF}}}{\lambda\!\!\!^{-}} \frac{mc^2}{\hbar\omega} \tag{57}$$

and determine this maximum rate. Clearly, the position of the maximum goes towards the perfect alignment for increasing energy, whereas at 150 GeV in Ge $\langle 110 \rangle$ the maximum yield is obtained at 0.7 mrad, slightly larger than the Baier-angle, 0.6 mrad ($U_0 = 318$eV). This behaviour agrees qualitatively with the approach by Baier *et al.* where the F_2 angular correction term changes sign at an energy of roughly $7 - 7.5\hbar\omega_t$.

As for the calculation of peaks in a coherent bremsstrahlung spectrum, the condition for the coherent resonances when passing the strong field axes along the plane is

$$\lambda_{\mathrm{coh.}}(\xi_+, \omega)\theta \simeq \frac{d_a}{2\pi i} \tag{58}$$

where i is an integer and θ is the angle of incidence with respect to the axis. By eq. (23) this translates into an expression of the coherent-resonance angle

$$\theta_{\mathrm{res.}}(\xi_+, \omega, i) \simeq \frac{mc^2 d_a}{4\pi i \xi_+(1-\xi_+)\hbar\omega\lambda\!\!\!^{-}} \tag{59}$$

In order not to smear the effect of coherence, the divergence of the incident photon beam is restricted by

$$\Delta\theta \leq \frac{2a_{\mathrm{TF}}}{d}\theta \tag{60}$$

as follows from eq. (58) by replacing θ by $\Delta\theta$ and d_a by the transverse dimension of an axial string, $2a_{\mathrm{TF}}$. This corresponds to $\Delta\theta \leq 0.075 \cdot \theta$, which is only problematic for $\theta < 1$ mrad in the case of the below mentioned experimental conditions.

The effect of the coherent resonances in pair production and for radiation emission are investigated experimentally in section 10.2, p. 65, section 12, p. 70 and section 14, p. 76.

6 Inhibiting effects

Above it has been shown that radiation emission and pair production are enhanced in crystals for incidence near axes and planes. However, a number of effects may reduce the probability of these processes and thus, for crystals, reduce the enhancement. One inhibiting effect, doughnut scattering, is in fact only present for emission in crystals.

6.1 Landau-Pomeranchuk effect

If the charged particle or the pair is disturbed enough to be scattered outside the radiation cone, $\theta \simeq 1/\gamma$, within the formation length, the probability for photon emission or pair production decreases. This phenomenon, called the Landau-Pomeranchuk (LP) effect [80], affects photon emission and possibly also pair production in both amorphous and crystalline materials. In some sense it is analogous to the mentioned self-suppression effect due to the shortening of the effective formation length - for the LP effect this is due to incoherent scattering, in the CFA it is due to coherent scattering. Since the LP effect influences the basic QED processes it affects the development of electromagnetic showers as well. It is therefore of importance for the determination of the energies of high energy particles, both in air-showers and in calorimetry [81].

6.1.1 Multiple Coulomb scattering (MCS)

The length over which a particle statistically scatters an angle $1/\gamma$ in an amorphous material due to MCS is given by

$$l_\gamma = \frac{\alpha}{4\pi} X_0 \tag{61}$$

where α is the fine-structure constant and X_0 the radiation length given by eq. (34). For pair production the typical length, l_γ^{PP}, is twice as large as l_γ.

If the formation length exceeds this length, the pair production or emission probability decreases. Eq. (22) and eq. (23) combined with eq. (61) lead to the onset of the LP effect at energies:

$$\hbar\omega \leq \hbar\omega_{\rm LP}^{\rm RE} = \frac{E}{1+\frac{X_0}{8\pi a_0 \gamma}} \quad (\hbar\omega_{\rm LP} = \frac{E}{1+\frac{X_0}{4\pi a_0 \gamma}}) \tag{62}$$

for emission of quanta of energy $\hbar\omega$ from e.g. an electron and by use of $l_\gamma^{\rm PP}$

$$\hbar\omega \geq \hbar\omega_{\rm LP}^{\rm PP} = \frac{X_0 mc^2}{4\pi a_0 \xi_+ \xi_-} \quad (\hbar\omega_{\rm LP} = \frac{8X_0 mc^2}{\pi a_0}) \tag{63}$$

for a pair created by a photon of energy $\hbar\omega$. In agreement with the discussion on p. 24 the LP effect arises for low emitted energies for radiation and for high photon energies in pair production. The values in parenthesis are those found by a more careful analysis, [59], [67], [82]. Hardly surprising, the simplified method of deriving the threshold energies is not quantitatively accurate, but qualitatively it is correct. Moreover it assumes the equivalence of the formation- and coherence-lengths, i.e. $\chi \leq 1$

In a crystal, for angles smaller than the critical angle, the multiple Coulomb scattering can be enhanced drastically for electrons and reduced for positrons due to the redistribution of channeled particles. It is therefore in a crystal possible to observe a suppression of radiation of the Landau-Pomeranchuk type at significantly higher energies than given by eq. (62). This has been demonstrated recently by NA43 [71] where radiation up to *at least* 3 GeV from 150 GeV electrons in 1.5 mm diamond along the $\langle 100 \rangle$ axis is suppressed, this effect being connected with *polar* scattering angles 5-6 times larger than expected. For comparison eq. (62) leads to $\hbar\omega_{\rm LP}$=240 MeV and an effect extending to the conservative limit 3 GeV would require a beam of more than 500 GeV in an amorphous material.

On the other hand, the threshold in eq. (63) will be reduced drastically to values of energy within reach for experiments. As an example the pair production in a W $\langle 111 \rangle$ crystal at 77 K will have $\hbar\omega_{\rm LP}^{\rm PP} \simeq 80$ GeV due to the increased scattering along an axial direction [67]. However, a mosaic spread significantly larger than ψ_1 will lead to a threshold close to that of an amorphous material such that the effect would be unobservable at presently available energies. This can be an advantage if the desired effect should be as uniform as possible as a function of angle.

6.1.2 Doughnut scattering

Ignoring the small effect of Delbrück scattering, only charged particles can doughnut scatter (see however [68]). The suppression due to doughnut scattering can be even more severe than due to MCS: If the particle is incident with a fixed angle ψ to the axis and deflects through an azimuthal angle ϕ, the change in angle becomes $\phi\psi$ and

equating this with $2/\gamma$ an estimate for the length over which the particle scatters outside the radiation cone is obtained [15]:

$$l_{1/\gamma} = (\frac{\phi}{2\pi})^2 \lambda_\perp = \frac{\lambda_\perp}{\gamma^2 \psi^2 \pi^2} \tag{64}$$

with $\lambda_\perp$ given by eq. (7), p. 10 which denotes the length required for the doughnut to develop fully. The length $l_{1/\gamma}$ can become smaller than l_γ, even along an axis where MCS is enhanced for negatively charged particles. Therefore suppression of radiation as well as for pair production can occur if the incident or produced particles respectively doughnut scatter enough over one formation length to end outside the radiation cone. The energy at which this happens can be estimated by use of eqs. (64), (6), (7) and (23) as:

$$\hbar\omega \geq \hbar\omega_{\mathrm{LP}}^{\mathrm{in}} = \frac{2mc^2}{\xi_+ \xi_- \not{\chi} \pi^4 N d a_{\mathrm{TF}} \psi_1^2 \gamma^2} \cdot \psi^{-1} \tag{65}$$

for pair production with the produced particles inside the critical angle and:

$$\hbar\omega \geq \hbar\omega_{\mathrm{LP}}^{\mathrm{out}} = \frac{8mc^2 u_1}{\xi_+ \xi_- \not{\chi} \pi^4 N d a_{\mathrm{TF}}^2 \psi_1^4 \gamma^2} \cdot \psi \tag{66}$$

for pair production with the produced particles outside the critical angle. Note that $\hbar\omega_{\mathrm{LP}}^{\mathrm{out}}$ does not depend on γ. As an example, consider the production of symmetric pairs along the $\langle 100 \rangle$ axis in a diamond at room temperature - in this case $\hbar\omega_{\mathrm{LP}}^{\mathrm{out}} \simeq \psi mc^2 \cdot 4 \cdot 10^9 \simeq 2$ GeV$\cdot\psi[\mu\mathrm{rad}]$ such that the effect should be observable down to ≈50 GeV. Likewise, for Ge $\langle 110 \rangle$ the effect should extend down to ≈180 GeV for incidence outside ψ_1 and down to ≈80 GeV for incidence of a 150 GeV photon inside ψ_1 where the critical angle is calculated for an positron of the same energy. Note that again these estimates are qualitatively correct, but not quantitatively precise. Furthermore, the effect of the reduced formation length in the strong field has not been taken into account, i.e. the formulas have been found for $\chi \leq 1$ as above for the original LP effect.

One way to avoid the above mentioned LP suppression effects in crystals is to use a crystal with a mosaic spread, ψ_m, given by $\psi_c \leq \psi_m \leq \Theta_0$, such that the strong field effects remain whereas the suppression effects are diluted due to the mosaicity. However, this only accounts for the Landau-Pomeranchuk effect due to (increased) MCS - the LP effect arising from doughnut scattering may persist even beyond Θ_0.

6.1.3 Reduction of incoherent contribution

Another effect of the Landau-Pomeranchuk type is the reduction of the incoherent contribution due to the coherent effects[13]. It is analogous to the mentioned self-suppression

[13] This section is based on a recent idea by Kononets [67] whom I thank for letting me mention it here.

effect as a result of the diminishing formation length, only in this case the suppression is of the incoherent contribution.

Such an effect may lead to large deviations from the theoretical enhancements hitherto obtained, at least for energies around threshold where the incoherent contribution plays a significant role. Theoretical investigations of this effect and its influence on spectra for pair production are underway [67].

6.2 Chudakov effect

The Chudakov effect [83], [84] is a reduction in ionization energy-loss of a pair at small distances from the creation vertex. The effect arises due to the electron's screening of the positron field and vice versa when the pair has separated only little. This is expected to result in an energy-loss due to ionization which is smaller than for two separate, charged particles. The observation of the effect could possibly be done in a sufficiently thin solid-state detector where a significant fraction of pairs of the appropriate energy would deposit an energy corresponding to less than 2 MIPs.

For pair production, the same screening effect can be considered present during formation of the pair (the transverse separation is smaller than $2\lambda\!\!\!^{-}$ for distances smaller than the formation length). This means that, depending on the energy of the photon, the pair production yield may be reduced if the thickness of the target in which the conversion takes place is smaller than the formation length. Presented like this, the Chudakov effect then originates from the existence of a formation length and thus estimates of the required energies and thicknesses for an experiment to observe the effect can be based on knowledge of this formation length. Note, however, that since the Chudakov effect is concerning loss due to ionization, the appropriate scale of length, $\approx \hbar/p$, is much larger than $\lambda\!\!\!^{-}$ due to the much smaller characteristic energy such that the true Chudakov effect should be observable for much larger thicknesses than a reduced pair production yield.

Part IV
Experiments on strong field effects in crystals

7 Experiment

The experiments with NA43 were performed in the H2 beam-line in the North-Hall of the CERN SPS (Super Proton Synchrotron), where a 450 GeV/c beam of protons is available with high intensity: 1-5·10^{12} protons per spill of duration 2.5 seconds every 14.4 seconds. The SPS uses protons injected from the PS (Proton Synchrotron) coming from the proton linear accelerator through the PS-Booster.

7.1 Beam and equipment

The principle of the experimental setup is basically relatively simple, but is complicated by the large number of detectors and therefore a sketch of the layout is appropriate to keep track of the basics in the following discussion of all the ingredients.

7.1.1 Basic parts

A beam of electrons (or positrons) of known energy passes a target in position I - 'the radiator' - where it radiates a number of photons, see figure 11. The electrons are then separated from the emitted photons in a magnet and the deflection of the electrons, i.e. their momentum, is determined. Thus the photon beam generated is of a known total energy - it is tagged (but it may consist of several photons, the energy of each being unknown). This beam of photons hits a downstream target in position II - 'the converter' - where a photon may convert into a pair. As for the tagging system using the primary electron, the momentum of the electrons and positrons created in target II is determined by letting them pass a magnetic field in which they are deflected. If only one photon has converted it is then possible to reconstruct the energy of the impinging photon simply by adding the momenta of the electron and positron. Finally, a calorimeter confirms the energy of the tagged photon(s).

The opportunity of using aligned crystals or amorphous foils (and/or a randomly oriented crystal) in both position I and II opens the possibility of investigating interactions of electrons/positrons *as well as* photons with strong crystalline fields. For investigations of radiation emission, a crystal in position I is aligned and the target in position II may be either a foil, a misaligned crystal or both. In the case of investigations of pair production, the tagged photon beam is generated by passing a foil, a misaligned crystal or both in position I while there is an aligned crystal in position II. In a special case, the polarization experiment, the two methods are combined with an

aligned crystal in position I which generates a polarized photon beam while another aligned crystal in position II detects the level of polarization. For calibration purposes both the radiator and the converter are randomly oriented crystals and/or amorphous materials.

7.1.2 Detailed description

Initially, the experiments investigating emission from strong crystalline fields were relatively simple with only a few scintillators, some collimators and a calorimeter [85], [86], [87]. Gradually these setups were improved to incorporate measurements of other important quantities like photon multiplicities, photon intensity spectra, i.e. reconstruction of energies of single photons, incident- and exit-angles and -positions for radiating particles as well as determination of differential spectra in pair production. The setup used by NA43 in later years, see figure 11, has been such a multi-purpose setup to investigate in detail different phenomena as radiation emission, pair production and shower formation.

The proton beam used for secondary beams in the beamline H2 is focussed on a Be target, T2, producing among other particles neutral pions. The π^0's decay fast into two photons some of which are then converted in a lead-sheet of one radiation length to electron-positron pairs, which in turn are momentum- and polarity- selected, defocused and collimated to generate a nearly parallel beam of electrons or positrons with an energy between 10 and 300 GeV/c. This procedure also leaves the possibility of making a beam of charged pions or protons from K^0 or Λ-decay or, for that matter, a muon beam of low intensity.

Due to synchrotron radiation losses in the beam transport (which scale as γ^2), the electron beam delivered to NA43 has a momentum which is lower than the nominal, for instance a beam of originally 150 GeV/c at T2 arrives with 149.1 GeV/c at the experiment. In H2 the beam is initially parallel displaced vertically by two dipole magnets, each giving a 1 mrad bend, to reduce the background of photons upstream of the radiator. The beam divergence is measured to be 40 μrad (σ) and 50 μrad (σ) in the horizontal and vertical plane respectively for the optimally parallel beam. Between the vertical deflection magnets a number of scintillators used for the calibration of the chambers, $\overline{\text{Sc3a}}$, $\overline{\text{Sc3b}}$, and a drift chamber, DC1, are positioned (see figure 11). Two additional scintillators, Sc1 and Sc2 provide a signal used in coincidence with $\overline{\text{Sc4}}$ for the primary trigger ('Norm', see figure 13). Roughly 40 m downstream $\overline{\text{Sc4}}$ with a 15 mm hole is placed $\simeq$60 cm upstream of the first crystal which, in turn, is $\simeq$10 cm upstream of the second drift chamber, DC2. Tracking between DC1 and DC2 provides information on the angles of incidence and on the impact-point on crystal 1. The 90 degree rotation of the phase-space of the beam between T2 and H2 makes the average angle in the NA43 setup somewhat sensitive to the position of the primary beam on the target. However, due to the long transport of some 100 m from the last active

dipole to $\overline{\text{Sc4}}$ an optimization of the beam on this veto counter results in a beam which is directionally reproducible to within a few tens of μrad. The first crystal is placed on a goniometer with 1.7 μrad stepsize in a vacuum chamber which is temperature stabilized inside a hut built of insulating materials[14].

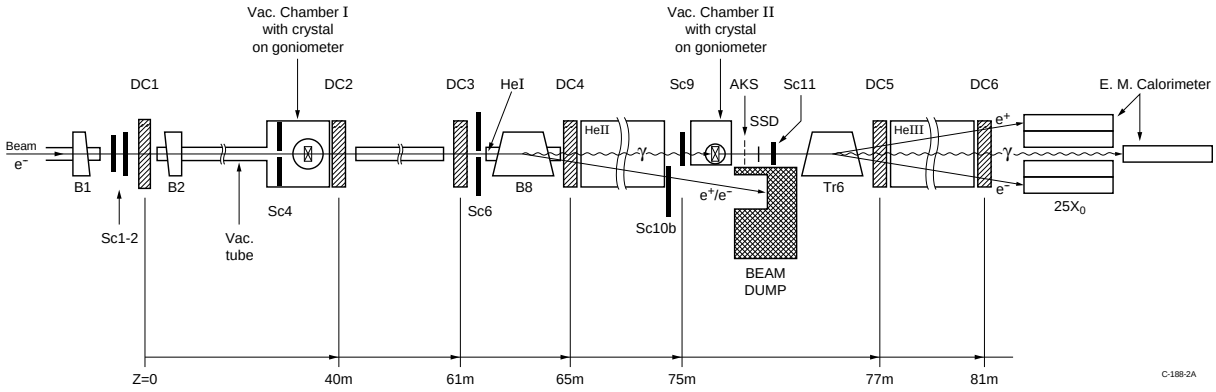

Figure 11: *A schematical drawing of the setup used in the H2 beamline with NA43. See text or the figures in appendix D for details.*

Further downstream, at $\simeq$61 m from DC1 and approximately 1 m upstream of the deflection magnet, B8 ($Bl \leq 4.2$ Tm), the third drift chamber, DC3, is positioned and immediately hereafter another scintillator, Sc6 with a 50 mm hole. Sc6 detects wide-angle scattering events, while DC3 in combination with DC2 gives information on the exit angle from the first crystal.

Some 75 cm downstream of B8 drift chamber 4 (DC4) is situated with a veto counter, $\overline{\text{Sc7}}$, that can reject events (through a pattern bit) which hit the DC4 frame, possibly creating an electromagnetic shower from which particles can be observed in the downstream detectors. Photons of a total energy $\hbar\omega$ emitted in the first crystal are tagged in DC4 which determines this energy from the deflection of the primary electron and the known (calibrated) integrated field in B8. Note that the tagging procedure cannot distinguish several photons with energies adding up to $\hbar\omega$ from a single photon of energy $\hbar\omega$. Three additional scintillators, $\overline{\text{Sc8a}}$, $\overline{\text{Sc8b}}$, Sc10a , are put in this region for the chamber-calibration, see section 8, p. 49.

Between DC4 and the second crystal, a He tank is installed to reduce MCS and a large scintillator, Sc10b, covers the solid angle of $\overline{\text{Sc8b}}$. Another veto-counter, $\overline{\text{Sc9}}$, is situated immediately upstream of the vacuum chamber in which the second crystal is put on a goniometer with $\simeq 20\mu$rad stepsize. $\overline{\text{Sc9}}$ rejects radiation events for which the tagged photon has converted upstream of the second crystal. The second crystal could be cooled to a temperature close to that of liquid nitrogen (lN_2) by cooling a

[14] Typical heat expansion coefficients are $\simeq 20 \cdot 10^{-6}$/K such that the change in determination of angles from the DCs is of the order 1μrad/K. Therefore thermal disturbances from exterior sources, which have given problems before [89], must be sufficiently reduced.

surrounding Cu-tube through a Cu-braid from a lN_2-dewar. A temperature reading of the Cu-tube showed -179° C, ie. the temperature of the cooled crystal can be assumed to have been $\simeq$100 K.

Downstream of the vacuum chamber containing the second crystal, detectors for registration of the produced pairs are positioned. Depending on the experiment, a solid-state detector (500 μm thick Si, 600 mm^2), a scintillator, Sc11, or a scintillator array, the AKS[15] was used.

To absorb the deflected primary electron a dump was constructed on the deflection side of the vacuum chamber from concrete, lead and iron. Care was taken in the construction of the dump such that secondary particles would not hit the region of counters near the crystal. The second vacuum chamber was positioned transversely such that a 150 GeV electron in the nominal beam was deflected outside the chamber wall by 20 mm.

For the pair spectrometer a dipole magnet, Tr6 (Bl $\leq$0.6 Tm) was put $\simeq$0.5 m downstream of the vacuum chamber. Two drift chambers, DC5 and DC6, with distances 97 cm and 461 cm from the center of Tr6 detected the deflected pairs produced in crystal 2. Another He tank was inserted between DC5 and DC6 to reduce MCS and immediately in front of DC6 two veto-counters, $\overline{\text{Sc12}}$ and $\overline{\text{Sc13}}$ rejected (by a pattern bit) events incident on the DC6 frame.

Three scintillators, $\overline{\text{Sc14a}}$, $\overline{\text{Sc14b}}$ and Sc15 were used to calibrate the chambers for the pair spectrometer. Finally, around 82 m downstream of DC1, was placed a LeadGlass array consisting of 4 Lead Glass detectors LGb1, LGb2, LGa1, LGa2, each 9×9 cm^2 in transverse dimension and 70 cm long, i.e. 25 radiation lengths. LGb2 was centered on the direct electron beam and positioned 96 cm downstream of the 3 others which left a 30 mm wide channel for the photon beam to pass down to LGb2.

7.2 Drift chambers

At high energies, the almost undisturbed penetration of charged particles through thin films enables the use of a sequence of position sensitive devices, such that tracking between these devices becomes possible. For the experiments described in this thesis, drift chambers constructed by Kirsebom and Aggerholm following layouts and principles from Charpak and Sauli [93], were used.

The drift chamber operates on the principle that a penetrating charged particle ionizes the gas in the chamber, and the liberated electrons drift towards the anode-wire - also known as the sense-wire - where an electron avalanche is created in the electric field present. If the electric field is (almost) constant over the drift-region and the gas-mixture chosen appropriately, the drift-time for the electrons to reach the sense-wire, depends (almost) linearly on the distance from the sense-wire at which

[15]This was used for the NA48 tests for the Anti-K-Short rejection system using a crystal [90], [91].

the particle passed. Figure 12 shows the principle of construction and indicates the homogeneity of the field by equipotential-lines.

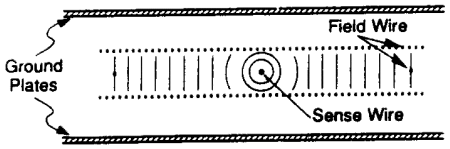

Figure 12: *Sketch of construction principle in a drift chamber. Two cells are shown [94].*

The gas-mixture with 31% argon/methylal, 42% argon and 26% isobutane has been shown to be a good choice to optimize the performance and lifetime of the chambers. The isobutane prevents electrical break-down in the gas, but is destroyed by the beam and tends to create carbon-layers on the wires. Therefore, the methylal (with a final concentration of 2.5%) is added to keep the wires clean in order to prolong the lifetime of the chambers.

The electric field is kept approximately homogenous by a voltage division along the cathode drift wires of the -4kV on the field wire and the +2kV on the anode (sense)-wire. The approximate drift velocity of the drifting electron avalanche is 50 μm/ns though with a small acceleration (section 8, p. 49). The separation between anode- and field-wire is 25 mm and the two adjacent anode-wires (each detecting particles on one side) are separated by 50 μm. This means that the chamber, which has a sensitive region of 15 cm by 15 cm is made from 36 cells, each 25×25 mm^2. Neighbouring cells are not completely independent due to cross-talk and left/right ambiguity across the sense-wire which can result in the confusion of two simultaneous particles on either side of the sense-wire, see p. 51. For this reason, in the pair production experiment the drift chambers 5 and 6 were positioned asymmetrically with respect to the beam, such that the nominal beam was incident on the field-wire. In order not to create electrical break-down in the gas or wear the chambers too quickly, the drift chambers can normally not run in intensities above $\simeq 5 \cdot 10^4$ s^{-1} and for the low energy (i.e. high intensity) beams in H2 this sets the upper limit for the used intensity.

To compensate for the non-uniform drift velocity of the electrons in the drift chambers and the resulting non-linear dependence of the real hit-position on the registered hit-position, a number of 'slit-counters' were used. These slit-counters consisted of a thin scintillator (3 mm) with 0.3×3 mm^2 holes, accurately spaced 3 mm apart as a veto. This was counted in coincidence with another overlapping scintillator and Sc1·Sc2 (to avoid rejection by $\overline{\text{Sc4}}$) as pre-scaled events in the trigger.

7.3 Data acquisition system and electronics

In order not to fill the data tapes with uninteresting events, the acceptance or rejection of a particular event is determined by a number of triggers defined by the hardware.

The design of these triggers is a question of balance - if the triggers are too restrictive, good events may be lost and if the triggers are not restrictive enough one may collect uninteresting events at the expense of the interesting ones. Four triggers were defined: Norm, Pair, Rad and DC Calib:

Norm The so-called Norm events set by Sc1·Sc2·$\overline{\text{Sc4}}$ were scaled down by passing them through a prescaler unit. These events counted the number of electrons incident within the accepted region which is essentially given by $\overline{\text{Sc4}}$. As the name indicates these events are used to normalize the radiation or pair production yield to the number of incoming electrons in the accepted range.

Rad The prescaled Radiation trigger counted the number of Sc1·Sc2·$\overline{\text{Sc4}}$ events where either LGb2 or Sc11 had fired above a given threshold, set to $\simeq$7 GeV and $\simeq$1.5 MIPs, respectively. The idea behind using the logic 'LGb2 or Sc11' was to accept all events where radiation was generated. Some of these events may generate a pair which is deflected enough in the pair spectrometer magnet to end outside the geometrical acceptance of the Lead Glass in the forward direction, but these events will then be registered in Sc11. However, Sc11 will accept any pair irrespective of the energy of the photon that generated the pair such that one has to use the pair spectrometer to define a real threshold for the radiation trigger when Sc11 is used.

Pair The Pair trigger was a logic *and* of the Radiation trigger and a firing of one of the relevant y-cells in DC5. The geometrical acceptance of DC5 is discussed in section 9.1, p. 59. Since this was the most restrictive trigger, no prescaling was required.

DC Calib The prescaled DC Calib trigger was connected to four individually prescaled coincidences for the chamber-calibrations: Sc1·Sc2·$\overline{\text{Sc3a}}$+Sc1·Sc2·$\overline{\text{Sc3b}}$, Sc10a·$\overline{\text{Sc8a}}$, Sc10b·$\overline{\text{Sc8b}}$ and Sc15·$\overline{\text{Sc14a}}$+Sc15·$\overline{\text{Sc14b}}$. Distinction between the elements in each logic *or* was done by setting a pattern bit. Note that for the DC Calib trigger the primary veto, $\overline{\text{Sc4}}$, was not in coincidence - this was done to ensure as large an effective area as possible for the calibration counters.

The 'doublehit' timer (see figure 13) was introduced to reject events where two particles are separated in the Sc1·Sc2 coincidence by a time short enough to cause confusion during the reading of the event in the CAMAC (e.g. on the peak-sensing ADC which is strobed over a time of the order of μs). Any registered doublehit within the time given by this doublehit timer is cleared in the CAMAC. The 'master' consists of a coincidence that registers the hit in Sc1·Sc2 during the time in which the CAMAC is not busy reading the inputs and there is burst, given that the event has not been cleared and the event time (given by the doublehit time) is over. The 'master' is used

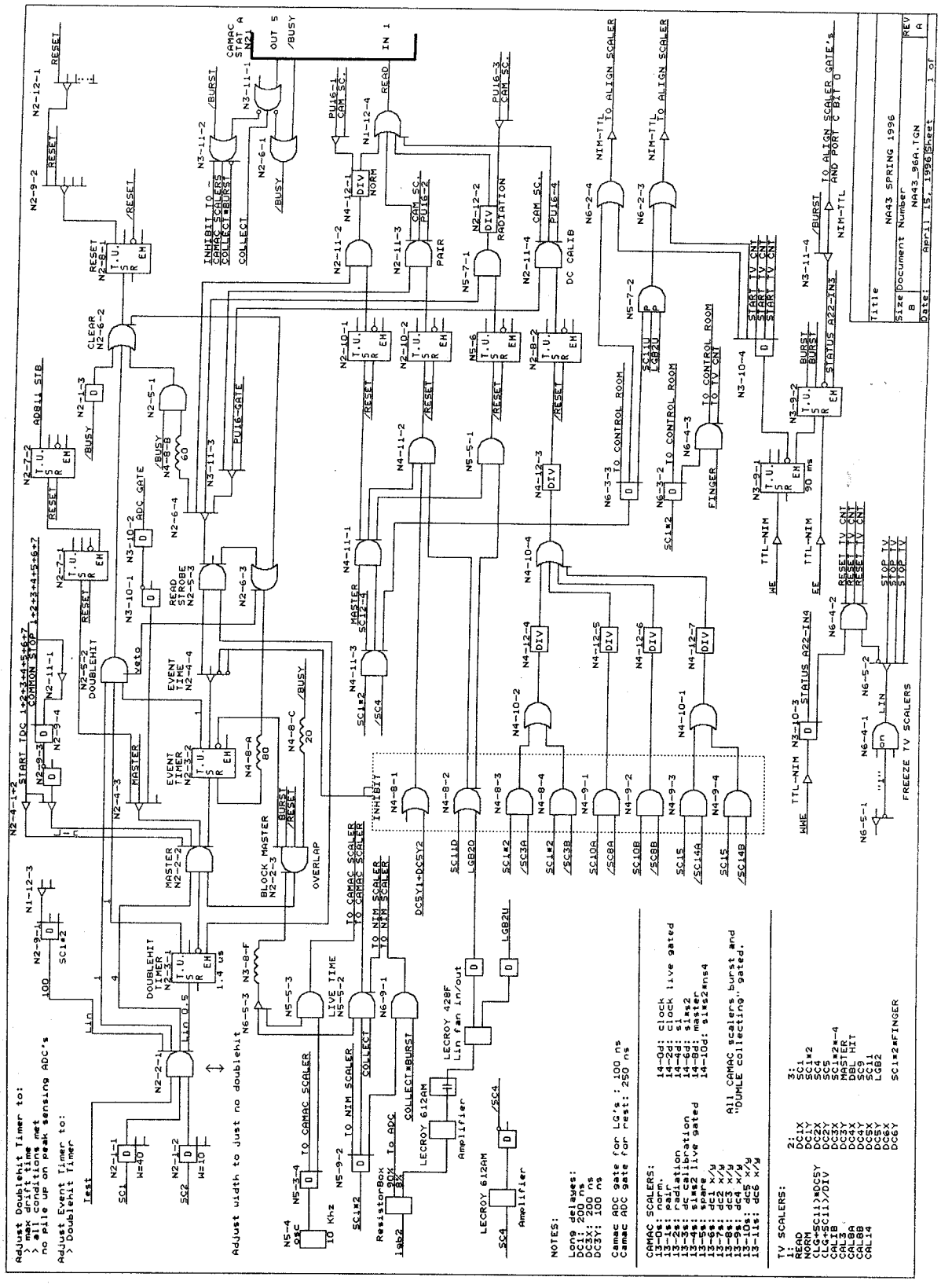

Figure 13: *Layout of the electronics for the data acquisition system.*

as the start for the TDCs which are stopped by the signal from the drift chambers - this starting signal is delayed by roughly 400 ns to generate the 'common stop' for the TDCs to stop the cells which were not hit in the particular drift chamber. For each accepted event a gate for the ADC and for the pattern unit is generated by the 'master' (through the 'read').

7.4 Crystal alignment

Since the beam in H2 can be relatively parallel compared to typical critical angles, see section 7.1, p. 41, the channeling radiation generated when passing the crystal planes in angular space can be used to align the crystal in the first goniometer. An angular scan is made by turning or tilting the crystal and registering the normalized yield of radiation above a given threshold, normally set to 10-20 GeV.

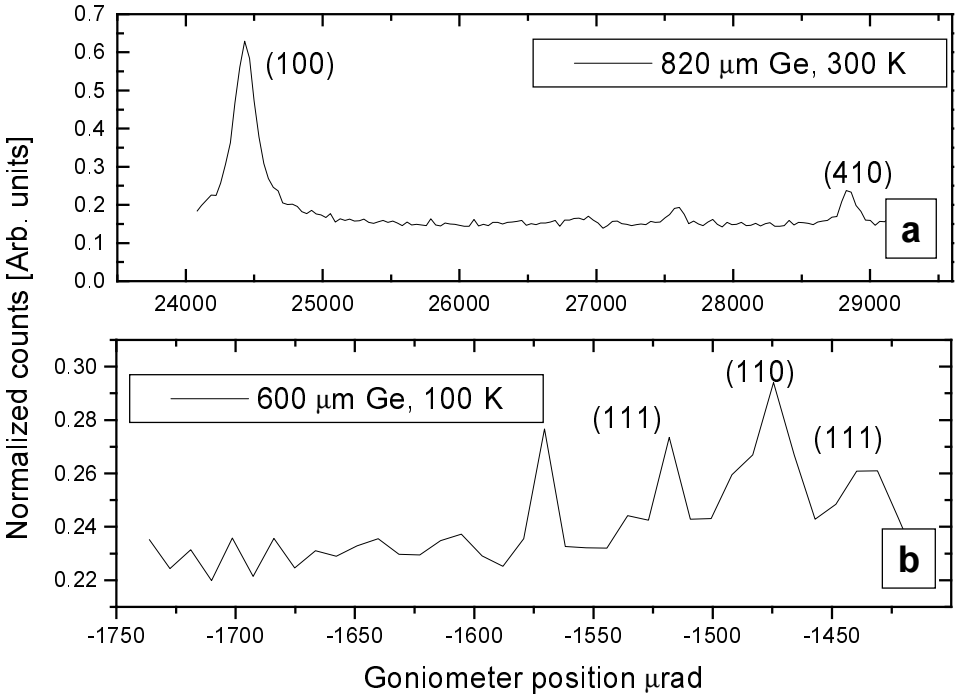

Figure 14: *Angular scans for the alignment of the two* ⟨110⟩ *Ge crystals used for radiation (a) and pair production (b) experiments. Note the decreased sensitivity - the suppressed zero - in (b) compared to (a).*

For the crystal in the second goniometer two methods are possible. To align this crystal by the use of electrons one uses the fact that at incidence of the electron along crystallographic directions the photon-multiplicity - the mean number of photons emitted averaged over all radiative events - is larger than one. Therefore, in the absence of a powerful downstream deflection magnet, a downstream scintillator covered with approximately one radiation length of material for conversion of the photons can be

used to register the angular positions of planes and axes. The threshold for this scintillator is typically set to 3-4 MIPs since the probability of detecting more than 3 MIPs including the undeflected incident electron depends sensitively on the multiplicity.

The second option is to use the photon beam generated by bremsstrahlung of the primary electron which is then deflected before reaching the crystal. For this option the bare scintillator downstream of the crystal can detect the pairs generated in the crystal, where one relies on the enhanced pair production along planes and axes. Two typical angular scans are shown in figure 14 from which it is easy to identify even higher-order planes.

8 Analysis

The setup used by NA43 in later years has been a multi-purpose setup to investigate the basic QED processes in crystals: radiation emission, pair production and shower formation. As shown in section 7.1, p. 41 it therefore included a fairly large number of detectors and other types of equipment. These installations enabled a determination of impact-positions and -angles, multiplicities of photons and charged particles, determination of lost and deposited energies and registration of beam intensities as well as the vetoing or dumping of disturbing events. On the other hand, this also means that the analysis became quite complex. The emphasis in the following will be on the analysis of pair production since this involves essentially all detectors, i.e. it represents the most extensive analysis and therefore to a large extent it encompasses the analysis necessary for the investigation of e.g. radiation emission.

8.1 Calibration of the setup

A calibration program with different nominal momenta (10, 22, 35, 70, 110, 150 and 200 GeV/c) and different currents for B8 (0, 400 and 800 A) and Tr6 (0, $\pm$250 A) was performed in order to be able to calibrate the LeadGlass array, the tagging system and the pair spectrometer in the analysis. For pair production data-taking the magnets, B8 and Tr6, were set to 850 A = 4.058 Tm and 250 A = 0.5236 Tm, respectively.

Due to the low divergence of the beam, tracking of slits from one of the calibration slit-counters through many chambers was possible and therefore a common coordinate system could be defined. Least-squares fits to the centroids of the profiles resulting from the slits gave the drift velocity and acceleration of the drift electrons, such that each chamber could be calibrated. Comparisons between calibrated and non-calibrated data show that errors as large as 2 mm near the field wire can be found in the determination of the hit-position if the calibration is skipped. This would seriously affect the determination of the momentum of the pair.

A calibration of the LG-calorimeter was done by use of the stored files from the cali-

bration program - the mean value of the peak in the ADC-spectrum for the LG was plotted as a function of energy and a 3rd order polynomial fit gave the calibration. The response can be non-linear with momentum due to incomplete containment of the electromagnetic shower. The resolution of the LG, σ_{LG}, was found to be $\sigma_{\mathrm{LG}} \simeq 20\%/\sqrt{E[\mathrm{GeV}]}$ at 150 GeV, whereas one should generally expect $\sigma_{\mathrm{LG}} \leq 7\%/\sqrt{E[\mathrm{GeV}]}$ [17, p. 146]. Better resolution, $\sigma_{\mathrm{LG}} \simeq 11\%/\sqrt{E[\mathrm{GeV}]}$, was obtained at 10 GeV, which indicates a non-complete shower-containment at high energies. Laterally, the LG is $3.2X_0 \times 3.2X_0$ and longitudinally $25X_0$. Theoretically [95], the necessary length and radius to contain 98% and 95% of the shower amount to $\simeq 21X_0$ and $\simeq 2.4X_0$, respectively for this type of Lead Glass in which case the resolution should be $\sigma_{\mathrm{LG}} \simeq 6\%/\sqrt{E[\mathrm{GeV}]}$. The beam size of some 20 mm at the Lead Glass may contribute to the resolution as well, especially if the beam is not well centered on the 9×9 cm^2 front-face of the Lead Glass. The small FWHM of the pedestal indicated no serious errors in the electronics.

Another effect, namely material in the beam, may give rise to an apparent decreased resolution of the LG. The trigger scintillators Sc1 and Sc2 and the drift chamber DC1 (its radiation length corresponding to approximately 100 μm amorphous Si) contribute with $\approx 5\%X_0$, giving rise to additional smearing due to the distribution of the radiative energy-loss. The reason is that photons emitted at DC1 will not hit the Lead Glass calorimeter due to the vertical deflection of 1 mrad. Therefore, the beam will gain an additional energy spread resembling lack of resolution in the calorimeter.

8.2 Reconstruction of photon energies

Tracking the emitting electron through the chambers DC1, DC2 and DC3 enables a fairly precise prediction of the impact point of the emitted photon at positions further downstream. This is due to the small angles obtained from MCS and the small typical angle for emission, $1/\gamma$. Likewise, a pair for which both the electron and positron give signals in DC5 and DC6 can be tracked 'backwards' to the vertex. Correspondence between the position of the vertex and the projected photon track was confirmed. Further, for events with one or two tracks from the pair, the angle of this track with respect to the direction of the incoming photon, the so-called opening angle, could be found. Equivalently, the transverse distance, x, between the projected impact point of the photon and the impact point of the electron or positron was determined.

In order to reconstruct the energy of the incoming photon from the tracks of the electron and positron, each event was subjected to a selection according to the number of hits in DC5 and DC6 respectively. The momentum in GeV/c of a particle detected by one of the drift chambers is given as:

$$p = 300\frac{Bl \cdot L_{\mathrm{DC}}}{x} \tag{67}$$

where Bl is the integrated field in the magnet in Tm, L_{DC} is the distance from the center of the magnet to the chamber in m and x is the deflected distance in mm

as measured by the chamber. Several additional checks such as a required minimal distance between hits in either chamber and a rejection of photon energies above 180 GeV and below -10 GeV (as a result of e.g. the finite resolution of the impact point of the photon) were imposed for all reconstructions.

In the 'cleanest' case with two hits in both chambers, each one on either side of the middle field wire, the momentum of each of the particles was determined from eq. (67). If the result from DC5 and DC6 agreed within 10%, the event was accepted as a good event and the total momentum obtained by adding the momenta of the electron and positron determined from DC6 (with better momentum-resolution) was used as the photon energy.

All events with only one track (one hit in both chambers with an opening angle less than 3.47 mrad, corresponding to an energy of 180 GeV for a symmetric pair) were rejected. Likewise, events with 3 or more hits in both chambers were rejected.

For events with two hits in one chamber and not two hits in the other chamber, the photon energy was found from the chamber with two hits by use of eq. (67), without testing correspondence with hit(s) in the other.

8.2.1 Drift chamber related problems

A few problems are related to the fact that a drift chamber is not uniformly sensitive, does not cope with simultaneous hits in one cell and has cross-talk between cells for hits close to the field-wire.

An incident high energy photon on the edge of the accepted beam may generate two particles which hit DC5 in one cell thus giving only the signal from the particle closest to the anode-wire. However, due to the relatively small beam-size compared to the separation of the electron and positron at DC6, this event will give two hits in DC6 (neglecting inefficiency), since it cannot give both hits on the 'wrong' side of the DC5 field wire and escape detection in DC6 at the same time.

Due to cross-talk between cells (generated by ionisation across the field-wire for hits close to this) a single hit in the chamber may resemble a double hit. These events are taken as one hit at the average position if both hits appear within $\simeq 2$ mm to the field-wire.

8.3 Determination of backgrounds

An important point is to determine the backgrounds, since for an enhancement spectrum the background contributes in the numerator as well as the denominator through:

$$\eta_{\text{exp.}} = \frac{W_{\text{alg.}} - W_{\text{bck.}}}{W_{\text{rnd.}} - W_{\text{bck.}}} \tag{68}$$

where $\eta_{\text{exp.}}$ is the experimentally determined enhancement with $W_{\text{alg.}}$ and $W_{\text{rnd.}}$ being the measured probabilities of pair creation for the crystal in aligned and random

situation respectively and $W_{\text{bck.}}$ the probability of pair creation when the target has been removed. For this reason, the absolute value of the background at the crystalline converter is probably the largest source of systematic error. This error is estimated to be around 10% as shown in the following.

8.3.1 Backgrounds at the radiator

Since all runs for the pair production experiments were taken with the same thickness of the radiator, the background at this point only influences the determination of the multi-photon emission probability. The knowledge of the multi-photon composition of the tagged beam affects the determination of the background at the converter since there the conversion probability was calculated requiring at least 1 pair produced and this probability depends on the photon multiplicity. Unfortunately, no clean measurement of the background was performed for the pair production experiments[16]. However, the precise knowledge of the background at the radiator is not essential for an accurate measurement in this case and for the presented radiation experiments, measurements without target were performed.

For the case without inserted material apart from the first crystal in random, 0.82 mm Ge = 3.6% X_0, the probability of emission of photons above a given energy threshold was found as a function of this threshold. A fit based on eq. (35) gave the absolute converter thickness from which the known Ge thickness could be subtracted giving the background. Since the energy is found as the emitted energy, this procedure relies on the effect of pile-up (multi-photons) being small. The background was found to be 2.2±0.3% X_0 where the error from the fit is negligible compared to the radiator thickness for the datataking runs: 19.8% X_0 (2 mm Cu, 0.82 mm Ge and background).

8.3.2 Backgrounds at the converter

For the run with the thin radiator, 5.8% X_0 (0.82 mm Ge and background), and an additional 2.02±0.01 mm Cu radiator, the conversion probability was calculated according to the expected distribution of photons from the radiator (eq. (36)), requiring at least 1 pair produced. Experimentally this probability was found by requiring a signal of at least 1.4 MIPs in the SSD *and* in Sc11 and the calculated value (the theoretical conversion probability in 600 μm amorphous Ge) was subtracted to give the background: 2.0±0.2% X_0 corresponding to 370 μm amorphous Ge or 7 mm scintillator. The error was estimated based on the sensitivity on the cut-off for the SSD and Sc11. Note that the background can not be determined without reference to the theoretical

[16]The intention was to use different radiator- and converter-thicknesses and afterwards do an extrapolation to zero inserted material. This reduces data-taking time due to increase in emission and conversion probability with respect to a 'no-target' run. However, too many parameters were changed at the same time for these runs for this procedure to work and thus the determination of background complicated considerably.

conversion probability in the target, since there is no 'no-target' data available. The background, having excluded photons which converted upstream of $\overline{\text{Sc9}}$, originates from conversions in air, the scintillator-wrappings and -insensitive layers and a very small fraction from the mylar-windows (22 μm thick) to the vacuum-chamber. However, also an inefficiency of the veto-counter would resemble background and may explain the relatively high value for this.

8.4 Energy-loss in the converter

Due to the enhancements of up to $\simeq 20$ for radiation by electrons and positrons in the strong field of a germanium crystal [96], it is likely that a pair after conversion will lose energy by radiation, even in a thin crystal. Moreover, since the pair is created primarily in the region of high fields, the probability of radiative loss is high. This effect has to be accounted for to determine the true energy of the incident photon by reconstruction in the pair spectrometer.

8.4.1 True energy-loss

Several experiments have shown that electrons and positrons incident within the critical angle suffer different energy-loss due to the redistribution of the channeled particles [97], [75], [98], [101], see for instance figure 15.

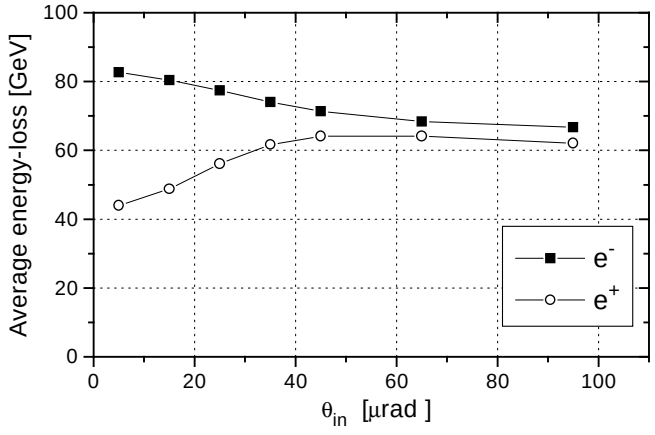

Figure 15: *Average energy losses for 150 GeV electrons and positrons incident on a 1.5 mm diamond crystal for different polar angles to the axis* $\langle 100 \rangle$*, ref. [101].*

Likewise, charged particles from the pair production will lose energy in the converter with the distinctive difference that for the produced pair the initial distribution is not uniform since the pair is preferentially produced in the region of high fields near the nuclei in the string.

On the other hand one could use an analogy with blocking experiments where the emitted particle experiences a close-encounter with one of the following nuclei and gets transferred to the random beam. In this case a pair created in the vicinity of the string can be expected to lose energy as in random. The pair will therefore lose less energy compared to an incident charged particle, since in the first case it is an indirect process - pair production and subsequent energy loss - in the second it is direct.

The experiment NA46, which was also involved in the search for the previously mentioned 'Darmstadton' (p. 20) produced in strong crystalline fields, has investigated the effect of blocking of the positron and focussing of the electron. They also find an asymmetry in the distribution of $\xi_{\pm} = (E_{e^+} - E_{e^-})/(E_{e^+} + E_{e^-})$ reflecting an increased energy loss of the electron with respect to that of the positron [99]. However, the detection of blocking and focusing requires a long field-free region after the converter which was not possible for the NA43 setup.

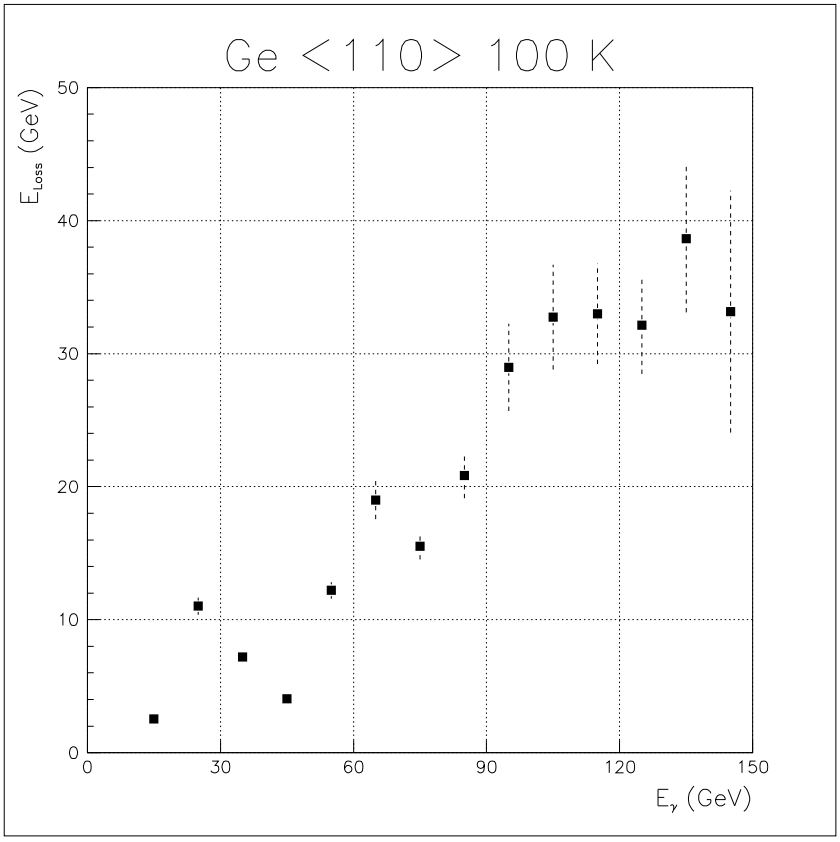

Figure 16: *Energy-loss of the e^+, e^--pair after conversion in the crystal.*

Clearly, the energy of the pair detected in the pair spectrometer is the energy after radiative loss in the converter. However, the energy balance can be recuperated by use of the tagged photon energy and the calorimeter, such that the *total* energy radiated in the crystalline converter can be found. This was done for the photons incident on axis and the approximate average energy loss was found to be $\overline{\Delta E_\gamma / E_\gamma} \approx 1/5$, see

figure 16. Multi-photon effects were taken into account (see below).

For higher energies there were indications of a non-increasing, maybe even reduced, energy-loss, hinting at the passage between the two domains of energy-loss, $\Delta E \propto \gamma^2$ for $\chi < 1$ and $\Delta E \propto \gamma^{2/3}$ for $\chi > 1$. Naively, one would expect this passage to take place in the region of energies near twice the threshold energy since the pair typically divides the available energy evenly, i.e. at around 100 GeV in good agreement with observations, see figure 16. The fluctuations at low energies in figure 16 are connected to the multi-photon subtraction procedure that may even generate a negative average energy-loss.

For each event, the pair energy was determined as the energy detected by the pair spectrometer if this coincided with the energy determined by the tagging system and the calorimeter energy within 8 GeV. Otherwise, the calorimeter and tagged energy was used. Events above the geometrically imposed energy threshold of the calorimeter, $\simeq$ 16 GeV, where the energy determined by the tagging system and the calorimeter energy do not coincide within 8 GeV were rejected. The value 8 GeV was chosen on the basis of an examination of the missing detection of an electron or a positron due to impact points at the edge or outside the full lead glass calorimeter. In this way the geometrically imposed energy threshold of the calorimeter is defined.

8.4.2 Multi-photons

Another type of events may resemble a pair where energy has been lost in the passage of the converter. These are the multi-photon events originating from the relatively large thickness of the emitter-foil. If two photons are emitted from one incident electron and only one of them converts, this will appear as a photon emitted in the converter, since both the tagging system and the calorimeter can detect only the sum of emitted energies in a multi-photon chain.

Events where more than one photon convert can not be reconstructed in the pair spectrometer and are disregarded in the analysis. These events were found to contribute only a small fraction. The contribution was found by fitting to the observed distribution of the energy loss in the solid state detector which gives information on the number of single pairs, N_1, (2 MIPs) and double pairs, N_2, (4 MIPs). The ratios of these were found in the aligned case for different energy intervals as registered by the tagging system to be $\simeq$5%, increasing with increasing energy to $\simeq$10%. The increase with energy of this ratio is due to the increasing enhancement and therefore events where the pair emits a photon which subsequently converts become more probable as do events where two photons emitted in the radiator both convert. In other words, as the energy rises, the point where multiple processes occur can be reached and the formation of a proto-shower can take place.

As a first approximation these multi-photon events have been accounted for by counting the number of multi-photon/energy-loss events, $N_{n\gamma}^{\mathrm{ran}}$, where the second (con-

verter) crystal was in random. Since in this case the effective radiation length of the converter, $X_{\rm c}^{\rm eff}$, is much less than that of the radiator, $X_{\rm r}$, the majority will actually be two-photon events. With $N_{n\gamma}^{\rm ran}$ normalized to the number of incoming electrons (norm events), $N_{\rm e^-}^{\rm ran}$, is subtracted from the corresponding number in the aligned case: $N_{n\gamma}^{\rm alg} - \Lambda \cdot N_{n\gamma}^{\rm ran} N_{\rm e^-}^{\rm alg}/N_{\rm e^-}^{\rm ran}$. By use of the factor $\Lambda = (1-\exp(-7\eta(E_\gamma^{\rm prev})\Delta t/9X_0))/(1-\exp(-7\Delta t/9X_0))$, where $\eta(E_\gamma^{\rm prev})$ is the enhancement corresponding to the preceding bin (initially taken as 1), the change of conversion probability with energy is taken into account. As a first approximation, each of the multi-photons belong to $E_\gamma^{\rm prev}$ in terms of enhancement. The whole procedure, taking into account that the requirement $X_{\rm c}^{\rm eff}(E_\gamma) << X_r$ is more severe the higher the energy, is only valid as long as the probability for multi-photon emission *and* conversion of two or more photons is low (a few percent).

8.5 Enhancements

The total and differential enhancements are defined in this section and the procedure of analysis to determine them is described in detail.

8.5.1 Total enhancement

For pair production the total enhancement as a function of photon energy is obtained by integration over ξ_+ of the conversion probabilities in the random and aligned situation for a given interval of photon energies, ΔE_γ, around the central point in the bin, E_γ, (again having subtracted backgrounds) and then taking the ratio of the corresponding radiation lengths, averaged over the bin, ΔE_γ:

$$\eta(E_\gamma) = \frac{X_0(E_\gamma)}{X_{\rm a}(E_\gamma)} = \frac{W_{\rm a}(E_\gamma)}{W_0(E_\gamma)} = \int \frac{dW_{\rm a}}{d\xi_+} d\xi_+ \Big/ \int \frac{dW_0}{d\xi_+} d\xi_+ \tag{69}$$

where the 'radiation length' in the aligned case, $X_{\rm a}(E_\gamma)$, is related to the conversion probability[17], $p_{\rm a}(E_\gamma)$, as $p_{\rm a}(E_\gamma) = 1 - \exp(7\Delta t/9X_{\rm a}(E_\gamma))$.

For radiation the enhancement is found as

$$\eta(E_{\rm r}) = \frac{X_0(E_{\rm r}}{X_a(E_{\rm r})} = \frac{X_0}{\Delta t}\frac{E_{\rm r}}{N_e}\frac{dN_e}{dE_{\rm r}} \tag{70}$$

where $E_{\rm r}$ is the radiated energy and N_e the number of projectiles, i.e. the enhancement is the factor by which the radiation yield exceeds the Bethe-Heitler yield.

The enhancements are defined as above to take into account that if the pair production probability is large (e.g. for a thick crystal), the flux of photons diminishes as the photon-beam penetrates the crystal. In other words, the approximation $p_a(E_\gamma) \simeq W_a(E_\gamma) \equiv 7\Delta t/9X_a(E_\gamma)$ is not sufficient.

[17] The average fraction of a beam of photons that have converted after passing e.g. a foil, p, is also called the conversion probability. It coincides with the 'true' conversion probability, W, in the limit of a thin converter.

Note that X_0 does not depend on E_γ, but the flux of the incident photon beam does depend on E_γ and the flux of the *accepted* photon beam depends on E_γ in a non-trivial fashion when the pair spectrometer is used. Therefore, since the total number of photons accepted by the pair spectrometer depends sensitively on the differential distribution in (E_γ, ξ_+) the ratios were taken bin by bin in (E_γ, ξ_+). Had this procedure not been necessary, it would have been advantageous in terms of statistics to normalize to the total random (integrated over ξ_+), taking into account the known variation with energy.

Due to the dependence of the acceptance on the photon energy, $E_\gamma(\xi_+)$, integral values for the enhancement can according to the simulations (section 9.1, p. 59) only be obtained for energies above 20 GeV. Below this value, the different differential distributions in aligned and random will affect the fraction of all created pairs which hit the 5th drift chamber. It is therefore possible that events are lost due to geometry because e.g. a 10 GeV photon converting along a random direction where asymmetric pairs are favoured has a higher probability that the positron or electron escapes DC5 than if it were converted along the axis where symmetric pairs are favoured. At 20 GeV the fraction of photons lost due to geometrical acceptance in random amounts to less than a few percent and already at 30 GeV this fraction is beyond the precision of the simulations, see section 9.1, p. 59.

Runs with the pair spectrometer magnet at 0A were performed to be able to determine the total pair-yields as a function of energy - this provides a cross-check of the total enhancements found by use of the pair spectrometer and extends the measurements down to the lead-glass threshold. These runs, however, were taken with quite limited statistics. On the other hand, the runs with Tr6 at 250A can be used to determine the total enhancement independently of the pair spectrometer by defining the emitted energy as the tagged energy for low energy photons and the calorimeter energy for high energy photons and then detecting the pairs in Sc11 *and* the SSD. This procedure gives results in agreement with those obtained by use of the pair spectrometer, since essentially the detector has been replaced by one with a much larger acceptance in (E_γ, ξ), see figure 28, p. 74). Also in this case, multi-photon events have to be accounted for.

8.5.2 Differential enhancement

The differential enhancement for a given photon energy, E_γ, in the pair production experiment was defined as

$$\eta(E_\gamma, \xi_+) = \frac{dW_a(E_\gamma, \xi_+)}{d\xi_+} \Big/ \frac{dW_0(E_\gamma, \xi_+)}{d\xi_+} \tag{71}$$

where $W_a(E_\gamma, \xi_+)$ is the *true* pair production probability, i.e. the probability of converting a photon in a thin converter. $W_a(E_\gamma, \xi_+)$ is for a particular photon energy, E_γ,

averaged over an energy interval, ΔE_γ, and for a particular relative positron energy, ξ_+, in the aligned situation (for subtraction of backgrounds, see the discussion in section 8.3, p. 51). The 'radiation length' $X_a(E_\gamma, \xi_+)$ is related to the conversion probability, $p_a(E_\gamma, \xi_+)$, as $p_a(E_\gamma, \xi_+) = 1 - \exp(7\Delta t/9X_a(E_\gamma, \xi_+))$, see footnote 17.

Since the pair energy is determined after the radiative loss in the converter, a possible difference in loss between e^+ and e^- will distort the differential spectra. The fraction of the total energy carried by the positron, ξ'_+, detected in the spectrometer is given as $\xi'_+ = E(e^+)/(E(e^+) + E(e^-))$, whereas the original distribution (before radiation) was $\xi_+ = (E(e^+) + E_\gamma(e^+))/(E(e^+) + E(e^-) + E_\gamma(e^+) + E_\gamma(e^-))$, where $E_\gamma(e^\pm)$ is the energy of the photon emitted from the $e^\pm$ after the conversion.

The relation connecting the real, ξ_+, and detected, ξ'_+, differential spectra is thus:

$$\xi_+ = \xi'_+(1 + \xi'_+ \frac{E_\gamma(e^+) + E_\gamma(e^-)}{E(e^+)})^{-1} \cdot (1 + \frac{E_\gamma(e^+)}{E(e^+)}) \tag{72}$$

which means that for the measured energy losses, the distortion - defined as $\xi_+/\xi'_+ - 1$ - will be $\leq 10\%$, i.e. a barely visible effect even in the case of very asymmetric losses of the electron and positron.

On the other hand, the losses in the converter may affect the magnitude of the yield as

$$W(\xi'_+) \simeq W(\xi_+)(1 - \frac{\overline{E_\gamma}}{E}) \tag{73}$$

where $\overline{E_\gamma/E} \approx 1/5$ is the average total energy loss relative to the incident energy. The reason for this reduction is that the range of values for ξ_+ is modified from $0 \leq \xi_+ \leq 1$ to $0 < E_\gamma(e^+)/E \leq \xi'_+ \leq 1 - E_\gamma(e^-)/E < 1$. In other words, for the pairs where one or both particles would hit close to the edge of the drift chamber in the absence of radiative loss, the loss may bring the particle(s) outside the acceptance such that the pair will not be counted. For photon energies well above the geometrical limit of chamber 5, 4.6 GeV, only the very asymmetric pairs will be affected by this[18]. For the remaining pairs the 'loss' indicated by eq. (73) will only amount to the above mentioned redistribution (particles 'lost' at one ξ_+ will appear at another ξ_+ within the accepted range).

9 Pair spectrometer tests

In order to ensure that the acceptance and momentum-resolution of the pair-spectrometer was understood, two tests were performed in which a comparison was made between simulated/calculated values and data for which the physics is known, namely coherent and incoherent bremsstrahlung.

[18] As examples, a 20 GeV photon will appear with a reduction according to eq. (73) for $\xi_+ < 0.08; \xi_+ > 0.85$ whereas an 80 GeV photon is only affected marginally for $\xi_+ < 0.02; \xi_+ > 0.96$

9.1 Monte Carlo simulation

A Monte Carlo simulation with a Pascal program was performed by use of the so-called Von Neumann Monte Carlo technique [17, p. 168]. The principle of the Monte Carlo was to imitate as closely as possible the experimental situation in NA43 although ingredients like inefficiencies were not known and could not be simulated. Furthermore, only the situation with both the radiator and the converter in random was simulated.

The simulation begins with an incident electron beam of 149.1 GeV/c which passes through a radiator of predefined thickness by which the electron radiates a Bethe-Heitler spectrum of photons according to eq. (33). For the appropriate fraction of events two photons are emitted according to the behaviour in eq. (36), one with E fixed at E_e =149.1 GeV/c and one with E set as the remaining energy, $E_e - \hbar\omega_1$. These photons were given equal conversion probability, but only single conversions were registered. Each primary electron was tracked through the set-up, including multiple Coulomb scattering (MCS) in air, helium, mylar-foils and scintillator and including drift chamber resolution. These uncertainties were generated as Gaussian distributions based on (pseudo-)random numbers [17, p. 169]. Electrons deflected outside the range of DC4 were rejected for the reconstruction of the tagging spectrum - the energy distribution of the radiating electron after passage of B8 - which coincided well with the measured one.

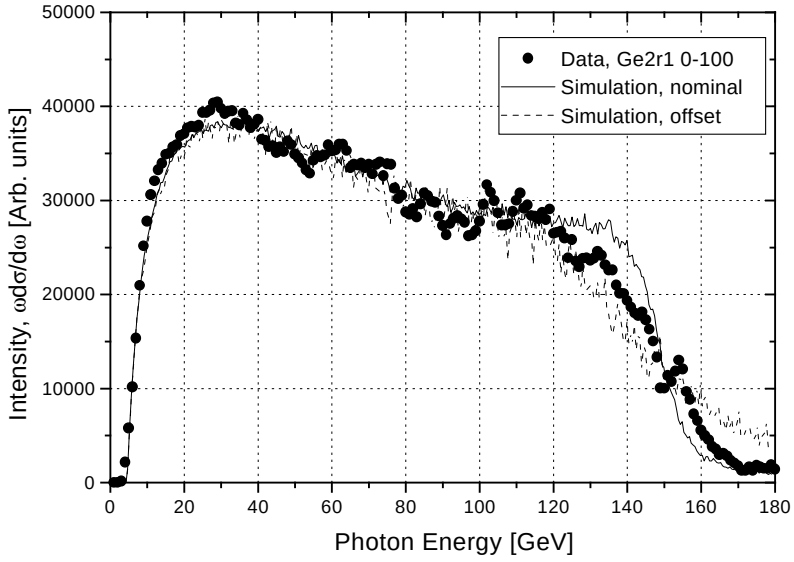

Figure 17: *Results of the Monte Carlo simulation compared with data for radiation from 0.82 mm Ge in random plus a 2 mm Cu foil. Photon energy reconstructed by use of the pair spectrometer. The filled dots are experimental points, the full-drawn curve is the simulation for the photon beam center incident on the field wire and the dashed curve includes the measured offset with respect to the field wire.*

Conversion of the emitted photons was calculated as a Bethe-Heitler distribution

of the photon energy among the positron, $\xi_+\hbar\omega$ and the electron, $\xi_-\hbar\omega$ according to eq. (38). The created particles were then sent through the pair spectrometer magnet, Tr6, deflected and momentum analyzed in DC5 and DC6, again including MCS and resolution. Only pairs fulfilling exactly the criteria as in the analysis of the experiment were accepted, so for instance any pair where only one particle was registered (e.g. due to acceptance of DC5) was rejected. From this, the incident photon energy and the relative positron energy, ξ_+, could be reconstructed.

As figure 17 shows, there is good agreement between the shape of the experimental spectrum and that of the simulated spectrum. The geometrically imposed cut-offs convoluted with the resolution in both spectra, i.e. the energy thresholds in figure 17 and the differential thresholds in figure 18, show almost perfect agreement between simulation and data. In this connection it is worth noting that events with e.g. 3 particles detected in one or more of the chambers (which can be the result of the deflected primary electron not being fully contained in the dump for instance) are not simulated nor is the cross-talk between DC cells. This type of events may contribute to some extent to the difference between simulated and real data. Also the absolute value of the resolution of a drift chamber affects sensitively the high energy end of the simulated spectrum of photon energies and is thus another source of the slight disagreement there.

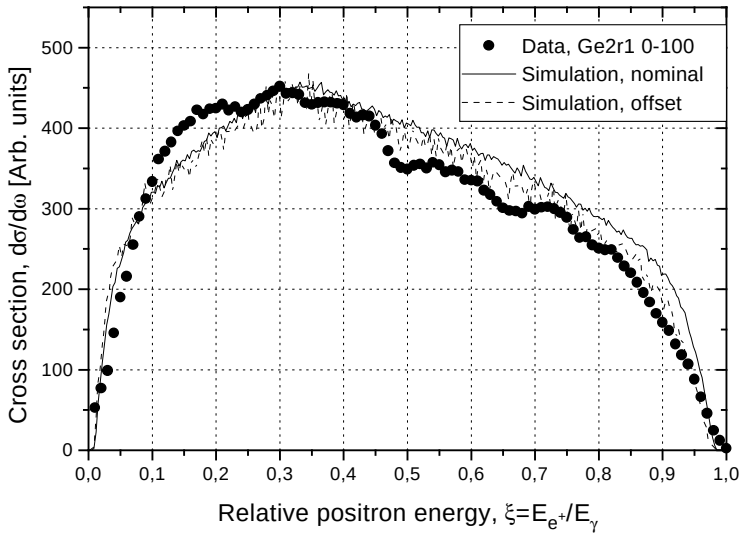

Figure 18: *Results of the Monte Carlo simulation compared with data for radiation from 0.82 mm Ge in random plus a 2 mm Cu foil. Relative positron energy reconstructed by use of the pair spectrometer. The filled dots are experimental points, the full-drawn curve is the simulation for the photon beam center incident on the field wire and the dashed curve includes the measured offset with respect to the field wire.*

In order to reduce computer-time[19] the simulation code was written such that all incident electrons radiate and all emitted photons convert. This means that the absolute values are arbitrary and the agreement in intensity is only a result of scaling. However, since the expected and measured integral conversion efficiency as found in the determination of backgrounds, see section 8.3, p. 51, gave a reasonable value for the background, the absolute scales are in good agreement as well.

The differing behaviour inbetween the cut-offs can be due to inefficiencies of the drift chambers which are not taken into account or variations of the true positions - notably in the deflection direction - with respect to those used in the simulations: The offset of the photon beam with respect to the field-wire in the two chambers can be found by determining the position of the vertex from those events with two hits in both chambers and relating this to the position of the field-wire which becomes visible due to cross-talk (section 8, p. 49). This offset is 0.4 mm and 1.4 mm in DC5 and DC6 respectively for the data considered. Taking this offset into account improves the agreement between simulation and data slightly as the figures show (dashed curves).

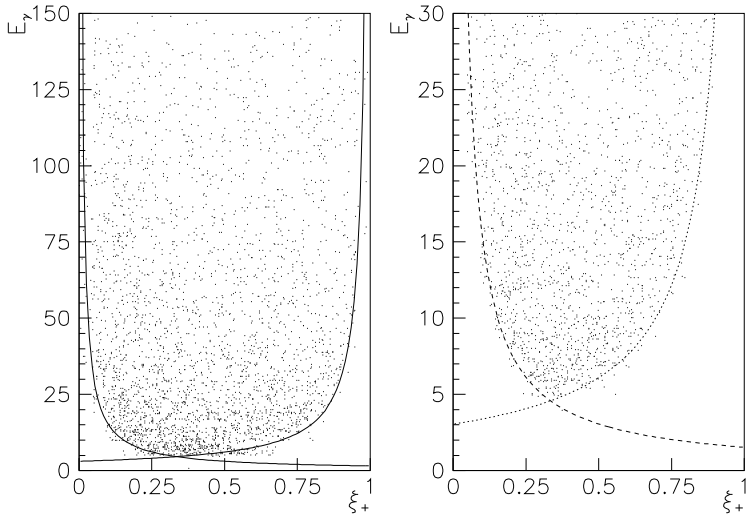

Figure 19: *The reconstructed photon energy, E_γ, vs. the relative positron energy, ξ_+, showing the limits set by the geometry from data (dots) and from eq. (74) (lines). The two graphs display the same data with different scaling of the photon energy.*

The shape of the energy- and differential spectrum, figures 17 and 18, are far from resembling the Bethe-Heitler spectrum - this is due to the geometrical constraints on the photon energy imposed by DC5. In a plot of the reconstructed photon energy, E_γ, vs. the relative positron energy, ξ_+, see figure 19, the limits are set by the minimal

[19] The simulations shown in figure 17 and figure 18 took 8-10 days with a dedicated Pascal program running on a 133 MHz Pentium PC.

accepted positron energy, $E_{e^+}^{min}$, and the minimal accepted electron energy, $E_{e^-}^{min}$, as

$$E_\gamma \geq \frac{E_{e^+}^{min}}{\xi_+} \quad \text{and} \quad E_\gamma \geq \frac{E_{e^-}^{min}}{1-\xi_+} \tag{74}$$

The figures 17 and 18 correspond to projections of figure 19 onto the y- and x-axis, respectively. The minimal accepted energies, in this case $E_{e^-}^{min} = 3.05$ GeV and $E_{e^+}^{min} = 1.53$ GeV for the nominal beam, are inversely proportional to the distance from the impact of the photon beam (the vertex) to the edge of the drift chamber, d_{edge}. This means that if the chamber is asymmetrically positioned, the differential spectrum becomes asymmetric with a peak at d_{edge}/D where D is the width of the chamber. In the present case $d_{edge}/D \simeq 0.33$ in good agreement with data.

9.2 Coherent bremsstrahlung spectrum

Another test of the pair spectrometer was performed with a coherent bremsstrahlung (CB) spectrum. For CB, distinct peaks of enhancement with respect to random incidence at a photon energy $\hbar\omega_{CB}$ appear when the inverse formation length is equal to a reciprocal lattice vector [59]

$$\frac{1}{\lambda_{coh.}} = \phi \cdot n\frac{2\pi}{d_p} \tag{75}$$

which leads to

$$\hbar\omega_{CB} = E_e \cdot (1 + \frac{d_p}{n \cdot 2\pi \cdot 2\gamma\lambda\!\!\!^{-} \sin\phi})^{-1} \tag{76}$$

where n is an integer and ϕ is the angle to the plane. Due to the thick converter (4 mm Cu=$0.28X_0$) and the non-collimated photon beam, the low-energy side of the peak is 'smeared out', whereas the drop-off at the high-energy side of $\hbar\omega_{CB}$ is clearly visible.

The appearance of other peaks stemming from lower-index planes is proposed in [100] for high energy beams with $E_{CB} \gg 4Z_2^2e^2/\theta^2\phi a_{TF}$. In this case with the angle to the axis, ϕ=40 mrad and the angle to the plane, θ=0.22 mrad, E_{CB} is in the multi-TeV region and therefore these peaks should not be seen.

Figure 20 shows the spectrum obtained by reconstruction of the photon energy using the pair spectrometer and a curve according to eq. (76) where θ=220 μrad. In the pre-alignment with the goniometer, θ was set such that the part of the beam used for the analysis here corresponds to 200-220 μrad from the plane. This pre-alignment can not be performed much better than 5-10 μrad due to the beam divergence, so the numbers for θ agree within the desired accuracy.

The above two tests of the pair spectrometer clearly indicate that the behaviour of the pair spectrometer in the analysis is well understood. Furthermore, it seems reliable to use the spectra for random incidence as normalization for the determination of enhancements as well as for the analysis of differential spectra.

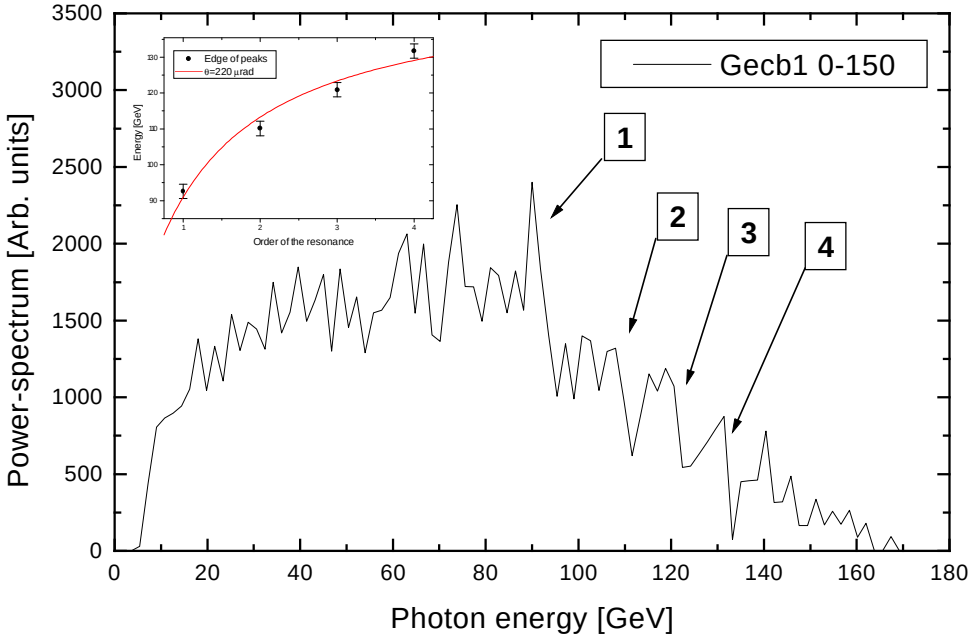

Figure 20: *Intensity-spectrum for coherent bremsstrahlung from 0.82 mm Ge* $\langle 110 \rangle$*, 40 mrad from the axis and 220 μrad from the (110) plane. The insert shows positions,* $\hbar\omega_{\mathrm{CB}}$*, of the peaks as a function of the order,* n*, with the full-drawn curve according to eq. (76).*

10 Enhanced radiation emission

The investigation of emission of radiation from the passage of ultrarelativistic electrons and positrons in different single crystals was initiated in [75, 85, 97] and has been investigated in detail by the NA43 experiment at CERN, see [76, 73, 86, 88, 89], and the recent paper [101]. The latest measurements by NA43 have been performed with essentially the same setup as for the pair production experiments mentioned below, except for the tagging system and the pair spectrometer. In short, the electron/positron passes a crystalline target at the first goniometer where entry- and exit-angles and positions can be specified by means of the 3 position sensitive detectors, DC1, DC2, DC3. The particle is separated from the radiation emitted in the crystal by deflection in the magnet, B8, and the energy of the radiation is detected by the lead glass calorimeter. The photon multiplicity is inferred from the distribution of Minimum Ionizing Particles (MIPs) stemming from conversions in a 1 mm Pb foil and detected in the solid-state detector which is positioned immediately upstream of the calorimeter.

10.1 Axial orientation

As a recent example of radiation effects for $\chi \simeq 1$, a 150 GeV electron in a 1.5 mm diamond crystal typically radiates $\simeq$10 photons for incidence along the $\langle 100 \rangle$ axis, losing $\simeq$110 GeV i.e. a very large fraction of its energy[20], see figure 21.

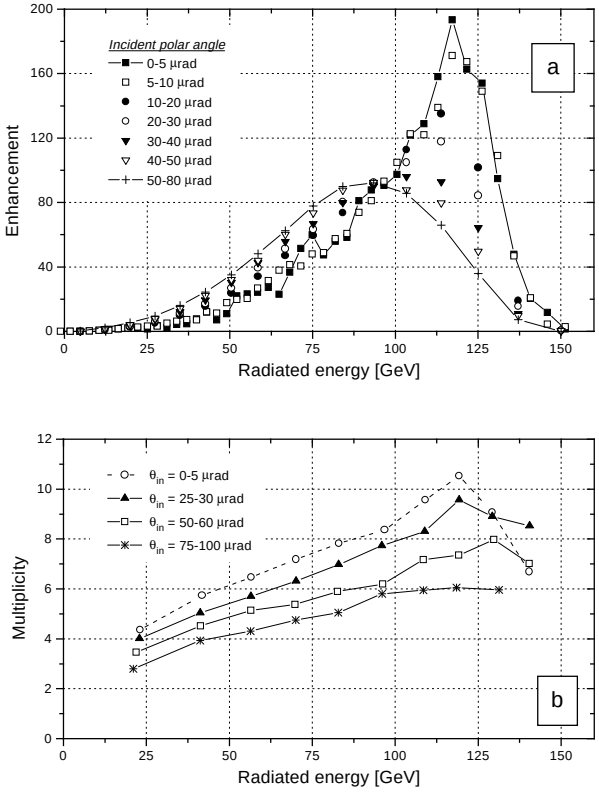

Figure 21: *Enhancement (a) and photon multiplicity (b) spectra for 150 GeV electrons incident on a 1.5 mm diamond crystal for different polar angles to the axis* $\langle 100 \rangle$*, ref. [101].*

This takes place with a probability almost 200 times larger than for incidence in the amorphous material. At angles corresponding to a few critical angles ($\psi_1 = 25\mu$rad) these values have decreased to $\simeq$6 photons adding up to an energy loss of $\simeq$80 GeV with an enhancement with respect to random of barely 100.

For 150 GeV positrons, see figure 22, the typical energy loss is $\simeq$60 GeV for incidence along the axis, increasing to short of 100 GeV for angles around ψ_1 whereas the average photon multiplicity varies between 4.5 and $\simeq$6.

[20]Note that the spectrum shows enhancements with respect to the Bethe-Heitler value such that the raw photon-spectrum is roughly $1/E_r$ times the shown spectrum, where E_r is the radiated energy. Nevertheless, due to the extremely rapid rise with E_r the typical radiated energy is close to 110 GeV.

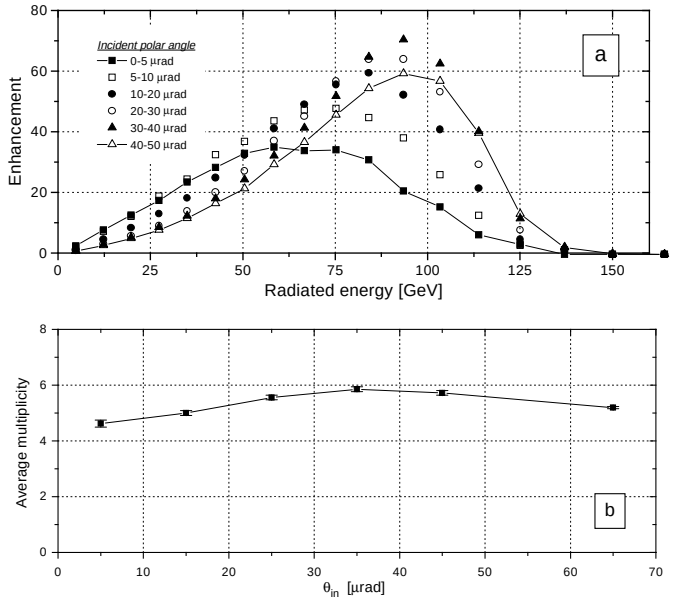

Figure 22: *Enhancement for different polar angles to the axis* ⟨100⟩ *(a) and average photon multiplicity (b) spectra for 150 GeV positrons incident on a 1.5 mm diamond crystal, ref. [101].*

The difference in average energy loss between like particles of opposite charges and the connection of this loss with the critical angle shows that an important feature is the redistribution of the charged particles under channeling conditions, see figure 15. Electrons are attracted to the areas where the field is strongest whereas positrons are repelled from these regions. The reason why the curves do not merge exactly for large angles is that the radiation from the positrons is slightly underestimated due to a small content of non-radiating particles (mainly protons) in the positively charged beam.

The large number of photons emitted further corroborates the realization [76] that the initially unexplained radiation peak for 150 GeV electrons in a thin Ge crystal [75] is due to the emission of a cascade of photons in the strong field of the crystal.

10.2 Strings-of-strings orientation

For incidence of 150 GeV electrons at an angle 0.3 mrad to the ⟨100⟩ axis and along the plane in e.g. a 0.5 mm diamond crystal a characteristic peak around 100 GeV was found [73] to develop in the spectrum of enhancement, see figure 23 and section 5.1, p. 35. However, the photon multiplicity was not known.

Recent experiments [101] have shown the photon multiplicity to be $\simeq$2.5 for the emitted energy in the region of the peak which is superimposed on a background of planar channeling radiation. However, it is not possible to tell the energy of the individual photons so it is very likely[21] that the multiplicity is due to a high energy

[21] At least it is hard to imagine a mechanism that emits two or more photons of roughly equal energy

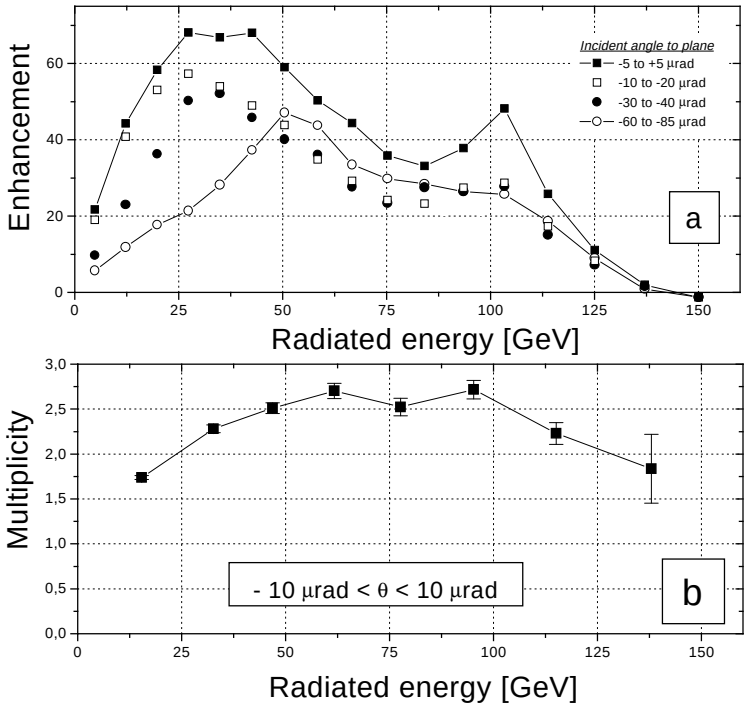

Figure 23: *Energy losses (a) and photon multiplicities (b) for 150 GeV electrons incident on a 0.5 mm diamond crystal at the angle 0.3 mrad to the axis* ⟨100⟩. *In (a) different angles to the (110) plane are given whereas in (b) the angles are less than 10 μrad to the plane, ref. [101].*

photon followed by photons of sub-GeV energies. This is furthermore supported by the observation of the planar channeling radiation which is most intense at 25-40 GeV, but possibly extends to the endpoint of the spectrum, thus contributing to the multiplicity as a 'background' to the coherent peak. The question of the distribution of energy among the two-three photons can be resolved by means of a photon intensity spectrum.

10.3 Photon intensity spectra

As demonstrated in section 9.1, p. 59 the behaviour of the pair spectrometer and the reconstruction of photon energies from this is remarkably well understood. This means that if the amorphous radiation foil is replaced by a crystal and the thickness of the amorphous converter is sufficiently small, it is possible to reconstruct the so-called photon intensity spectrum. A photon intensity spectrum gives information on the composition of the beam, not only in terms of photon multiplicities, but also on what energies the different photons possess. The presented spectrum for coherent bremsstrahlung, section 9.2, p. 62, is a nice example of this. Clearly, this kind of information will be able to confirm/reject the hypothesis of single photons in the coherent peak around 100 GeV for incidence in the strings-of-strings region (see above). It is there-

that add up to a peak in the middle of the spectrum.

fore of great interest to obtain such a photon intensity spectrum. It must be noted, though, that a photon intensity spectrum does not provide information on the energy of the emitting particle in case of the emission of several photons. In other words, there is no experimental difference between the spectrum for e.g. a 150 GeV electron that radiates a 10 GeV photon followed by a 100 GeV photon compared to the spectrum where the emission sequence has been reversed. It is therefore not the 'single photon spectrum' which eases comparison with theory [46], since this would require a photon multiplicity of essentially 1. This in turn would - for incidence along axes in low-Z materials - imply crystal thicknesses which are difficult to manage experimentally due to the decrease of the signal-to-noise ratio and which become comparable to the formation length for the photons whereby the emission is disturbed, see section 6.2, p. 40.

Experiments with 150 GeV electrons aligned on the $\langle 110 \rangle$ axis in 0.6 mm Si and 0.54 mrad off the axis on the (110) plane (the strings-of-strings region) as well as a wealth of angular settings for electrons and positrons on and near the $\langle 100 \rangle$ axis in 1.5 mm diamond were performed recently by NA43 and analysis is in progress.

11 Radiative cooling

In the 70's it was suggested that the emission of channeling radiation could lead to radiative cooling of a charged beam [102] understood as a reduction of the average angles to the axis during the passage of the crystal. The mechanism responsible for this is the photon emission which, because it originates from a transition between states in the transverse potential, reduces the transverse energy of the particle. The two definitions: Radiative cooling as a reduction in transverse energy and angular cooling as a reduction in average angular divergence will be used in the following. This is done since it turns out that radiative cooling does not necessarily imply angular cooling for emission in crystals, as shown later. This was not realized until recently [71], and is contrary to the case of radiation emission in a synchrotron.

11.1 Indications of radiative cooling

Following the discovery of the high energy peak of photon emission from 150 GeV electrons in a thin Ge crystal [75], a series of papers [66] explained the phenomenon by use of radiative cooling that would provide a 'self-amplification' mechanism since the loss of transverse energy under photon emission would lead to capture of the electron into channeled states where the field, and thus the probability of emitting another photon, is high. Later it was found that radiative cooling was not required to explain the radiation peak [103] a conclusion which has been relaxed [67], [104] since the Molière potential used in [103] overestimates the radiation probability, leading to an effect that

resembles that of the self-amplified radiative cooling.

11.2 First direct evidence for radiative cooling

The following is in large parts due to an analysis of radiative cooling by Kononets [67]: For an ultrarelativistic particle the velocity before and after emission of a photon is conserved since the emission angle is small and the radiative energy-loss is followed by a reduction of the γ-factor of the particle from $\gamma_\mathrm{i} = E/mc^2$ to $\gamma_\mathrm{f} = (E - \hbar\omega)/mc^2$. Furthermore, the transverse energy, $E_\perp = \gamma m v^2 \theta^2/2 + U(\boldsymbol{r}_\perp)$ is conserved between emission events such that setting $\theta = v_\perp/c$ it follows:

$$\langle\theta^2\rangle_\mathrm{f} = \langle\theta^2\rangle_\mathrm{i} + \frac{2}{E - \hbar\omega}[U(\boldsymbol{r}_\perp^0) - \langle U\rangle_\mathrm{f}] - \frac{2}{E}[U(\boldsymbol{r}_\perp^0) - \langle U\rangle_\mathrm{i}] \tag{77}$$

where $\boldsymbol{r}_\perp^0$ denotes the transverse position of the radiation event with respect to the string and $\langle ...\rangle_{\mathrm{i/f}}$ are averages over initial or final states. To first approximation these averages can be neglected since they are numerically far smaller than $U(\boldsymbol{r}_\perp^0)$ so the basic equation for angular cooling is obtained:

$$\langle\theta^2\rangle_\mathrm{f} - \langle\theta^2\rangle_\mathrm{i} \simeq \frac{2\hbar\omega}{E(E - \hbar\omega)} U(\boldsymbol{r}_\perp^0) \tag{78}$$

Radiative cooling affects the angular spread of the emitting particles differently such that three domains must be distinguished:

1. Positrons
2. Electrons with $\theta_\mathrm{in} > \psi_c$
3. Electrons with $\theta_\mathrm{in} \ll \psi_c$

Positrons experience angular heating, even during radiative cooling (reduction of transverse energy) since in eq. (78) the first factor on the rhs. is always positive such that the difference between exit- and entry-angles depends on the sign of the potential. The heating is a result of the transition in transverse energy being too small compared to the loss of longitudinal energy to cool the beam.

For electrons with angles $\theta_\mathrm{in} > \psi_c$ the same analysis as for positrons applies, but here the potential has the opposite sign resulting in angular cooling. On the other hand, for angles $\theta_\mathrm{in} \ll \psi_c$ radiation emission leads to capture to high-lying states in the potential well (due to the low surface transmission for negatively charged particles most particles with angles $\theta_\mathrm{in} \ll \psi_c$ are in a state just above the barrier). For such states characteristic transverse velocities are larger than in the initial state, $v_{\perp\mathrm{f}} > v_{\perp\mathrm{i}}$, such that $\theta_\mathrm{f} > \theta_\mathrm{i}$, i.e. angular heating.

Clearly, a process competing with the radiative cooling is the (enhanced) multiple Coulomb scattering. Note that for the electrons captured in states just below the

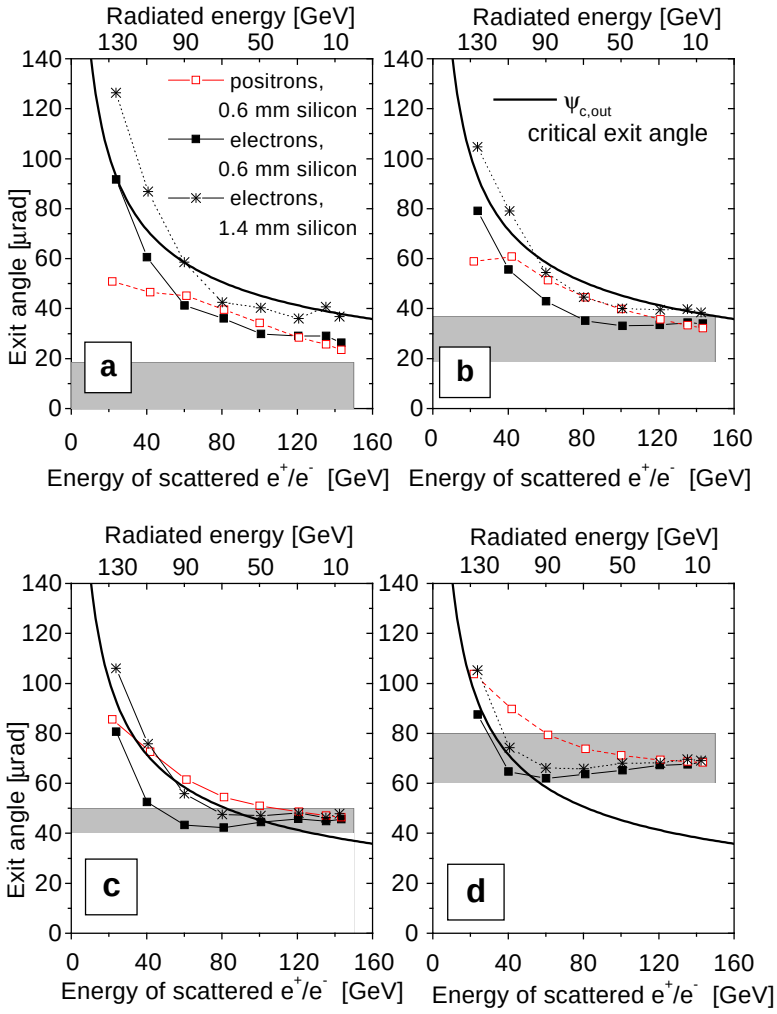

Figure 24: *Average exit polar angles for 150 GeV electrons (filled squares and stars) and positrons (open squares) traversing a 0.6 mm (squares) and a 1.4 mm (stars) thick* $\langle 110 \rangle$ *Si crystal. The lower x-axis is the energy of the exiting electron,* (E_e) *and the upper shows the radiated energy, i.e. radiated energies increase towards the left. The 4 regions of incident angles in (a)-(d) are shown as hatched areas and the Lindhard angle,* $\psi_1(E_e)$*, is the full-drawn line. Figures (a) and (b) are for incidence within the critical angle and figures (c) and (d) are for incidence outside the critical angle [71].*

barrier, MCS would initially lead to angular cooling! Furthermore, the particles will remain near the barrier due to the 'symbiosis' of MCS and radiation cooling, with transverse energy transitions in opposite directions. This is one reason why so many photons are emitted from an axially channeled electron.

In figure 24 is shown new data [71] for 150 GeV electrons and positrons traversing a 0.6 mm and a 1.4 mm thick $\langle 110 \rangle$ Si crystal. The hatched areas indicate the regions of incident angles used for the analysis and the data points denote the polar exit angle

of the electron/positron with respect to the $\langle 110 \rangle$ axis. A full-drawn line is drawn to show the axial critical angle as a function of the exit energy (after radition) of the particle. For comparison, the multiple Coulomb scattering for a 150 GeV/c singly charged particle in 1 mm amorphous silicon is 8 μrad.

For incidence nearly parallel to the axis, figure 24 (a), positrons are scattered less than electrons at low energies and - for the thicker crystal - those electrons that radiate more than $\simeq$90 GeV emerge with an angle larger than ψ_1. As the angle of incidence is increased, figures 24 (b)-(d), the situation for electrons and positrons is reversed and for incidence angles larger than the critical angle, (c) and (d), the average electron beam is in fact cooled in angles for photon emissions less than $\simeq$120 GeV ($\simeq$100 GeV for the thick crystal)! Considering that the MCS increases with decreasing momentum of the radiating particle this 'lower limit' is not surprising. The observations are in remarkably good agreement with the simple estimates of the three domains given above.

Further analyses [71] show that the net cooling effect - the ratio of decrease in angular spread due to radiation emission to the increase due to MCS - is proportional to the average enhancement times the square of the critical angle such that a strong axis in a low-Z material is preferable.

12 Polarization of high energy photons

It has been shown that planar channeling radiation is completely linearly polarized for 63 MeV electrons [105] and linearly polarized to a large extent at 900 MeV [106]. As opposed to the case of coherent bremsstrahlung, the enhancement and maximum polarization in this case occur for the same photon energies.

Encouraged by this and the possibility of making a polarized high energy photon beam for photoproduction, a proof-of-principle experiment performed by NA43 [107] showed that a crystal can be used to

1. Produce a linearly polarized beam of high energy photons

2. Measure the degree of linear polarization in a linearly polarized γ-beam

In the experiment, the photons were produced in the strings-of-strings region in a 0.5 mm diamond aligned 0.3 mrad from the $\langle 100 \rangle$ axis on the (110) plane, where 150 GeV electrons radiate a spectrum with a distinct peak at $\simeq$100 GeV, believed to be linearly polarized, single photons [74], [73], [101], see section 5.1, 35.

The detection of the polarization was based on an effect proposed by Cabibbo and others [108] and later extended to higher energies [109]. The method uses the different pair production cross sections for photons polarized perpendicular to and parallel to a crystal plane, $p_{\parallel}$ and $p_{\perp}$, respectively[22]. The analyzing crystal was a 1.5 mm diamond oriented 1 and 2 mrad from the $\langle 100 \rangle$ axis on the two orthogonal (110) planes.

[22]The 'reverse' naming for the cross sections are due to the orientation of the planes: If the planes

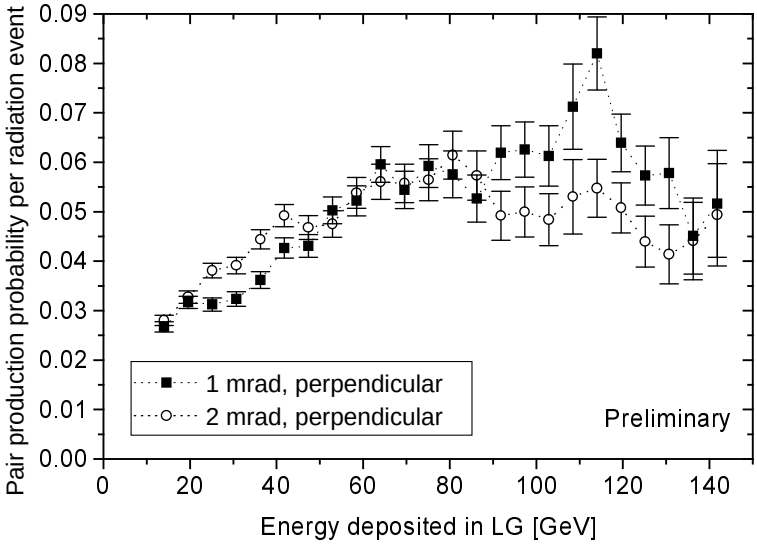

Figure 25: *A comparison of the two angular settings 1 and 2 mrad from the* $\langle 100 \rangle$ *axis on the (110) plane for the analyzing crystal.*

As seen from figure 25 the pair production probability per radiation event, p, (the photon multiplicity is not taken into account) depends on the angular distance to the axis for the analyzing crystal, in other words the analyzing crystal has an analyzing power depending on this angle.

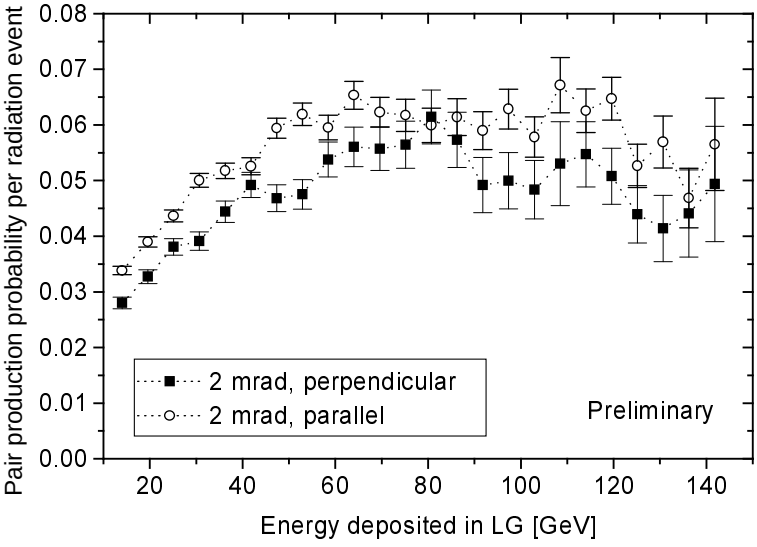

Figure 26: *A comparison of the two angular settings 2 mrad from the* $\langle 100 \rangle$ *axis on the parallel and perpendicular (110) plane for the analyzing crystal.*

in the two crystals are parallel, the photons have polarization perpendicular to the analyzing crystal plane.

In figure 26 is shown the pair production probability per radiation event for the settings where the photon beam is incident on the plane parallel or perpendicular to the plane where the radiation is produced. From this and a similar result for incidence 1 mrad from the axis, the so-called asymmetry parameter is derived.

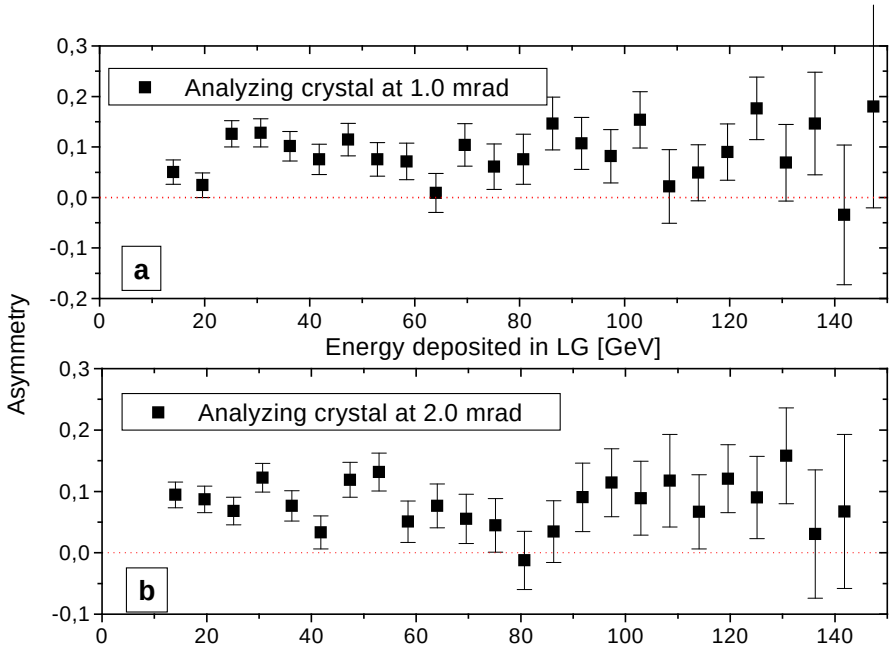

Figure 27: *The asymmetry parameter as a function of the energy deposited in the lead glass. The analyzing crystal is at an angular distance of 1.0 mrad (a) and 2.0 mrad (b) from the* $\langle 100 \rangle$ *axis on the (110) plane.*

The asymmetry parameter, $a = (p_{\parallel} - p_{\perp})/(p_{\parallel} + p_{\perp})$ amounts to $\simeq$0.1 with some variation with energy and incident angle and depending on the angular distance to the axis for the analyzing crystal, see figure 27.

From the asymmetry and a calculation of the analyzing power of the conversion crystal, it was concluded in a preliminary analysis[23] that the degree of linear polarization was 90%$\pm$40% for photons with energies 10-45 GeV [110]. Clearly, this result is very uncertain reflecting the fact that it is hard to calculate the analyzing power of the second crystal in the configurations used. Moreover, in the most interesting region of photon energies - around 100 GeV in this case - no calculations of the analyzing power of the second crystal exist. This means that the absolute degree of polarization of the coherent peak can not be determined yet.

[23]This analysis was based on a Monte-Carlo simulation to include effects of multi-photon emission.

13 Pair production on axis

As an additional check of the apparatus and the analysis-procedure the data obtained for pair production in alignment with the $\langle 110 \rangle$ axis on the 0.6 mm Ge crystal could be compared with earlier measurements [75], [97], [98], [111], [112], see also [45], [72]. Moreover, as described above, the total enhancement data found by use of the pair spectrometer in the axially aligned situation could be compared to those found by a completely independent procedure. The agreement between these data again indicates that the operation and analysis connected with the pair spectrometer is functioning. On the other hand, it would probably have improved the experiment, had the thickness of the radiator been somewhat smaller to avoid the problems connected to emission of two or more simultaneous photons, see section 8.4.2, p. 55.

13.1 Total enhancements

Of prime interest to a potential application of the strong field effect is the total enhancement, i.e. the enhancement of the production of pairs on axis compared to random incidence and irrespective of their differential distribution. It is therefore reassuring that the CFA predicts $\eta(E_\gamma)$ with good accuracy for Ge as well as for W, see figures 28 and 35. Figure 28 shows the total enhancements as a function of photon energy, analyzed by use of the pair spectrometer (filled dots) and more directly by use of Sc11 and the SSD (open squares). The overall behaviour agrees well within the two data sets as well as with theory, although fluctuations e.g. at 100-120 GeV indicate some disagreement. Further, it must be noted that the determination of the point at the upper end of the spectrum, 140-150 GeV, is difficult. This is due to the limited extent of DC4, which implies that the energy binning must be based only on the deposition in the calorimeter, where, as earlier [91] some energy has been observed to be lost. These losses are presumably due to incomplete shower containment in the lead-glass resulting from geometrical acceptance combined with the relatively large distance between conversion and the calorimeter.

For the determination by use of the SSD and Sc11, the emission of multi-photons from the radiator is only accounted for by rejection of the very low energy pairs due to the requirement of a coincidence by two counters. These multiphotons can be accounted for much more accurately by use of the pair spectrometer as described in section 8.4.2, p. 55. On the other hand, in the pair spectrometer analysis where events with two pairs are produced, these are rejected due to the ambiguity in the reconstruction (there is no way of telling which electron belongs to which positron and if incident on the same cell, only the one closest to the anode is detected). This leads to a slightly reduced enhancement, since good events are discarded. For the analysis with the SSD and Sc11 pairs giving a signal higher than $\simeq 3/2$ MIP is considered a good event such that a multiphoton chain will contribute artificially to the measured enhancement. For the

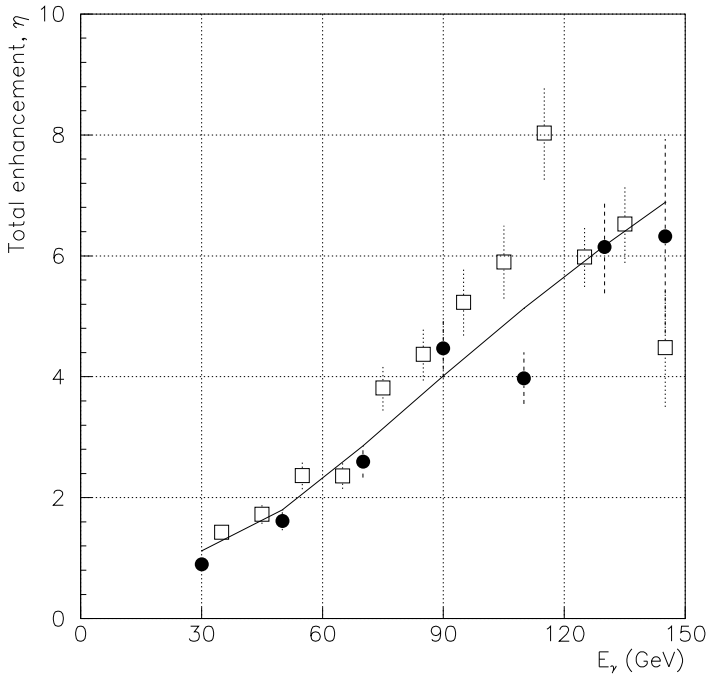

Figure 28: *Total enhancement, η, as a function of photon energy, E_γ, analyzed by use of the pair spectrometer (filled dots) and by use of Sc11 and the SSD (open squares). The full-drawn line is the expected value according to the Constant Field Approximation. The energy binning is in both cases equal to the distance between points.*

described experiment, the contribution of events with two pairs or more amounts to $\simeq 5-10\%$ over the whole range of photon energies. This contribution is a mixture of events originating from multi-photons or from a proto-shower event (primary pair creation - radiation emission - secondary pair creation), see section 8.4.2, p. 55.

13.2 Differential spectra

The differential distribution of pair production in $\langle 110 \rangle$ Ge has so far only been measured by Bak *et al.* [98] and in a different experimental situation. These measurements showed good agreement with the Constant Field Approximation for photons aligned with the axis and as well a good agreement with a calculation using Coherent Pair Production (CPP) for photons with an angle 2.75 to 3.25 mrad with respect to the axis and an angle 0.2 rad to the (110) plane. Clearly, as discussed above, the energy-loss of the produced pair after the conversion possibly affects the distribution in ξ. In [98] this was circumvented by ignoring those events (98%) where the energy of the pair and the energy of the tagged incident photon did not agree to within 3%. This raises a serious question: Is the distribution of the low-radiating pairs equal to that of all pairs irrespective of their subsequent loss? There is no theoretical answer to this, but

one may imagine that a pair produced close to the string loses more energy than a pair produced far from the string and that the distributions of such pairs are markedly different. This is also supported by the measurements showing asymmetry in the loss of electrons and positrons [99].

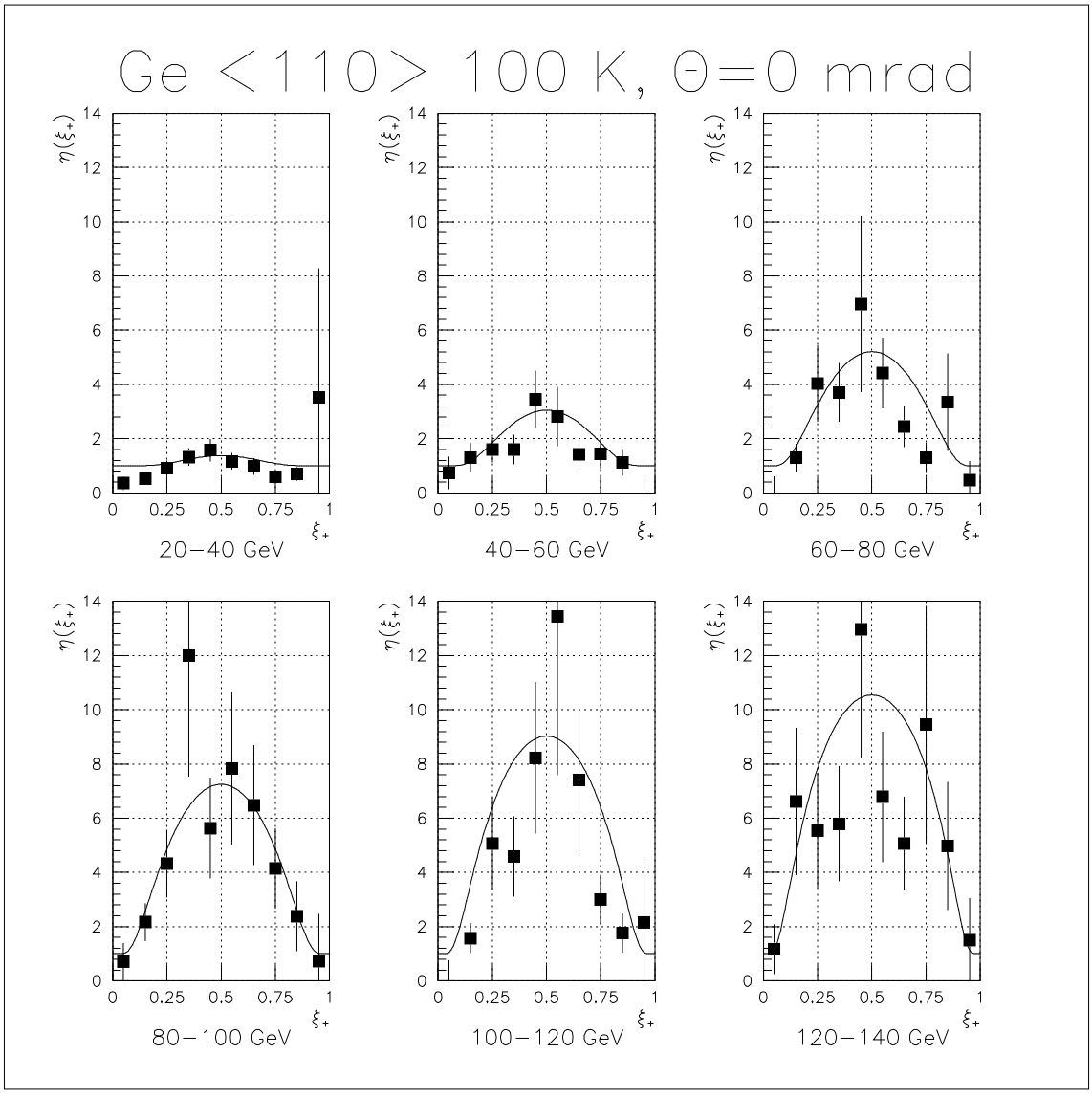

Figure 29: *Spectra showing the differential enhancement, $\eta(\xi_+)$, for different photon energy intervals for incidence along the axis. The solid line is the theoretical value according to the Constant Field Approximation (CFA).*

The present work shows good agreement with the shape of the differential enhancement, $\eta(\xi_+)$, calculated by use of the CFA. At the energy interval 120-140 GeV, the shape of the spectrum is difficult to confirm due to the scatter of points. Yet the overall agreement for the variation of $\eta(\xi_+)$ gives confidence in the new results obtained off axis along the (110) plane, although already at this point it is clear that the statistical uncertainties are too large for a precise evaluation of the differential spectrum.

14 Pair production off axis

In the following, measurements are presented of the differential and integral pair production yield for 20-150 GeV photons incident on a 0.6 mm Ge $\langle 110 \rangle$ crystal along the (110) plane and for different angles, $0 < \theta < 4.5$ mrad, to the axis. The prime goal is the investigation of the presence of coherent resonances in pair production.

14.1 Alignment with the (110) plane

For the alignment of the crystal, it as advantageous to use the large enhancement of radiation rather than the comparatively low enhancement of pair creation. The procedure was therefore to put a converter of relatively large thickness (5 mm Pb and 1.5 mm Cu was used) on the scintillator behind the second crystal, detect the pairs above a well-defined threshold (strictly larger than the signal of 1 MIP, 2.5 MIPs was chosen) and register the number of counts as a function of goniometer angle, see also section 7.4, p. 48.

The step-size of the goniometer for the second crystal was $\simeq$ 20 μrad and the alignment precision on the plane is estimated as $\approx$ 30 μrad. The stability over the run was high: during 24 hours the angular position of the axis drifted less than the precision of alignment.

In order to be influenced as little as possible from systematic errors in the alignment procedure, the variation of angle to the axis was done taking first the angles $\theta = n \cdot 0.5$mrad in increasing order and then the angles $\theta = n \cdot 0.25 + 0.5$mrad in decreasing order, with n integer. Following this procedure, it is improbable that two adjacent points along the plane are low or high due to alignment problems.

On the other hand, no reliable method of aligning to the plane in the off-line analysis was found: Assume the beam is aligned with an azimuthal angle ϕ to the plane and a polar angle θ to the axis. The variation within the available beam defined by the divergence of the enhancements, say at (θ, ϕ)=(1 mrad,0.1 rad) and (θ, ϕ)=(1 mrad,0.0 rad) is too small to detect with statistical significance. This means that this alignment was done with an uncertainty of $\approx$ 30 μrad as in the pre-alignment. Furthermore, it means that off-line selections of specific angular regions have little influence on the result, so these were not performed.

14.2 Total enhancements

In this section the total enhancements are investigated as a function of angle to the axis and photon energy. Further, in order to enhance the effect of the coherent oscillations in pair production along the plane, the enhancement of symmetric (in ξ_+) pairs as a function of angle and photon energy is examined.

14.2.1 All pairs

In figure 30 the total enhancement as a function of angle θ to the $\langle 110 \rangle$ axis is shown for different energy intervals.

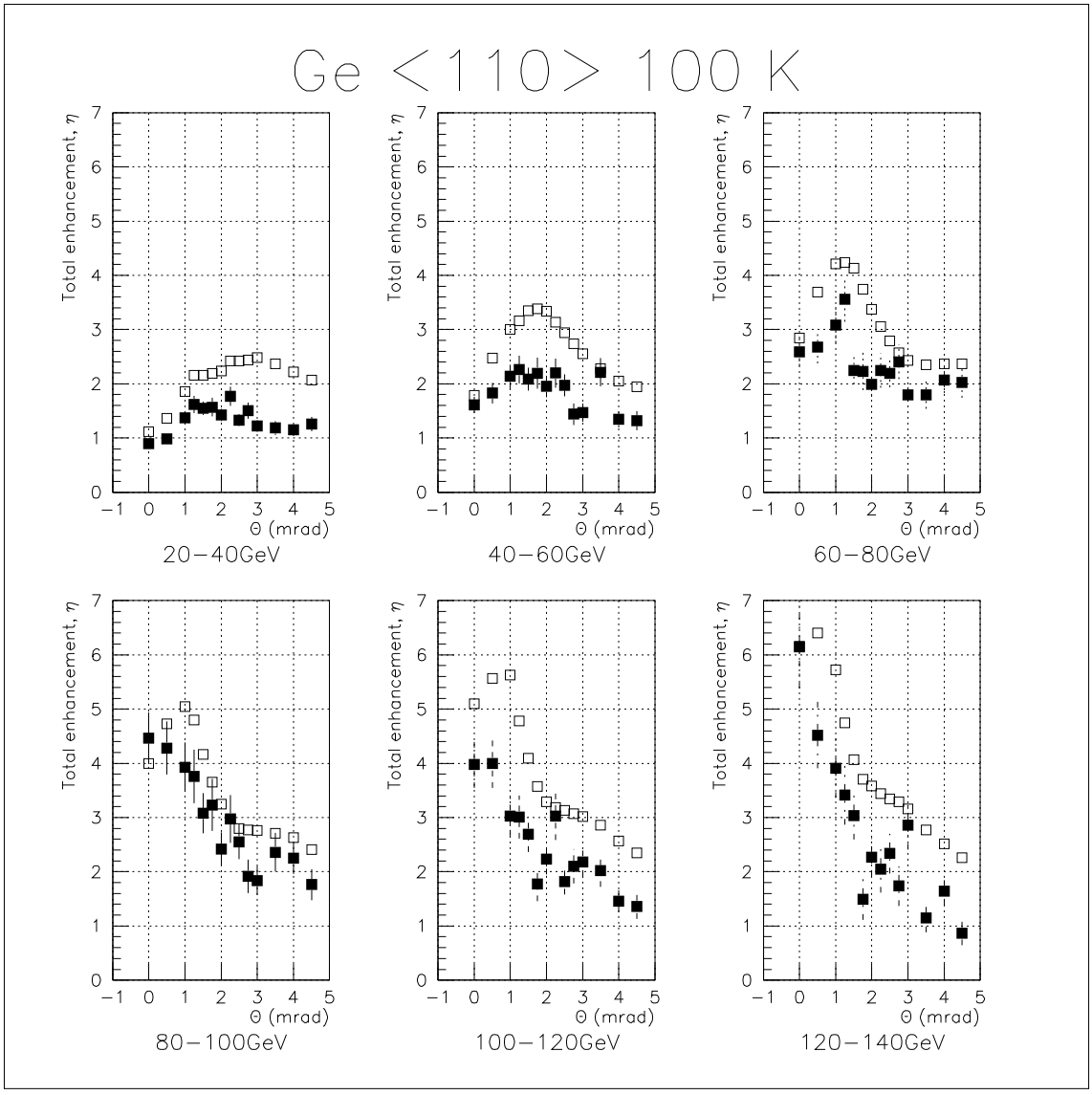

Figure 30: *Variation of the enhancement with angle θ to the $\langle 110 \rangle$ axis for different energy intervals. The filled squares are experimental points with error bars denoting the statistical uncertainty and the open squares represent values calculated in the semi-classical approximation for the central photon energy [113], [67].*

The maximum enhancement appears for smaller angles the higher the energy and the overall enhancement increases with increasing energy in accordance with the discussion connected to eq. (57), where the angle at which the maximum appears should be $\theta_m \simeq 0.7\text{mrad} \cdot 150/\hbar\omega(\text{GeV})$. This is nicely confirmed in the recent calculation of Kononets [67] (figure 30, open squares) where the crystal and crystallographic orienta-

tion used for the present experiment is considered. Moreover, the experimental points (filled squares) show good agreement with this dependency and the shape of each spectrum corresponding to an energy interval reproduces to a large extent the calculated one, except maybe for the very low energy point. In all cases the calculated value is for the central photon energy, i.e. 30, 50, 70, 90, 110 and 130 GeV.

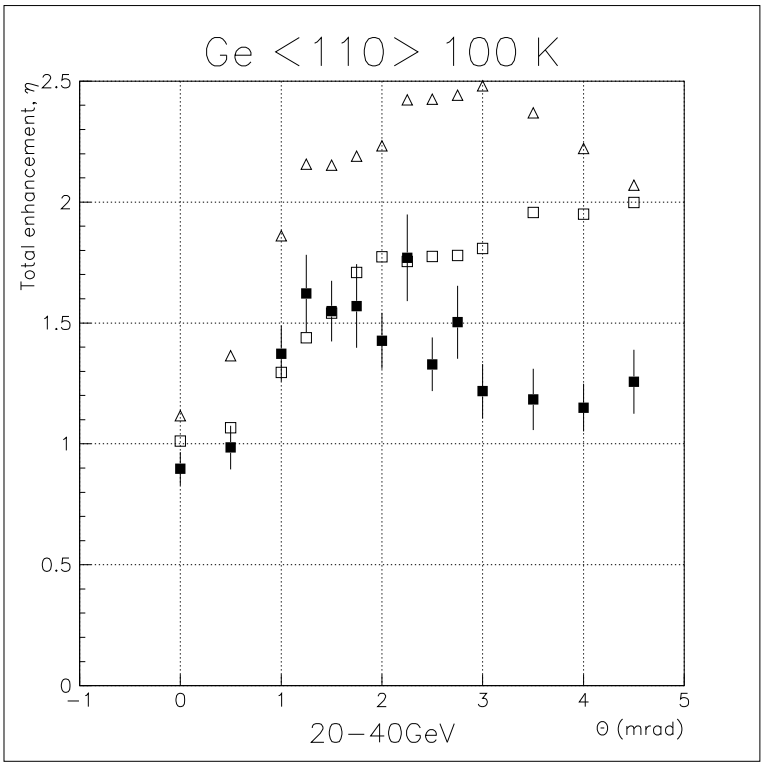

Figure 31: *Variation of the enhancement with angle θ to the $\langle 110 \rangle$ axis for photons in the 20-40 GeV range. The filled squares are experimental points with error bars denoting the statistical uncertainty, the open squares represent values calculated in the semi-classical approximation for the photon energy 20 GeV and the open triangles for 30 GeV [113], [67].*

With respect to the overall scale, though, the experimental points are somewhat low compared to the calculation, especially for the low and high energies. This discrepancy is not completely understood, but the higher flux of 20 GeV photons compared to 40 GeV photons (a factor of $\simeq 2.2$) means that the measurement which is a flux-weighted average over the bin 20-40 GeV must be somewhat lower than the calculated value for 30 GeV. This effect is smaller at higher energies since the bin-size relative to the central photon energy decreases.

Furthermore, effects of the Landau-Pomeranchuk type, see section 6.1, p. 37, which have not been taken into account in the calculation, may affect the theoretical values for both the coherent and incoherent contributions thus influencing the expected values of enhancement.

As shown in figure 31 the agreement with the theoretical points for 20 GeV (open squares) is better than with the 30 GeV points (open triangles) although at large angles to the axis there is still a significant discrepancy.

The same type of discrepancy (experimental values somewhat below theory for non-zero angles to the axis, especially at low energies) was found in the previous measurements by Bak *et al.* [98], whereas Belkacem *et al.* [112] found good agreement between theory and measurements for nearly all angles and energies in Ge $\langle 110 \rangle$, see also [46]. In this context it is worth noting that according to Baier *et al.* [60], the correction term for the non-uniformity of the field, F_2, which is proportional to θ^2 is large relative to the main term, F_1, for small energies. This may be part of the explanation for the discrepancy seen in figure 31.

14.2.2 Symmetrical pairs

In order that the mentioned coherent resonances in pair production appear as a more pronounced effect, one must consider only a fraction of the available values for the relative energy of the positron. This is to be expected since the formation length depends upon ξ_+, see eq. (59), and therefore the resonances get stronger by choosing a restricted interval for ξ_+. This is the case because the 'smearing' arising from different formation lengths is eliminated to a large extent when using e.g. only symmetrical pairs.

The enhancement for a certain interval, $b \leq \xi_+ \leq a$, in the relative positron energy has been defined as

$$\eta_i(a,b) = \frac{1}{a-b} \cdot \int_b^a \eta(\xi_+) d\xi_+ \tag{79}$$

Note that from this definition $\eta_i(1,0) \neq \eta$ since the Bethe-Heitler spectrum is not uniform in the interval $0 \leq \xi_+ \leq 1$. This is why the differential enhancement is called $\eta(\xi_+)$ and not $d\eta/d\xi_+$. The case of symmetrical pairs has been treated with $0.3 \leq \xi_+ \leq 0.7$ since for this interval the statistical uncertainty of the experimentally determined enhancement is still acceptable while the coherent resonances in pair production are strong enough to be visible.

The coherent resonances are clearly visible for the theoretical points, see figure 32 (open squares), in the ranges $\simeq$4-5 mrad, $\simeq$3-4 mrad and $\simeq$2-3 mrad for the energy intervals 60-80 GeV, 80-100 GeV and 100-120 GeV, respectively. For the experimental data (filled squares), the overall agreement with theory is very good for these energy intervals considering the statistical uncertainties, whereas for the remaining energies the shape of the spectra are fairly well reproduced while the scale is a factor $\approx$1.5-2 too low. So as for the total enhancement as a function of angle to the $\langle 110 \rangle$ axis, the enhancement for symmetrical pairs shows some disagreement with theory for low and high energies. This discrepancy is partly understood in terms of the varying flux of photons over the bin (see figure 31 and the discussion connected to this).

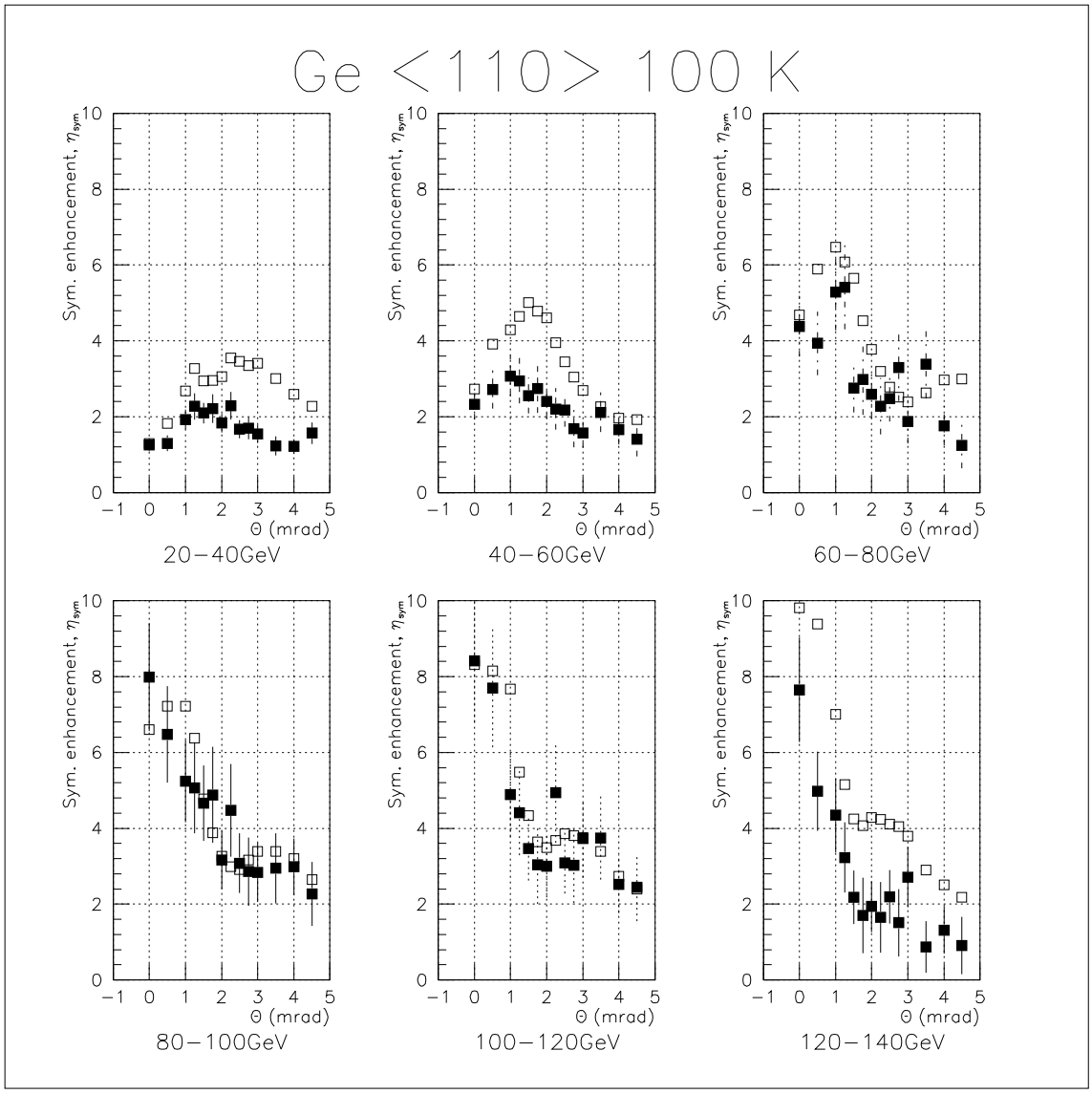

Figure 32: *Variation of the enhancement for symmetrical pairs,* $0.3 \leq \xi_+ \leq 0.7$*, with angle* θ *to the* $\langle 110 \rangle$ *axis for different energy intervals. The filled squares are experimental points with error bars denoting the statistical uncertainty and the open squares represent values calculated in the semi-classical approximation for the central photon energy [113], [113].*

14.3 Differential spectra

The figures 33 and 34 on the following two pages show the experimental values (filled squares with error bars denoting statistical uncertainty) obtained for the differential enhancement, $\eta(\xi_+)$, for different angles to the axis of photons in the energy range 80-100 GeV. Figures for the energy intervals 20-40 GeV, 40-60 GeV, 60-80 GeV, 100-120 GeV and 120-140 GeV can be found in appendix C. The full-drawn curve represents the calculation of Kononets [67], [113] who used the semi-classical approximation for

the central photon energy. For incidence along the axis, this calculation agrees with the CFA, whereas for non-zero angles to the axis the calculation shows oscillatory phenomena not present in CFA or coherent pair production theory.

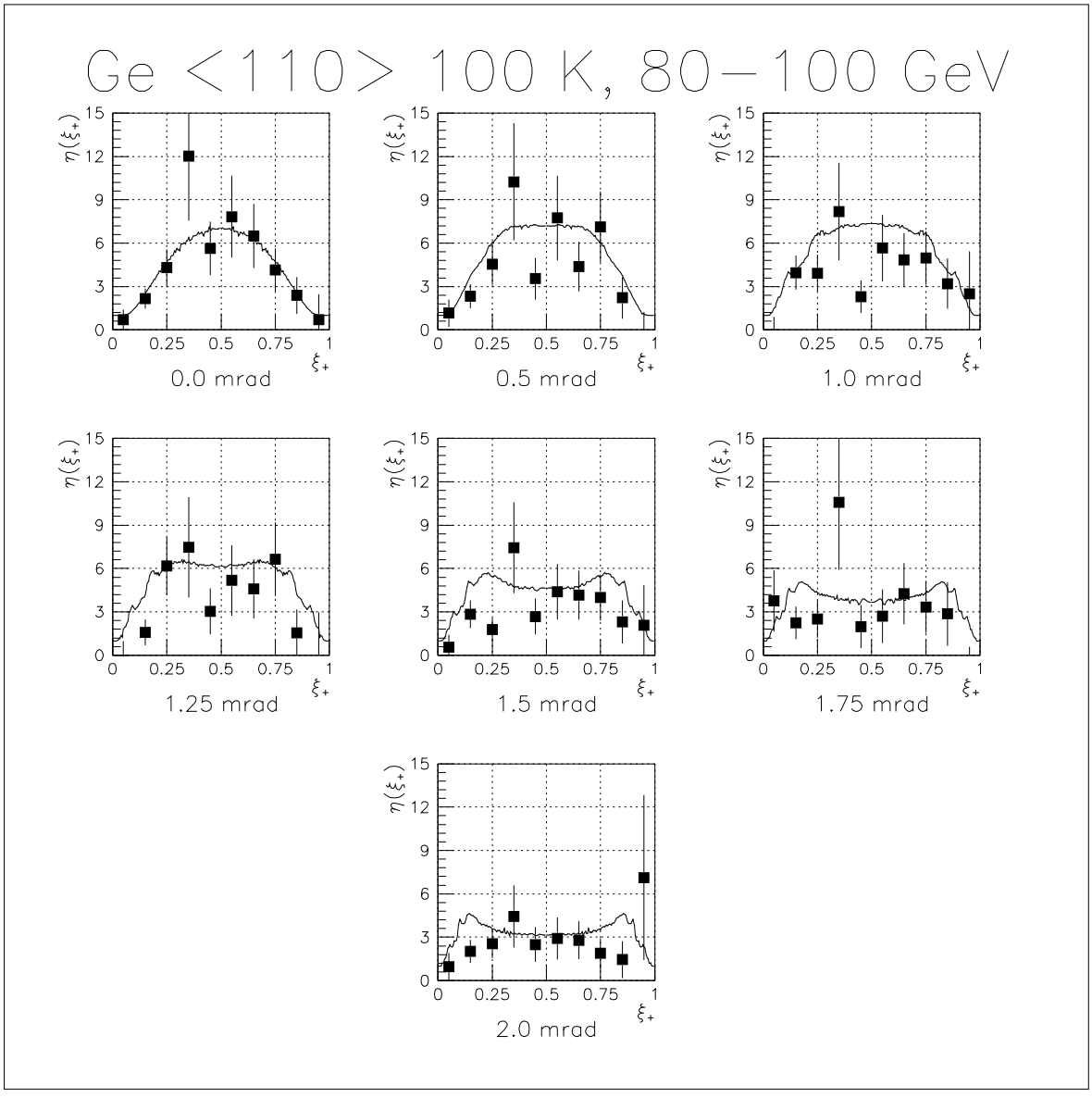

Figure 33: *The differential enhancement, $\eta(\xi_+)$, as a function of the relative positron energy, ξ_+. The photon energy is between 80 and 100 GeV and the direction of incidence is along the (110) plane in Ge for different angles, 0.0-2.0 mrad, to the $\langle 110 \rangle$ axis. The full-drawn curve is a calculation by Kononets using the semi-classical approximation for the central photon energy [113], [67] and the filled squares are experimental points with error bars denoting the statistical uncertainty.*

The overall agreement between theory and measurement in figures 33 and 34 is good - there are only few deviations of the experiment with respect to the calculated curves and it is questionable if they are statistically significant. This is not the case

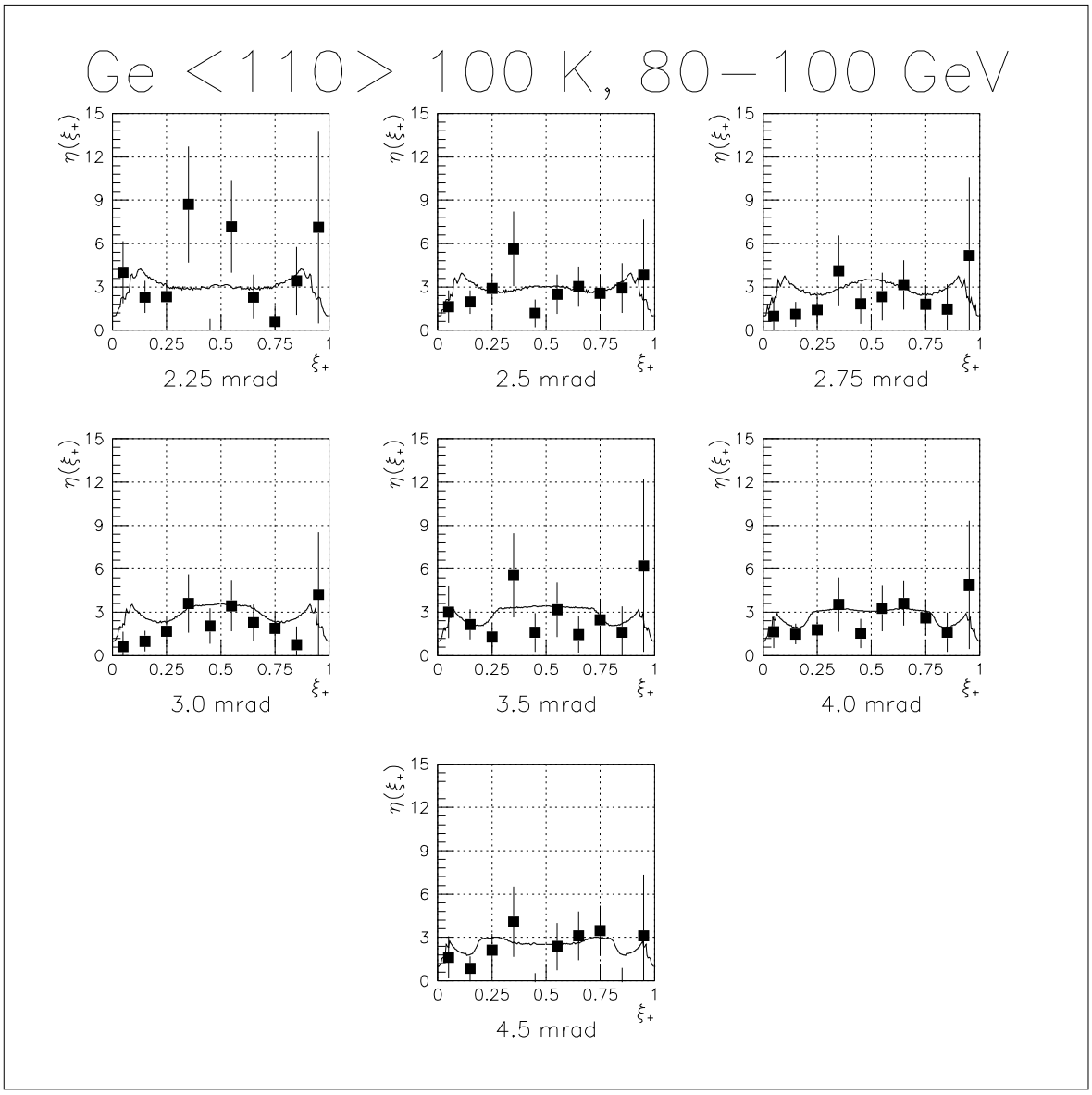

Figure 34: *The differential enhancement, $\eta(\xi_+)$, as a function of the relative positron energy, ξ_+. The photon energy is between 80 and 100 GeV and the direction of incidence is along the (110) plane in Ge for different angles, 2.25-4.5 mrad, to the $\langle 110 \rangle$ axis. The full-drawn curve is a calculation by Kononets using the semi-classical approximation [113], [67] and the filled squares are experimental points with error bars denoting the statistical uncertainty.*

for the remaining figures 55-64 (see appendix C), yet in most cases the shape of the differential spectrum does not disagree significantly with the calculated shape, although the details are difficult to extract from the measured points and the scales are not everywhere in agreement. The question of scale is dealt with in the discussion of total enhancement (see above). With respect to the details, the limited statistics for the measured points and the disagreement for the total enhancement makes a

comparison of small-scale variations in the theory and the measurements a difficult task. Moreover, 'systematic' effects arising from the insufficient random run influence the spectra such that a comparison between spectra also becomes hard. Note for example that for the energy interval 80-100 GeV the point at $0.3 \leq \xi_+ \leq 0.4$ is consistently above the calculated value (although never outside 2σ), most likely reflecting that the corresponding 'random' point is low due to a statistical fluctuation. These 'systematic' effects are present for all the spectra to some extent. Finally, the averaging resulting from the binning in the photon energy will 'smear' the details in the experimental spectra such that they are in any case not directly comparable with the theoretical spectra which are calculated for the central photon energy point.

15 Applications of the strong field effect

It has been demonstrated in the theory section (section 4.1, p. 21) that the strong field effects give information on QED processes in the extension of the classical synchrotron emission to the quantum version with emission under recoil. Therefore these phenomena are of fundamental interest for QED as they test the behaviour of synchrotron radiation in strong fields. On the other hand, applications of the strong field effect have also emerged where the drastic reduction in effective radiation length in crystallographic directions is being used.

15.1 Efficient conversion of photons in NA48

As described later in section 22.2, p. 117, the aim of the NA48 experiment is to measure accurately the decays of K_L and K_S to charged and neutral pions, thereby obtaining information on the CP-violation parameter ϵ'/ϵ, see e.g. [90].

In order to achieve a precise definition of the decay region of the K_S, those events where a K_S has decayed prematurely must be vetoed. This is done by insertion of a converter to make pairs from the $\pi^0 \to 2\gamma$ events and detecting the charged particles (which can also be π^+ and $\pi^-$from the kaon decay) in a sequence of scintillators, whereby the event can be rejected. The photons from the pion decay are typically in the energy range 10-80 GeV and with a divergence of $\simeq$10 mrad. The detection device is a scintillator array, the so-called AKS (Anti decayed K Short). However, in order to disturb the undecayed neutral kaons as little as possible, the converter should be of a short nuclear interaction length while maintaining a high conversion efficiency. For this application, a crystal of high Z aligned preferably along the strongest axis and of fairly large size is very well suited. The mosaic spread must be smaller than or of the order of the characteristic angle for the strong field effects, Θ_0, and somewhat larger than the critical angle for channeling in order to maintain a relatively uniform enhancement over the relevant angular range. Investigations using a 3.2 mm thick $\langle 100 \rangle$ tungsten crystal

of mosaic spread $\simeq$300 μrad (FWHM) were undertaken by NA43 in collaboration with NA48 and remarkably good agreement with calculations based on the Constant Field Approximation was obtained, see figure 35 [91]. At high photon energies, though, a slight disagreement between measurements and theory was observed. The nature of this disagreement is not fully explained, but may indicate the presence of a suppression of the Landau-Pomeranchuk type, see section 6.1, p. 37 especially section 6.1.2, p. 38. Recent experiments confirm this discrepancy for 5-55 GeV photons incident on a $\langle 111 \rangle$ W crystal and a $\langle 110 \rangle$ Ir crystal both at temperatures 100 and 300 K [92]. However, the discrepancy between measured values and theory diminishes when the more accurate Waasmeier-Kirfel potential [9] is used instead of the Molière potential. It can thus be concluded that accurate potentials - also at large distances from the axis where the contribution becomes significant for high energies - are important for a proper description of these phenomena.

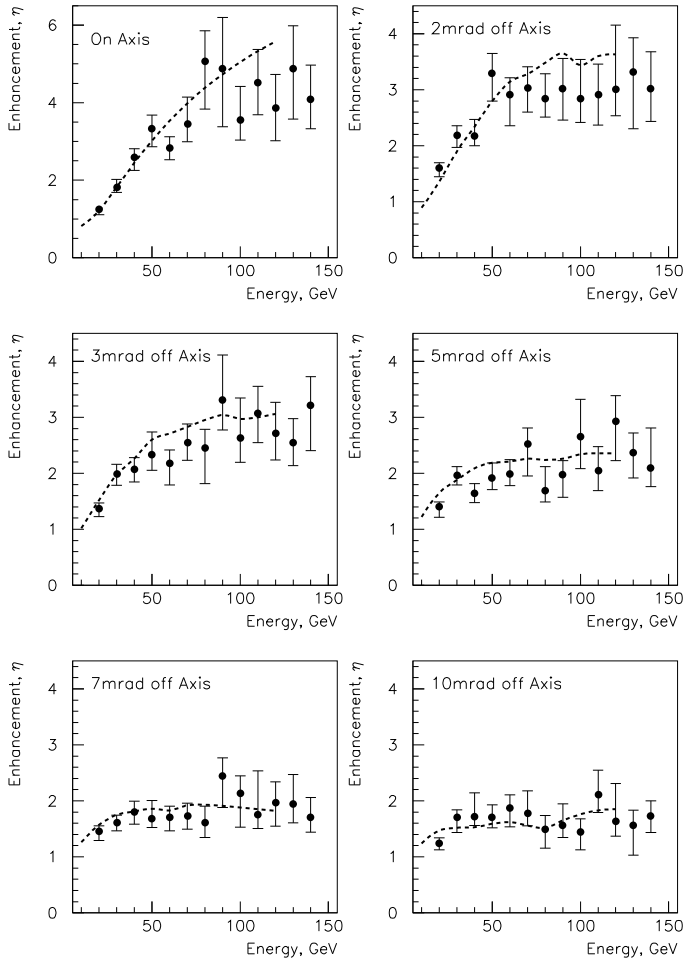

Figure 35: *Enhancement in pair production as a function of photon energy for a 3.2 mm thick $\langle 100 \rangle$ tungsten crystal for incidence along the axis. Dots with error bars are experimental points and the dashed curve shows a calculation based on the CFA [91].*

15.2 Beam diagnostics tools

Due to the small characteristic angles and the enhancements for the above mentioned effects in crystals, the directional effects and effectively short radiation length is useful for many purposes, also as beam diagnostics tools.

As discussed by Piotrzkowski in [114] and above, the polarizing and polarization-analyzing coherent effects of crystals can be used to monitor the polarization of bremsstrahlung originating from a polarized electron beam, thus in effect measuring the degree of polarization of this beam.

It has also been suggested [115] to use single crystals for fast measurements of the phase-space of high energy beams by use of bent crystals/crystalline collimators for which the critical angle is small. This effect may find application in investigations of non-linearly excited beams as has been done in test-experiments at the CERN SPS [116][24].

15.3 Particle production in a beamline

At the CERN SPS, the production of tertiary electron and positron beams is by conversion of photons originating from π^0 decay. This is typically done in a 5 mm ($\simeq 1 X_0$) Pb amorphous foil. In order to reduce the emittance of the produced beam, one could replace the amorphous converter by a crystal of smaller thickness. However, due to the difference in differential distributions, this would affect the intensity of high energy positrons and electrons.

This procedure could be foreseen for example for the E687/E831 beam at Fermilab [117] where high energy photons are produced in a fashion similar to the one used in H2 at CERN: 800 GeV/c protons interact in a liquid deuterium target where among others neutral pions are produced. One of the two photons from the pion decay is converted to an electron-positron pair in an amorphous foil, the 'converter' and the produced particles are transported around a dump for neutral particles whereafter they are refocussed and produce photons by bremsstrahlung in another amorphous foil, the 'radiator'. The main aim in this design of the beam is to reduce the fraction of neutral hadrons in the beam. The collection of electrons and positrons for the transport to the 'radiator' is done with a range of $\pm 15\%$ around the central momentum setting, typically 250 GeV/c or 350 GeV/c [117]. This is in the region where the pair production in the strong field of a crystal is enhanced with respect to the incoherent process. Possibly an increase in the flux of electrons and positrons to the 'radiator' by use of a crystalline 'converter' would be the result, however the careful Monte Carlo study of the E687/E831 beam would have to confirm this using the relevant conversion probabilities.

[24] The aim originally was to enhance extraction efficiencies by non-linear excitation of the beam, possibly leading to larger impact parameters (see also section 22.1, p. 116).

In a lepton collider with linacs (as for example the proposed CLIC or Next Linear Collider), the production of positrons will typically take place by electrons impinging on a foil creating bremsstrahlung which subsequently converts to pairs. This requires a fairly thick target with resulting large emittance for the positron beam thus reducing the luminosity. On the other hand, as proposed by Artru *et al.* [118], one might use a crystalline target for the production of photons and the subsequent conversion such that MCS of the produced positrons and heat dissipation in the converter is reduced.

15.4 Energetic photon beams for photoproduction

In the context of photoproduction of e.g. charmed particles as in the Fermilab E687-E831 experiment [119] it is crucial to obtain as many high energy photons as possible from an electron beam, yet the photon multiplicity must be kept low. Since the energy-loss of an ultrarelativistic electron aligned along a crystalline axis is a very large fraction of the incident energy this could be expected to be a good source. However, the main part of the spectrum consists of photons of relatively small energy, explaining the high multiplicity leading to a pile-up at the end of the spectrum.

The coherence peak, however, immediately suggests a crystal as the source of photons for photoproduction[25] - if the high energy photons have a low multiplicity. Nevertheless, in E687/E831 low energy photons create problems such that a better solution may be to use the region 'inbetween' the coherent resonances and the coherent bremsstrahlung with small angles to the axis *and* the plane. These combined coherent effects - though with an enhancement smaller than 50 - are not on a background of soft photons from the planar channeling radiation, see e.g. [78, fig. 1d curves 3-5, fig. 2b curve 4]. For the continuation of E831, a Si crystal oriented to give coherent bremsstrahlung is intended to be used to produce photons [120].

It has also been suggested to use crystals to achieve high fluxes of energetic photons for the exploration of gamma-gamma collisions. [68], [121]. The idea is that two colliding high energy electron beams will emit energetic photons collinearly such that the photons may collide. Thus it becomes possible to investigate non-linear QED effects. For axially channeled electrons, however, a problem is that the more energetic photons are believed to be created at larger distances from the axis [68]. If this is true[26] then only photons of approximately equal energy may collide which reduces the interaction rate drastically such that this method may not be advantageous.

[25] The use of coherent bremsstrahlung for photoproduction at the CERN SPS was suggested in [77].

[26] It should be noted that as the incident energy is increased, the main region which contribute to the radiation are at large transverse distances to the axis according to the CFA [46].

15.5 Directionally sensitive gamma-ray detection

As for the beam diagnostics tools, one can make effective use of the effectively short radiation length and the directional dependence of this shortening in the construction of detectors with energy- and/or angular- resolution in gamma-ray detection.

15.5.1 Telescope for gamma-ray astronomy

It has been suggested to use the very rapid development of electromagnetic showers along axial and planar directions as a means to detect high energy photons from the Universe [122], [123]. The investigation of high energy cosmic rays has so far extended to observations of particles with energies in excess of 10^{20} eV, but in the region $10^{10} - 10^{14}$ eV the information is rather sparse. Moreover, interstellar magnetic fields deviate charged cosmic rays of these energies such that the direction of the original source can not be inferred [124]. It is these gaps of information that a crystalline gamma-ray detector is intended to fill. Since the enhancement in crystals is restricted to an angular interval $\pm\Theta_0 = U/mc^2$ around the particular crystallographic direction, the effect is sensitive to angles of the order 0.5 mrad for the axial orientation and around 9-10 times smaller for the planar effects. This effect is actually used in alignment of thick crystals, where a solid-state detector detects the number of charged particles above a given threshold (e.g. more than 5 Minimum Ionizing Particles), see [125].

One severe limitation is the rather low flux of high energy photons from e.g. active galactic nuclei or gamma ray bursts for which the emission mechanisms are poorly understood [126]. This implies large arrays (square meters) of crystals to obtain a countrate of one per day. However, the detection of charged particles without knowledge of the position of origin is also of interest in the 10 GeV - 10 TeV region and for these the flux is of the order of 1 particle per square meter per minute [124]. Another limitation is the exclusion of highly charged ions which in the solid-state detector may resemble a shower stemming from a showering gamma-ray [127]. These ions are much more abundant than the photons and therefore vetoing must be very effective to discriminate photons from ions. One could therefore imagine a detector combination where the outer veto, simultaneously with vetoing for the inner detector, could register the charged cosmic rays. The inner detector would then be a crystalline detector for determination of flux and direction of high energy gamma rays.

Recent experiments by NA43 have been utilizing 'garnet' crystals which can be manufactured as perfect single crystals in the very large sizes required - analysis for the experiments is in progress, see also [128]. It is at present doubtful, though, if these crystals are advantageous compared to Ge, apart from the size. Measurements for electron impact on Ge have been extended to include impact of tagged photons up to 200 GeV and preliminary analysis show, as expected, that the shower does not develop as much for photon impact as for electron impact [63].

15.5.2 'Calorimeters'

Since the enhancement depends on the energy of the impinging γ-ray, one might speculate to use a crystal as a compact, direction sensitive (e.g. pointing at a vertex) 'calorimeter'. Of course, this will not be a true calorimeter since the shower will not be fully contained and therefore the energy-resolution will be lower than for a real calorimeter. As suggested by Sona, an alternative would be to slice a thick crystal ($\simeq 30X_0/\eta$) and sample each section for the shower containment [63]. This would initially provide information on the shower development and improve upon the performance as a 'calorimeter'.

Part V
Additional theory for deflection in bent crystals

In the introduction it was shown that a channeled particle is subject to correlated scattering off many atoms which results in a guidance of the particle by the crystal lattice. This effect finds an application in many areas including the 'basic' beam deflection from which the other applications are derived. The theory for this has evolved since the early 80's and here the main concepts are presented in a relatively simple model that incorporates the main effects such as decreased effective dechanneling length and direct losses due to the curvature as well as surface transmission.

16 Deflection by planar and axial channeling

The enormously strong fields present near the nuclei in the lattice of a crystal are in the continuum approximation of macroscopic extension in the direction the particle is traveling. This means that a positively charged particle inside the crystal is subject to forces that tend to keep it at a distance to the plane or string formed by the atoms in the crystal. When the crystal lattice is bent and the particle is in a transverse state below the barrier of the potential, the lattice can thus provide the necessary centripetal force to curve the trajectory of the penetrating particle.

16.1 Planar deflection

The deflection by planar channeling provides the basis for all the applications of bent crystals implemented at accelerator facilities to date. It is therefore of prime importance for a potential application that explores new territory in terms of e.g. energy, that the behaviour of planar deflection at energies available to today's experiments are well understood such that a relatively safe extrapolation to e.g. higher energies can be performed.

16.1.1 Centrifugal term, critical radius and dechanneling fraction

Even if the crystal lattice is slightly deformed, the steering effect of the lattice is maintained for a channeled particle. This means that in a curved crystal, the incident, channeled particles will be deflected with respect to their original direction of motion. However, due to the curvature, the penetrating particle is subject to a centrifugal force in the transverse direction. This means that the potential, $U(x)$, is modified by U_{cf}:

$$U_{\mathrm{eff}}(x) = U(x) + U_{\mathrm{cf}} = U(x) - pv\kappa x \tag{80}$$

where x is the transverse distance from the middle of two adjacent planes and $\kappa = 1/R$ is the curvature corresponding to the radius of curvature, R.

The centrifugal force directs the particle towards the outer plane where it suffers increased multiple Coulomb scattering. Furthermore, for a given distribution in the transverse direction the fraction of particles having a transverse energy near or above the potential height - the (curvature) dechanneling fraction, F - increases with increasing curvature. Thus, the effective area of phase-space which can channel through a bent crystal decreases with increasing bend.

In figure 36 the area in the channel potential available for channeling, A_1, is shown in the 'harmonic' approximation where the potential for a positively charged particle is approximated by a harmonic potential.

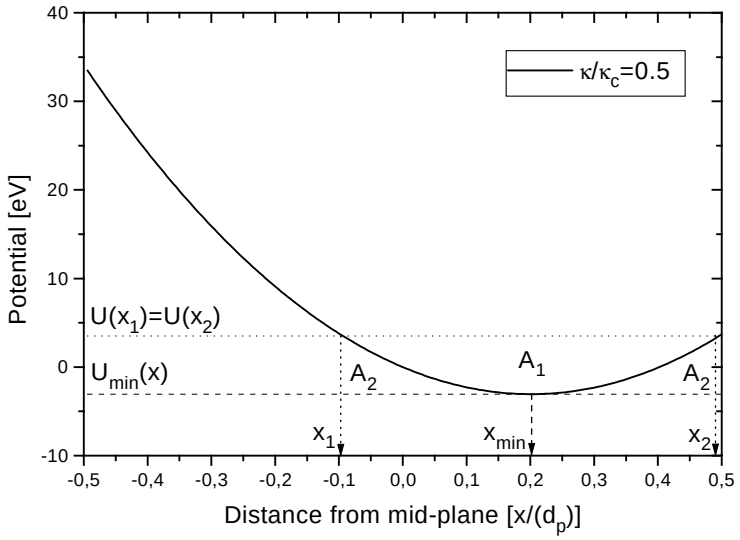

Figure 36: *The potential from eq. (80) at $\kappa/\kappa_c = 0.5$ in the harmonic approximation. Here, $U(x) = kx^2/2$ is a fit to the Doyle-Turner potential for Si (110) at 300 K. For details see also appendix A.*

Since the centrifugal term lowers the potential barrier at the outside plane, there is a certain curvature at which the potential minimum is reached at the distance x_c from the plane where the particles will dechannel. Estimating this curvature Tsyganov found that as long as the curvature fulfills the condition [129]:

$$\kappa \leq \kappa_c = \frac{\pi Z_1 Z_2 e^2 N d_p}{pv} \tag{81}$$

the charged particle can channel in a curved crystal. The same expression can be obtained by setting $x_c = Ca_{\mathrm{TF}}$ and using the 'standard' potential. Equivalently, one may fix the maximum curvature by requiring that the bending angle, θ, over one

oscillation length in the channel, λ_ψ, must be smaller than the critical angle [130]:

$$\theta(\lambda_\psi) < \psi_p \tag{82}$$

These definitions agree within a factor of $\simeq$2 which is sufficient since the critical curvature is an overestimate of at least a factor 5 for reasonable efficiencies, as will become clear later.

For Si (110), Ge (110) and W (110) the values for the minimum radius of curvature, $R_c = 1/\kappa_c$, are given in table 5. Note that for a diamond lattice the planar density in the (111) plane is found by $N\overline{d_p}$, where $\overline{d_p}$ is the average planar spacing. This means that deflection along the (110) plane is more efficient than along the (111) plane (even neglecting surface transmission and dechanneling losses).

	Si	Ge	W
(100)	2.3	1.1	0.3
(110)	1.6	0.8	0.2
(111)	1.8	0.9	0.5

Table 5: *Critical radii in m at 1 TeV for Si, Ge and W according to eq. (81)*

In consideration of the strong fields in a crystal it is understandable that a crystal has a superb bending power. As an alternative to the estimate of the crystalline field, eq. (12), one can calculate the equivalent magnetic field, $B = \kappa p/(Z_1 e)$, corresponding to the critical curvature, eq. (81) as (using eq. (67)):

$$B_c[\mathrm{T}] = 1.5 \cdot 10^3 Z_2 \cdot N d_p[\mathrm{\AA}^{-2}] \tag{83}$$

which is of the order of 2500 Tesla for a silicon crystal. Clearly, since $U_0 \propto Z_2$ eqs. (12) and (83) show that a high-Z material is preferable for deflection. Moreover, since the dechanneling length, eq. (10), and the equivalent field are both proportional to d_p, one would expect the 'usefulness', i.e. the equivalent integrated field, of a particular crystalline plane to depend on d_p^2, such that the widest plane is preferred. As concerns the behaviour with energy, the dechanneling length is proportional to p such that a longer crystal with lower average curvature can be used. However, the critical angle is proportional to $1/\sqrt{p}$, so at higher energies one might lose due to the incident beam divergence.

Papers by Kudo [131] and by Ellison and Picraux [132], [133] covered the calculation of the dechanneling fraction, F, by use of the Molière potential. The calculation involves an integration over phase-space, (x, ψ), in a fashion analogous to that for the calculation of the surface transmission, only in this case the available values are limited due to the shrinking potential (see section 16.1.2 below).

Reference [133] gives 'Universal curves' from which F can be determined as a function of normalized curvature, $\Gamma = \kappa/2\kappa_c$, for different values of d_p and x_c and for

a completely parallel beam. Later experiments showed that the theory was in good agreement with experimental results obtained for a crystal of uniform curvature in a divergent beam, [134].

16.1.2 Multiple scattering dechanneling

To account for the increase in multiple Coulomb scattering due to the centrifugal term, the dechanneling length is modified to $L_{\mathrm{D}}(F) = L_{\mathrm{D}}(0)(1-F)^2$. This can be justified, since in the harmonic approximation to the potential for positive particles, $U(x) = \frac{1}{2}kx^2$, the depth of the well which is effective for channeling, E_{depth}, depends on the curvature as

$$E_{\mathrm{depth}}(\kappa) = (1 - \frac{pv\kappa}{k(d_p/2 - x_c)})^2 \cdot E_{\mathrm{depth}}(0) = (1 - \frac{\kappa}{\kappa_c})^2 \cdot E_{\mathrm{depth}}(0) \tag{84}$$

Therefore, for small F where $F \propto \kappa/\kappa_c$ to a good approximation, E_{depth} decreases as $E_{\mathrm{depth}}(\kappa) = E_{\mathrm{depth}}(0)(1-F)^2$, see also the discussion in appendix A, p. 131. Finally, $L_{\mathrm{D}} \propto E_{\mathrm{depth}}$ which yields the desired scaling law for the dechanneling length [135] [19].

16.1.3 Model for deflection efficiency

Summarizing, consider a crystal of length, L, which is bent over the length, L_{B}, where $L - L_{\mathrm{B}} = L_{\mathrm{S}}$. The surface transmission is ε_{S}. The efficiency will then be approximately:

$$\varepsilon \simeq \varepsilon_{\mathrm{S}} \cdot \exp(-\frac{L_{\mathrm{B}}}{L_{\mathrm{D}}(1-F)^2}) \cdot \exp(-\frac{L_{\mathrm{S}}}{L_{\mathrm{D}}}) \cdot (1 - F_{\max}) \tag{85}$$

Note that in the case of a uniformly bent crystal, $F = F_{\max}$, otherwise in general one must calculate $F(\kappa)$ according to the local curvature and find the total multiple scattering dechanneling by multiplication of the contributions: $\exp(-L/L_{\mathrm{D}}(1-F)^2) = \prod \exp(-L_{\mathrm{local}}/L_{\mathrm{D}}(1 - F_{\mathrm{local}})^2)$.

For a non-uniformly bent crystal, the curvature dechanneling takes place in the part of the crystal where the curvature increases. Therefore, for instance for an ideal three-point bender where the curvature increases in the first half of the crystal, the modification $L_{\mathrm{B}} \to L_{\mathrm{B}}/2$ must be made.

For small F one can expand eq. (85) to give

$$\varepsilon \approx \varepsilon_{\mathrm{S}} \cdot \exp(-\frac{L}{L_{\mathrm{D}}}) \cdot (1 - \frac{2FL_{\mathrm{B}}}{L_{\mathrm{D}}}) \cdot (1 - F_{\max}),\ F_{\max} \ll 1 \tag{86}$$

which, in the case of a uniformly bent crystal, simplifies to

$$\varepsilon \approx \varepsilon_{\mathrm{S}} \cdot \exp(-\frac{L}{L_{\mathrm{D}}}) \cdot (1 - F(1 + \frac{2L_{\mathrm{B}}}{L_{\mathrm{D}}})),\ F = F_{\max} \ll 1, \tag{87}$$

For an application, typically the angle would be fixed to match some external constraints. Since the straight crystal dechanneling favours small crystal lengths and the

curvature dechanneling long crystal lengths (for fixed angle), there is an optimum crystal length which depends on the angle and which is only weakly dependent on energy when the length is expressed in units of the dechanneling length. As a further simplification one may consider a crystal which is bent uniformly all the way to the edge[27] and a large deflection efficiency implying small F ($F < 0.5$ or so). In that case eq. (87) applies and since $\theta = \kappa L$ and $F \simeq \eta\kappa/\kappa_c$, see appendix A, p. 131, we have the approximate efficiency

$$\varepsilon_{\text{appr.}} = \varepsilon_{\text{S}} \cdot \exp(-\frac{L}{L_{\text{D}}}) \cdot (1 - \eta \frac{\theta}{\frac{L}{L_{\text{D}}} L_{\text{D}} \kappa_c} (1 + 2\frac{L}{L_{\text{D}}})) \tag{88}$$

where

$$L_{\text{D}}\kappa_c = \frac{256}{9\pi} \frac{Z_2 N d_p^2 a_{\text{TF}}}{ln(2\gamma mc^2/I)} \tag{89}$$

is only weakly dependent on energy, see table 6. Note that the approximation is more inaccurate for small efficiencies and for small values of L/L_{D}.

	Si (110)	Ge (110)	W (110)
450 GeV	0.301	0.544	1.84
7.0 TeV	0.251	0.451	1.51

Table 6: *$L_{\text{D}}\kappa_c$ for Si, Ge and W according to eq. (89)*

Eq. (88) has a maximum at

$$\frac{L}{L_{\text{D}}} = -\frac{1 + \sqrt{1 - 4(2 - \frac{L_{\text{D}}\kappa_c}{\eta \cdot \theta})}}{2(2 - \frac{L_{\text{D}}\kappa_c}{\eta \cdot \theta})} \simeq \frac{\eta \cdot \theta}{2L_{\text{D}}\kappa_c} + \sqrt{\frac{\eta \cdot \theta}{L_{\text{D}}\kappa_c}} \tag{90}$$

with an efficiency value at this maximum of

$$\varepsilon_{\text{max}}^{\text{appr.}} \simeq \varepsilon_{\text{S}}[(1 - \sqrt{\frac{\eta \cdot \theta}{L_{\text{D}}\kappa_c}})^2 - 2\frac{\eta \cdot \theta}{L_{\text{D}}\kappa_c}(1 - \sqrt{\frac{\eta \cdot \theta}{L_{\text{D}}\kappa_c}})] \approx \varepsilon_{\text{S}}(1 - \sqrt{\frac{\eta \cdot \theta}{L_{\text{D}}\kappa_c}})^2 \tag{91}$$

where the last approximations are for $\eta \cdot \theta / L_{\text{D}}\kappa_c$ small. An example of values is given in figure 37. Essentially the optimum length in units of the dechanneling length is fixed by the choice of angle for a wide range of energies.

For small F a good approximation is found by fitting to data [134], giving $F \simeq 1.04 \tanh(6\Gamma) \approx 6.2\Gamma = 6.2\kappa/2\kappa_c$, i.e. $\eta \approx 3.1$, see also appendix A, eq. (104), p. 132. This value for η is for a beam with a divergence much larger than the critical angle. In the case of a completely parallel beam a calculation using the Doyle-Turner potential leads to values $\eta \simeq 1.5 - 2$ depending on the shape of the potential, i.e. some variation

[27] This can be realized by evaporating a material with a slightly different lattice constant onto the crystal, see [134] and [138].

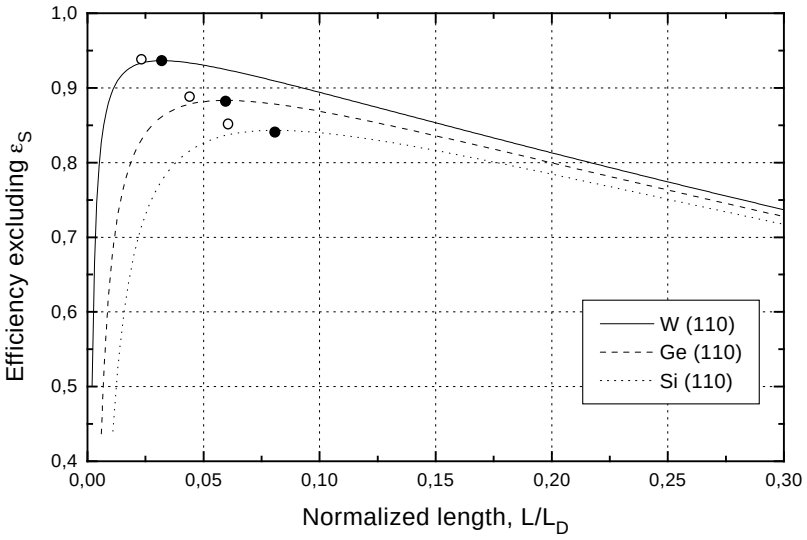

Figure 37: *Efficiency excluding the surface transmission as a function of length at 7 TeV and $\theta = 0.5$ mrad according to eq. (88) (lines) for W (110), Ge (110) and Si (110). The value $\eta = 3$ was used (see text). Also shown (filled dots) is the efficiency, eq. (91), at optimum length eq. (90) and where the last approximations in the eqs. have been used (open dots).*

with the material due to variations of u_1/d_p. Moreover, the linear approximation is not as good as for the wide beam for small F, but for intermediate F ($\approx 0.1 - 0.5$) a linear relation between F and κ is a good approximation (see e.g. [139]).

If $F \simeq \eta \cdot \theta/((L/L_{\rm D})L_{\rm D}\kappa_c)$ has to remain small, say $F \leq 0.2$, while $L/L_{\rm D} \leq 1$ is not suppressingly high in the exponential factor, possible values for θ are of the order $\theta \leq 20$ mrad for Si at high energies. Compared to the angle calculated from $\theta_{\rm max}$[mrad]=$0.3 \cdot B_c L_{\rm D}/pv$[Tm/TeV], see eq. (83), which is roughly 500 mrad, it is seen that the critical curvature largely overestimates the deflection power for efficiencies larger than a few %. In other words, the deflection efficiency decreases drastically long before the critical curvature has been reached.

Note that the deflection is essentially dispersion-free, but that losses are momentum-dependent. This, on the other hand, also means that no momentum or charge selection can be performed with a bent crystal in contrast to in a magnet.

16.1.4 Volume capture

The reverse effect of the multiple scattering dechanneling in a curved crystal, the so-called feed-in or volume capture exists according to Lindhard's reversibility rule [2]. The effect arises because the particles in the beam will enter the crystal and at some point during the bend, the planar tangent will coincide with the direction of motion of the particles, independent of the critical angle. At this point, the particle may lose

transverse energy in a collision with e.g. an electron. Thus, in principle, the capture of particles to channeled states can take place for all angles smaller than the bend angle, see ref. [140] and [141]. However, the probability varies as $w \approx R\psi_c/L_{\rm D} \propto R/p^{3/2}$, since only near-barrier states can enter the channel which happens with a probability $\propto 1/L_{\rm D}$, [135], [136].

Volume capture is quite small in Si already at 70 GeV, $w_{70} \simeq 0.08\% \cdot R[\mathrm{m}]$, see [142], [19]. Nevertheless, volume capture can be used to measure (bending-) dechanneling lengths in materials in which it is not possible to select channeled particles by means of energy-loss discrimination (section 19.2, p. 100). A uniformly bent crystal is used and the number of fully deflected particles registered as a function of impact position on the periphery. This number decreases exponentially as $\exp(-L(\phi)/L_{\rm D}(\kappa))$, where $L(\phi)$ is the length of the crystal from impact point to endface. From this one can extract the dechanneling length, $L_{\rm D}(0)$ by scaling, see eq. (84) and the following discussion, p. 92. Good agreement with theory, eq. (10), has been demonstrated [20].

In a similar fashion one can derive the reverse of the curvature dechanneling, the so-called gradient volume capture [19], [137], [142]. As the particle is incident on a centrifugally distorted planar potential for which the shape changes towards a non-distorted potential (when the curvature diminishes in the direction of motion), a particle can get caught if it enters within $\Delta E \simeq pv\lambda\overline{x} \cdot d\kappa/dz$ above the lower potential barrier. Here, λ is the wavelength of the oscillation imposed by the potential barrier and $\overline{x}$ is the average transverse coordinate. Thus, it is possible to capture a fraction of the beam if the curvature changes rapidly and $\lambda_\psi \propto 1/\psi_p \propto \sqrt{pv}$ is large.

16.2 Axial deflection

If the dechanneling is a smaller effect than the redistribution around the direction of the string caused by doughnut scattering, bending can take place, i.e. if $L_{\rm D}^{\rm doughnut} \gg \lambda_\perp$ which leads to [12]:

$$R\frac{\psi_1}{\lambda_\perp} > 1 \tag{92}$$

This condition translates into a condition similar to the one for planar deflection, namely that the deflection angle over one redistribution length (in this context similar to a channeling oscillation length) must be smaller than the critical angle as in eq. (82):

$$\theta(\lambda_\perp) < \psi_1 \tag{93}$$

The axial and planar deflection mechanisms can thus be described qualitatively in the same terms by use of the characteristic lengths $\lambda_\perp$ and λ_ψ, respectively.

One of the reasons to consider axial beam deflection, is that it applies both for negative and positive particles (although not in the same way) as has been shown in simulations [143]. Deflection of negatively charged particles by planar channeling in a

bent crystal would suffer heavily from the increased multiple scattering such that mechanically feasible crystal lengths would correspond to several L_{D} at sub-TeV energies. Further, the surface transmission for negatively charged particles is much smaller than for positively charged.

Another reason to consider axial beam deflection is that the critical angle is a factor $\simeq 3$ larger for axial channeling than for planar channeling and that the dechanneling length is larger. However, axial deflection requires a beam which is well-defined in angles in both planes, whereas the angular acceptance along the planes for planar deflection is limited by the shape of the crystal only.

17 Effects of irradiation

Clearly, the effects of irradiation pose a major restriction on the applicability of the deflection phenomenon in a bent crystal. If the deflection would have been as strongly influenced by radiation as e.g. a solid-state detector, the usefulness of bent crystals would have been very limited.

The irradiation must affect a significant fraction of the atoms encountered in one oscillation in the channel in order to reduce the deflection efficiency. This is due to the 'smearing' of the potential over of the order $\lambda_\psi/d \simeq 10^5$ atoms for channeled particles and therefore the influence of only a few vacancies or interstitials will be 'averaged out'.

17.1 Imperfections and radiation damage

17.1.1 Imperfections

It is expected that the contribution to dechanneling from stacking faults remain constant with energy, and point defects decrease as $1/\lambda_\psi \propto 1/\sqrt{pv}$ [172]. In the case of dislocations the contribution grows with increasing energy: By use of the length of the so-called Burgers vector [173, p. 634], b, the local curvature at a distance, r, from a dislocation is given by $\kappa \simeq b/7r^2$ [132]. If then the dechanneling length is taken as $L_{\mathrm{n_D}} = 1/n_D 2r_D$, where n_D is the areal dislocation density (assuming that the dislocations extend transversely all along the crystal) and r_D is the distance within which the particle is dechanneled one gets $L_{\mathrm{n_D}} \propto 1/\sqrt{pv}$ since $\kappa_c \propto pv$. In other words, the influence of dislocations increases with energy since a larger fraction of the beam experiences curvatures near or in excess of κ_c.

Therefore, at high energies it is necessary to have a crystal of not only low mosaic spread, but also low dislocation density. This, together with requirements on the size, sets rather stringent limits on the choice of material [174]. For this reason, only Ge and Si have been used as crystal deflectors so far, although studies are being made to improve the quality of higher-Z crystals like W and Mo and possibly use them as deflection devices [175], [176].

Note that for $\theta = 0.5$ mrad (of the order of that required to extract protons to a magnetic septum at the LHC) the optimum length for W is only 9 cm, see eq. (90). Nevertheless, at 7 TeV, bent tungsten crystals may be unusable due to the dislocation density and the gain for deflection at these energies and angles compared to the use of Ge is anyway marginal, unless one can gain from the surface transmission.

17.1.2 Radiation damage

Detectors implanted on the crystal deteriorate seriously after irradiation by 10^{13} protons/cm^2 and cease to function at a fluence of 10^{16} protons/cm^2 [179]. This magnitude of limit of radiation, of course, would be completely devastating for a potential application of bent crystals in a high-intensity beam.

The question about the influence of radiation damage on the channeling-, and therefore bending-, properties was investigated in a series of papers with increasing dose to the crystals examined, but no conclusion could be drawn as to the onset of influential damage in terms of exposure. Throughout, the lower limit for the acceptable dose kept increasing towards the limit of the realistic dose in different applications.

The first paper on the important question of radiation damage concluded a change in dechanneling length at an exposure of only $1.0 \cdot 10^{17}$ protons/cm^2 at 400 GeV/c. However, the deflection efficiency was 'not appreciably reduced by the irradiation' [180]. Later studies with a crystal irradiated by $1 \cdot 10^{18}$ protons/cm^2 and examined by Rutherford Backscattering (RBS) did not detect any damage [179]. At Serpukhov a crystal septum was irradiated by $\simeq 10^{19}$ protons/cm^2 'without any noticeable deterioration' [181]. Finally, a silicon crystal was irradiated with $(4.1 \pm 1.4) \cdot 10^{20}$ protons per cm^2 at 28 GeV and examined by RBS (2-3.5 MeV He^+ ions) with the conclusion that damage had occured [182]. What remained to be answered was the effect this would have on the deflection properties.

Since the number of atoms participating in the deflection of a channeled particle over one wavelength in the oscillatory motion in a planar channel, λ_ψ, is proportional to $\sqrt{pv}$ it is difficult to relate the behaviour at low energy to that at high energies. Similarly, the total nuclear cross section varies significantly for energies below $\approx$1 GeV [183, p. 156], such that irradiation at low energies does not lead to the same effect as at high energies. Clearly, the best test to decide whether or not a crystal will be affected by irradiation, is to subject it to a beam with the same energy as that it is intended to deflect, and thereafter examine its deflection properties with this beam.

Part VI
Experiments with bent crystals

18 Historical development of deflection in crystals

Following the prediction by Tsyganov [129] that particle deflection in crystals would be possible, an experiment was performed at JINR, Dubna, for planar deflection by channeling of 8.4 GeV protons [144], [145], [146]. Shortly after, experiments at CERN confirmed the effect for axial channeling of 12 GeV/c positive and negative pions [12], [147]. Efficiencies up to 20% were observed, but in the case of negative pions, no particles were deflected through the full bend angle, 4 mrad. In all succesful cases of axial deflection a strong feed-in to the planes was observed. Meanwhile, volume capture was shown to be a significant effect in experiments at low energy (few GeV), [148].

To test the newly developed theory of dechanneling in a bent crystal, several experiments were performed on one hand to measure dechanneling fractions and -lengths [134], [149], [150], [151] and on the other hand to prove the feasibility of using a bent crystal as a septum at low and high energies [152], [153], [154]. Different bending devices were used, a three-point bender, a four-point bender (to reduce dechanneling loss) and finally a ZnO coating giving a uniform curvature. The agreement with Ellison's theory for dechanneling was shown to be within experimental errors when the change from $x_c = a_{\mathrm{TF}}$ to $x_c = 2.5u_1$ had been made. Moreover, the behaviour of L_{D} with angle and energy in a bent crystal was (at least phenomenologically) understood.

More than ten years after the first experiments on deflection in crystals, the Aarhus-CERN-Strasbourg collaboration managed to deflect 10% of an external proton beam at 450 GeV/c through an angle of 7 mrad. The dechanneling fraction was found to be roughly the value predicted by Ellison's theory [155]. At this point, investigations were made in view of applications for beam deflection in the CERN K12 beam for NA48 and for extraction at the LHC and SSC [156].

Later, experiments at CERN confirmed expectations on the behaviour of the efficiency as a function of angle for a 450 GeV/c proton beam in a bent Si (111) crystal [157]. This study measured efficiencies as high as 50% at small angles and included different angles up to $\simeq$12 mrad, see figure 38.

The most recent experiments on deflection in bent crystals done at CERN (apart from those reported in this thesis) investigated planar deflection of a 200 GeV/c positive pion beam compared to 450 GeV/c protons and deflection of negative pions along planar and axial directions in a Si crystal. At 450 GeV/c, another attempt at deflecting positively charged particles along an axial direction was done [158], with results similar to those obtained at 12 GeV/c.

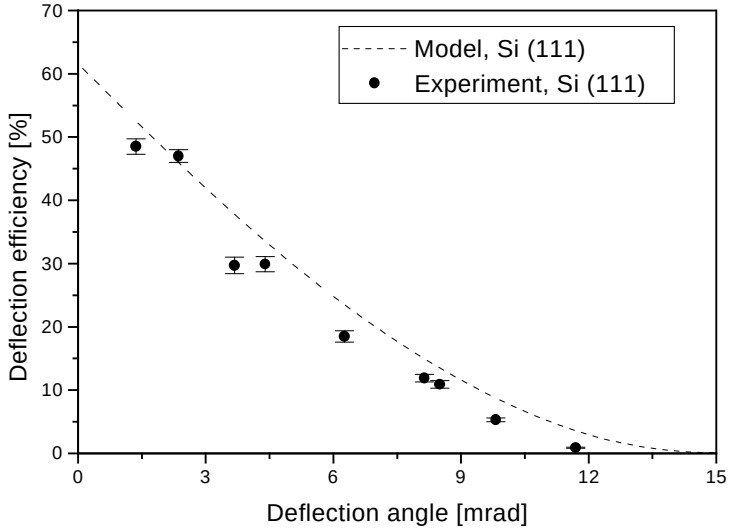

Figure 38: *The deflection efficiency as a function of angle for 450 GeV protons channeled along the (111) planes in a silicon crystal. The filled dots are experimental points with error bars denoting the statistical uncertainty and the dashed line is the expected value according to the model given in section 16.1.3 [157].*

19 Beam and experimental setup

19.1 The H8 beam at the CERN SPS

Common for the two experiments on the Ge and irradiated Si crystal is the beamline, H8 in the North Area of the CERN SPS. In the so-called micro-beam option at H8, protons are available with very low divergence over the crystal front-face, less than $\simeq 3$ μrad. The 450 GeV/c proton beam is directed onto the T4 Be target of length 300 mm from which 3 secondary beams are derived, the P0 beam and the H8 and H6 beams. These beams are strongly correlated in terms of available energies and particle types (positively or negatively charged) and for instance the H8 beam can only be run in the 450 GeV/c micro-beam mode, with zero production angle on T4, if P0 is off. Extraction from the SPS takes place 414 m upstream of the crystal experiment, some 20 m underground. Two sets of vertical dipole magnets and a series of quadropole magnets bring the beam to ground level and for the secondary beams it selects the appropriate momentum by use of dispersion and collimation. The beam can be well-defined in angles due to very tight collimation between the two vertical bends, which also reduces the intensity considerably. Alternatively, by stretching and rotating the phase-space of the beam by use of quadropoles, the fraction of the beam that intercepts the front-face of the crystal will have very low divergence [192]. The 200 GeV/c hadron beam is composed of $\approx$60% protons and $\approx$40% pions. Electrons are removed by insertion of a Pb absorber.

19.2 Energy loss and straggling in a crystal

Positively charged particles are kept away from the large electron densities in crystals when channeled. The long dechanneling length is clear evidence for this. On the other hand, this means that the energy-loss and straggling is also reduced under channeling conditions compared to in an amorphous material. Previously, this reduction was used to align the crystal planes to the incident beam by simply counting the fraction of particles with reduced energy loss in a solid state detector, prepared in the crystal material, as a function of goniometer-angle. However, this technique was not possible to use in the two experiments mentioned below.

19.3 The three-point bender

According to classical deformation theory [184], [185], a crystal-plate which is bent along one direction as a result of bending moments, will also be bent in a direction perpendicular to the desired bending. This is the so-called anticlastic bending [186]. The anticlastic effect is caused by the compression on the concave side leading to a pressure that tends to elongate the crystal in the perpendicular direction and vice versa for the convex side[28]. Therefore the shape of the crystalline plate is similar to a saddle [187, p. 44-45]. The ratio of these curvatures in an isotropic material is determined by the Poisson ratio, $\mu_P = E_Y/2G_S - 1$, where E_Y is Young's modulus and G_S the modulus of shear[29].

With respect to the primary bending, the pressure, q, originating from the three pressing points in the bending device, gives rise to a shearing stress, V_shear, which in turn leads to the bending moment, M, responsible for the curvature, κ:

$$q = -\frac{dV_\mathrm{shear}}{dx_\mathrm{bend}},\ V_\mathrm{shear} = \frac{dM}{dx_\mathrm{bend}},\ M = \kappa E_Y I_z,\ \kappa = \frac{d^2y}{dx_\mathrm{bend}^2},\ \theta = \frac{dy}{dx_\mathrm{bend}} \qquad (94)$$

where x_bend is the coordinate along which the bending takes place, I_z is the moment of inertia with respect to the bending axis, z, and θ the angle at any point along the crystal. The variable y, describes the shape of the crystal as a function of x. For small deformations (maximum excursion smaller than the thickness), the maximum curvature scales as L^2/t^3, such that for mechanical reasons one might prefer a longer crystal if a certain thickness is needed.

Crystals like Ge and Si grow preferably in the $\langle 110 \rangle$ direction, and the size of a typical ingot is 50 cm long and 10 cm in radius. The length is only limited by the size of the floating-zone apparatus, but the radius is more difficult to increase, since a crystal of good quality requires a small temperature gradient over the growth surface,

[28] If the two curvatures are in the same direction the effect is called *syn*clastic bending.

[29] Young's modulus can be defined as the tensile stress necessary to double the length of the specimen. Likewise, the modulus of shear is the shear stress on the surface of a cylindrical specimen of length and diameter 1, twisted 1 rad.

thus limiting the available lengths for Ge and Si crystals cut along other planes than (110) and (100). Also the anisotropy in the Young's modulus of the crystal severely limits the directions along which the crystal can be cut [177].

Typical dimensions for the crystals used in the bending experiments in H8 are $50 \times 10 \times 1$ mm^3. A 'classical' three-point bender is shown in figure 39.

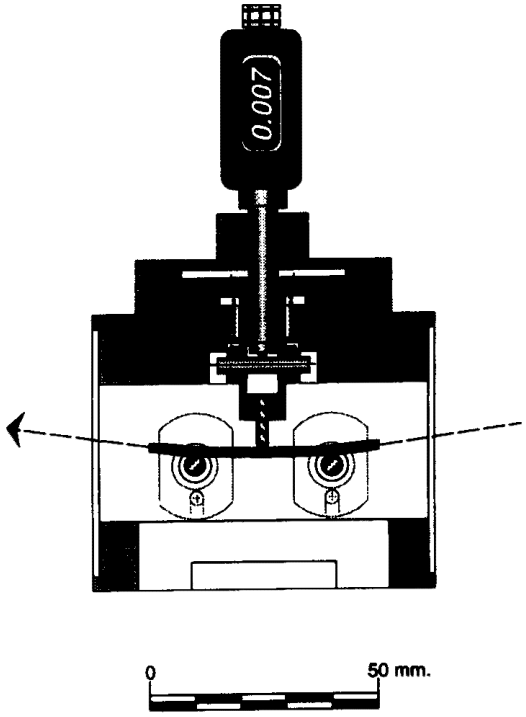

Figure 39: *The latest version of the 'classical' three-point bender with a mounted crystal. A micrometer read-out of the middle pressing point assists in changing the bend angle in a controlled way.*

Therefore, for small radii of curvature of the pressing points (1 mm in the latest version of the three-point bender used), the curvature increases linearly from near the first pressing point to near the middle, whereafter it decreases linearly again. Assuming a uniform pressure over a 1 mm pressing point, the curvature in this small region around a presssing point will be parabolic rather than linear. However, the difference between the full bending angle calculated from the first (linear everywhere) and the second (linear except around pressing points) approach is less than 5% when the distance between the outer pressing points is 30 mm.

All of the above has been derived for an infinitely thin crystal in an ideal three-point bender and obviously there are corrections to this model. The most important correction is the local distortion around the pressing points, which can lead to an increase in dechanneling.

Measurements of the curvature of different crystals were performed by laser-reflection off the surface, detected by a position-sensitive detector [188]. These measurements

were vital for the below mentioned experiments as well as for the experiment investigating the deflection of 33 TeV Pb^{82+}_{208} [192], [193], but also for installation of new crystals for extraction experiments at the CERN SPS, since an accurate knowledge of the bend-angle is required.

19.4 Data acquisition system

The data acquisition system was consisting of a few CAMAC units read by a PC. Timing signals from the drift chambers were read by an 11-bit TDC with a common start given by the beam trigger which was defined according to the experiment. In the experiments, the trigger was gated by signals from the SPS-control, the so-called WE (warning extraction) and EE (end extraction), ensuring that only during the 2.5 second burst in the 14.4 second cycle did the data enter[30]. Scintillator counters were either read as bits in a pattern unit, a 16-bit register, used in the trigger or read as analogue signals in a charge-sensitive ADC for later analysis.

Depending on the number of detectors, n, every good event (defined by the trigger) has an n-tuple with the read-out coordinates stored on disk. The datataking rate was typically 5000 good events per burst.

20 Deflection of 450 GeV/c protons in irradiated Si

In order to investigate the influence of radiation damage on the deflection properties of a silicon crystal, an experiment was performed using a crystal which was irradiated all along the direction of the 52 mm plane, but transversely in a small part only due to the focus on the target. This meant that the observation of degradation could be limited to a comparison between irradiated and non-irradiated areas, i.e. a relative measurement and not an absolute. Furthermore, an important point was that the beam used for the deflection experiment was of the same nature as that used for the irradiation. This situation resembles the one used in an application almost exactly and enables one to draw conclusions with respect to the durability of the a crystal as a deflector in a high-intensity beam.

20.1 Irradiation of the Si (111) crystal

Irradiation of the $52 \times 10 \times 1$ mm^3 Si (111) crystal was performed in one of the target-stations, T6, at the CERN SPS during one year of operation. The crystal chosen for the experiment had been used previously, giving high deflection efficiencies. At T6, the number of protons per burst can be as high as 10^{13} as measured by secondary

[30]This is also done to block the PC from interruption during burst, which would reduce the speed of datataking.

emission monitors and the burst duration is 2.5 s in a 14.4 s cycle. The total integrated fluence was found to have a nearly gaussian distribution with a peak value of $5.0 \cdot 10^{20}$ protons/cm^2 over an area of 0.8×0.3 mm^2 (FWHM). The exact location of irradiation on the crystal was found by contact radiography, where an activity-sensitive film is placed on top of the specimen - a picture from this is shown in figure 40.

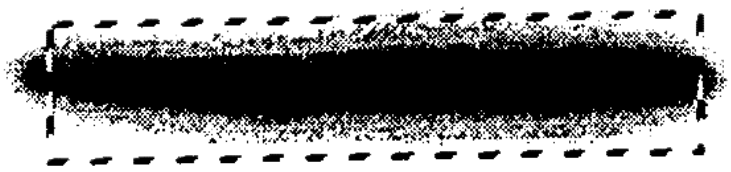

Figure 40: *Picture of the irradiated silicon crystal (broken into two pieces). Exposure: 20 s, Kodak X-Omat AR film. The contour shows the 10×50 mm^2 surface of the crystal.*

Unfortunately, during this process the crystal broke in two pieces of which one had a length ≃31 mm, with a somewhat irregular endface owing to the fracture. Before the deflection experiment, the crystal 'cooled' for about one year such that the radioactivity, mainly ^{22}Na β^+ decays, had decreased to a safe level for handling.

Annealing as a result of high temperatures may have reduced the effects of the irradiation on the lattice. As an estimate of the heating of the crystal during irradiation one can assume that the restricted energy loss of the proton beam heats up the crystal during the 2.5 s spill, whereafter the heat conduction to the surrounding Be and Al target head brings the crystal to ambient temperature. The cut-off in energy loss, $T_{\rm cut}$, can be taken as the energy at which the range of an electron corresponds to the length of the crystal. The precise value $T_{\rm cut} \approx 50$ MeV [61, p. 376] is not so important, since the dependence is logarithmic. In this approximation the crystal temperature may have risen by:

$$T_{\rm rise} = \frac{1}{V_{\rm zone} c_V} \cdot N_{\rm protons} \cdot \rho_{\rm Si} l_{\rm Si} \cdot \frac{dE}{dx}_{T<T_{\rm cut}} \tag{95}$$

where $dE/dx \simeq 1.3$ MeV/(g/cm^2) at 450 GeV/c in Si leading to $T_{\rm rise}^{\rm avg.} \simeq 7°$ for $V_{\rm zone} = 0.52$ cm^3. Locally, however, the temperature may have been substantially higher, $T_{\rm rise}^{\rm local} \simeq 280°$ C$\ll T_{\rm melt} = 1683°$ C if $V_{\rm zone}$ is taken as $0.8 \times 0.3 \times 52$ mm^3. An annealing effect may be the result of such high temperatures and thus a reduction of the influence of radiation damage could have been present.

In the measurements to test the bent crystal to be installed in the CERN K12 beam (protons per spill of the order $6 \cdot 10^{11}$, with an intensity $\approx 10^{12}$ protons/cm^2, see [163]), a thermometer indicated an increase in temperature of the whole device of 2.5° C over a few hours with no indications of a rise during the spill [189].

20.2 Experimental procedure in the beam

The 31 mm long piece of the broken Si (111) crystal was mounted in a modified three-point bender, in which the distance between the outer pressing points was 25 mm and not 30 mm as used in previous H8 experiments. The three-point bender was fixed on a goniometer turntable with 2 degrees of freedom, tilt and turn, i.e. rotation around the axis perpendicular to the crystal planes and rotation around the vertical axis. The goniometer used has a minimum step-size of $1/10000^\circ \simeq 1.75\mu$rad, but the orientation is not reproducible to better than $\simeq 5$ steps.

Due to the radioactivity of the crystal, the above mentioned energy-loss technique for alignment, see 19.2, p. 100, was not possible since a detector implemented in the crystal can not operate. Therefore the alignment procedure relied on the detection of the bent beam in the scintillator hodoscope, H1, H2, H3. The experiment is sketched in figure 41.

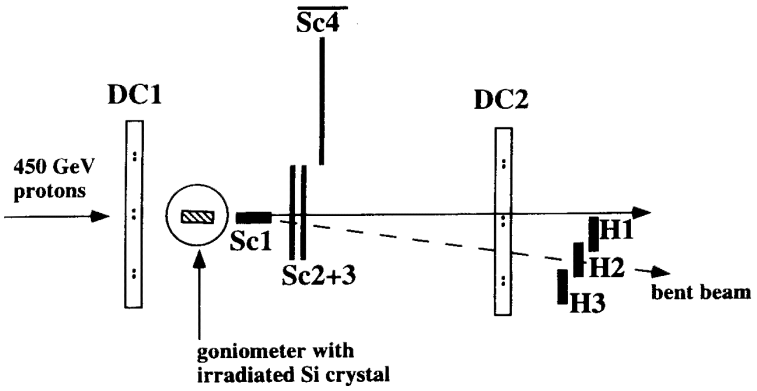

Figure 41: *The experimental configuration for the irradiated Si (111) crystal. Shown are the scintillators, Sc1 (motorized), Sc2, Sc3 and* $\overline{\text{Sc4}}$ *used to define the beam and veto interactions with origin in the bending device; the scintillator hodoscope, H1, H2, H3, to detect the deflected beam, and the two drift chambers, DC1 and DC2, from which beam profiles were determined.*

To reduce the effective beam size a $2 \times 7 \times 10$ mm^3 scintillator was positioned immediately downstream of the crystal, such that its 2×10 mm^2 face overlapped with the endface of the crystal. The reasoning behind putting it downstream of the crystal was to reduce material, i.e. multiple scattering, upstream of the crystal. However, the selection of particles from a downstream scintillator is not as effective as for an upstream one, since a proton hitting the bending device is likely to be accompanied by e.g. a δ-electron which can fire the scintillator, thus imitating a good event.

For alignment the coincidence counts during one burst of e.g. H1·Sc1·Sc2 was normalized to Sc1·Sc2 and this ratio was measured as a function of the goniometer-angle. In this way an angular scan could be performed with steps of typically 10 μrad per burst, see also figure 42. To be able to position the hodoscope properly, the approxi-

mate bend-angle had to be known. This was checked by scans on the SL-EA laser-table, see 19.3, p. 100. To enable the observation of beam profiles a pair of large scintillators, Sc2 and Sc3 10×10 cm^2, were positioned downstream of the crystal. By use of these as the beam-trigger in the data acquisition system, beam profiles could be made using the drift chambers. Two drift chambers were installed. One $\simeq$0.5 meters upstream and the other 4.1 meters downstream of the crystal. With these, the incident, straight and deflected beam could be determined in both planes.

In earlier years, the beam divergence had been determined from two observations: The steep sides of the angular scans and the fraction of initially channeled particles as determined from the energy-loss in a solid state detector. Evidently, the latter technique was impossible to use here and therefore the optimization of the beam divergence relied on the first criterion in combination with a series of efficiency-optimisation measurements as a function of Q19 current. In the optics used, Q19 is the quadropole which is used to adjust the beam divergence. Angular scans of the first experiment with germanium (110)[31], done prior to the ones with the irradiated silicon crystal, indicated a divergence of ≤ 5 μrad, although with some variation from scan to scan.

Another large scintillator counter, $\overline{\text{Sc4}}$, 30×10 cm^2, was positioned outside the beam, on the side opposite to the deflection direction. With this as a veto-counter, a reduction in background events is possible, since an event with a violent collision such as a nuclear interaction creating a debris of particles, has a large probability of triggering the veto. Notwithstanding, this veto may introduce a bias to the data, since a dechanneled particle has a higher probability of violent collisions than a channeled one. As expected, this effect turned out to be quite small (a few percent in efficiency), but for data-taking the veto was left out. The upper and lower edges of the crystal were determined by the onset of decrease in the efficiency and consistency with the 10 mm endface was checked.

20.3 Analysis

Already from the angular scans it was evident that the irradiated crystal was suffering from a severe anticlastic bending, possibly due to the fracture or the irradiation, but certainly also due to the shorter unbent ends compared to previously used crystals ((31-25)/2 mm compared to (50-30)/2 mm). This effect, which meant a new alignment angle for every vertical position on the crystal, made the analysis more complicated. Two variables had to be maximized for every beam position: horizontal position and vertical position[32].

The efficiency for all calculations was defined as the number of fully deflected par-

[31] This experiment was reported in [158], and gave results with somewhat lower efficiency than expected.

[32] This is due to the anticlastic effect which couples the vertical position and the horizontal angle, since the optimum channeling angle changes as a function of vertical position.

ticles originating from a specified region on the front-face of the crystal, divided by the number of particles incident on this region.

An angular scan was made by taking data for different goniometer settings around the optimum value. In the analysis each of these points were optimized in efficiency and plotted. The resulting efficiency curve is shown in figure 42, showing a FWHM of 50-55 μrad, whereas the expected value disregarding the anticlastic effect would be $2\psi_p \simeq 14$ μrad. The points in the figure are averaged efficiencies over the vertical beam-size of 1.5 mm.

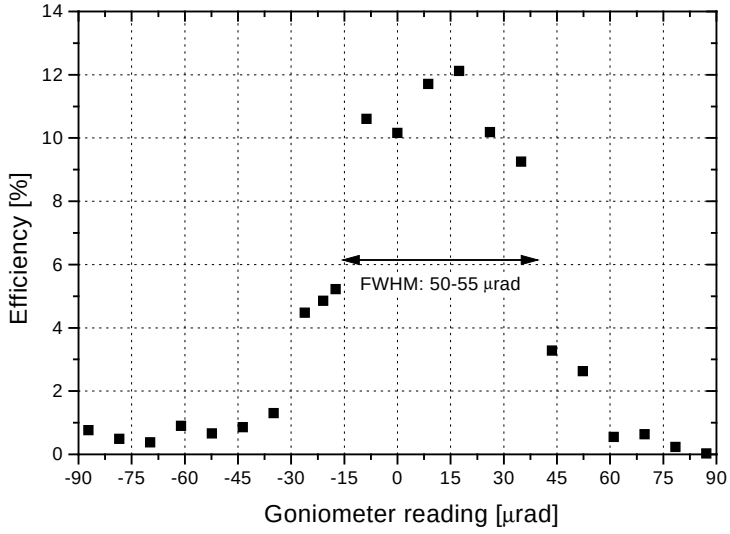

Figure 42: *An off-line angular scan, showing the efficiency as a function of goniometer reading. The FWHM is about a factor 4 wider than expected, indicating severe anticlastic bending of the crystal.*

The detection efficiency of the drift chambers was checked by counting the number of particles which had been detected in the second chamber, but did not get registered in the first chamber for a run without crystal nor bending device. This number was 1/3280, which means that the efficiency of the chambers was essentially 1 as expected. For the same run without target, the approximate drift chamber resolution was found by applying cuts of different width in the first chamber, plotting the observed width in the second chamber and extrapolating this to zero cut-width in chamber 1. From the width found by this procedure was then subtracted the expected multiple scattering from the material between the chambers and the combined resolution of the two chambers was given. The position resolution of the drift chambers in the present experiments was 100 ± 50 μm (σ). This procedure assumes that the beam divergence is much smaller than the angular resolution of the chambers, which was the case judging from the steep sides of the angular scans obtained with a Ge crystal.

To determine the relative effect of the irradiation, the beam was vertically displaced

in steps of 0.5-1 mm across the front-face of the crystal. In each case the vertical position with respect to the lower and upper edge of the crystal was determined. For these data an off-line scan in horizontal position and vertical position versus efficiency was made. Those horizontal regions corresponding to maximum deflection efficiency were then transferred to a plot of efficiency versus vertical position. A miscut of the crystal will give an inefficient region near one side and on either side the observed efficiency may be smeared out by the resolution of the chambers, since particles hitting near, but outside the side of the crystal can be counted as having hit the crystal. Furthermore, as has been seen in other experiments [149], a clear effect of increased dechanneling on the side of the middle push-pin, leading to particles lost half-way through the crystal, was observed. Finally, all beam-settings, i.e. vertical positions, were gathered on one plot, see figure 43.

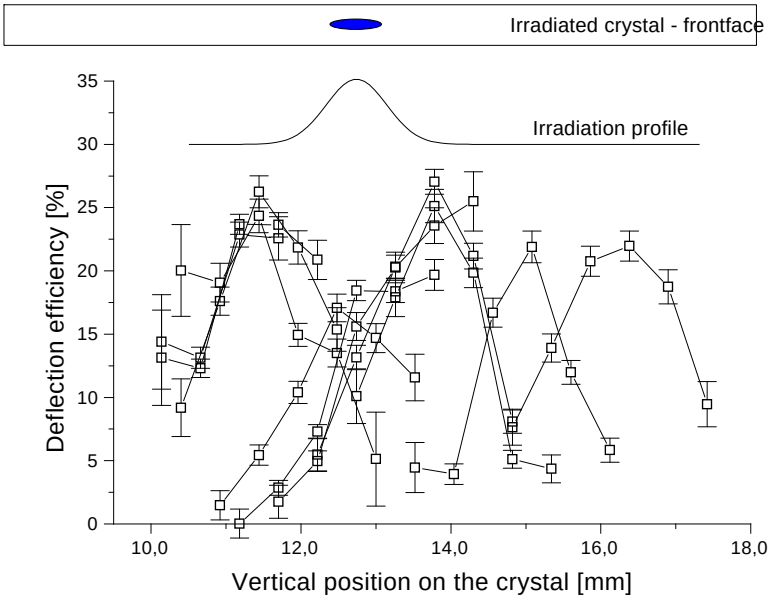

Figure 43: *Efficiency as a function of vertical position for the irradiated crystal. Each 'bell-shaped' curve corresponds to one vertical position of the beam - the shape stems from the anticlastic bending which couples the vertical position and the optimum angle. At the top the 1×10 mm^2 front-face is indicated with the irradiation profile immediately below. The results shown are for the setting where the beam was parallel in both planes.*

The deflection angle, 1.1 mrad, was determined through a calibration of the drift chambers and TDCs by moving the small scintillator, Sc1, across the relevant cell in small steps with a precision of 0.1 mm.

20.4 Results

In a comparison with results obtained earlier for the non-irradiated Si (111) crystal [157], where ≈50% deflection efficiency was observed at small angles, the overall level of deflection efficiency in the present experiment is low, ≃ 22%. An explanation for this could be the severe anticlastic bending, combined with the fact that due to the finite resolution of the drift chambers this cannot be entirely counterbalanced by off-line cuts in the vertical position. Bearing in mind the low efficiencies in Ge obtained with the same beamline during the same run [158], it cannot be ruled out that the beam divergence was larger than the angular scans indicated, see also 21.1, p. 109, however, this alone could hardly be enough to explain a factor ≃2.

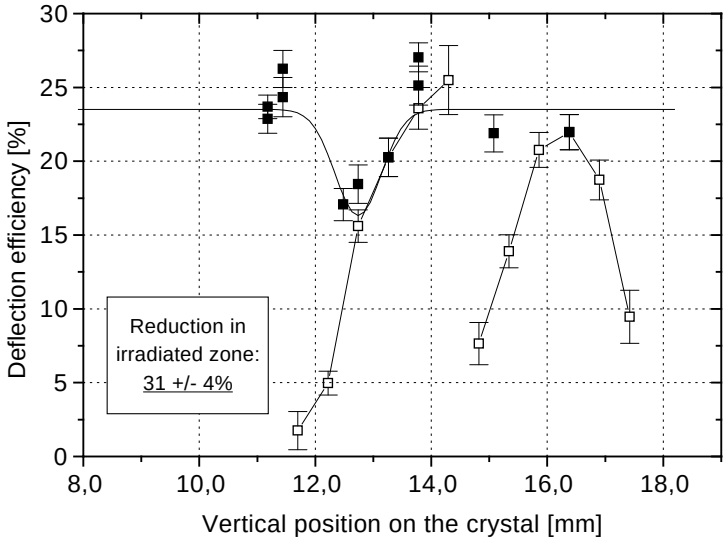

Figure 44: *Efficiency as a function of vertical position for the irradiated crystal. The full squares are for the points at calculated optimum alignment. The full-drawn curve is a least-squares fit, with boundary condition on the FWHM and position, imposed by knowledge of the irradiation profile. Shown with open squares are two different vertical off-line scans.*

As figure 44 shows, two different kinds of off-line scans (open squares) were observed. The rightmost, bell-shaped is explained by the anticlastic bending, whereas for the leftmost there are two possible explanations: Either the pre-alignment with the goniometer was not done properly or the pre-alignment was done properly, but the efficiency is suppressed in the middle due to the irradiation. The fact that the second kind of curve only appears near the zone of irradiation points in the direction of the second interpretation. Moreover, it can be checked how accurate the pre-alignment was by plotting the goniometer angle as a function of vertical position and register the deviation from the parabolic shape expected for an anticlastically bent crystal. This deviation was nowhere larger than 0.7 mm.

In figure 44 is shown the points at calculated optimum alignment by use of the procedure outlined above, see also [190]. The full-drawn curve is a Gaussian least-squares fit to the points with the boundary conditions on FWHM and position imposed by knowledge of the irradiation profile. The fit gives a peak reduction in efficiency in the irradiated region of 31±4%. This number should be compared to the peak intensity of irradiation: $5.0 \cdot 10^{20}$ protons/cm^2 from which it becomes evident that even in a beam as intense as the primary SPS beam of up to $6{\cdot}10^{12}$ protons per spill, a bent crystal can be used for a year without deteriorating more than ≃30%. Assuming a linear relationship between irradiated intensity and the efficiency deterioration, the deterioration coefficient is $6\% \pm 2\%$ per 10^{20} protons/cm^2. Moreover, in more intense beams, one could imagine a construction in which the crystal could be moved slowly, such that the beam eventually would have covered the entire endface area.

21 Deflection of 450 GeV/c and 200 GeV/c hadrons in Ge

A first experiment in 1995 to measure the deflection efficiency of Ge at different angles gave results which were unexpectedly low compared to the model presented [158]. It was soon realized, though, that a parameter like the divergence of the incident beam was not fully under control although the angular scans indicated a relatively low divergence. Moreover, it was suspected that the crystal of Ge, being a softer material than Si, could have suffered from the many bending tests performed to determine the curvature. Finally, the first bending angle examined in the beam was measured by laser-reflection off the surface to be ≃4.6 mrad and turned out to be ≃3 mrad in the beam - this lead to speculations about instability, possibly due to thermal effects. The crystal was of the 'standard' size, $50 \times 10 \times 1$ mm^3 and mounted in a three-point bender with 30 mm between the outer pressing points.

21.1 Experimental procedure

A number of points were improved considerably in the experiment with Ge (110) in comparison with the earlier Ge (110) experiment and the experiment with the irradiated crystal [158].

The old veto-counter was replaced by a large counter with a 5×15 mm^2 hole and this counter was used as a veto only during crystal alignment. In the data-taking the veto counter was recorded as a pattern bit. The setup for the experiment investigating deflection in the germanium (110) crystal is shown in figure 45.

Care was taken not to bend the new germanium crystal unnecessarily, since it was feared that germanium, which is a softer material than silicon, would deteriorate in terms of dislocation density etc. if bent too often.

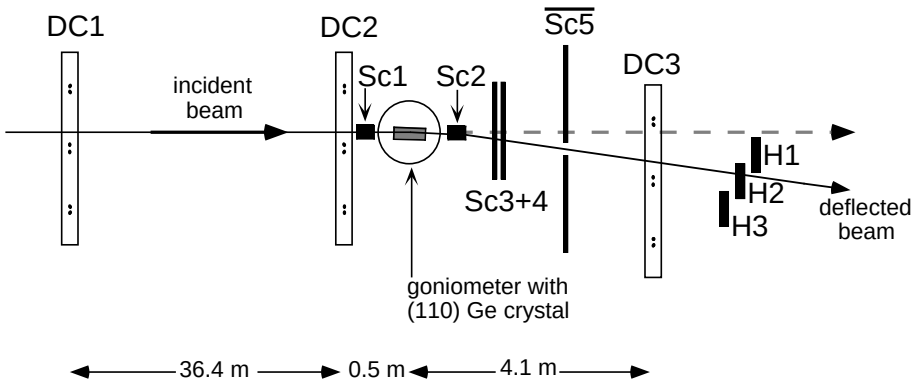

Figure 45: *The experimental configuration for the germanium (110) crystal. Shown are the scintillators, Sc1 (motorized), Sc2 (motorized), Sc3, Sc4 and* $\overline{\text{Sc5}}$ *used to define the beam and veto interactions with origin in the bending device; the scintillator hodoscope, H1, H2, H3, to detect the deflected beam, and the three drift chambers, DC1, DC2 and DC3, from which beam profiles were determined.*

The micrometer-screw for the adjustment of the bend angle was replaced by one with a digital read-out in μm and the entire bending device was re-designed using materials with low expansion-coefficients such that a change in temperature would not affect the bending angle seriously.

An additional drift chamber, DC1, was used, 36.37 m upstream of the following drift chamber. This enabled a fine-tuning and cross-check of the divergence of the beam as well as off-line cuts in the incident beam direction, although with a resolution of only $\simeq$4 μrad (σ).

To check the precision of the micrometer reading in the bending device, this reading was plotted on-line as a function of goniometer reading at the optimum alignment. The bending angle of the crystal depends linearly on the push for small angles, 5.1 μm/mrad in the configuration used. It turned out that the micrometer reading (accuracy: $\pm 1\mu$m) was indeed very precise in prediciting the new bend angle, a fact which helped in the search for alignment at large angles where the efficiency was low. In fact, the angular region to search for the new alignment after a change of bend angle was only around $\pm$0.2 mrad. Even with this improvement, it turned out to be neccessary to use a five-fold coincidence, e.g. H1$\cdot$Sc2$\cdot$Sc3$\cdot$Sc4$\cdot\overline{\text{Sc5}}$/ Sc2$\cdot$Sc3$\cdot$Sc4$\cdot\overline{\text{Sc5}}$ to be able to align the crystal at large bend angles where the efficiency was as low as 2% for the 450 GeV/c beam.

21.2 Analysis

For this experiment many deflection angles up to $\simeq$ 20 mrad were examined and at angles larger than $\simeq$ 4 mrad the bent, dechanneled and non-bent (straight) beam were sufficiently separated to enter two different drift chamber cells, for large angles even

three or four. Therefore, to determine the correct deflection angle, the cells had to be patched together correctly. A 'patched' raw beam profile is shown in figure 46 where the undeflected, dechanneled and bent beam are clearly seen. Also seen in the figure is the excess of particles around the anode wire and the inefficient region around the field-wire. The excess around the anode-wire is due to multiple hits in the same cell; only the hit closest to the anode-wire will be registered. To a large extent these 'bumps' disappear, when conditions on the particle entry on the front-face are imposed. The remaining background events are reduced to a negligible level by requiring that there can be only one hit in the entire chamber for the fully deflected particles. For the dechanneled particles, hits in neighbouring cells are registered as only one hit in total.

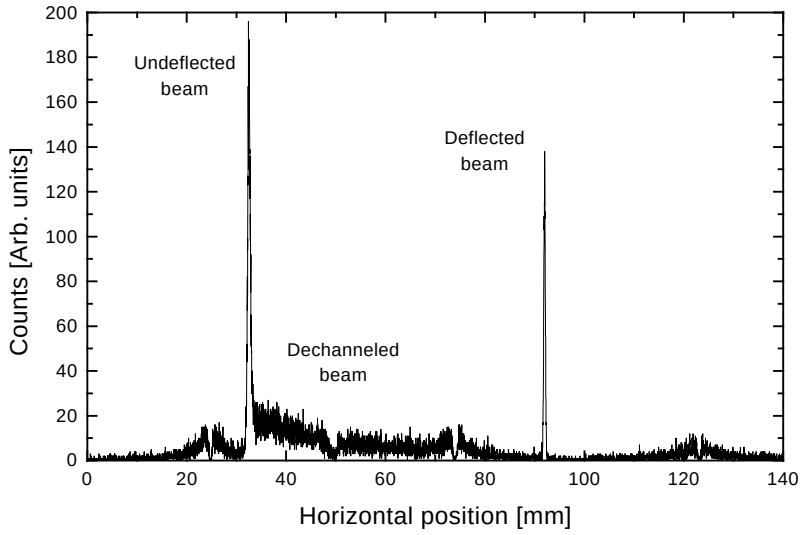

Figure 46: *The beam profile as seen in drift chamber 3 for the bend angle 14.9 mrad. Clearly visible are the straight, dechanneled and deflected beam, as well as the inefficient regions around the field wires and anode wires.*

A possible way of determining the deflection angle is to observe the distance between the peaks corresponding to the straight and deflected beams and dividing this distance by the one between the chamber and the crystal. This procedure relies on the accurate calibration of all the cells used in the chamber in question. Connecting the cells accurately in the off-line analysis is complicated - one has to take the acceleration of the drift electrons into account to convert from TDC signal to position (section 8, p. 49) and offsets of one cell with respect to another must be taken into account. However, the angle read from the goniometer at optimal alignment is proportional to the bend angle and has a very small uncertainty, $\Delta\theta \simeq 5$ μrad. After determining each angle as precisely as possible from the distance as seen in the drift chamber, a linear fit of goniometer angle as a function of that from the chambers was made. This calibrated

the goniometer angle quite precisely by a linear relationship between the goniometer reading and the observed deflection angle. The deviations of the angle determined from the chamber with respect to that detected by the (calibrated) goniometer were up to 5-6% due to non-uniform drift velocity in the chambers.

The anticlastic effect in the crystal was accounted for by determining the efficiency as a function of vertical position within the beam-size. A typical scan is shown in figure 47 which shows the characteristic parabolic shape for an anticlastic effect. By taking

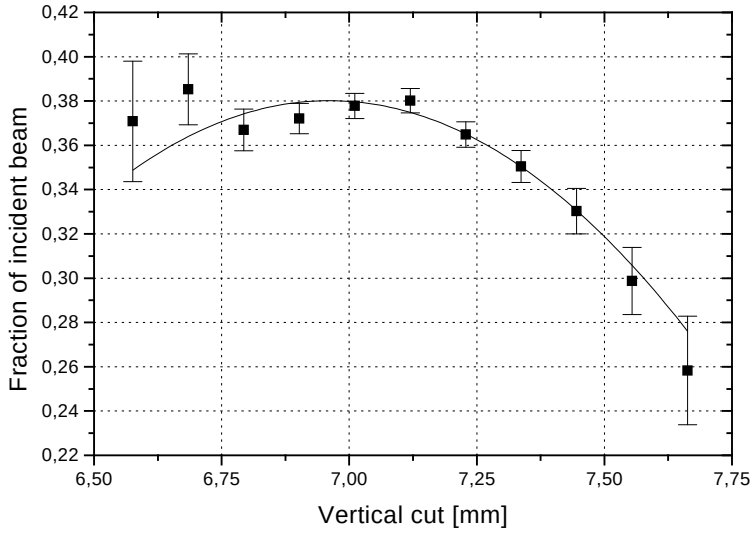

Figure 47: *Efficiency as a function of the vertical position for 450 GeV/c protons deflected 6.2 mrad. The dotted curve is a least-squares fit by a parabola, i.e. the expected shape for an anticlastically bent crystal.*

the vertical distance over which the efficiency drops by a factor of 2 as corresponding to $\psi_p/2$, it is possible to derive an approximate expression for the anticlastic bending of the crystal and an estimate of the effective Poisson ratio: μ_{eff}, cf. 19.3, p. 100. Typical values were $\mu_{\text{eff}} \approx 1/25$ to be compared with the expected μ=1/2.4 which states that the anticlastic effect is substantially reduced due to the non-bent ends.

For a vertical cut of typically 15 channels $\simeq$0.35 mm around the optimized vertical position, four values were determined by integrating the profiles as a function of horizontal cut (1 channel $\simeq$ 23.2 μm) for each angular setting: The number of incident, A_i, undeflected, A_u, and fully deflected particles, A_b, and the number of those particles that dechanneled in the bent part of the crystal, A_d, see figure 48.

The ratio A_b/A_i determined the deflection efficiency according to the definition given above. The ratio A_d/A_i gave the curvature dechanneling fraction and the multiple scattering dechanneling in the bent part. Finally, the ratio A_u/A_i extrapolated to zero bend angle gave the surface transmission by $\varepsilon_{\text{S}} = \lim_{\theta\to 0} 1 - A_u/A_i$, see figure 49.

The reason for the extrapolation is that at large angles the local curvature at the

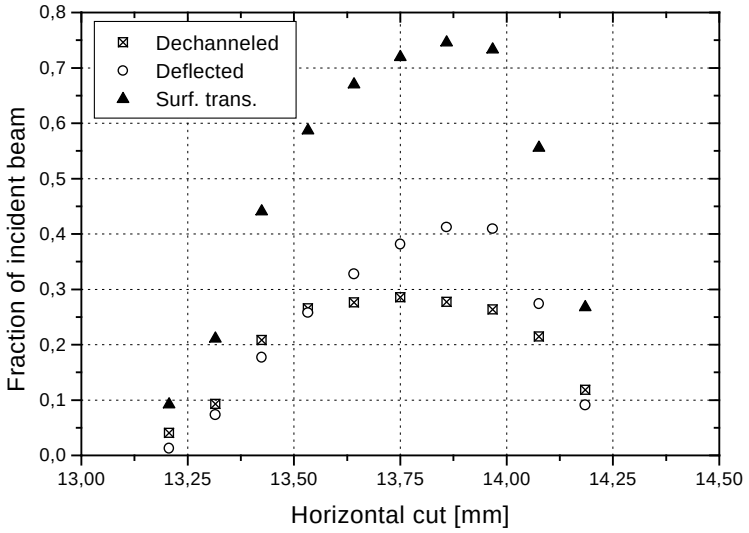

Figure 48: *Counts normalized to incident beam as a function of horizontal position for the fully deflected (open circles) and the dechanneled beam (squares with crosses) at 6.2 mrad. The points labelled surf. trans. (filled triangles) is one minus the fraction of incident beam that appears not to be deflected (see text).*

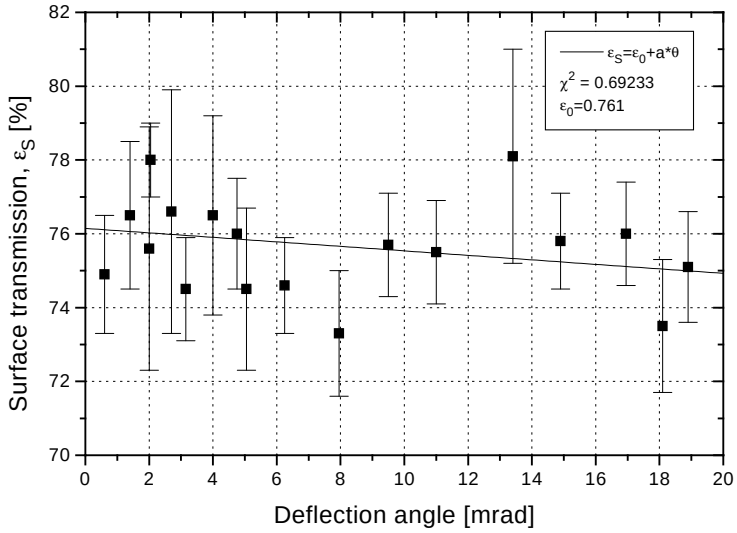

Figure 49: *Surface transmission determined as described in the text. Note the suppressed zero for the vertical axis.*

first pressing point can cause curvature dechanneling, leading to particles detected in the undeflected beam. By extrapolation, this contribution is removed. To get a hint of the divergence of the beam, angular cuts were imposed with the result that the efficiency was essentially unchanged, again indicating a divergence well below the

critical angle.

With the 450 GeV/c beam an approximate calibration of the drift velocity was performed by moving Sc1 across the chamber in small steps and determining the position of the beam on the chamber. A linear fit gave an average drift-velocity of 46$\pm$1 μm/ns.

For the 200 GeV/c beam consisting of mainly protons and pions, the horizontal divergence was determined in two ways. As a function of cut-width in the first chamber, Gaussian fits to the angular profile calculated from the chambers 1 and 2 and extrapolated to zero cut-width gave a measurement of the divergence convoluted with the chamber resolution. By deconvolution (they add in quadrature) using the chamber resolution determined as outlined above, a divergence of $\simeq$11 μrad (2σ) was found. The second method relies on the experimentally determined surface transmission, as was also done for the 450 GeV/c beam (figure 49), in a comparison with a calculation based on the Doyle-Turner potential. For the 200 GeV/c beam this lead to $\simeq$6 μrad (σ), i.e. in very good agreement with the estimate of $\simeq$11 μrad (2σ).

21.3 Results

In figure 50 are shown the experimental results for the deflection efficiency of 450 GeV/c protons along the (110) planes in a germanium crystal [191]. The full-drawn line is a theoretical curve calculated from the model following Ellison's approach to calculate the dechanneling fraction, section 16.1.3, p. 92. The dechanneling fraction as a function of curvature was calculated for a perfectly parallel beam by use of the Doyle-Turner potential with a critical distance of approach to the plane set to $x_c = 2.5u_1$. The calculation was done by numerical integration in a fashion very similar to the one used in appendix A, except that the true distribution of transverse energies is used instead of assuming a uniform distribution which is only a good approximation if the divergence is large. Very good agreement between theory and experiment is obtained, even at large angles.

In the case of 200 GeV/c hadrons, however, the model overestimates the efficiency slightly when a beam divergence of 6 μrad (σ) is used, see figure 51. If instead a divergence of 8 μrad (σ) is used, very good agreement is obtained and this is certainly within the uncertainty of the determination of the divergence.

In a comparison, the two data sets, 450 and 200 GeV/c, show different trends: the high energy results show a higher efficiency at low angles and drops off relatively rapidly with increasing angle, whereas the lower energy starts out at a not very high efficiency, but drops slowly with increasing angle. The reason for this is the interplay of dechanneling length and curvature dechanneling. At the lower energy, the dechanneling length is comparatively low and the critical curvature high, and vice versa for the higher energy, leading to the cross-over in efficiencies.

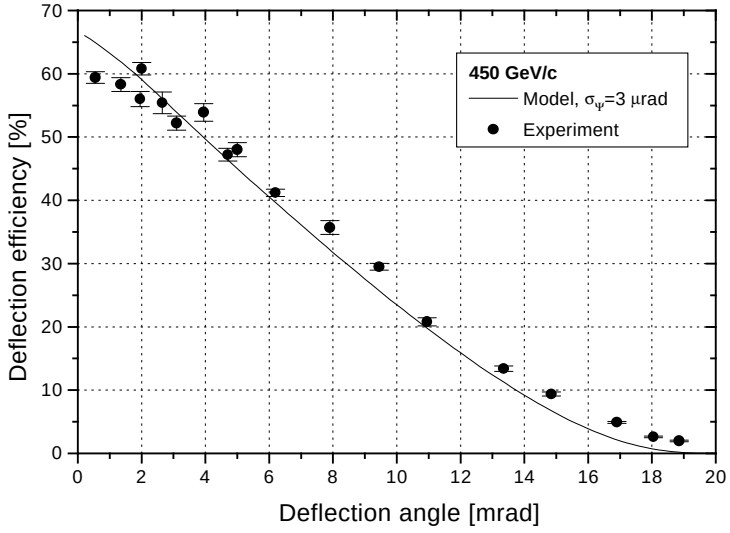

Figure 50: *Experimental results (full squares) for deflection of 450 GeV/c protons in Ge compared to a calculation (line) following the approach described in 16.1.3, based on dechanneling fractions as calculated from the model.*

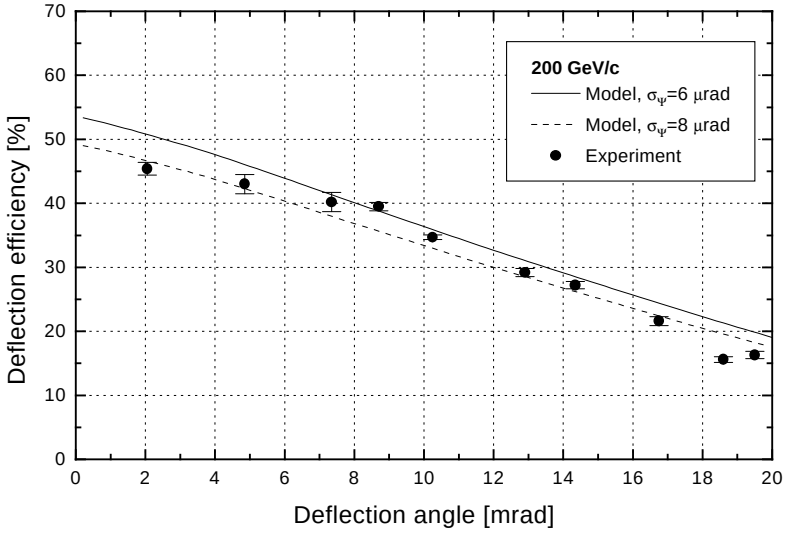

Figure 51: *Experimental results (full squares) for deflection of 200 GeV/c protons in Ge compared to a calculation (line) following the approach described in 16.1.3, based on dechanneling fractions as calculated from the model.*

21.4 Limitations of the model

Evidently, the model for the deflection efficiency described in section 16.1.3 has several limitations. The harmonic approximation leading to $L_{\mathrm{D}}(F) = (1-F)^2 L_{\mathrm{D}}(0)$ is better for low-lying states in the potential, i.e. at relatively large curvatures, whereas the

dechanneling length itself may be different in the extreme cases of very short or very long crystals. Likewise, the 'replacement rule' $L_{\mathrm{B}} \rightarrow L_{\mathrm{B}}/2$ for a three-point bender must be increasingly inaccurate with lowering curvature, since in the limit of a straight crystal, the full length must be used. At large curvatures, the dependence of the modified dechanneling length on F and the exponential dependence of the efficiency on $L_{\mathrm{D}}(F)$ means that a small error on L_{D} will propagate into a larger error for the deflection efficiency. Therefore it is not surprising to see some disagreement at large angles, since for Ge at these energies the dechanneling length has not been measured thus there is no certainty that the theoretical value is correct.

These points do not represent severe limitations as it should be clear from the above comparisons of model and experiment. However, it must be emphasized that extrapolations to other energies, curvatures and materials may challenge one or more of the limitations, leading to imprecise results. The precision in the result of such an extrapolation will of course depend on the degree of the extrapolation.

22 Applications of deflection in bent crystals

This section treats the field of applications of the deflection effect of bent crystals for high energy particles. These applications range from the extraction of external beams from a circular accelerator through beam transport and focussing effects obtained by use of bent crystals to the use of bent crystals for the detection of the spin of particles with a short half-life. A number of these effects are being used routinely.

22.1 Extraction from an accelerator by means of bent crystals

Since another thesis concentrates on this subject [159] this section just contains a few remarks on this important field for the use of crystals.

The importance comes from the fact that at colliders operating at several TeV, a conventional extraction scheme would be very costly, take up a lot of space (many hundreds of meters) and would not be able to run simultaneously with collider operation. In contrast, extraction by means of bent crystals, where the crystal removes particles from the beam 'halo' (which has to be scraped away anyway to avoid a quench of the superconducting magnets in the case of the LHC) is cheap, reliable and *can* be run simultaneously with optimum collider performance.

What distinguishes extraction by bent crystals from the deflection of an external beam by a bent crystal is the interplay between accelerator and crystal, due to the repeated passage of particles. A crucial parameter is the impact parameter, defined as the distance from the surface parallel to the bent planes to the impact point of the particle on the crystal. The mean impact parameter for extraction at the SPS is estimated to be between 50 nm and 1 μm [160]. Clearly, if the particle were to be

extracted at the first passage of the crystal, this would put severe constraints on the surface quality of the crystal. Moreover, in order to estimate the expected extraction efficiency at e.g. the LHC, one would rely heavily on the knowledge of the impact parameter distribution. Owing to non-linearities in the super-conducting magnets it is not possible to predict the average impact parameter for the LHC to better precision than within a factor of ≈10000 [178].

However, it was recently demonstrated at the SPS that multi-pass extraction is an important mechanism [161]. Multi-pass extraction means that the particle can interact with the crystal several times before it is extracted. Therefore, if at the first pass the angle to the planes is not within ψ_p, the particle can suffer multiple Coulomb scattering in the crystalline material and appear within ψ_p at a later pass.

At the CERN SPS, the first extraction experiments gave efficiencies of 9-10%, a large factor above those observed previously, with the use of plane crystals bent in the so-called 'Serpukhov' bending device.

Later, extraction efficiencies as high as 15% have been observed at the SPS [115] with the use of U-shaped bent crystals for which the anticlastic deformation of the endface is small. However, simulations indicate that up to a factor of ≃3 more could be extracted.

22.2 The K12 beam at CERN and the NA48 experiment

One application of crystals in a beamline is already fully operational in the CERN K12 beam for NA48[33]. NA48 is an experiment dedicated to measuring the CP-violation parameter ε'/ε. A brief discussion of the characteristics of the experiment and the use of the crystal in the beamline follows here - a more complete coverage can be found in [163] and [90].

CP-violation can be incorporated in the Standard Model of particle physics, but the amount can not be predicted - moreover, it does not predict if CP-violation is indirect (through mixing of K_1 and K_2) or direct (the decay itself violates CP). A direct CP-violation means $\varepsilon'/\varepsilon \neq 0$. Moreover, understanding CP-violation may give hints at why there are three families of elementary particles, since CP-violation is not possible within the Standard Model for less than three families.

Based on experience gained at the NA31 experiment, the beam design has aimed at obtaining the two simultaneous K-beams, K_L and K_S, as collinear as possible. At the same time, the intensity of the proton beam creating the K_S beam has to be reduced substantially, while maintaining a low emittance. For this, a bent crystal has been implemented to deflect a small fraction of the incident particles upwards. Before this application, bent crystal channeling had always been done by using the straight part at the end of the crystal as entrance. In order to be able to vary the deflection angle in

[33] NA48 will also make use of a crystal as an efficient photon converter, section 15.1, p. 83.

a well-defined way without changing the curvature of the crystal, a deflection scheme using a fraction of the curved crystal by aiming at the side was chosen, see figure 52.

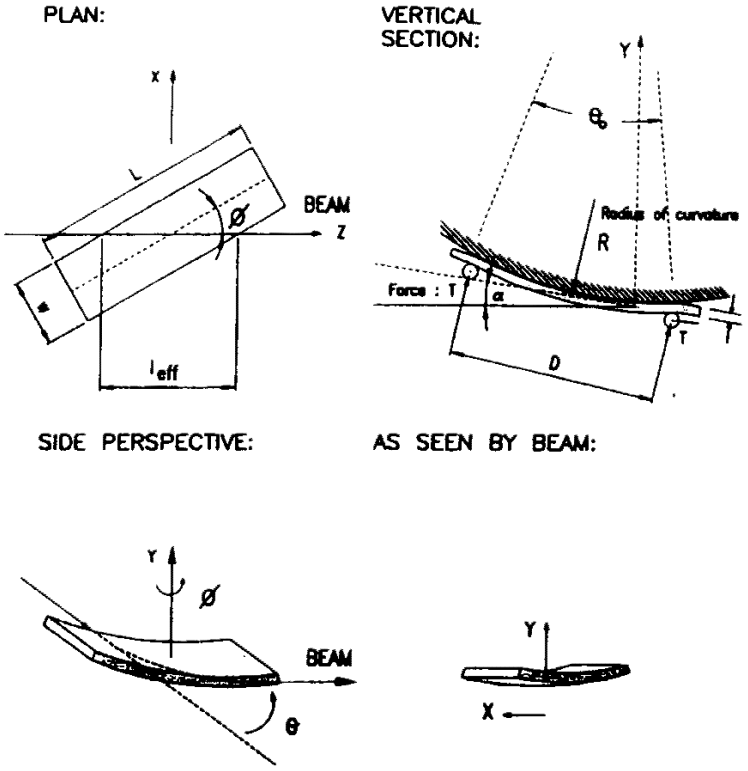

Figure 52: *The novel application of a bent crystal for the production of two simultaneous, almost collinear beams [163].*

In fact, using the side of the crystal actually turns out to be a virtue since in that case there is a coupling between the horizontal position and the vertical angle, such that the channeled beam that exits is well defined in both planes. The deflection efficiency, $1.0 \cdot 10^{-4}$, is in good agreement with a calculation based on the model and suits the purpose of reduction of the intensity perfectly.

22.3 Other applications of bent crystals in beamlines

Two other applications have been shown to be feasible - focussing and spin precession. Since these are beyond the scope of the present experimental work, but nicely demonstrate the diversity of applications of crystals, this section will be rather cursory. Finally, also to put things in perspective, a short section on a few speculative ideas using crystals is included.

22.3.1 Focusing

Until 1992, focusing beams by means of crystal steering was considered through rather complex devices, where the crystal would be compressed in one end to focus the beam. The compression could be either by mechanical means [164] or by mixing crystals with slightly different lattice constants [138].

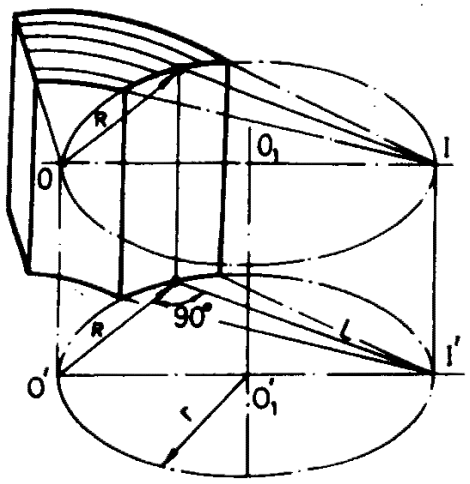

Figure 53: *Shaping of a bent crystal for focusing a beam. The endface must be cut such that it describes a perfect circular arc of radius r when the crystal is bent with a radius of curvature, R [165].*

It turned out [165] that by shaping the endface of the crystal properly and bending the crystal *all* the way to the edge, a focusing effect could be obtained with the focal length given as $f = \sqrt{4r^2 - R^2}$, where r is the curvature radius in the endface of the shaped crystal and R is the curvature radius of the bent crystal, see figure 53. Possible focal lengths are of the order a few tens of centimeters and since the achievable spotsize is $2\psi_p \cdot f$ a spotsize of the order microns is possible [166]. Note also that this 'quadropole effect' is only in the plane perpendicular to the crystal planes, but that it is essentially dispersion-free as for the deflection.

22.3.2 Spin precession

In analogy with a top possessing an angular momentum in the gravitational field of the earth, a moving particle possessing a magnetic moment will precess in an inclined magnetic field. Therefore, since the field in a bent crystal is equivalent to a strong magnetic field, a charged particle with spin, s, and magnetic moment, $\mu = g\mu_B s$, will precess during the passage of a bent crystal if the spin and magnetic field are inclined. Here, g is the gyromagnetic moment and $\mu_B = e\hbar/2mc, \mu_N = e\hbar/2m_pc$ the Bohr magneton and the nuclear magneton, respectively, m_p being the mass of the proton.

For an ultrarelativistic particle with $g \neq 2$ there exists a connection between the spin precession, θ_s and the change of momentum direction, θ_p:

$$\theta_s = \frac{g-2}{2}\gamma\theta_p \tag{96}$$

Therefore, as $\gamma \gg 1$, a polarized beam will appear with a markedly different polarization after the bending, even if the bending angle is small. So, since the distance over which it will precess through a given angle in a crystal is drastically shortened compared to in a magnet one may use this effect to measure magnetic moments of shortlived particles. This effect has been used in a proof-of-principle experiment to measure the magnetic moment of the Σ^+ [167], a hyperon with $\mu = 2.46\mu_N$ and a short lifetime in its rest-system, $c\tau = 2.4$ cm [17], see also [168].

It has been proposed to measure the magnetic moments of charmed baryons by use of the spin precession in bent crystals. For these, the typical lifetime is shorter than for hyperons by a factor ≈500, so very short crystals have to be used [169], [170]. In this case, evidently, a high-Z crystal would be preferred.

22.3.3 A speculative idea

It has been suggested to construct an entire accelerator by the use of bent crystals as deflection magnets and with intermediate sections consisting of straight crystals for a modified version of ionization cooling [171]. There are a few unclear points in this suggestion: It seems that the concept of surface transmission has been neglected - after N passes of a bent crystal, the remaining fraction of the beam will be ε_S^{-N}, which for $\varepsilon_S \leq 0.9$ is an *extremely* small number for the suggested N ($N = 1000$ per turn with $\simeq 3 \cdot 10^5$ turns). Furthermore it disregards the difficulties in deflection of negative particles. Last, it treats the fields in a crystal as if they have a focusing effect. This last postulate is true if one considers a thin crystal, less than one wavelength of the channeling oscillation, and a beam with a focus at exactly the focal length from the crystal. To obtain this one would have severe fine-tuning problems. The conclusion concerning this suggestion must be that it is interesting, but does not seam feasible using today's technology.

Part VII
Summary and conclusions

23 Channeling

When a charged particle is incident on a crystal with a sufficiently small angle to crystallographic directions, the scattering off the atomic constituents are correlated such that the particle is guided by the coherent effect of the nuclear fields in the lattice. Thus the particle is steered through the crystal by the lattice which in the so-called continuum approximation can be considered as being 'smeared' along the particular direction resulting in a string or plane of uniformly distributed charge. If further the momentum perpendicular to the crystallographic direction for a positively/negatively charged particle is too small to overcome the Coulomb repulsion/attraction of the screened field from the nuclei, it is channeled. This particle will experience reduced/increased close-encounter interactions due to a redistribution resulting from the repulsion/attraction from the nuclear fields.

24 QED in strong crystalline fields

A channeled particle may emit radiation originating from transitions in the transverse potential. This radiation is boosted by the relativistic Lorentz factor squared such that it becomes easily observable for relativistic, light particles. Alternatively, one may consider this radiation as originating from the scatter of the virtual photons constituting the field from the nuclei. In consideration of this, it is not surprising that also non-channeled particles - i.e. particles moving above the barrier of the transverse potential - may emit radiation in the collective fields of the nuclei. Owing to the relatively short formation length of the photon, this radiation is similar to ordinary synchrotron radiation for angles of incidence smaller than a certain angle, the so-called Baier angle.

Due to the extremely strong electric fields present in crystals, it is possible with ultra-relativistic particles to investigate radiation and pair creation effects in fields comparable to or stronger than the critical field. This is because the mentioned effects can be calculated in the rest-frame of the radiating (emerging) particle, where the crystalline field is Lorentz-boosted by large factors, 10^5-10^6 for presently available beams. In this case the synchrotron radiation emitted acquires a new behaviour stemming from the fact that the loss of energy to the photon becomes a significant fraction of the energy of the incident particle. The radiation becomes dominated by the recoil. The new behaviour appears as a different scaling with incident energy of the characteristic photon frequency, the emission probability and the intensity.

Thus, experiments with ultra-relativistic beams in single crystals represent another

step in the investigations of fundamental effects that influence the radiation and pair production in crystals. It has been shown that with increasing energy these fundamental effects range from the quantisation of the transverse potential through classical electrodynamics with non-relativistic and relativistic description of the transverse motion to the quantum effects of radiation under recoil in synchrotron motion. The behaviour as a function of the relativistic Lorentz factor of for example the energy loss for an electron which emits synchrotron radiation is completely different in the case where the quantum recoil is significant compared to the classical case. These effects reappear to some extent in pair production.

24.1 Pair production

It has been demonstrated, in accordance with earlier experiments, that incidence of ultra-high energy photons along the axis in a $\langle 110 \rangle$ Ge crystal results in a drastic enhancement of pair production compared to random incidence. Theoretical and experimental results are in good agreement and it is thus concluded that the quantum-electrodynamical processes in a uniform electromagnetic field of a strength larger than the critical field are well understood for this type of crystal. However, for heavy crystals experiments and theoretical estimates diverge at high energies hinting at an insufficient description of the pair production phenomenon. Nevertheless, large factors can be gained with respect to amorphous materials, thus offering the possibility of efficient conversion as e.g. in the NA48 application used at CERN.

On the other hand, by use of the results presented, it is for the first time possible to compare theoretical and experimental results for pair creation in a periodic electromagnetic field of a peak strength comparable to the critical field. These results are obtained when ultra-high energy photons are incident along the (110) plane with a small angle to the $\langle 110 \rangle$ axis in the germanium crystal. In this case, the theoretical and experimental results presented are not in good agreement for all energy intervals. A number of possible experimental explanations for parts of this discrepancy have been given above, but it is not unlikely that the theory overestimates the values because important effects are not included (see below). In any case, it is striking for the case of germanium that the experimental and theoretical results are alike for incidence along the axis and significantly different for non-zero angles to the axis. Moreover, one of two previous experiments using Ge has found a similar discrepancy for incidence far from the plane.

24.1.1 Presence of inhibiting effects

Indications for the presence of inhibiting effects of the Landau-Pomeranchuk type have been found for pair production in W and the possibility of observing the Chudakov effect has been discussed. Furthermore, it is not unlikely that Landau-Pomeranchuk-

like effects are responsible for some of the discrepancy mentioned above for Ge, W and Ir. Another contribution to the discrepancy can possibly be traced to the calculations for pair production which for heavy elements are based on the Molière potential. This potential may lead to an overestimate of the crystalline field and thus an exaggeration of the enhancement. Recent calculations by use of the Waasmaier-Kirfel potential support this conclusion.

Furthermore, reduced radiation probability connected to large deflection angles for 150 GeV electrons passing a 1.5 mm $\langle 100 \rangle$ diamond crystal near the axis have shown that the Landau-Pomeranchuk is an important process for these radiation processes.

Landau-Pomeranchuk effects can be important for the understanding of the development of electromagnetic showers in the above-TeV region, e.g. for the detection of very high energy cosmic rays. In this connection, single crystals provide a unique tool for the investigation of such effects at extremely high energies with particles available from today's accelerators.

24.2 Polarized hard photons from electrons in crystals

When an energetic electron passes a crystal in a direction close to an axis and along a plane, the crossing of the strings in the plane generates a coherent radiation of typical energy around 0.7 times the incident energy. This radiation is believed to be linearly polarized. Following this expectation, it has been shown in a proof-of-principle experiment that a crystalline target can be used to generate and detect a high energy polarized photon beam. The detection makes use of the difference in conversion probability for photons polarized parallel and perpendicular to a plane. The effect shown amounts to $\simeq 10\%$ with some variation with angle to the axis and photon energy, but the conversion of this to the degree of linear polarization of the photon beam requires calculations of the analyzing power of the crystal.

24.3 Radiative cooling

Radiative cooling - the decrease in transverse energy of a particle in a crystal - can influence the emission probability for electrons and positrons. This is the case since for example electrons which suffer radiative cooling are brought closer to the regions of high fields in the transverse potential whereby their emission probability increases. It is thus a very important process for the description of radiation emission from crystals. Further, it has a potential application since radiative cooling may lead to angular cooling - the decrease in angular spread of the beam.

In remarkable agreement with theoretical estimates it has been shown that radiative cooling takes place for electrons incident on a silicon crystal outside, but near, the critical angle of channeling for the $\langle 110 \rangle$ axis. As well in agreement with the theoretical estimates, electrons aligned with the axis and positrons at any angle suffer angular

heating, i.e. the average angle with respect to the axis increases.

25 Deflection of charged particles in crystals

Since the late seventies, the deflection of charged particles by the use of channeling in crystals has been investigated at high energy physics laboratories around the world. It has been shown that the deflection efficiency is substantial for deflection angles relevant for many applications.

However, until the above described experiments, two important questions remained to be answered:

1. What is the level of irradiation at which the deflection efficiency begins to decline in a silicon crystal?

2. Is the deflection efficiency in heavier crystals as well described by the classical model as the deflection efficiency in silicon crystals and do heavier crystals therefore offer higher efficiencies?

The presented experimental work has answered these questions.

25.1 Effect of irradiation

It has been shown in an experiment with a silicon crystal that the deflection efficiency deteriorates with a relative deterioration coefficient of $6\% \pm 2\%$ per 10^{20} protons/cm^2 for a 450 GeV beam. Therefore, even in very intense beams, the deflection of charged particles at high energies will be almost unaffected by the radiation damage. The prime reason for this enormously high radiation tolerance is that the channeling responsible for the deflection involves an average over $\approx 10^5$ atoms in the lattice such that the displacement or substitution of a few of these bears little effect on the deflection efficiency. However, due to the increasing significance of local curvatures, large dislocation densities may affect the efficiency at higher energies.

25.2 Applicability of heavy crystals

Encouraged by the expectation of higher deflection efficiencies the higher the charge of the lattice nuclei, a measurement of the deflection efficiency in germanium was undertaken. Extraordinary good agreement between the now 'classical' model and the experimental results has been shown and it is therefore concluded that germanium is the most well-suited crystal for deflection so far tested. This agreement is also encouraging for deflection in crystals of even higher charge, if these can be made of sufficient quality. Furthermore, the good agreement for two energies gives confidence in the extrapolation of the model to energies to be obtained eg. at the LHC.

26 Outlook

Several of the latest experiments give new perspectives for the investigations of effects of relevance to fundamental physics as well as applications of crystals and therefore they may hint at the direction of future experiments in the field.

26.1 Radiation and pair production

Data for photon intensity spectra have been taken and are in the process of being analyzed. These results may among other things confirm or reject the hypothesis that the characteristic photon peak which appears at high energies for electrons incident in the strings-of-strings region consists of a very energetic photon followed by photons of sub-GeV energies.

Fundamental effects as the Landau-Pomeranchuk effect have also been investigated for electrons incident on heavy crystals - preliminary results show a very pronounced reduction of emission at energies up to more than half the incident energy. This opens the possibility of using single crystals to 'simulate' Landau-Pomeranchuk effects which would otherwise only be accessible at extremely high energies, 10-100 TeV.

Radiation cooling will be subject of detailed analysis, e.g. with data which is taken recently for the $\langle 110 \rangle$ axis in diamond where the effect should be even more remarkable than for the weaker $\langle 100 \rangle$ direction investigated in diamond and the $\langle 110 \rangle$ axis in silicon.

The very clear difference in energy loss of electrons in the two domains of classical and quantum synchrotron radiation has also recently been examined experimentally. These data should show a clear effect of the transition from one region to the other since statistical and systematical errors are small for this type of experiment.

In terms of applications, a crystalline converter for the AKS veto in the NA48 experiment at CERN is used. This is the first direct application of the strong field effect in a beamline. However, a few of the other interesting proposals are a compact, space-borne crystalline detector for the search of the origin of gamma-rays from the Universe and the generation of energetic (polarized) high energy photon beams for experiments.

26.2 Deflection in bent crystals

Having shown the superiority of Ge crystals compared to Si crystals in terms of deflection efficiencies at large angles, it remains to be tested if the sensitivity to radiation damage for Ge is the same as for Si. Clearly, an application of germanium crystals in intense beams must await an investigation of this effect.

Important questions have been answered during the past ten years of investigations of applications of bent crystals. This may have supplied the missing information that

lead to the rejection of the LHC-B proposal based on a beam extracted from the LHC by means of a crystal. As it has been shown, the deflection of charged particles in bent crystals is not only cheap - both in terms of installation and running - and easy to operate, it also enables one to provide beams under conditions which would otherwise be impossible and last but not least it is very reliable.

Bent crystals have already been implemented as beam elements for the deflection of protons, but with the recent proof that the deflection mechanism works for highly charged ions at high energy as well, the perspective becomes even wider. It is indeed possible that for future accelerators as e.g. the LHC at CERN or RHIC at Brookhaven, the extraction of highly charged ions will be performed by the use of bent crystals.

However, it is clear that the deflection of highly charged ions is a subject that has only been touched upon. Many questions are still open, for example: What is the charge-state of the exiting ions and do they suffer neutron or proton-loss? Does the damage occur for lower fluences than for protons? Is the deflection process equal to that of protons at all angles and for all materials? Answers to these and other questions must await further investigations which will give important information not only on the fundamental processes, but also on parameters of relevance to an application.

Part VIII
Summary in danish

27 Indledning

Denne PhD-afhandling omhandler multi-GeV partiklers vekselvirkning med stærke felter i krystaller, herunder med henblik på anvendelser i partikeltransporten fra en accelerator til et eksperiment. Det eksperimentelle arbejde er udført på CERN ved Genève i samarbejde med eksperimentalfysikgruppen NA43 og CERNs SL-EA (SPS/LEP-Experimental Areas) gruppe.

Hvis ladede partikler gennemtrænger en krystal med en tilstrækkelig lille vinkel til en krystallinsk plan, mindre end den såkaldte Lindhard-vinkel, kan den transversale bevægelse være begrænset. Partiklen vil i dette tilfælde blive styret gennem krystallen af krystal-gitteret. Når partiklen i den såkaldte kontinuumsapproksimation kun bliver svagt påvirket af de enkelt atomer langs banen, kan de enkelte atomers felter adderes kohærent, således at de optræder som et kontinuum. Der er altså tale om et meget stærkt felt, der strækker sig over hele længden af krystallen, dvs. en makroskopisk længde i modsætning til feltet fra en kerne, der ganske vist er stærkt, men har en uhyre lille udstrækning. Dette felt kan også beskrives ved et transversalt potential.

28 Afbøjning af ladede partikler i krystaller

Kanaliseringseffekten er opretholdt selvom krystallen bliver udsat for små deformationer. Specielt vil en svagt bøjet krystal medføre at den passerende partikel bliver afbøjet som i et magnetisk felt. Årsagen til denne effekt er at partiklen pga. centrifugalkraften i det accelererede system i middel opholder sig i det stærke elektriske felt i krystallen, der således leverer den nødvendige centripetalkraft til cirkelbevægelsen. Eftersom feltet i krystallen langt overgår de makroskopiske felter man kan frembringe, kan afbøjningseffekten i en svagt bøjet krystal således blive flere hundrede gange større end i feks. en magnet. Effekten er dog ledsaget af tab, der afhænger af partiklens fart og krystallens krumning, materiale og temperatur.

Indtil det beskrevne arbejde har forsøg med afbøjning i krystaller kun været udført med silicium-krystaller. Det har dog, i henhold til teori, været ventet at krystaller med højere kerneladninger ville have mindre tab for samme afbøjningsvinkler. Det er i afhandlingen vist at eksperimentelle resultater med afbøjning i germanium-krystaller ved to energier er i god overensstemmelse med de forventede teoretiske værdier og at afbøjningseffektiviteten i germanium er forøget betragteligt i forhold til afbøjningseffektiviteten i silicium. De største afbøjningsvinkler for germaniumkrystallen svarer

til et effektivt felt på 2000 Tesla hvilket skal sammenlignes med 5-10 Tesla i en moderne superledende magnet.

Et afgørende punkt for krystallers anvendelighed til partikeltransport, er deres modstandsdygtighed overfor bestråling. Man har indtil dette arbejde ikke vidst ved hvilken grænse for bestråling, krystallers evne til at afbøje partikler vil aftage. Det er her vist at denne grænse er ved ekstremt store doser, som kun kan opnås i meget intense partikelstråler. Dette betyder, at krystallers anvendelighed som afbøjningselementer kun i meget lille udstrækning er begrænset af hensyn til bestråling.

29 Stærkfeltseffekter

I produktionen af elektron-positron par eller fotoner, der feks. finder sted når en foton eller en ladet partikel passerer en kernes elektromagnetiske felt, kan man også udnytte de stærke, makroskopiske felter i krystaller. Igen er det kohærensfænomenet der er årsag til en ny effekt. I dette tilfælde kan sandsynlighederne for feks. par-produktion i hvert atomart stød adderes kohærent, således at man opnår en kraftig forøgelse i sammenligning med passage af et amorft materiale. Disse kohærensfænomener har været kendt siden slutningen af tresserne for store indskudsvinkler i forhold til krystallografiske retninger. Først langt senere blev det klart at ved tilstrækkeligt høje energier og små indskudsvinkler optræder et nyt kohærensfænomen hvor en let, ultrarelativistisk partikel med en Lorentz-faktor af størrelsesordenen 10^5 'oplever' felterne i krystallen som et kontinuumsfelt af ekstremt høj styrke. Dette felt bliver sammenligneligt med det såkaldte kritiske felt, der iøvrigt kun kan tænkes at forekomme for yderst kraftige lasere eller i nærheden af kompakte astrofysiske objekter, såsom neutronstjerner. I et (over-)kritisk felt vil den store tæthed af virtuelle fotoner som repræsenterer feltet bevirke at der for feks. en passerende elektron vil være en kraftig forøgelse af strålingssandsynligheden i forhold til passage af et amorft materiale. Tilsvarende vil der opstå en betragtelig forøgelse af produktion af elektron-positron par ved indskud af fotoner af tilstrækkelig høj energi og tilpas lille vinkel til en krystallografisk retning. Disse effekter optræder løst sagt idet energien vundet ved ubestemtheden for feks. en elektrons position i et kritisk felt resulterer i hvileenergien for endnu en partikel hvorved den kan skabes.

29.1 Strålingsudsendelse

En ladet partikel kan udsende stråling forbundet med overgange mellem tilstande i det transversale potential. Denne såkaldte strålingskøling har tidligere været benyttet for præcist at kunne beskrive observerede strålingsspektre, idet feks. en elektron der udsender stråling vil bevæge sig i retning af et stærkere felt hvorved strålingssandsyn-

ligheden tiltager. Effekten af strålingsudsendelsen vil med andre ord være selvforstærkende. Imidlertid har der i mange år været tvivl om hvorvidt strålingskølingen kunne anvendes til også at køle partikelstrålen, forstået på den måde at vinkelspredningen vil aftage. Dette fænomen, som kan kaldes vinkelkøling, er fundamentalt for mange acceleratorers funktion.

Det er i afhandlingen vist at elektroner der indskydes med en vinkel til en krystallinsk akse som er større end Lindhard-vinklen vil undergå vinkelkøling som resultat af strålingsudsendelsen. Derimod vil elektroner med en meget lille vinkel til aksen samt positroner opnå større vinkler.

Det har i længere tid været kendt at stråling udsendt fra plan-kanaliserede elektroner ved sub-GeV energier er lineært polariseret. Tilsvarende kan parproduktionssandsynligheden for en lineært polariseret fotonstråle variere afhængigt af om fotonerne rammer en krystalplan der er vinkelret på eller parallel med polarisationsretningen. Sidstnævnte effekt har her været benyttet til at vise at det er muligt at producere og detektere polariserede fotoner i multi-GeV området.

29.2 Parproduktion

Indenfor det nye område af kohærent parproduktion kan der optræde resonanser mellem dannelseslængden (den typiske længde over hvilken et par bliver produceret) og afstanden mellem de passerede akser i krystallen. Dette bevirker en betydelig variation af den andel af energien som hhv. elektronen og positronen tager fra fotonen. Der vil derfor optræde markante oscillationer i parproduktionssandsynligheden for par der deler fotonenergien ligeligt, som funktion af vinklen til den atomare streng. Principielt er fænomenet ækvivalent med forstærkning af visse toner og undertrykkelse af andre i et resonansrum. Disse parproduktionsoscillationer blev behandlet teoretisk i 1993 af bla. Yuri Kononets og er eksperimentelt søgt påvist for første gang i denne afhandling.

Den nævnte forøgelseseffekt er bla. taget i betragtning for anvendelse ved NA48-eksperimentet på CERN, hvor man ønsker at afvise begivenheder hvor en kaon er henfaldet til fotoner (via henfald til neutrale pioner) før et bestemt henfaldsområde. Samtidig er det fordelagtigt at forstyrre de tilbageværende kaoner så lidt som muligt, hvorfor man vil benytte så tyndt et materiale som muligt til konvertering af fotonerne (hvorved de resulterende ladede partikler kan detekteres og begivenheden frasorteres på trigger-niveauet). For at opnå det optimale forhold mellem en stor konverteringseffektivitet og en lille forstyrrelse af kaonerne, vil man benytte en krystal hvor et tyndt materiale kan give samme konverteringseffektivitet som et noget tykkere (ca. dobbelt så tykt) amorft materiale.

Påvisningen af de nævnte stærkfeltseffekter har desuden betydning for den bedst afprøvede teori i fysikken: kvanteelektrodynamikken (QED). Det viser sig nemlig at

disse stærkfeltseffekter er processer der prober felter af en sådan karakter at den emitterende partikel bliver stærkt påvirket af det udsendte kvant under strålingsudsendelsen.

Det omtalte studium er udført under vejledning af professor, dr. scient. Erik Uggerhøj, ISA og PhD. Konrad Elsener, CERN.

Sluttelig vil jeg takke min familie, min kæreste og mine venner for opmuntring under hele mit fysikstudium.

Part IX
Appendices

A Dechanneling fraction

To evaluate the dechanneling fraction for positively charged particles channeled in a bent crystal, it suffices in the first approximation to use a harmonic potential with a centrifugal term added

$$U(x) = \frac{1}{2}kx^2 - pv\kappa x \tag{97}$$

Further, it is assumed that the available states for channeling are in the well between x_1 and x_2, where normally $x_2 = d_p/2 - x_c$. Now, if the incident beam has a divergence larger than ψ_p, the population of states in the upper part of the well will to a first approximation be uniformly distributed, since at distances larger than $2.5u_1$ to the plane the potential can be approximated by a linear function of x in the upper half. Therefore, to find the approximate dechanneling fraction the integral over the potential well as a function of curvature, $A_1(\kappa)$, must be divided by the number found for a straight crystal, $A_1(0)$, and then subtracted from 1, see also figure 36, p. 90.

From eq. (97) follows, since the minimum is at x_2 when $\kappa = \kappa_c$:

$$k = \frac{pv\kappa_c}{x_2} \tag{98}$$

and since x_1 and x_2 are the borders of the well, one can express x_1 as a function of x_2 by use of $U(x_1) = U(x_2)$:

$$x_1 = \frac{pv\kappa - \sqrt{(pv\kappa)^2 - 2k(pv\kappa x_2 - kx_2/2)}}{k} \tag{99}$$

After some manipulation this gives

$$x_1 = x_2(2\frac{\kappa}{\kappa_c} - 1) \tag{100}$$

The depth of the potential, $E_{\text{depth}} = U(x_2) - U(x_{\min})$, where $x_{\min} = pv\kappa/k$ is thus given by

$$E_{\text{depth}}(\kappa) = E_{\text{depth}}(0)(1 - \frac{pv\kappa}{kx_2})^2 \tag{101}$$

Integration of eq. (97) from x_1 to x_2 gives

$$A_2 = pv\kappa_c x_2^2(\frac{1}{3} - \frac{\kappa}{\kappa_c} + \frac{2}{3}(\frac{\kappa}{\kappa_c})^3) \tag{102}$$

which must be subtracted from $(x_2 - x_1)E_{\text{depth}}$ to give A_1, where $E_{\text{depth}} = (kx_2^2/2)(1 - \kappa/\kappa_c)^2$ is the depth of the potential as a function of κ, see also [131], [132]. This leads to

$$A_1 = pv\kappa_c x_2^2[\frac{2}{3} - 2\frac{\kappa}{\kappa_c} + 3(\frac{\kappa}{\kappa_c})^2 - \frac{5}{3}(\frac{\kappa}{\kappa_c})^3] \tag{103}$$

and by $F = 1 - A_1(\kappa)/A_1(0)$ the final result is:

$$F = 3\frac{\kappa}{\kappa_c} - \frac{9}{2}(\frac{\kappa}{\kappa_c})^2 + \frac{5}{2}(\frac{\kappa}{\kappa_c})^3 \tag{104}$$

Obviously, higher order terms in the potential and a non-uniform distribution of states will modify this for large κ/κ_c, but for small curvatures, the dechanneling fraction is proportional to the curvature with constant of proportionality, $\eta = 3$. This is confirmed by measurements in a uniformly bent crystal where an 'eyeballing' fit to data gives $F \simeq 1.04 \tanh(6\Gamma)$ with $\Gamma = \kappa/2\kappa_c$, i.e. $F \simeq 3.1\kappa/\kappa_c$, [134], see figure 54.

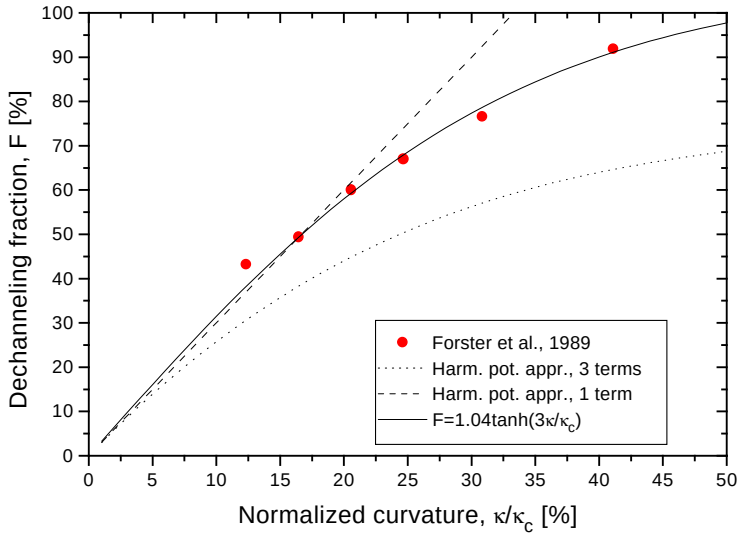

Figure 54: *Dechanneling fraction as a function of curvature (for details see text).*

Note the generality of the result, eq. (104) - it does only depend on x_2 and pv through κ_c and it is valid for any Z_2.

B Integral for the semi-classical approximation

According to [56, eqs. (59.10) and (59.20)] the probability of pair production in a strong field is based on the calculation of the integral[34]:

$$M = \int \exp[i\omega(\tau - \boldsymbol{n}/c \cdot (\boldsymbol{r}_\pm(t_1) - \boldsymbol{r}_\pm(t_2)))]d\Omega \tag{105}$$

Here $\boldsymbol{n}/n$ determines the direction of the photon, the substitution $\omega \to \omega^\#$ must be performed in the result and $\tau = t_2 - t_1$. By insertion of the solid angle, $\mathrm{d}\Omega$, and $\boldsymbol{r}_{\pm i} \equiv \boldsymbol{r}_\pm(t_i)$:

$$M = 2\pi \cdot \exp(i\omega\tau) \int_{-1}^{1} \exp(i|\boldsymbol{r}_{\pm 1} - \boldsymbol{r}_{\pm 2}|\omega/c \cdot \cos\theta) d\cos\theta \quad \Leftrightarrow \tag{106}$$

$$M = 2\pi \cdot \exp(i\omega\tau) \frac{\exp(i|\boldsymbol{r}_{\pm 1} - \boldsymbol{r}_{\pm 2}|\omega/c) + \exp(i|\boldsymbol{r}_{\pm 1} - \boldsymbol{r}_{\pm 2}|\omega/c)}{i|\boldsymbol{r}_{\pm 1} - \boldsymbol{r}_{\pm 2}|\omega/c} \quad \Leftrightarrow \tag{107}$$

$$M = \frac{4\pi}{|\boldsymbol{r}_{\pm 1} - \boldsymbol{r}_{\pm 2}|\omega/c} \exp(i\omega\tau) \sin(|\boldsymbol{r}_{\pm 1} - \boldsymbol{r}_{\pm 2}|\omega/c) \tag{108}$$

where θ is the angle between $\boldsymbol{r}_{\pm 1} - \boldsymbol{r}_{\pm 2}$ and $\boldsymbol{n}/n$. Taking the real part the following intermediate result is obtained:

$$Re(M) = \frac{4\pi}{|\boldsymbol{r}_{\pm 1} - \boldsymbol{r}_{\pm 2}|\omega/c} \cos(\omega\tau) \sin(|\boldsymbol{r}_{\pm 1} - \boldsymbol{r}_{\pm 2}|\omega/c) \quad \Leftrightarrow \tag{109}$$

$$Re(M) = 2\pi \frac{\sin(\omega\tau - |\boldsymbol{r}_{\pm 1} - \boldsymbol{r}_{\pm 2}|\omega/c) - \sin(\omega\tau + |\boldsymbol{r}_{\pm 1} - \boldsymbol{r}_{\pm 2}|\omega/c)}{|\boldsymbol{r}_{\pm 1} - \boldsymbol{r}_{\pm 2}|\omega/c} \tag{110}$$

To evaluate this, $|\boldsymbol{r}_{\pm 1} - \boldsymbol{r}_{\pm 2}|$ must be determined from kinematics:

$$|\boldsymbol{r}_{\pm 1} - \boldsymbol{r}_{\pm 2}| = \sqrt{(z_{\pm 1} - z_{\pm 2})^2 + (r_{\perp \pm 1} - r_{\perp \pm 2})^2} \simeq |z_{\pm 1} - z_{\pm 2}| + \frac{(r_{\perp \pm 1} - r_{\perp \pm 2})^2}{2|z_{\pm 1} - z_{\pm 2}|} \tag{111}$$

where

$$z_{\pm 1} - z_{\pm 2} = \int_{t_2}^{t_1} v_{z\pm} dt \quad \text{and} \quad \boldsymbol{r}_{\perp \pm 1} - \boldsymbol{r}_{\perp \pm 2} = (\int_{t_2}^{t_1} \boldsymbol{v}_{\perp \pm} dt)^2 \tag{112}$$

Furthermore $v_{z\pm}$ can be approximated by:

$$v_{z\pm} \simeq c(1 - \frac{1}{2\gamma_\pm^2} - \frac{v_{\perp \pm}^2}{2c^2}) \tag{113}$$

[34] This appendix does not derive rigorously the formula for pair production in a strong field. Rather, it aims at explaining the origin of each of the terms.

which leads to:

$$\tau - \frac{|\boldsymbol{r}_{\pm 1} - \boldsymbol{r}_{\pm 2}|}{c} \simeq \frac{1}{2}[\frac{\tau}{\gamma_\pm^2} + \frac{1}{c^2}\int_{t_1}^{t_2} \boldsymbol{v}_{\perp\pm}^2 dt - \frac{1}{c^2\tau}(\int_{t_1}^{t_2} \boldsymbol{v}_{\perp\pm} dt)^2] \tag{114}$$

The second term in eq. (110) is approximately equal to $\sin(2\omega\tau)/\omega\tau$ and therefore gives $\pi/2\omega$ when integrated over τ [195, p. 96]. Finally the formation length, $\lambda_{\text{coh.}} = 2\gamma^2 c/\omega$ (eq. (23), with the substitution $\omega \to \omega^\#$), leads to

$$\int_0^\infty Re(M) d\tau = 2\pi/\omega \cdot (\int_0^\infty \frac{\sin A_\pm(\tau)}{\tau} d\tau + \frac{\pi}{2}) \tag{115}$$

$$A_\pm(\tau) = \frac{c}{\lambda_{\text{coh.}}(\xi_\pm, \omega)}[\tau + \frac{\gamma_\pm^2}{c^2}\int_{t_1}^{t_2} \boldsymbol{v}_{\perp\pm}^2 dt - \frac{\gamma_\pm^2}{c^2\tau}(\int_{t_1}^{t_2} \boldsymbol{v}_{\perp\pm} dt)^2] \tag{116}$$

The remaining factor in obtaining the expression eq. (118):

$$\frac{\xi_+^2 + \xi_-^2}{4\xi_+\xi_-}\frac{\gamma_\pm^2}{c^2}(v_\perp^\pm(\tau) - v_\perp^\pm(-\tau))^2 - 1 \tag{117}$$

originates from the average over the polarization of the initial photon and the summation over final spin states of the electron and positron, (compare [56, p. 185] with [78, eq. (2)]).

The result, the so-called Baier-Katkov formula, becomes [113]

$$\frac{dN_p}{d\xi_\pm} = \frac{e^2 m^2 c^3}{\pi\hbar^3\omega}\{\int_0^\infty [\frac{\xi_+^2 + \xi_-^2}{4\xi_+\xi_-}\frac{\gamma_\pm^2}{c^2}(v_\perp^\pm(\tau) - v_\perp^\pm(-\tau))^2 - 1]\frac{\sin A_\pm(\tau)}{\tau} d\tau + \frac{\pi}{2}\} \tag{118}$$

with $A_\pm(\tau)$ given by eq. (116).

In the limit where MCS can be neglected and the coherent mechanism dominates for incidence along an axis, eq. (118) leads to the Constant Field Approximation, eq. (48) by insertion of $r_\perp(\tau) = r_\perp^0 + v_\perp^0\tau + F_\perp\tau^2/2m\gamma$ and $v_\perp(\tau) = v_\perp^0 + F_\perp\tau/m\gamma$ [62] in eq. (116):

Thus the $A_\pm(\tau)$ term becomes

$$A_\pm(\tau) = \frac{\tau}{\tau_c} + \frac{\tau^3}{12\tau_c\tau_\gamma^2} \tag{119}$$

where $\tau_c = \lambda_{\text{coh.}}/c$ and $\tau_\gamma = mc/F_\perp$ is the field deflection time. Above (p. 26), the approximation for the transverse force $F_\perp = e\mathcal{E} = U_0/u_1$ was used. Then, since [18], [196, §59,§74], [62]

$$\int_0^\infty \frac{\tau}{\tau_\gamma^2}\sin(\frac{\tau}{\tau_c} + \frac{\tau^3}{12\tau_c\tau_\gamma^2}) d\tau = \frac{4}{\sqrt{3}} K_{2/3}(\frac{4\tau_\gamma}{3\tau_c}) \tag{120}$$

and

$$\int_0^\infty \frac{1}{\tau}\sin(\frac{\tau}{\tau_c}+\frac{\tau^3}{12\tau_c\tau_{\gamma f}^2})d\tau = \frac{\pi}{2}-\frac{1}{\sqrt{3}}\int_{\frac{4\tau_{\gamma f}}{3\tau_c}}^\infty K_{1/3}(t)dt \tag{121}$$

the CFA, eq. (48), is obtained:

$$\frac{dN_p}{d\xi_\pm} = \frac{2\alpha}{\sqrt{3}\pi\lambda_{\text{coh.}}}[(\xi_-^2+\xi_+^2)K_{2/3}(\frac{4\tau_\gamma}{3\tau_c})-\xi_-\xi_+\int_{\frac{4\tau_\gamma}{3\tau_c}}^\infty K_{1/3}(t)dt] \tag{122}$$

with $\chi = 2\lambda_{\text{sym.}}^{\text{pair}}/\lambda_\gamma$ in eq. (48) being twice the ratio of the central coherence length and the field deflection length, cf. eq. (31). Therefore the argument, $4\tau_\gamma/3\tau_c$, in the modified Bessel functions above become proportional to $1/\chi$ such that with increasing χ the formation length (the main contribution) shortens.

C Differential spectra in pair production

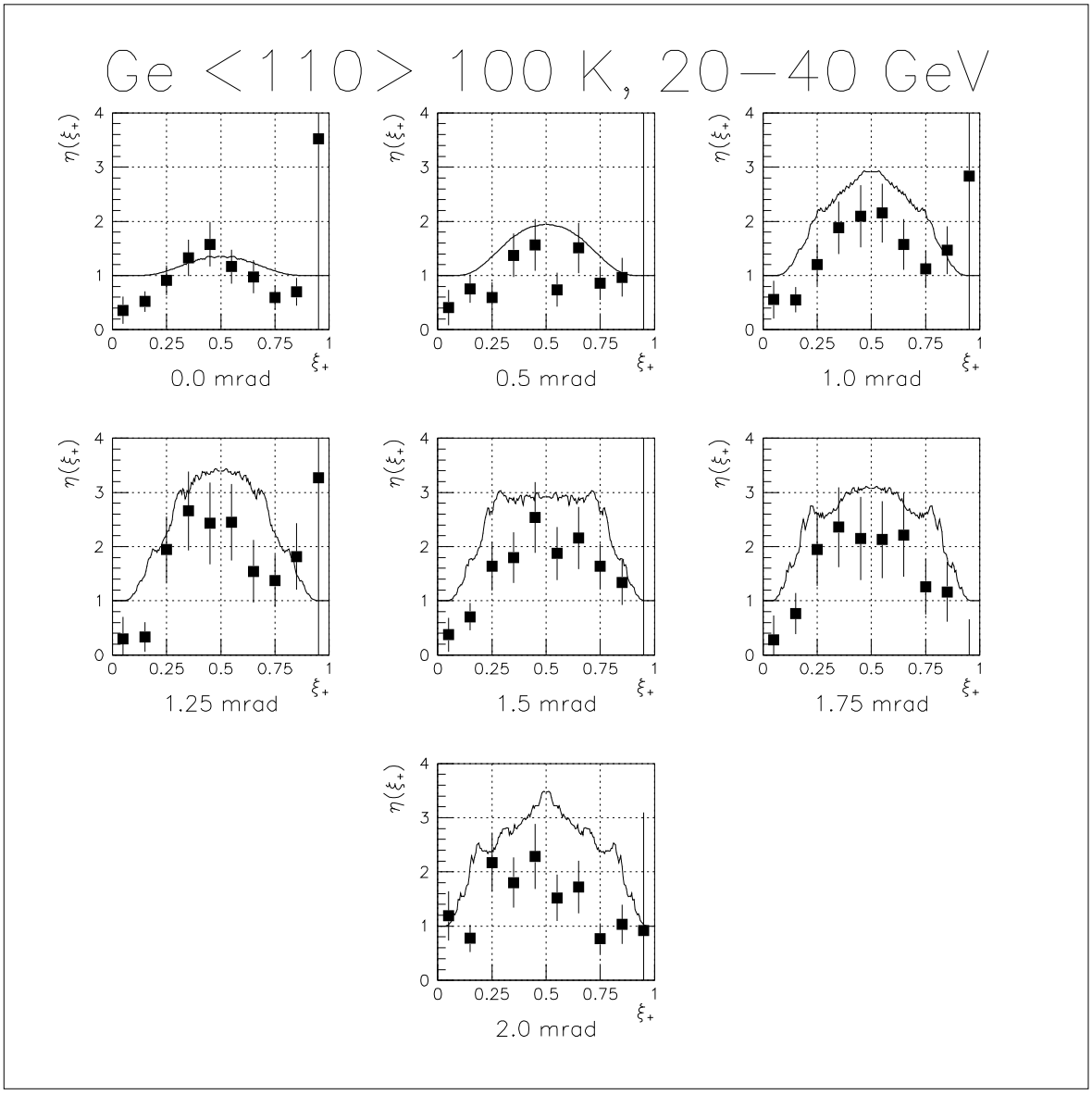

Figure 55: *The differential enhancement, $\eta(\xi_+)$, as a function of the relative positron energy, ξ_+. The photon energy is between 20 and 40 GeV and the direction of incidence is along the (110) plane in Ge for different angles, 0.0-2.0 mrad, to the $\langle 110 \rangle$ axis. The full-drawn curve is a calculation by Kononets using the semi-classical approximation [113], [67] and the filled squares are experimental points with error bars denoting the statistical uncertainty.*

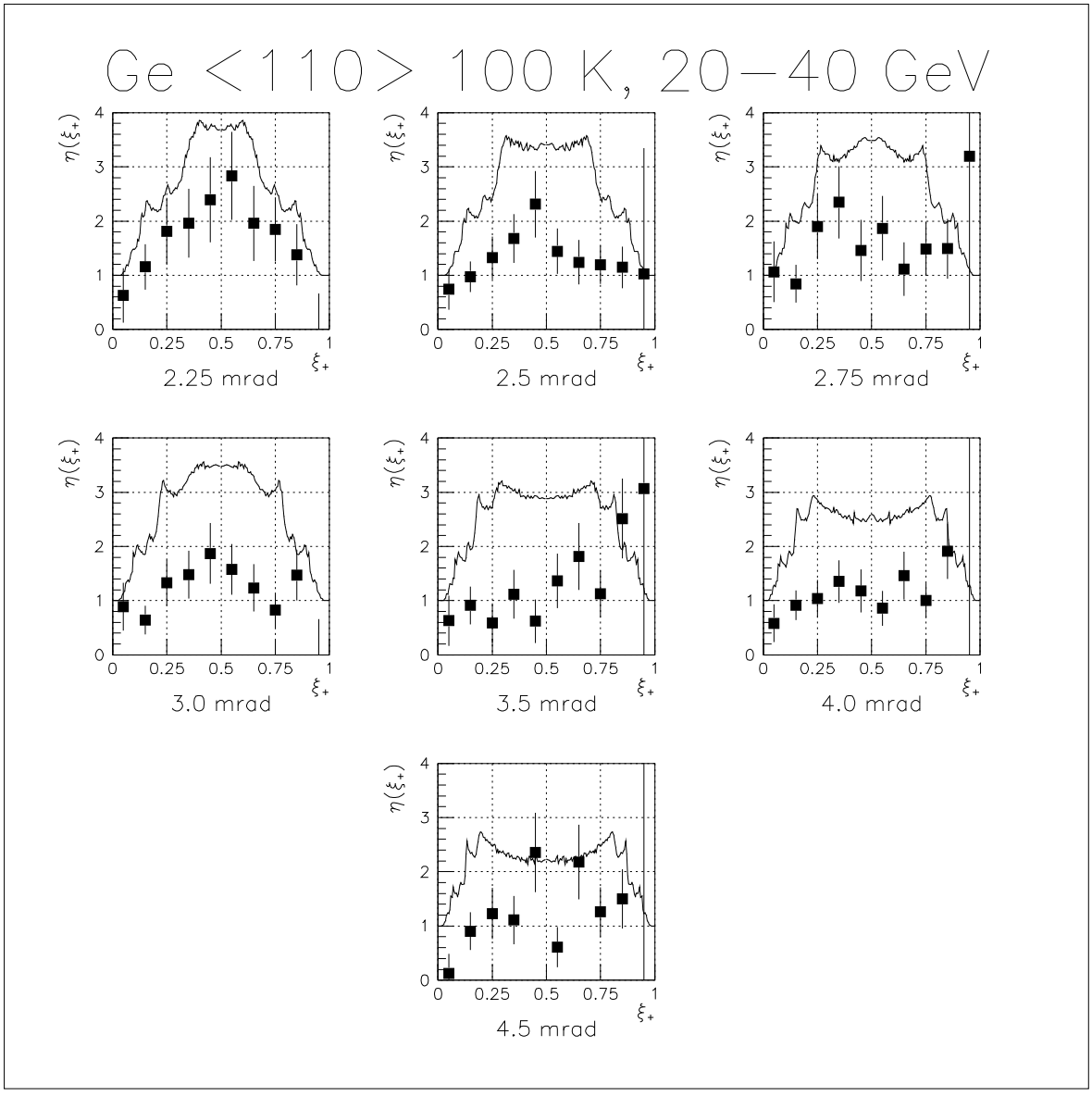

Figure 56: *The differential enhancement, $\eta(\xi_+)$, as a function of the relative positron energy, ξ_+. The photon energy is between 20 and 40 GeV and the direction of incidence is along the (110) plane in Ge for different angles, 2.25-4.5 mrad, to the $\langle 110 \rangle$ axis. The full-drawn curve is a calculation by Kononets using the semi-classical approximation [113], [67] and the filled squares are experimental points with error bars denoting the statistical uncertainty.*

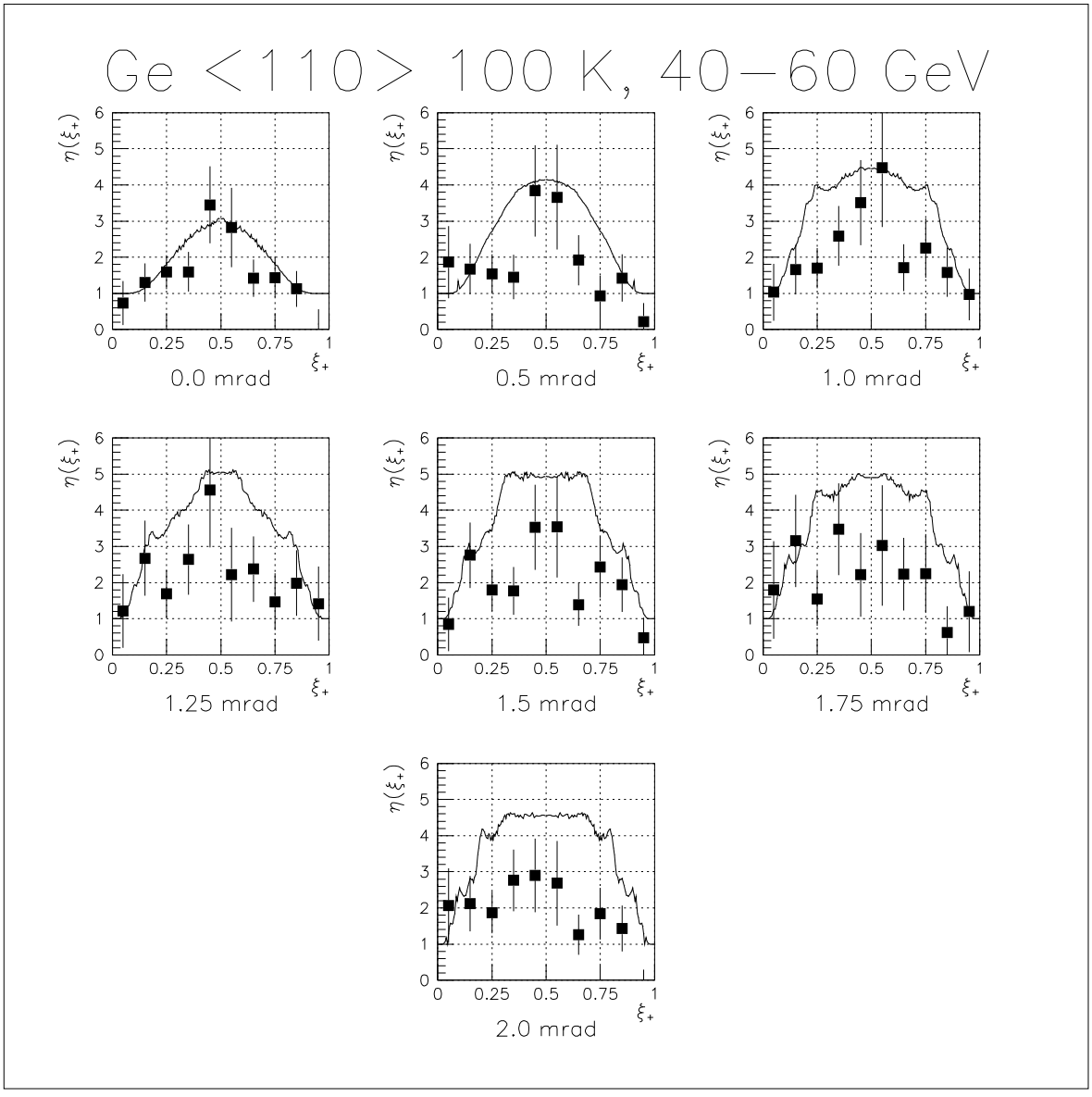

Figure 57: *The differential enhancement, $\eta(\xi_+)$, as a function of the relative positron energy, ξ_+. The photon energy is between 40 and 60 GeV and the direction of incidence is along the (110) plane in Ge for different angles, 0.0-2.0 mrad, to the $\langle 110 \rangle$ axis. The full-drawn curve is a calculation by Kononets using the semi-classical approximation [113], [67] and the filled squares are experimental points with error bars denoting the statistical uncertainty.*

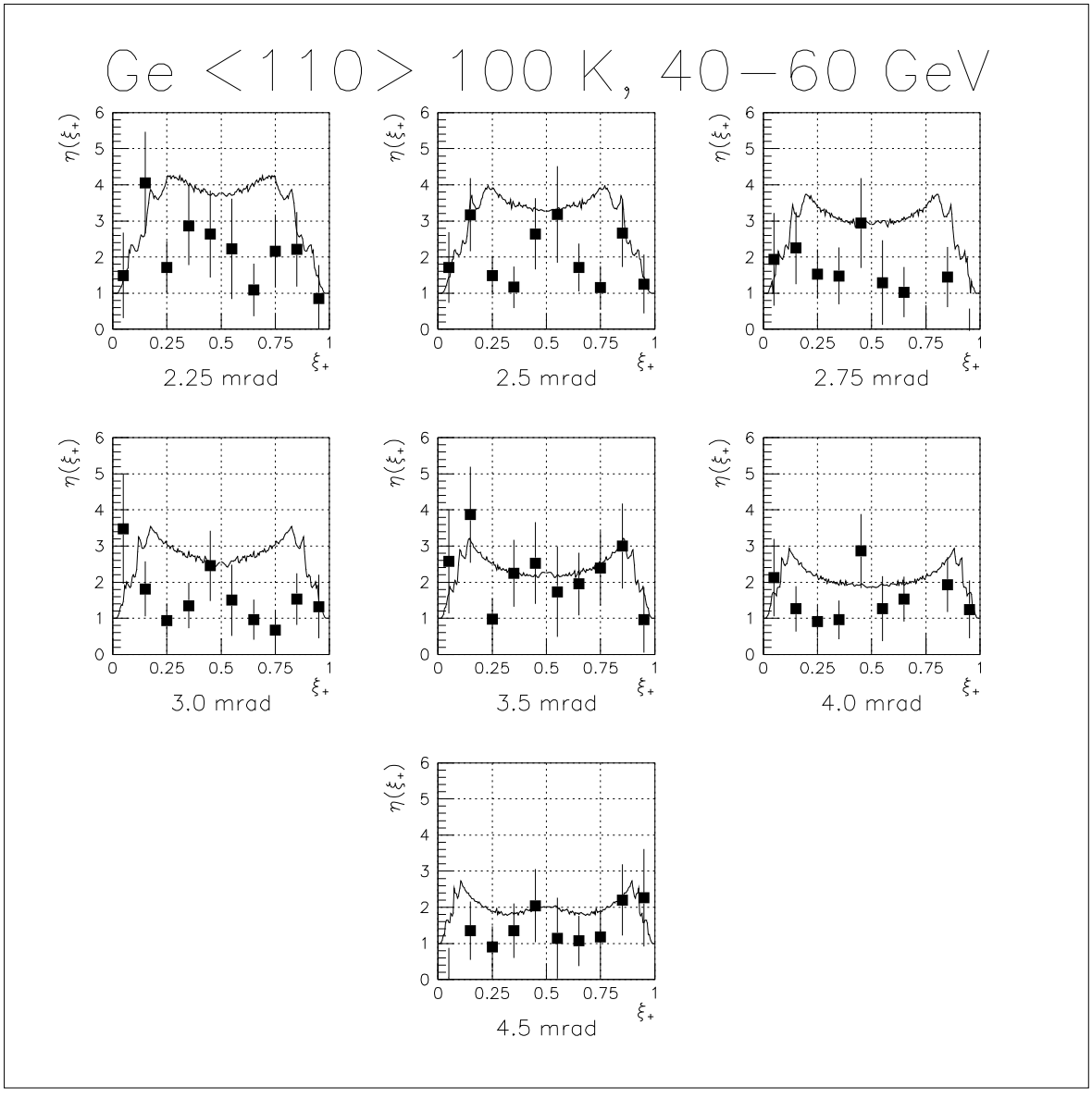

Figure 58: *The differential enhancement, $\eta(\xi_+)$, as a function of the relative positron energy, ξ_+. The photon energy is between 40 and 60 GeV and the direction of incidence is along the (110) plane in Ge for different angles, 2.25-4.5 mrad, to the $\langle 110 \rangle$ axis. The full-drawn curve is a calculation by Kononets using the semi-classical approximation [113], [67] and the filled squares are experimental points with error bars denoting the statistical uncertainty.*

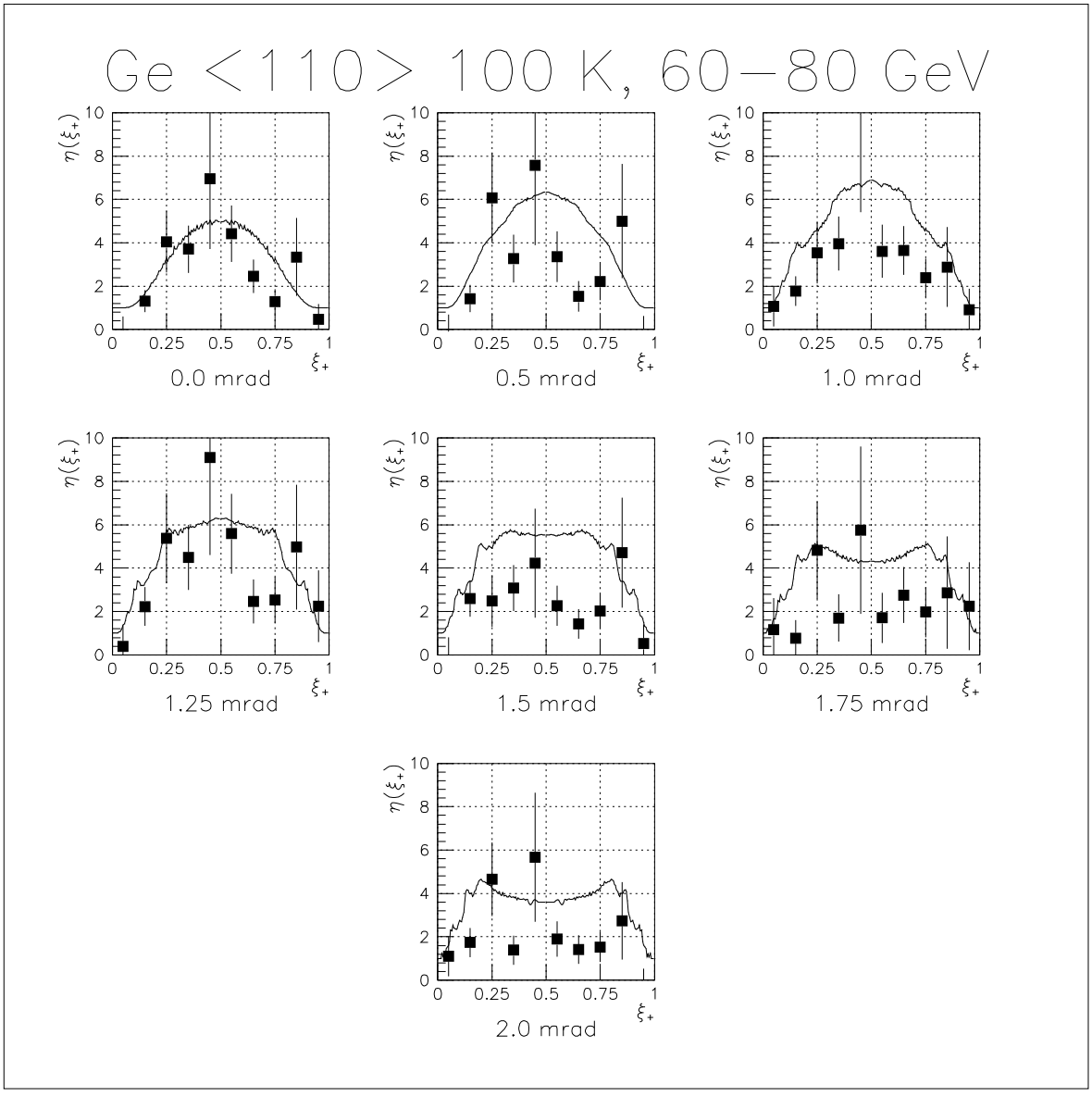

Figure 59: *The differential enhancement, $\eta(\xi_+)$, as a function of the relative positron energy, ξ_+. The photon energy is between 60 and 80 GeV and the direction of incidence is along the (110) plane in Ge for different angles, 0.0-2.0 mrad, to the $\langle 110 \rangle$ axis. The full-drawn curve is a calculation by Kononets using the semi-classical approximation [113], [67] and the filled squares are experimental points with error bars denoting the statistical uncertainty.*

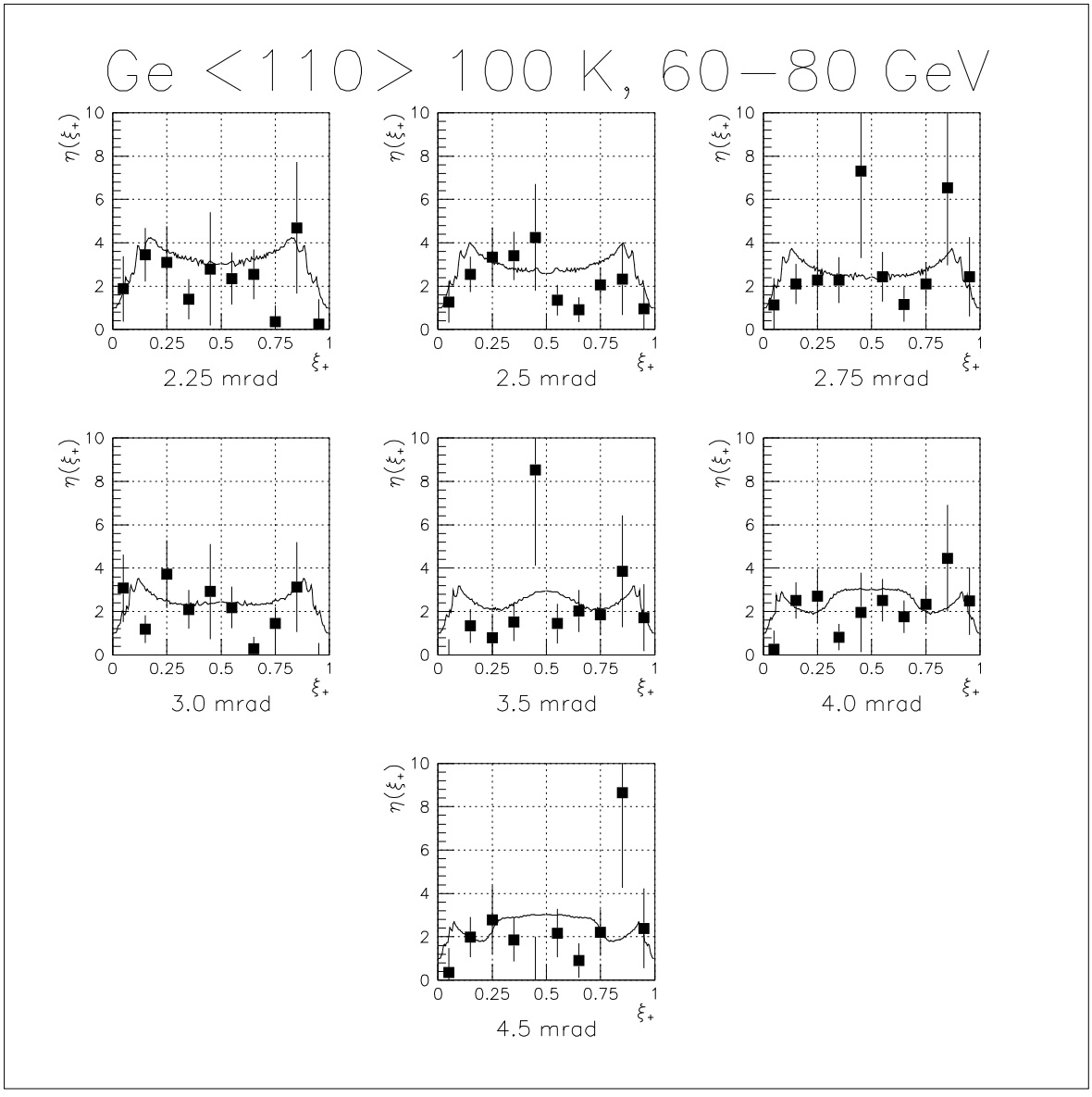

Figure 60: *The differential enhancement, $\eta(\xi_+)$, as a function of the relative positron energy, ξ_+. The photon energy is between 60 and 80 GeV and the direction of incidence is along the (110) plane in Ge for different angles, 2.25-4.5 mrad, to the $\langle 110 \rangle$ axis. The full-drawn curve is a calculation by Kononets using the semi-classical approximation [113], [67] and the filled squares are experimental points with error bars denoting the statistical uncertainty.*

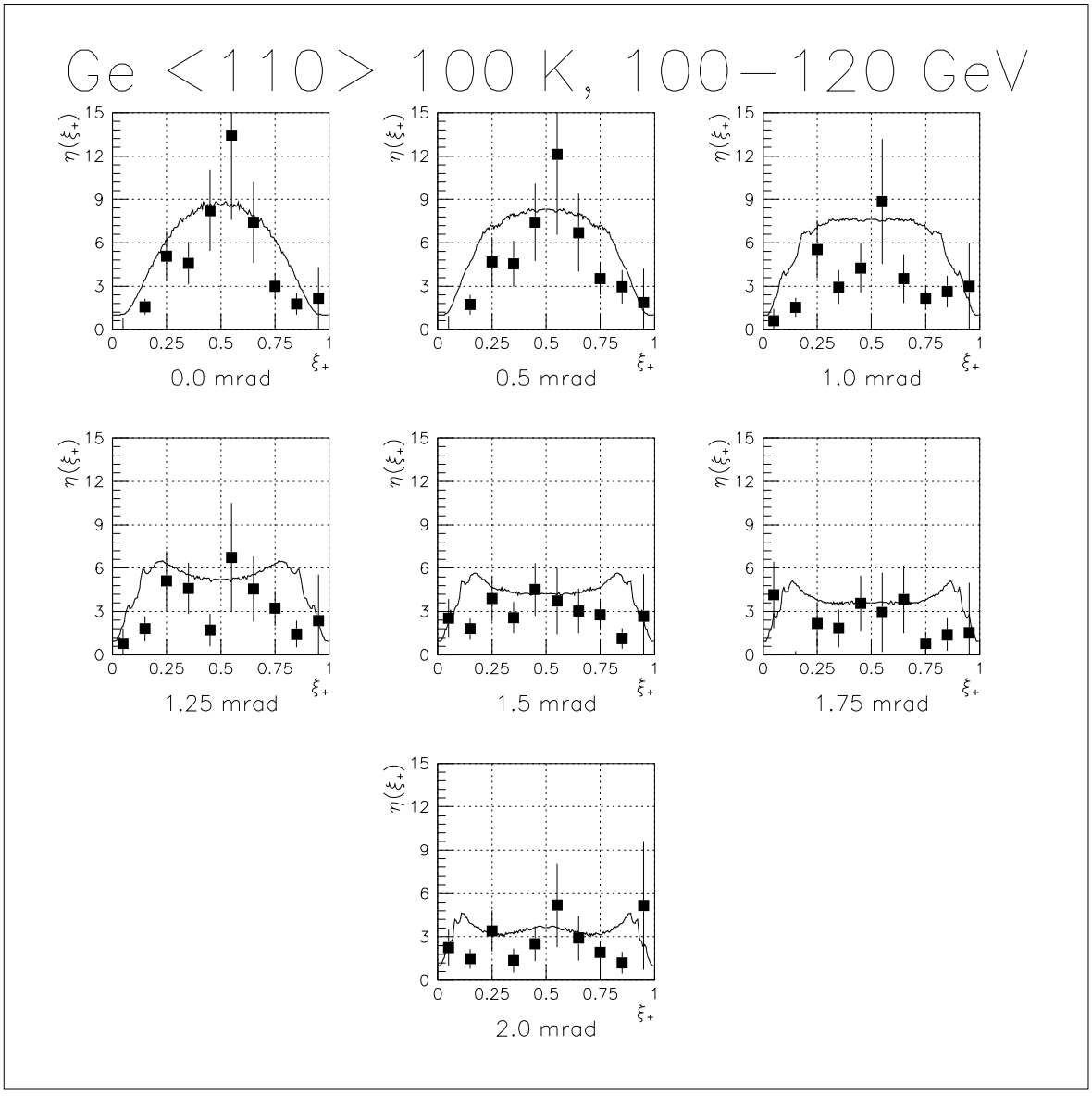

Figure 61: *The differential enhancement, $\eta(\xi_+)$, as a function of the relative positron energy, ξ_+. The photon energy is between 100 and 120 GeV and the direction of incidence is along the (110) plane in Ge for different angles, 0.0-2.0 mrad, to the $\langle 110 \rangle$ axis. The full-drawn curve is a calculation by Kononets using the semi-classical approximation [113], [67] and the filled squares are experimental points with error bars denoting the statistical uncertainty.*

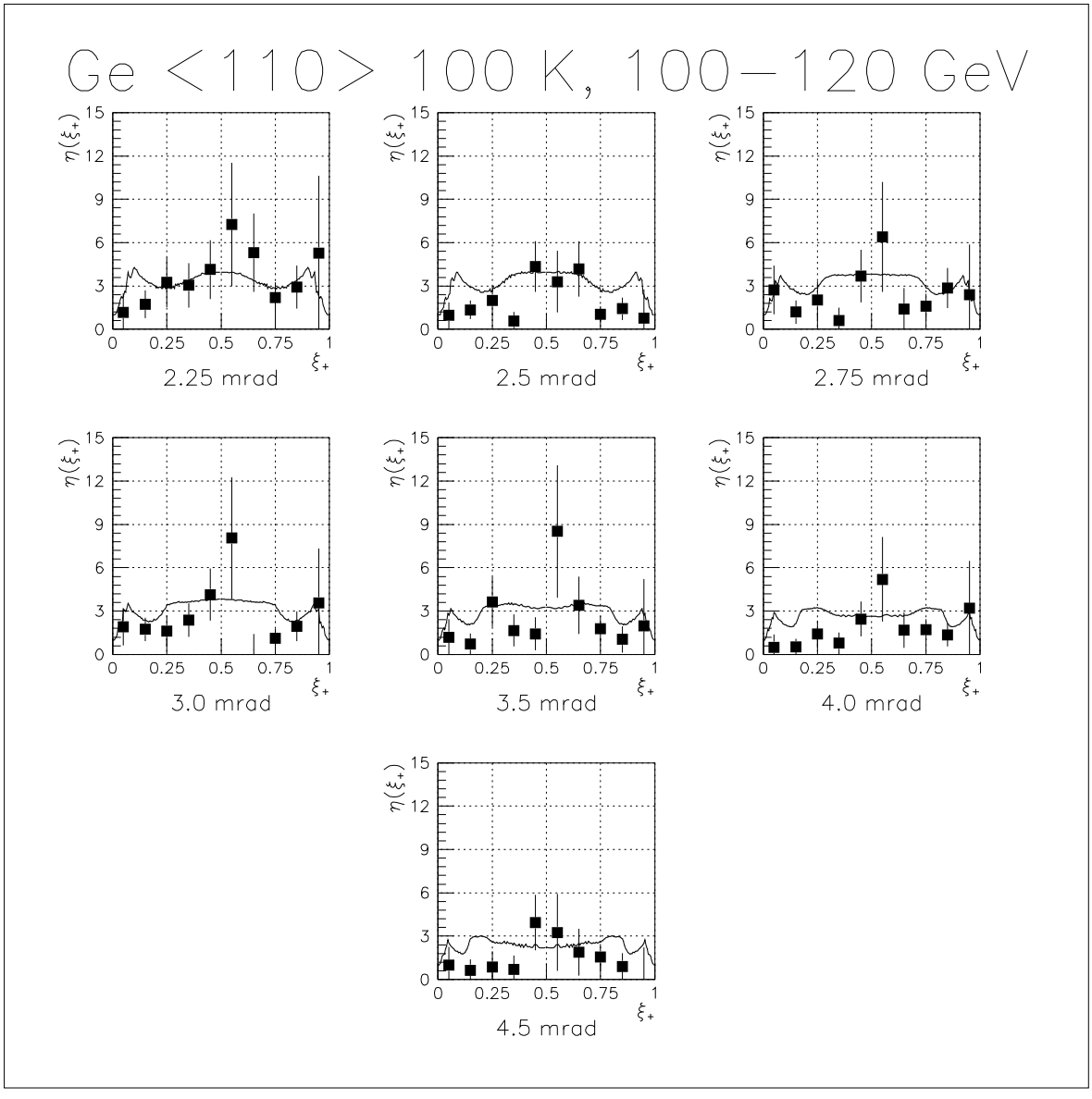

Figure 62: *The differential enhancement, $\eta(\xi_+)$, as a function of the relative positron energy, ξ_+. The photon energy is between 100 and 120 GeV and the direction of incidence is along the (110) plane in Ge for different angles, 2.25-4.5 mrad, to the $\langle 110 \rangle$ axis. The full-drawn curve is a calculation by Kononets using the semi-classical approximation [113], [67] and the filled squares are experimental points with error bars denoting the statistical uncertainty.*

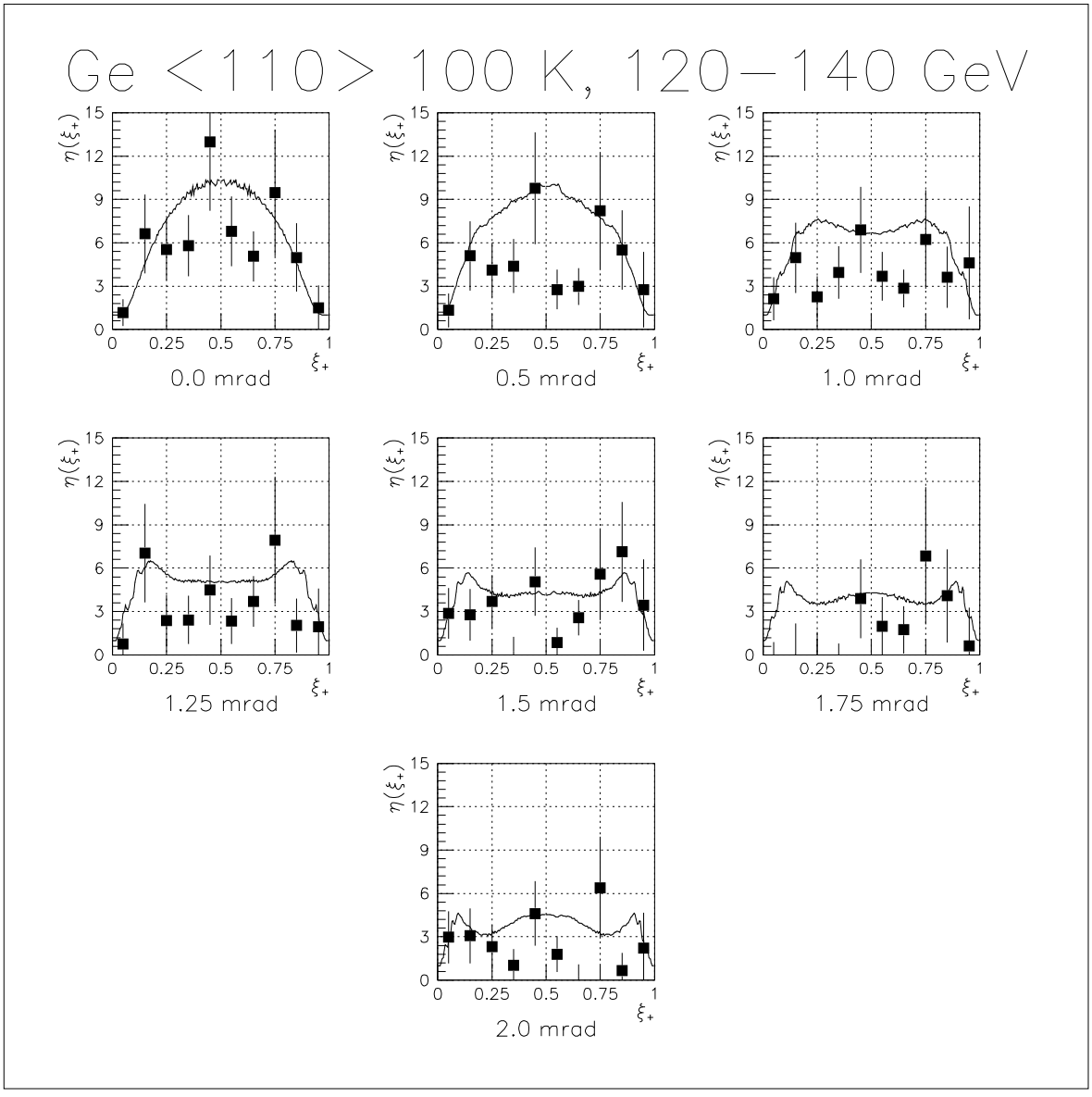

Figure 63: *The differential enhancement, $\eta(\xi_+)$, as a function of the relative positron energy, ξ_+. The photon energy is between 120 and 140 GeV and the direction of incidence is along the (110) plane in Ge for different angles, 0.0-2.0 mrad, to the $\langle 110 \rangle$ axis. The full-drawn curve is a calculation by Kononets using the semi-classical approximation [113], [67] and the filled squares are experimental points with error bars denoting the statistical uncertainty.*

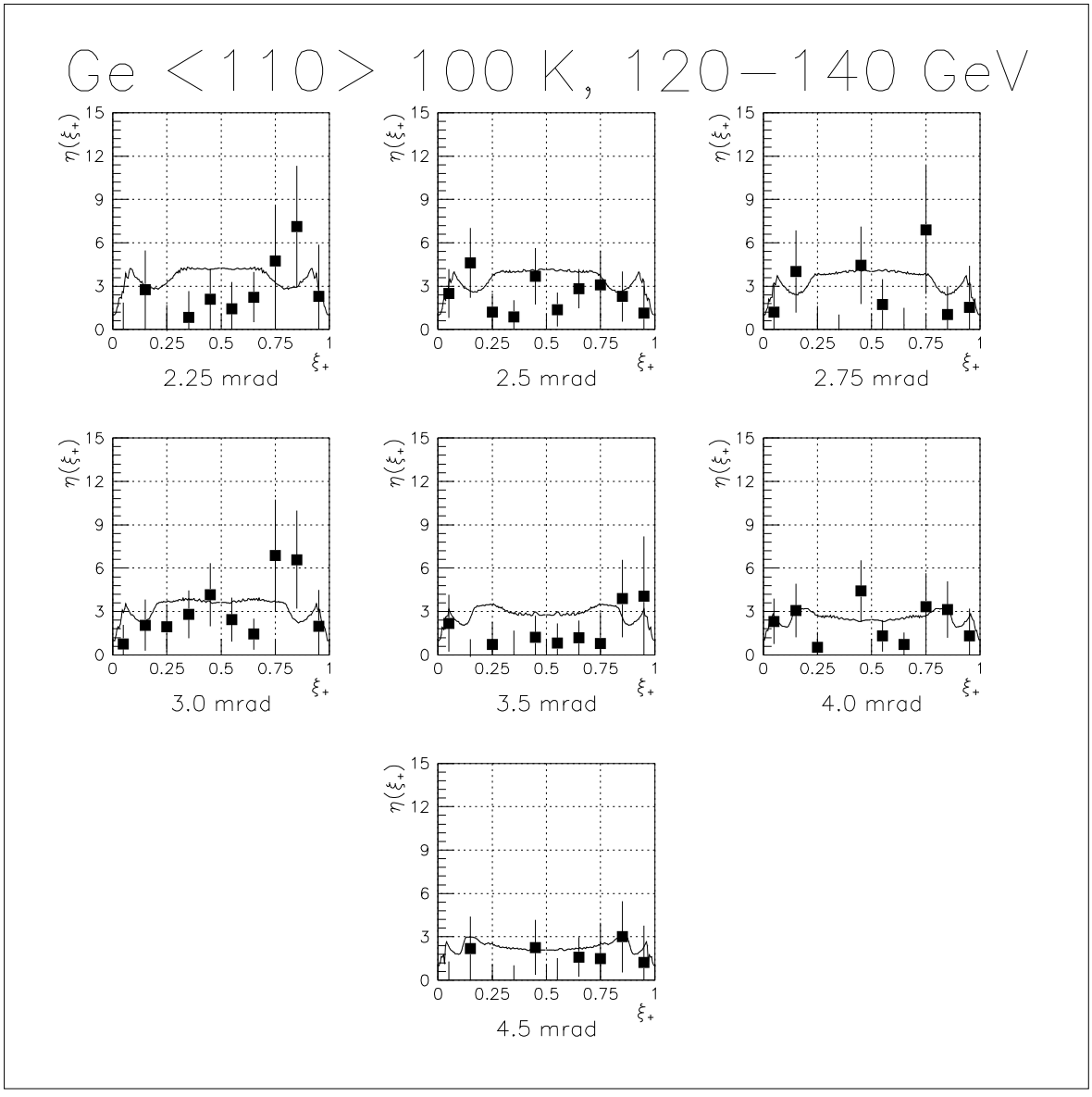

Figure 64: *The differential enhancement, $\eta(\xi_+)$, as a function of the relative positron energy, ξ_+. The photon energy is between 120 and 140 GeV and the direction of incidence is along the (110) plane in Ge for different angles, 2.25-4.5 mrad, to the $\langle 110 \rangle$ axis. The full-drawn curve is a calculation by Kononets using the semi-classical approximation [113], [67] and the filled squares are experimental points with error bars denoting the statistical uncertainty.*

D Details of the experimental setup, NA43

This appendix includes two figures showing, in greater detail than figure 11, the setup used in NA43 for the pair production experiments.

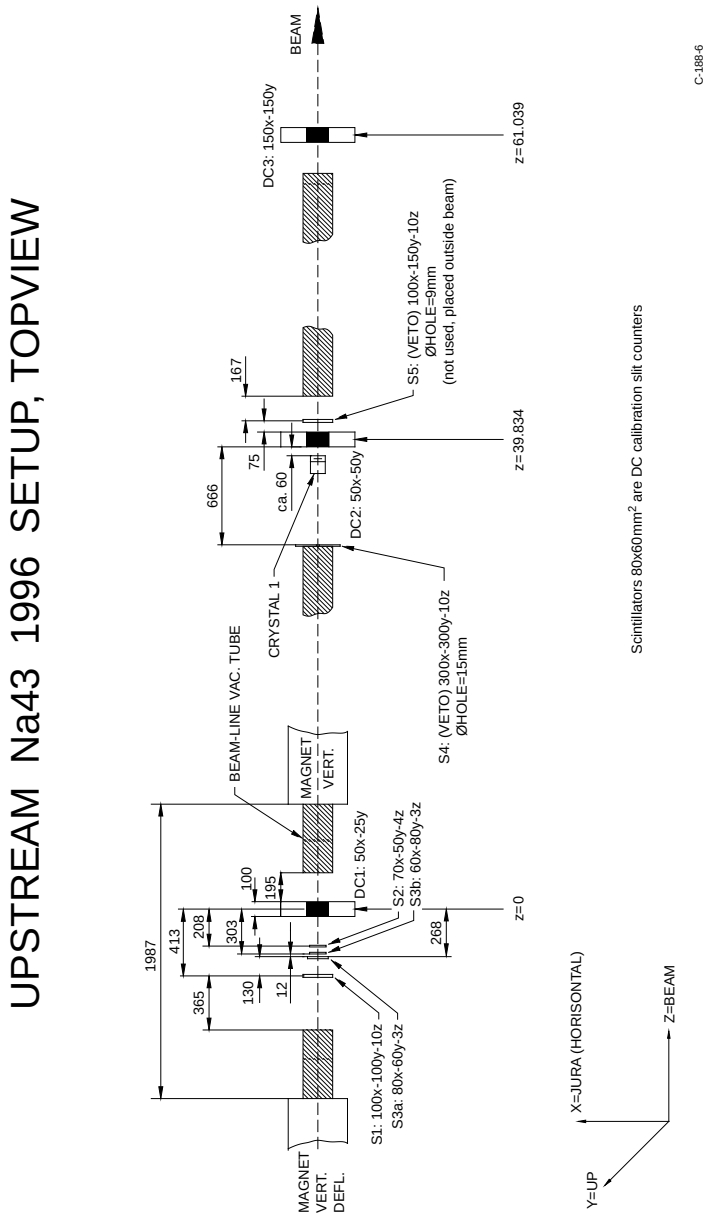

Figure 65: *Setup in the region upstream of the magnet B8.*

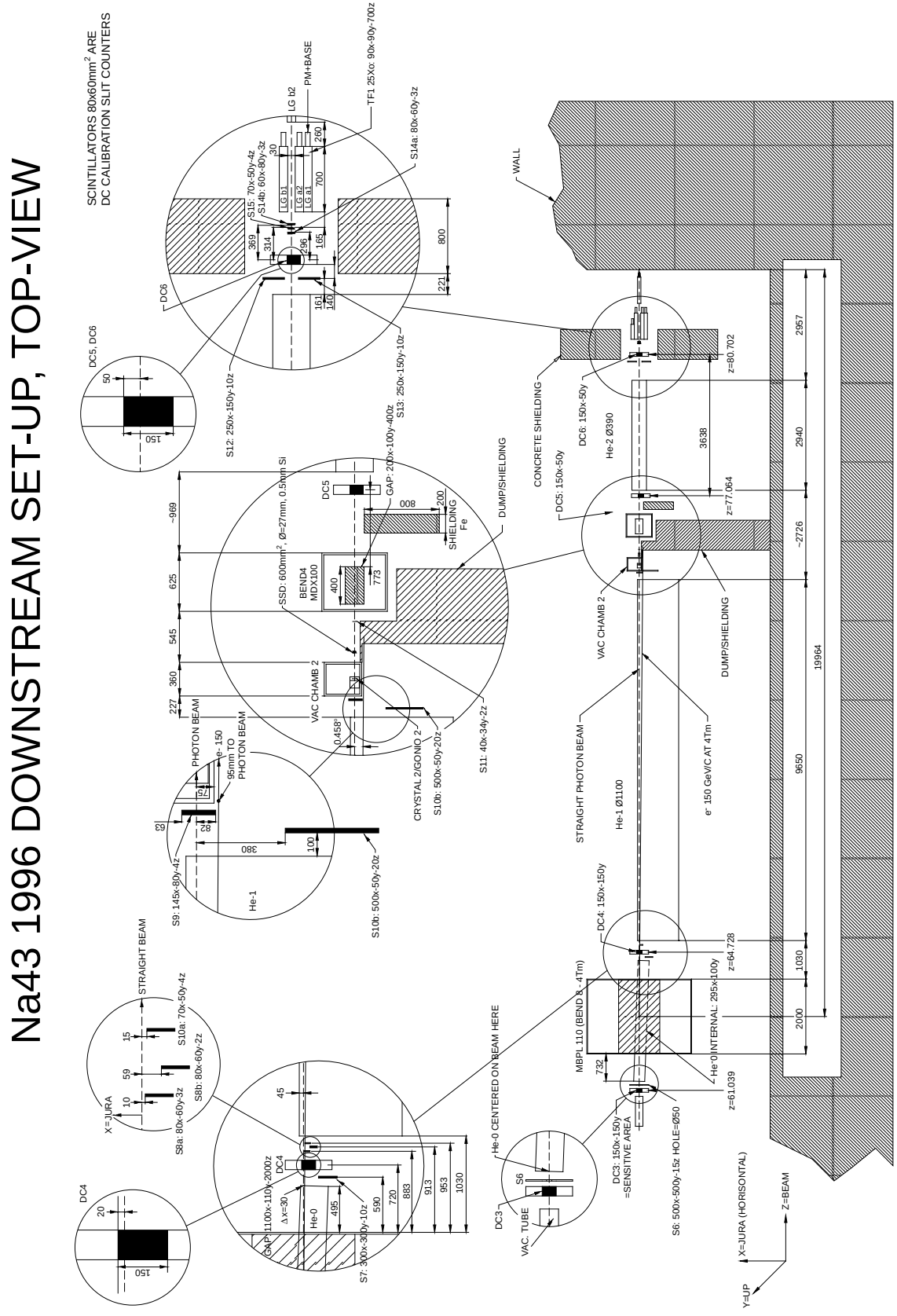

Figure 66: *Setup in the region downstream of the magnet B8.*

Part X
List of publications

The work presented has been published in some of the following papers and in the conference contributions: [92], [190], [191], [192]. Many of the remaining papers include experiments used for the Master's thesis: U. Mikkelsen - One- and two-electron processes in collisions with atoms and molecules, Institute of Physics and Astronomy, Aarhus University 1994 (unpublished).

1. D.M. Schrader, F.M. Jacobsen, N.P. Frandsen and U. Mikkelsen - Formation of Positronium Hydride, Phys. Rev. Lett. **69**, 57 (1992)
2. P. Hvelplund, H. Knudsen, U. Mikkelsen, E. Morenzoni, S.P. Møller, E. Uggerhøj and T. Worm - Ionization of helium and molecular hydrogen by slow antiprotons, J. Phys. B **27**, 925 (1994)
3. F.M. Jacobsen, N.P. Frandsen, H. Knudsen, U. Mikkelsen and D.M. Schrader - Single ionization of He, Ne and Ar by positron impact, J. Phys. B **28**, 4691 (1995)
4. F.M. Jacobsen, N.P. Frandsen, H. Knudsen and U. Mikkelsen - Non dissociative single ionization of molecular hydrogen by electron and positron impact, J. Phys. B **28**, 4675 (1995)
5. X. Altuna, M.P. Bussa, G. Carboni, B. Dehning, K. Elsener, A. Ferrari, G. Fidecaro, A. Freund, R. Guinand, M. Gyr, W. Herr, J. Klem, M. Laffin, L. Lanceri, U. Mikkelsen, S.P. Møller, W. Scandale, F. Tossello, E. Uggerhøj, G. Vuagnin, E. Weisse and S. Weisz - High efficiency multipass proton beam extraction with a bent crystal at the SPS, Phys. Lett. B **357**, 671 (1995)
6. H. Knudsen, U. Mikkelsen, K. Paludan, K. Kirsebom, S.P. Møller, E. Uggerhøj, J. Slevin, M. Charlton and E. Morenzoni - Ionization of atomic hydrogen by 30-1000 keV antiprotons, Phys. Rev. Lett. **74**, 4627 (1995)
7. H. Knudsen, U. Mikkelsen, K. Paludan, K. Kirsebom, S.P. Møller, E. Uggerhøj, J. Slevin, M. Charlton and E. Morenzoni - Nondissociative and dissociative Ionization of N_2, CO, CO_2 and CH_4 by 50-6000 keV antiprotons, J. Phys. B **28**, 3569 (1995)
8. I. Ben-Itzhak, V. Krishnamurthi, K.D. Carnes, H. Aliabadi, H. Knudsen and U. Mikkelsen - One and two electron processes in fast collisions between protons and hydrogen molecules, Nucl. Instr. Meth. B **99**, 104 (1995)
9. A. Baurichter, U. Mikkelsen, K. Kirsebom, R. Medenwaldt, S. P. Møller, E. Uggerhøj, T. Worm, K. Elsener, S. Ballestrero, P. Sona, J. Romano, C. Biino, R. Moore and Z.Z. Vilakazi - Enhancement of electromagnetic showers initiated by ultrarelativistic electrons in aligned thick germanium crystals, Nucl. Phys. B (Proc. Suppl.) **44**, 79 (1995)
10. S.P. Møller, E. Uggerhøj, H. Bluhme, H. Knudsen, U. Mikkelsen, K. Paludan, K. Kirsebom and E. Morenzoni - Measurement of the Barkas Effect around the stopping-power maximum for light and heavy targets, Nucl. Instr. Meth. B **122**, 162 (1996)
11. I. Ben-Itzhak, V. Krishnamurthi, K.D. Carnes, H. Aliabadi, H. Knudsen, U. Mikkelsen and B.D. Esry - Ionization and excitation of hydrogen molecules by fast proton impact, J. Phys. B **29**, L21 (1996)
12. K. Elsener, G. Fidecaro, M. Gyr, W. Herr, J. Klem, U. Mikkelsen, S.P. Møller, E. Uggerhøj, G. Vuagnin and E. Weisse - Proton Extraction from the CERN SPS using bent silicon crystals, Nucl. Instr. Meth. B **119**, 215 (1996)
13. R. Moore, M.A. Parker, A. Baurichter, K. Kirsebom, R. Medenwaldt, U. Mikkelsen, S.P Møller, E. Uggerhøj, T. Worm, N. Doble, K. Elsener, S. Ballestrero, P. Sona, V.M. Strakhovenko, C. Biino and Z.Z. Vilakazi - Measurement of pair-production by high energy photons in an aligned tungsten crystal, Nucl. Instr. Meth. B **119**, 149 (1996)

14. A. Baurichter, U. Mikkelsen, K. Kirsebom, R. Medenwaldt, S. P. Møller, E. Uggerhøj, T. Worm, K. Elsener, S. Ballestrero, P. Sona, J. Romano, C. Biino, R. Moore and Z.Z. Vilakazi - Enhancement of electromagnetic showers initiated by ultrarelativistic electrons in aligned thick germanium crystals, Nucl. Instr. Meth. B **119**, 143 (1996)

15. K. Kirsebom, R. Medenwaldt, U. Mikkelsen, S.P Møller, K. Paludan, E. Uggerhøj, T. Worm, K. Elsener, S. Ballestrero, P. Sona, J. Romano, S.H. Connell, J.P.F. Sellschop, R.O. Avakian, A.E. Avetisian and S.P. Taroian - Experimental Investigation of photon multiplicity and radiation cooling for 150 GeV electrons/positrons traversing diamond and Si crystals, Nucl. Instr. Meth. B **119**, 79 (1996)

16. A. Baurichter, K. Kirsebom, R. Medenwaldt, S.P. Møller, T. Worm, E. Uggerhøj, C. Biino, M. Clément, N. Doble, K. Elsener, L. Gatignon, P. Grafström, U. Mikkelsen, A. Freund, Z. Vilakazi, P. Siffert and M. Hage-Ali - New results from the CERN-SPS beam deflection experiments with bent crystals, Nucl. Instr. Meth. B **119**, 172 (1996)

17. S.P. Møller, E. Uggerhøj, H. Bluhme, H. Knudsen, U. Mikkelsen, K. Paludan, K. Kirsebom and E. Morenzoni - Direct measurements of the stopping-power in light and heavy targets, acc. for publ. in Phys. Rev. A, 1997

18. H. Bluhme, H. Knudsen, U. Mikkelsen, K. Paludan, K. Kirsebom, S.P. Møller, E. Uggerhøj and E. Morenzoni - Single, double and triple ionization of Ne, Ar, Kr and Xe by 30-1000 keV $\overline{\mathrm{p}}$ impact, acc. for publ. in J. Phys. B, 1997

19. H. Bluhme, H. Knudsen, U. Mikkelsen, K. Paludan, K. Kirsebom, S.P. Møller, E. Uggerhøj and E. Morenzoni - Non-dissociative and dissociative ionization of O_2 molecules by impact of 40-1000 keV antiprotons, acc. for publ. in J. Phys. B, 1997

20. K. Paludan, G. Laricchia, P. Ashley, V. Kara, J. Moxom, H. Bluhme, H. Knudsen, U. Mikkelsen, S.P. Møller, E. Uggerhøj and E. Morenzoni - Ionization of the rare gases by particle/antiparticle impact, acc. for publ. in J. Phys. B, 1997

21. I. Ben-Itzhak, E. Wells, V. Krishnamurthi, K.D. Carnes, H. Aliabadi, U. Mikkelsen, O.L. Weaver and B.D. Esry - An experimental method for evaluating the H_2 and D_2 contamination levels in a HD bottle, Nucl. Instr. Meth. B **129**, 117 (1997)

22. C. Biino, M. Clément, N. Doble, K. Elsener, L. Gatignon, P. Grafström, U. Mikkelsen, K. Kirsebom, S.P. Møller, E. Uggerhøj, T. Worm and A. Freund - Deflection of 200 GeV/c and 450 GeV/c positively charged particles in a bent germanium crystal, Phys. Lett. B **403**, 163 (1997)

23. A. Baurichter, K. Kirsebom, Yu. V. Kononets, R. Medenwaldt, U. Mikkelsen, S.P. Møller, T. Worm, E. Uggerhøj, K. Elsener, S. Ballestrero, P. Sona, J. Romano, S.H. Connell, J.P.F. Sellschop, R.O. Avakian, A.E. Avetisian and S.P. Taroian - Radiation emission and its influence on motion of multi-GeV electrons and positrons in strong crystalline fields, subm. to Phys. Rev. Lett., 1997

24. G. Arduini, C. Biino, M. Clément, K. Cornelis, N. Doble, K. Elsener, G. Ferioli, G. Fidecaro, L. Gatignon, P. Grafström, M. Gyr, W. Herr, J. Klem, U. Mikkelsen, E. Weisse, S.P. Møller, E. Uggerhøj, A. Freund, P. Keppler, J. Major and A. Taratin - Deflection and extraction of Pb ions up to 33 TeV/c by a bent silicon crystal, subm. to Phys. Rev. Lett. 1997

25. C. Biino, M. Clément, N. Doble, K. Elsener, L. Gatignon, P. Grafström, U. Mikkelsen, K. Kirsebom, S.P. Møller and E. Uggerhøj - Restricted energy-loss of fully stripped Pb ions at 33 TeV/c, in preparation

Part XI
Acknowledgments

The presented experimental work would not have been possible without the help of: Poul Aggerholm, R. Allegrini, Sergio Ballestrero, Arnd Baurichter, G. Bertuol, Cristina Biino, Alain Bonifas, Georges Caniac, Per Christensen, Michel Clément, Simon Connell, Niels Doble, Konrad Elsener, Andreas Freund, Lau Gatignon, Per Grafström, Kim Kirsebom, Søren Pape Møller, Patrice Pierre, Thierry Reynes, J.P.F. Sellschop, Pietro Sona, G. Stevenson, Erik Uggerhøj, Zeblon Vilakazi and Torben Worm along with the meticulous and enthusiastic work of the SL-EA group as well as the steady supply of beam from the CERN SPS.

A special thank to Erik Uggerhøj, Konrad Elsener and the rest of the SL-EA physicists for providing a nice framework for working and continuous interest, advice and encouragement in the process and to Yuri Kononets[35] and Kim Kirsebom for numerous enlightening discussions on theory and analysis.

I have furthermore benefitted from the theoretical insights of Jens Ulrik Andersen, Jens Lindhard and Allan Sørensen.

I would like to use this opportunity to thank all of you for your contributions!

[35] Appendix B leans heavily on his unpublished note: [62]

List of Figures

References

[1] J. Stark, Physik. Z. **13**, 973 (1912)

[2] J. Lindhard, Mat. Fys. Medd. Dan. Vid. Selsk. **34**, 1 (1965)

[3] A.H. Sørensen and E. Uggerhøj, Nucl. Sci. Appl. **3**, 147 (1989)

[4] J.U. Andersen, E, Bonderup and R.H. Pantell, Ann. Rev. Nucl. Part. Sci. **33**, 453 (1983)

[5] M.A. Kumakhov and Ch.G. Trikalinos, Phys. Stat. Sol. (b) **99**, 449 (1980)

[6] G. Molière, Z. Naturforsch. A **2**, 133 (1947)

[7] P.A. Doyle and P.S. Turner, Acta Cryst. A **24**, 390 (1968)

[8] J.U. Andersen *et al.*, Nucl. Instr. Meth. **194**, 209 (1982)

[9] D. Waasmaier and A. Kirfel, Acta Cryst. A **51**, 416 (1995)

[10] N. Bohr, Mat. Fys. Medd. Dan. Vid. Selsk. **18**, 1 (1948)

[11] P. Lervig, J. Lindhard and V. Nielsen, Nucl Phys. A **96**, 481 (1967)

[12] J.F. Bak *et al.*, Nucl. Phys. B **242**, 1 (1984)

[13] S.K. Andersen *et al.*, Nucl Phys. B **167**, 1 (1980)

[14] E. Uggerhøj, Phys. Scripta **28**, 331 (1983)

[15] J.F. Bak *et al.*, Nucl. Phys. B **302**, 525 (1988)

[16] J.U. Andersen *et al.*, Nucl. Instr. Meth. B **33**, 34 (1988)

[17] R.M. Barnett *et al.*, Phys. Rev. D **54**, Review of Particle Physics (1996)

[18] M. Abramowitz and I. Stegun, eds. - Handbook of mathematical functions, Dover, 1972

[19] V.M. Biryukov *et al.*, Physics-Uspekhi **37**, 937 (1994)

[20] V.M. Biryukov *et al.*, Nucl. Instr. Meth. B **86**, 245 (1994)

[21] D.S. Gemmell, Revs. Mod. Phys. **46**, 129 (1974)

[22] G. Boebinger, A. Passner and J. Bevk, Scientific American, 34, June 1995

[23] J. Schwinger, Phys. Rev. **75**, 1912 (1949)
J. Schwinger, Phys. Rev. **82**, 664 (1951)
J. Schwinger, Phys. Rev. D **7**, 1696 (1973)

[24] M.A. Kumakhov, Phys. Lett. A **57**, 17 (1976)
M.A. Kumakhov, Sov. Phys. JETP **45**, 781 (1977)

[25] J. Bak *et al.*, Nucl. Phys. B **254**, 491 (1985)
J. Bak, in: Relativistic Channeling, eds. R.A. Carrigan and J.A. Ellison, Plenum, 1987, p. 281
J. Bak, PhD. thesis, Aarhus University, unpublished, 1984

[26] F. Fujimoto and K. Komaki, in: Relativistic Channeling, eds. R.A. Carrigan and J.A. Ellison, Plenum, 1987, p. 239

[27] O. Klein, Zeitschr. f. Phys. **53**, 11 (1928)

[28] F. Sauter, Zeitschr. f. Phys. **69**, 742 (1931);
F. Sauter, Zeitschr. f. Phys. **73**, 547 (1931)

[29] C.D. Anderson, Science **76**, 238 (1932)

[30] R.P. Feynman, Phys. Rev. **74**, 939 (1948)

[31] O. Klein and Y. Nishina, Zeitschr. f. Phys. **52**, 853 (1929)

[32] H. Bethe and W. Heitler, Proc. Roy. Soc. A **146**, 83 (1934)

[33] E.J. Williams, Mat. Fys. Medd. Dan. Vid. Selsk. **13**, 4 (1965)

[34] J.P. Blewett, Phys Rev. **69**, 87 (1946)

[35] F. Elder, R. Langmuir and H. Pollock, Phys Rev. **74**, 52 (1948)

[36] T. Erber, Rev. Mod. Phys., **38**, 626 (1966)

[37] W. Tsai and T. Erber, Phys. Rev. D, **10**, 492 (1974)
W. Tsai and T. Erber, Phys. Rev. D, **12**, 1132 (1975)

[38] J. Schwinger, Proc. Nat. Acad. Sci. **40**, 132 (1954)

[39] N.P. Klepikov, Zh. Eksp. Teor. Fiz., **26**, 19 (1954); only available in russian

[40] V.N. Baier and V.M Katkov, Sov. Phys. JETP, **26**, 854 (1968)

[41] F.J. Dyson and H. Überall, Phys. Rev. **99**, 604 (1955)

[42] G.D. Palazzi, Rev. Mod. Phys. **40**, 611 (1968)

[43] J.C. Kimball, N. Cue, L.M. Roth and B.B. Marsch, Phys. Rev. Lett. **50**, 950 (1983)
J.C. Kimball and N. Cue, Phys. Rev. Lett. **52**, 1747 (1984)

[44] V.N. Baier, V.M. Katkov and V.M. Strakhovenko, Phys. Lett. A **104**, 231 (1984)
V.N. Baier, V.M. Katkov and V.M. Strakhovenko, Sov. Phys Dokl. **30**, 474 (1985)

[45] V.N. Baier, V.M. Katkov and V.M. Strakhovenko, Phys. Lett. A **109**, 179 (1985)

[46] V.N. Baier, V.M. Katkov and V.M. Strakhovenko, Sov. Phys. Usp. **32**, 972 (1989)

[47] J. Lindhard, Phys. Rev. A **43**, 6032 (1991)

[48] A.K. Harding, M.G. Baring and P.L. Gonthier, Astr. Astrophys. Suppl. Ser. **120**, 111 (1996)
R.A. Araya and A.K. Harding, Astrophys. Journ. **463**, L33 (1996)
D.J. Helfand, R.H. Becker and R.L. White, Astrophys. Journ. **453**, 741 (1995)

[49] C. Graziani, A.K. Harding and R. Sina, Phys. Rev. D **51**, 7097 (1995)

[50] W. Greiner, B. Müller and J. Rafelski - Quantum Electrodynamics of Strong Fields, Springer-Verlag, 1985

[51] A. Schäfer, Nucl. Instr. Meth. B **119**, 48 (1996)

[52] J. Maddox, Nature **335**, 293 (1988)

[53] G. Bassompierre *et al.*, Europhys. Lett. **22**, 239 (1993)
G. Bassompierre *et al.*, Phys. Lett. B **355**, 585 (1995)

[54] I. Ahmad *et al.*, Phys. Rev. Lett. **78**, 618 (1997)

[55] C.J. Joshi and P.B. Corkum, Physics Today, 36, Jan. 1995

[56] V.B. Berestetskii, E.M. Lifshitz and L.P. Pitaevskii - Relativistic Quantum Theory, Pergamon Press, 1971

[57] J.D. Jackson - Classical Electrodynamics, John Wiley, 1975

[58] A.H. Sørensen, Proc. NATO ASI **255**, 91, Plenum, 1991, reprinted in Nucl. Instr. Meth. B **119**, 1 (1996)

[59] M.L. Ter-Mikaelian - High-Energy Electromagnetic Processes in Condensed Media, Wiley Interscience, 1972

[60] V.N. Baier, V.M. Katkov and V.M. Strakhovenko, Nucl. Sci. Appl. **3**, 245 (1989), topical issue, ed. E. Uggerhøj
V.N. Baier, V.M. Katkov and V.M. Strakhovenko, Nucl. Instr. Meth. B **16**, 5 (1986)
V.N. Baier, V.M. Katkov and V.M. Strakhovenko, Nucl. Instr. Meth. B **34**, 521 (1988)
V.N. Baier, V.M. Katkov and V.M. Strakhovenko, Phys. Lett. A **109**, 179 (1985)

[61] W. Heitler - The quantum theory of radiation, Dover, 1954

[62] Yu.V. Kononets - The Basic QED Processes in Strong Crystalline Fields, 1996, unpublished

[63] P. Sona, private communication, 1996

[64] V.N. Baier, V.M. Katkov and V.M. Strakhovenko, Phys. Lett. A **117**, 251 (1986)

[65] J.C. Kimball and N. Cue, Phys. Rep. **125**, 69 (1985)

[66] V.V. Tikhomirov, Phys. Lett. A **125**, 411 (1987)
X. Artru, Phys. Lett. A **128**, 302 (1988)

[67] Yu.V. Kononets, private communication, 1996-97

[68] J. Augustin, A. Schäfer and W. Greiner, Phys. Rev. A **51**, 1367 (1995)
J. Klenner, J. Augustin, A. Schäfer and W. Greiner, Phys. Rev. A **50**, 1019 (1994)

[69] Yu.V. Kononets, Nucl. Instr. Meth. B **33**, 22 (1988)

[70] A.H. Sørensen, in: Relativistic Channeling, eds. R.A. Carrigan and J.A. Ellison, Plenum, 1987, p. 331

[71] A. Baurichter *et al.*, submitted to Phys. Rev. Lett. (1997)

[72] V.N. Baier, V.M. Katkov and V.M. Strakhovenko, Nucl. Instr. Meth. B **34**, 521 (1988)

[73] R. Medenwaldt *et al.*, Phys. Lett. B **281**, 153 (1992)

[74] V.N. Baier, V.M. Katkov and V.M. Strakhovenko, Nucl. Instr. Meth. B **69**, 258 (1992)

[75] A. Belkacem *et al.*, Phys. Lett. B **177**, 211 (1986)

[76] R. Medenwaldt *et al.*, Phys. Lett. B **242**, 517 (1990)

[77] H. Bilokon *et al.*, Nucl. Instr. Meth. **204**, 299 (1983)

[78] Yu.V. Kononets and I.S. Tupitsyn, Sov. Phys. JETP Lett. **59**, 516 (1994)

[79] V.N. Baier, V.M. Katkov and V.M. Strakhovenko, Nucl. Instr. Meth. B **35**, 21 (1988)

[80] L.D. Landau and I.Ya. Pomeranchuk, Dokl. Akad. Nauk USSR **92**, 535, 735 (1953)

[81] E. Konishi *et al.*, J. Phys. G **17**, 719 (1991)
T. Stanev *et al.*, Phys. Rev. D **25**, 1291 (1982)

[82] P.L. Anthony *et al.*, Phys. Rev. Lett. **75**, 1949 (1995)

[83] A.E. Chudakov, Izw. Akad. Nauk USSR **19**, 651 (1955)

[84] G. Yekutieli, Nuovo Cimento **6**, 1381 (1957)

[85] A. Belkacem *et al.*, Phys. Rev. Lett. **54**, 2667 (1985)

[86] R. Medenwaldt *et al.*, Phys. Rev. Lett. **63**, 2827 (1989)

[87] R. Medenwaldt *et al.*, Phys. Lett. B **227**, 483 (1989)

[88] R. Medenwaldt *et al.*, Phys. Lett. B **260**, 235 (1991)

[89] R. Medenwaldt *et al.*, Nucl. Instr. Meth. B **103**, 139 (1995)

[90] R. Moore, Ph.D. Thesis, University of Cambridge, 1996, unpublished

[91] R. Moore, *et al.*, Nucl. Instr. Meth. B **119**, 149 (1996)

[92] K. Kirsebom, *et al.*, Proc. Int. Conf. on Atomic Collisions in Solids, Beijing 1997

[93] G. Charpak, F. Sauli and W. Duinker, Nucl. Instr. Meth. **108**, 413 (1973)
F. Sauli, CERN-report 77-09 (1977)

[94] U. Becker, in: F. Sauli - Instrumentation in High Energy Physics, World Scientific, 2. ed., 1993

[95] U. Amaldi, Phys. Scr. **23**, 409 (1981)

[96] J.F. Bak *et al.*, Phys. Lett. B **213**, 242 (1988)

[97] A. Belkacem *et al.*, Nucl. Instr. Meth. B **13**, 9 (1986)

[98] J.F. Bak *et al.*, Phys. Lett. B **202**, 615 (1988)

[99] X. Artru *et al.*, Phys. Lett. B **313**, 483 (1993)
X. Artru *et al.*, Proc. Int. Symp. Rad. Rel. Electr. Per. Struct., Tomsk 1993, 149, eds. Yu.L. Pivovarov, A.P. Potylitsin

[100] N.F. Shul'ga, V.I. Truten and V.V. Syshchenko, Nucl. Instr. Meth. B **119**, 55 (1996)

[101] K. Kirsebom *et al.*, Nucl. Instr. Meth. B **119**, 79 (1996)

[102] V.G. Baryshevsky and I.Ya. Dubovskaya, Phys. Lett. A **62**, 45 (1977)

[103] Yu.V. Kononets and V.A. Ryabov, JETP Lett. **48**, 333 (1988)

[104] Yu.V. Kononets and V.A. Ryabov, Nucl. Instr. Meth. B **48**, 269 (1990)
Yu.V. Kononets and V.A. Ryabov, Nucl. Instr. Meth. B **48**, 274 (1990)

[105] M. Rzepka *et al.*, Nucl. Instr. Meth. B **90**, 186 (1994)

[106] Yu.N. Adischev *et al.*, Sov. Phys. JETP Lett., **33**, 462 (1981)

[107] U. Mikkelsen, Progress Report, Aarhus University, unpublished (1995)

[108] N. Cabibbo *et al.*, Phys. Rev. Lett. **9**, 270 (1962)
G. Barbiellini *et al.*, Nuovo Cimento **28**, 435 (1963)
N. Cabibbo *et al.*, Nuovo Cimento **27**, 979 (1963)

[109] R.O. Avakian *et al.*, Nucl. Instr. Meth. A **357**, 238 (1995)
R.O. Avakian *et al.*, Sov. Phys. JETP Lett., **54**, 259 (1991)

[110] K. Ispirian, private communication, 1995

[111] A. Belkacem *et al.*, Phys. Rev. Lett. **53**, 2371 (1984)
A. Belkacem *et al.*, Phys. Rev. Lett. **54**, 852 (1985); correction

[112] A. Belkacem *et al.*, Phys. Rev. Lett. **58**, 1196 (1987)

[113] Yu.V. Kononets and I.S. Tupitsyn, Sov. Phys. JETP Lett., **57**, 151 (1993)

[114] K. Piotrzkowski, Nucl. Instr. Meth. B **119**, 253 (1996)

[115] K. Elsener, *et al.*, Nucl. Instr. Meth. B **119**, 215 (1996)

[116] J. Klem *et al.*, SL-MD note 204, unpublished

[117] P.L. Frabetti *et al.* (E687 Coll.), Nucl. Instr. Meth. A **329**, 62 (1993)

[118] X. Artru *et al.*, Nucl. Instr. Meth. B **119**, 246 (1996)

[119] P.L. Frabetti *et al.* (E687 Coll.), Phys. Lett. B **370**, 222 (1996)

[120] P. Kaspar, private communication with K. Elsener, 1997

[121] A. Schäfer *et al.*, J. Phys. G **16**, L131 (1990)

[122] V.N. Baier, V.M. Katkov and V.M. Strakhovenko, Nucl. Instr. Meth. A **250**, 514 (1986)

[123] K. Elsener, S.P. Møller, J.B.B. Petersen and E. Uggerhøj, Phys. Lett. B **212**, 537 (1988)

[124] J.W. Cronin, T.K. Gaisser and S.P. Swordy, Scientific American, 32, Jan. 1997

[125] A. Baurichter *et al.*, Nucl. Instr. Meth. B **119**, 143 (1996)

[126] J.A. Gaidos *et al.*, Nature **383**, 319 (1996)
M. Vietri, Phys. Rev. Lett. **78**, 4328 (1997)

[127] A. Baurichter *et al.*, Nucl. Phys. B (Proc. Suppl.) **44**, 79 (1995)

[128] V.A. Baskov *et al.*, Nucl. Instr. Meth. B **122**, 194 (1997)

[129] E.N. Tsyganov, Fermilab TM-682, TM-684, Batavia (1976), unpublished

[130] A.V. Solov'yov, A. Schäfer and W. Greiner, Phys. Rev. E **53**, 1129 (1996)

[131] H. Kudo, Nucl. Instr. Meth. **189**, 609 (1981)

[132] J.A. Ellison and S.T. Picraux, Phys. Lett. A **83**, 271 (1981)

[133] J.A. Ellison, Nucl. Phys. B **206**, 205 (1982)

[134] J.S. Forster *et al.*, Nucl. Phys. B **318**, 301 (1989)

[135] A.M. Taratin and S.A. Vorobiev, Nucl. Instr. Meth. B **47**, 247 (1990)

[136] V. Biryukov, Phys. Lett. A **205**, 340 (1995)

[137] V. Biryukov, Phys. Lett. A **205**, 343 (1995)

[138] A. Schäfer and W. Greiner, J. Phys. G **17**, L217 (1991)

[139] A. Taratin, Nucl. Instr. Meth. B **119**, 156 (1996)

[140] O.I. Sumbaev, in: Relativistic Channeling, eds. R.A. Carrigan and J.A. Ellison, Plenum, 1987

[141] Yu.A. Chesnokov *et al.*, Nucl. Instr. Meth. B **69**, 247 (1992)

[142] V.M. Biryukov and Yu.A. Chesnokov, Nucl. Instr. Meth. B **73**, 153 (1993)

[143] A.A. Greenenko and N.F. Shul'ga, Nucl. Instr. Meth. B **67**, 212 (1992);
A.A. Greenenko and N.F. Shul'ga, Nucl. Instr. Meth. B **90**, 179 (1994);
N.F. Shul'ga and A.A. Greenenko, Phys. Lett. B **353**, 373 (1995)

[144] A.S. Vodop'yanov, *et al.*, Sov. Phys. JETP Lett. **30**, 442 (1979);
A.F. Elishev *et al.*, Phys. Lett. B **88**, 387 (1979)

[145] C.R. Sun *et al.*, Nucl. Instr. Meth. B **2**, 60 (1984)

[146] Physics Today, Search and discovery, 17, May 1980

[147] J.F. Bak *et al.*, Phys. Lett. B **93**, 505 (1980)

[148] V.V. Andreev *et al.*, Sov. Phys. JETP Lett. **36**, 415 (1982);
N.K Bulgakov *et al.*, JINR **1-83** (1983);
V.V. Andreev *et al.*, Sov. Phys. JETP Lett. **36**, 67 (1984);
V.V. Andreev *et al.*, Sov. Phys. JETP Lett. **44**, 129 (1986)

[149] W.M. Gibson *et al.*, Nucl. Instr. Meth. B **2**, 54 (1984)

[150] S.I. Baker *et al.*, Phys. Lett. B **137**, 129 (1984)

[151] J.A. Ellison *et al.*, Nucl. Instr. Meth. B **2**, 9 (1984)

[152] V.V. Avdeichikov *et al.*, JINR **1-84** (1984)

[153] S.I. Baker *et al.*, Nucl. Instr. Meth. A **234**, 602 (1985)

[154] S.I. Baker *et al.*, Nucl. Instr. Meth. A **248**, 301 (1986)

[155] S.P. Møller *et al.*, Phys. Lett. B, **256**, 91 (1991)

[156] H.W. Atherton *et al.*, SL/EA/Note 90-06 (1990), unpublished

[157] S.P. Møller *et al.*, Nucl Instr. Meth. B, **84**, 434 (1994)

[158] A. Baurichter *et al.*, Nucl Instr. Meth. B, **119**, 172 (1996)

[159] J. Klem, Ph.D. Thesis, Helsinki University of Technology, in preparation

[160] G. Vuagnin, CERN/SL/Note 95-24 (AP), unpublished

[161] X. Altuna *et al.*, Phys. Lett. B **357**, 671 (1995)

[162] H. Akbari *et al.*, Phys. Lett. B **313**, 491 (1993)

[163] N. Doble, P. Grafström and L. Gatignon, Nucl. Instr. Meth. B **119**, 181 (1996)

[164] R.A. Carrigan, in: Relativistic Channeling, eds. R.A. Carrigan and J.A. Ellison, Plenum, 1987

[165] A.S. Denisov *et al.*, Nucl. Instr. Meth. B **69**, 382 (1992)

[166] V.I. Baranov *et al.*, Int. J. Mod. Phys. A **2**, 128 (1993);
V.I. Baranov *et al.*, Nucl. Instr. Meth. B **95**, 449 (1995);
Yu.A. Chesnokov, Nucl. Instr. Meth. B **119**, 163 (1996)

[167] D. Chen *et al.*, Phys. Rev. Lett. **69**, 3286 (1992)

[168] D. Websdale, Physics World, 34, april 1993

[169] V.V. Baublis *et al.*, Nucl. Instr. Meth. B **90**, 112 (1994)

[170] V.M. Samsonov, Nucl. Instr. Meth. B **119**, 271 (1996)

[171] S.A. Bogacz, D.B. Cline and D.A. Sanders, Nucl Instr. Meth. B, **119**, 199 (1996)

[172] R.A. Carrigan, Fermilab-FN 454, (1987), unpublished

[173] N.W. Ashcroft and N.D. Mermin - Solid State Physics, Saunders College Publishing, 1976

[174] R.A. Carrigan, W.M. Gibson, C.R. Sun and E.N. Tsyganov, Nucl. Instr. Meth. B **194**, 205 (1982)

[175] V.V. Boiko *et al.*, Project proposal, JINR, subm. to International Science and Technology Center, 1995

[176] A.D. Kovalenko *et al.*, JINR **4**, 9 (1995);
A.D. Kovalenko, private communication, 1996

[177] A. Freund and R. Hustache, private communication, 1995

[178] W. Herr, private communication, 1995

[179] S.I. Baker, in: Relativistic Channeling, eds. R.A. Carrigan and J.A. Ellison, Plenum, 1987

[180] G.H. Wang *et al.*, Nucl. Instr. Meth. **218**, 669 (1983)

[181] Yu.A. Chesnokov *et al.*, Int. J. Mod. Phys. A **2**, 173 (1993)

[182] S.I. Baker *et al.*, Nucl. Instr. Meth. B **90**, 119 (1994)

[183] S.P. Ahlen, Rev. Mod. Phys. **52**, 121 (1980)

[184] S.P. Timoshenko and J.N. Goodier - Theory of elasticity, McGraw-Hill, 1970

[185] E. Schmid and W. Boas - Plasticity of crystals, F.A. Hughes, 1950

[186] M. Krisch, A. Freund, G. Marot and L. Zhang, Nucl. Instr. Meth. A **308**, 378 (1991)

[187] S.P. Timoshenko and S. Woinowsky-Krieger - Theory of Plates and shells, McGraw-Hill, 1968

[188] J. Klem and U. Mikkelsen, SL-MD Note 171, CERN, 1995, unpublished

[189] N. Doble, private communication, 1996

[190] C. Biino *et al.*, Proc. European Particle Accelerator Conference, Sitges, 2385 (1996)

[191] C. Biino *et al.*, Phys. Lett. B **403**, 163 (1997)
C. Biino *et al.*, Proc. Particle Accelerator Conference, Vancouver (1997)

[192] G. Arduini *et al.*, subm. to Phys. Rev. Lett. (1997)
C. Biino *et al.*, Proc. Particle Accelerator Conference, Vancouver (1997)
G. Arduini *et al.*, Proc. Particle Accelerator Conference, Vancouver (1997)

[193] G. Fraser (editor), CERN Courier, CERN, feb. 1997

[194] A. Taratin, private communication, 1996

[195] M.R. Spiegel - Mathematical Handbook, McGraw-Hill (Schaum's series), 1968
V.M. Biryukov, Rad. Eff. **25**, 143 (1993)

[196] L.D. Landau and E.M. Lifshitz - The Classical Theory of Fields, Pergamon Press, 1975